Single-photon detection techniques for underwater imaging

Aurora Maccarone

Submitted for the degree of Doctor of Philosophy

Heriot-Watt University

School of Engineering and Physical Sciences

October 2016

ABSTRACT

This Thesis investigates the potential of a single-photon depth profiling system for imaging in highly scattering underwater environments. This scanning system measured depth using the time-of-flight and the time-correlated single-photon counting (TCSPC) technique. The system comprised a pulsed laser source, a monostatic scanning transceiver, with a silicon single-photon avalanche diode (SPAD) used for detection of the returned optical signal.

Spectral transmittance measurements were performed on a number of different water samples in order to characterize the water types used in the experiments. This identified an optimum operational wavelength for each environment selected, which was in the wavelength region of 525 - 690 nm. Then, depth profiles measurements were performed in different scattering conditions, demonstrating high-resolution image re-construction for targets placed at stand-off distances up to nine attenuation lengths, using average optical power in the sub-milliwatt range. Depth and spatial resolution were investigated in several environments, demonstrating a depth resolution in the range of 500 μm to a few millimetres depending on the attenuation level of the medium. The angular resolution of the system was approximately 60 μrad in water with different levels of attenuation, illustrating that the narrow field of view helped preserve spatial resolution in the presence of high levels of forward scattering.

Bespoke algorithms were developed for image reconstruction in order to recover depth, intensity and reflectivity information, and to investigate shorter acquisition times, illustrating the practicality of the approach for rapid frame rates. In addition, advanced signal processing approaches were used to investigate the potential of multispectral single-photon depth imaging in target discrimination and recognition, in free-space and underwater environments. Finally, a LiDAR model was developed and validated using experimental data. The model was used to estimate the performance of the system under a variety of scattering conditions and system parameters.

Acknowledgements

Over these years I was extremely lucky to meet amazing people who made this journey unique.

Firstly, I want to thank my supervisor, Professor Gerald Buller, for his guidance and support during this PhD project. I am really grateful to him for directing me on the right way every time I run into problems with my work, and for pushing me to always achieve a better result. I would like to thank also my second supervisor Professor Yvan Petillot and Professor Andy Wallace for their support and suggestions during these years. Many thanks also to Dr. Aongus McCarthy for his priceless help and suggestions during each step of my work, and for dealing with all my questions, from the most difficult to the most stupid. I thank Dr. Ximing Ren for his help in the laboratory and following me in the first stage of the project. I want to express my gratitude also to the other members (old and new!) of the Single Photon Group, in particular to Dr. Robert Collins and Rachael Tobin for filtering my Italian English and helping me to provide a grammatically correct Thesis to Gerald. Thanks go also to Dr. Aongus McCarthy, Dr. Ross J. Donaldson, Dr. Ryan E. Warburton, and Dr. Giuseppe Intermite for all the effort they put in filling and emptying the tank every single time I asked for help because I couldn't make it. I want to thank also Dr. Yoann Altmann, Dr. Abderrahim Halimi, Puneet Chhabra, and Prof. Andy Wallace for their great contribution on processing the data collected during this PhD work. Thanks to the Defence Science and Technology Laboratory (DSTL) for funding this project; I would like to thank in particular Dr. Richard Hollins and Prof. James Moffat, who always followed this work with interest.

Thanks to my office mates Ross, Rachael, Kateryna, Adrian, Nathan, William, and Ugo. You always made my day. I want to dedicate also a special thanks to Ross, Rosario, Richard, Alice, Alessandro, Agata, Francesca, Giuseppe, Andrea, Shraddha, Eleonora…unfortunately I cannot mention you all, but thank you for being such a good company and friends!

Finally, the most grateful and important thanks is for my family. I love you all and I want to let you know that all my achievements were possible only because of your support and love, even during the most difficult times.

Once again, thank you all for this incredible experience!

ACADEMIC REGISTRY
Research Thesis Submission

Name*:*	
School:	
Version: *(i.e. First, Resubmission, Final)*	Degree Sought:

Declaration

In accordance with the appropriate regulations I hereby submit my thesis and I declare that:

1) the thesis embodies the results of my own work and has been composed by myself
2) where appropriate, I have made acknowledgement of the work of others and have made reference to work carried out in collaboration with other persons
3) the thesis is the correct version of the thesis for submission and is the same version as any electronic versions submitted*.
4) my thesis for the award referred to, deposited in the Heriot-Watt University Library, should be made available for loan or photocopying and be available via the Institutional Repository, subject to such conditions as the Librarian may require
5) I understand that as a student of the University I am required to abide by the Regulations of the University and to conform to its discipline.
6) I confirm that the thesis has been verified against plagiarism via an approved plagiarism detection application e.g. Turnitin.

* *Please note that it is the responsibility of the candidate to ensure that the correct version of the thesis is submitted.*

Signature of Candidate*:*		Date:	

Submission

Submitted By *(name in capitals):*	
Signature of Individual Submitting:	
Date Submitted:	

For Completion in the Student Service Centre (SSC)

Received in the SSC by *(name in capitals):*		
Method of Submission (Handed in to SSC; posted through internal/external mail):		
*E-thesis Submitted (**mandatory for final theses**)*		
Signature:		Date:

TABLE OF CONTENTS

LIST OF PUBLICATIONS BY THE CANDIDATE

Papers published in peer reviewed Journals

A. Maccarone, A. McCarthy, X. Ren, R. E. Warburton, A. M. Wallace, J. Moffat, Y. Petillot, G. S. Buller, *Underwater depth imaging using time-correlated single-photon counting*, Opt. Express, 23, 26, pp. 33911-33926 (2015).

A. Halimi, **A. Maccarone**, A. McCarthy, S. McLaughlin, G. S. Buller, *Object depth profile and reflectivity restoration from sparse single-photon data acquired in underwater environments*, arXiv: 1608.06143 (2016) − Submitted for publication to IEEE Trans. Comput. Imaging, Special Issue on Extreme Imaging.

Y. Altmann, **A. Maccarone**, A. McCarthy, G. Newstadt, G. S. Buller, S. McLaughlin, A. Hero, *Robust spectral unmixing of multispectral lidar waveforms using gamma markov random fields*, to be submitted to IEEE Trans. Comput. Imaging in October-November 2016.

Conference proceedings

A. Maccarone, A. McCarthy, X. Ren, R. E. Warburton, A. M. Wallace, J. Moffat, Y. Petillot, G. S. Buller, *Underwater depth imaging using time-correlated single-photon counting*, SPIE Security and Defence, Baltimore, USA (April 2015).

Y. Altmann, **A. Maccarone**, A. McCarthy, G. S. Buller, S. McLaughlin, *Joint range estimation and spectral classification for 3D scene reconstruction using multispectral LiDAR waveforms*, IEEE Statistical Signal Processing 2016, Palma De Mallorca, Spain (June 2016).

Y. Altmann, **A. Maccarone**, A. McCarthy, G. Newstadt, G. S. Buller, S. McLaughlin, A. Hero, *Robust spectral unmixing of multispectral LiDAR waveforms*, 8th Workshop on Hyperspectral Image and Signal Processing: Evolution in Remote Sensing (WHISPERS), Los Angeles, USA (August, 2016).

Y. Altmann, **A. Maccarone**, A. McCarthy, G. S. Buller, S. McLaughlin, *Joint spectral clustering and range estimation for 3D scene reconstruction using multispectral LiDAR waveforms*, IEEE European Signal Processing Conference (EUSIPCO), Budapest, Hungary (August 2016).

Y. Altmann, **A. Maccarone**, A. Halimi, A. McCarthy, G. S. Buller, S. McLaughlin, *Fast range estimation and material quantification from multispectral LiDAR waveforms*, Sensor Signal Processing for Defence, Edinburgh, UK (September 2016).

P. S. Chhabra, **A. Maccarone**, A. McCarthy, A. M. Wallace, G. S. Buller, *Discriminating underwater LiDAR target signatures using sparse multi-spectral depth codes*, Sensor Signal Processing for Defence, Edinburgh, UK (September 2016).

A. Maccarone, A. McCarthy, A. Halimi, R. Tobin, A. M. Wallace, Y. Petillot, G. S. Buller, *Depth imaging in highly scattering underwater environments using time-correlated single photon counting*, SPIE Security and Defence, Edinburgh, UK (September 2016).

Chapter 1

Introduction

The use of optical systems in exploring the underwater world has a long history which stretches back to ancient Greek and Roman times. According to a legend, Alexander The Great was fascinated by the underwater world, and it is thought that he actually had been underwater using a diving bell [1]. A tempera painting from the *Bellifortis*, a manuscript by the German military engineer Konrad Keyser of approximately 1405, reproduces Alexander The Great in a glass diving bell underwater (Figure 1.1a). In the same manuscript Konrad Keyser shows the first design of a diving suite (Figure 1.1b) [2]. Since then, underwater exploration techniques developed slowly over the centuries until the introduction of compressed air in 1825, which signed the beginning of advanced underwater exploration.

Figure 1.1. Tempera paintings from the Bellifortis (Konrad Keyser, 1405).
a) Alexander The Great in a glass diving bell underwater. From [1]. b)
First known design of a diving suite. From [3].

Development in diving techniques allowed for the establishment of underwater optical imaging as a useful tool in oceanography, marine zoology and exploration. Since the first underwater photography in the 1890s, underwater imaging has seen several landmarks.

One of the greatest advances was achieved with the invention of laser, which helped assist efforts in active imaging. However, due to the strong attenuation of light in water, obtaining high resolution images of targets placed at long stand-off distances was still a challenge. In particular, the main limitation is due to light forward and backscattered from underwater particles. Forward scattering is due to small angle scattering events that slightly deviate the light while travelling from the source to the target and on the way back to the receiver, causing the image to be blurred, hence reducing the spatial resolution of the image. Backscattering is due to light that has not interacted with the target, and it is scattered back to the receiver because of the turbidity of the medium, drastically reducing the contrast of the image. Several techniques were developed to limit the deleterious effect of scattering, and typically high resolution images can be obtained at short stand-off distances. If the application requires a longer range, resolution and contrast are strongly affected by scattering, eventually degrading the image to such an extent that it cannot perform target recognition.

The work performed during this PhD project aimed to characterise a depth imaging system based on single-photon detection techniques, in order to overcome some of limitations typically found in underwater active imaging. The depth imaging system discussed in this Thesis is based on the time-of-flight approach using the time-correlated single-photon counting (TCSPC) technique. In this work, the high sensitivity and picosecond resolution of the TCSPC technique were exploited to their full extent to obtain depth profiles of objects underwater at stand-off distances up to 9 attenuation lengths from the scanning unit. To the best of author's knowledge, this represents the first application of the TCSPC technique to underwater depth imaging, allowing the longest stand-off distance underwater observed using a monostatic optical system.

In addition, a number of algorithms based on spatial correlation between neighbouring pixels were developed in order to allow for the reconstruction of images in highly scattering environments, and the investigation of shorter acquisition times more compatible with the end applications. The potential of the system was also investigated for multispectral depth imaging, for the validation of bespoke advance signal processing.

The system used to obtain the results in this Thesis was originally designed and constructed by the Single-Photon Group at Heriot-Watt University for single-photon

depth imaging over long distances in free-space, typically with near-infrared wavelengths [4]. This system has been successfully used in free-space to demonstrate centimetre resolution at kilometre ranges using eye-safe levels of laser power, whilst operating under a variety of daylight and weather conditions [5].

1.1. Thesis structure

Chapter 2 gives a brief overview on the main optical system developed to image man-made objects underwater. Although few examples of early imagers are presented, particular attention is given to laser-based imaging systems. A discussion on the main limitations of underwater optical systems is performed in order to explain the most important techniques developed over the years.

Chapter 3 explains the time-correlated single-photon counting technique, highlighting why this technique is suitable for applications in photon-starved environments, for example imaging in highly attenuating environments. In addition, the principles of operation of single-photon detectors is outlined, as well with the key performance characteristics of the single-photon detectors. Specific attention is given to silicon single-photon detectors, which are the detectors used in the experiments reported in this Thesis. However, single photon detectors for the infrared wavelength range will be introduced for comparison and completeness.

Chapter 4 discusses propagation of light in water, relating absorption and scattering to the total attenuation coefficient of the propagation medium. On the basis of the Lambert-Beer law, the chapter describes also the experiments performed to obtain transmittance and attenuation spectra of the water samples subsequently used for the depth profiles measurements. These measurements permitted the selection of an appropriate operational wavelength for each of the different scattering levels of the environments considered in this Thesis.

Chapter 5 provides a full description of the system used to obtain the results reported in this Thesis, as well with the alignment procedure followed before each experiment. Then, the potential of the system is investigated for different optical configurations of the scanning unit. Firstly, preliminary measurements were performed to study the major issues with the system, and identify suitable solutions to improve the system for

underwater imaging. Secondly, several modifications were made to the system on the basis of the preliminary measurements. The improved system was characterised in several underwater environments, demonstrating depth imaging performed at target distances of up to 6 attenuation lengths using average optical power in the sub-milliwatt range [6, 7]. Thirdly, further improvements were performed in order to allow for imaging in highly scattering environments, demonstrating depth imaging performed over distances of up to 9 attenuation lengths [8]. Additionally, the chapter reports a study on the spatial and depth resolution in several underwater conditions.

Chapter 6 show three different methods which allow for the reconstruction of depth and intensity images by means of exploiting spatial correlations between neighbouring pixels. The first algorithm is based on the sparseness of the Discrete Cosine Transformation (DCT) coefficients. This model allowed for depth and intensity images reconstruction when short acquisition times per pixel are considered [8]. Two other analysis techniques based on Markov Chain Monte Carlo (MCMC) and Coordinate Descent Algorithm (CDA) are proposed, allowing for joint depth and reflectivity restoration in different scattering conditions [9].

Chapter 7 proposes a model based on a photon-counting version of the LiDAR range equation. The model aims to evaluate the system's time-of-flight ranging performance in water, on the basis of several parameters, including average optical power, attenuation of optical components, and attenuation of the environment. The chapter shows also the results of several simulations, which were carried out in order to evaluate the maximum achievable distance for different environments.

Chapter 8 investigates the potential of the system for multispectral depth imaging. The chapter describes several experiments performed to validate bespoke algorithms based on MCMC approach using spatial correlations. The models allow for spectral classification of different targets, and for quantification of known materials in the targets in free-space [10-13] and in unfiltered tap water [14].

Chapter 9 summarises the experimental results obtained and the conclusions for each chapter, as well with a discussion about future work.

References

1.   J. S. Jaffe, "Underwater optical imaging - The past, the present, and the prospects," IEEE J. Oceanic Eng. **40**, 3, 1-18 (2015).

2.   J. Watson, and O. Zielinski, *Subsea optics and imaging* (Woodhead Publishing Limited, 2013).

3.   H. Talhoffer, "Thott Fechtbuch," (1459).

4.   A. McCarthy, R. J. Collins, N. J. Krichel, V. Fernandez, A. M. Wallace, and G. S. Buller, "Long-range time-of-flight scanning sensor based on high-speed time-correlated single-photon counting," Appl. Opt. **48**, 32, 6241-6252 (2009).

5.   A. McCarthy, X. Ren, A. Della Frera, N. R. Gemmell, N. J. Krichel, C. Scarcella, A. Ruggeri, A. Tosi, and G. S. Buller, "Kilometer-range depth imaging at 1550 nm wavelength using an InGaAs/InP single-photon avalanche diode detector," Opt. Express **21**, 19, 22098-22114 (2013).

6.   A. Maccarone, A. McCarthy, X. Ren, R. E. Warburton, A. M. Wallace, J. Moffat, Y. Petillot, and G. S. Buller, "Underwater depth imaging using time-correlated single-photon counting," Opt. Express **23**, 26, 33911-33926 (2015).

7.   A. Maccarone, A. McCarthy, X. Ren, R. E. Warburton, A. M. Wallace, J. Moffat, Y. Petillot, and G. S. Buller, "Underwater depth imaging using time-correlated single photon counting," in Proc. SPIE 9492, Advanced Photon Counting Techniques IX, 94920I (SPIE, Baltimore, USA, 2015).

8.   A. Maccarone, A. McCarthy, A. Halimi, R. Tobin, A. M. Wallace, Y. Petillot, and G. S. Buller, "Depth imaging in highly scattering underwater environments using time correlated single photon counting," in *SPIE Security and Defence* (Edinburgh, UK, September 2016).

9.   A. Halimi, A. Maccarone, A. McCarthy, S. McLaughlin, and G. S. Buller, "Object depth profile and reflectivity restoration from sparse single-photon data acquired in underwater environments," arXiv: 1608.06143 (2016).

10.   Y. Altmann, A. Maccarone, A. Halimi, A. McCarthy, G. S. Buller, and S. McLaughlin, "Fast range estimation and material quantification from multispectral LiDAR waveforms," in *Sensor Signal Processing for Defence*(Edinburgh, UK, September 2016).

11.   Y. Altmann, A. Maccarone, A. McCarthy, G. S. Buller, and S. McLaughlin, "Joint spectral clustering and range estimation for 3D scene reconstruction using multispectral LiDAR waveforms," in *European Signal Processing Conference (EUSIPCO)*(IEEE, Budapest, Hungary, August 2016).

12.   Y. Altmann, A. Maccarone, A. McCarthy, G. S. Buller, and S. McLaughlin, "Joint range estimation and spectral classification for 3D scene reconstruction using multispectral LiDAR waveforms," in *IEEE Statistical Signal Processing 2016*(Palma De Mallorca, June 2016).

13.   Y. Altmann, A. Maccarone, A. McCarthy, G. Newstadt, G. S. Buller, S. McLaughlin, and A. Hero, "Robust spectral unmixing of multispectral LiDAR waveforms," in *8th Workshop on Hyperspectral Image and Signal Processing: Evolution in Remote Sensing (WHISPERS)*(Los Angeles, USA, August 2016).

14.   P. S. Chhabra, A. Maccarone, A. McCarthy, A. M. Wallace, and G. S. Buller, "Discriminating underwater LiDAR target signatures using sparse multi-spectral depth codes," in *Sensor Signal Processing for Defence* (Edinburgh, UK, September 2016).

Chapter 2

Underwater optical imaging systems

2.1. Introduction

Imaging in an underwater environment with an optical system presents several challenges for optics, robotics, and signal processing communities. This chapter aims to give a brief overview on the main optical system developed to image man-made objects underwater. The systems will be classified depending on the technology, light source, and technique used to obtain the image. A wide classification will be given in section 2.2, as well with a few examples of early imagers. Then, particular attention will be given to laser-based systems, and section 2.3 will highlight the main limitation of these systems. Sections 2.4 - 2.8 will describe the main techniques developed to overcome these limitations.

2.2. Underwater imaging system classification

Underwater optical imaging is a field of increasing interest in a range of applications, including defence [1], marine science [2], and civil engineering [3]. Obtaining two- and three-dimensional images of underwater terrains has long been the domain of sonar-based systems. The main advantage of sonar is that a long range can be achieved, as sound propagates for long distances underwater and it is less affected by scattering from particles in the water. However, acoustic underwater systems are not able to achieve a high spatial resolution, limiting the quality of the image. On the contrary, optical systems allow for high resolution images, but this comes at the cost of a much shorter achievable range due to the high optical attenuation levels in water. Hence, acoustic and optical approaches are complementary, offering very different performance. In this chapter, specific attention will be given to optical systems in order to provide a review of the main techniques used and existing optical systems for underwater imaging.

The performance of underwater optical systems is strongly limited by the attenuation of light in water. This results in photons being absorbed or scattered on the way from the system to the target and on the way back to the system. These two effects can be described through the absorption coefficient a and the scattering coefficient b, respectively, which both contribute to the total attenuation coefficient $\alpha = a + b$. Therefore, the optical power

which propagates a distance x, decays exponentially as a function of the attenuation coefficient [4]:

$$P(x) = P_0 e^{-(a+b)x} = P_0 e^{-\alpha x} \qquad \text{Equation 2.1}$$

The product αx in the exponent defines the number of attenuation lengths, meaning that one attenuation length is the distance after which the light power is reduced to 1/e of its initial value. This parameter allows for the comparison of underwater optical imaging systems based on different technologies.

Several optical imaging systems are available and they can be divided in two main classes, passive and active systems. Passive systems use natural light for illumination, while active systems employ an artificial light source. In the latter case, the source and the receiver can be arranged in three different architectures: monostatic, pseudo-monostatic, and bi-static. In a monostatic configuration, the source and the receiver are in the same system platform and share one or more optical elements. While in a pseudo-monostatic configuration, source and receiver are on the same system platform but have dedicated optical setups. A bi-static configuration uses two separated platforms for the source and receiver [5].

When not coupled with a strobe or an artificial light, cameras are an example of a passive imaging system. According to a communication with the British Journal of Photography in 1985, the first underwater photograph was taken by solicitor and natural historian William Thompson [6]. In 1856 Thompson lowered to a depth of approximately 6 metres a wooden box containing a 13×10 cm^2 plate camera, obtaining the first underwater image using an exposure of ten minutes. Unfortunately, the pressure underwater was high enough to allow water to leak into the wooden box, ruining the image taken by Thompson. For this reason, some of the literature reports the French marine zoologist Louis Boutan [6] as the first who took a photograph underwater. In 1893, Boutan used a plate camera in a wooden box similar to Thompson's equipment, but manually used the camera underwater. He was able to take a photograph of himself at a depth of approximately 50 metres in the French Mediterranean coast. The photograph is shown in Figure 2.1. Due to the depth and the low light level, Boutan used an exposure of 30 minutes, requiring him to stay underwater for hours. Eventually, Boutan was able to include a magnesium

powder lamp in his equipment, which drastically reduced the exposure time [6], and represented the first example of an active system used underwater.

Figure 2.1. First published underwater photograph. The photograph was taken by the marine zoologist Louis Boutan. From [6].

Since the first photograph, underwater photography has seen several landmarks. For example, improvements in photography films brought about the first underwater colour photograph in 1926, taken by scientist William Longley and photographer Charles Martin. Advances in underwater cameras, lighting, and robotics led to the historical photographs set of the Titanic shipwreck in 1985. Oceanographer Robert Ballard and photographer Emory Kristof used the remotely operated vehicle ARGO [7], shown in the photograph in Figure 2.2a), which was equipped with film and video cameras. The video system inspected the seabed at a depth of approximately 3800 metres in the North Atlantic Ocean, which allowed for the location of the shipwreck. The first image obtained with the video system revealed one of the boilers of the Titanic (Figure 2.2b), confirming in real-time that the shipwreck was nearby. Once the shipwreck was identified, the film cameras recorded more than 20,000 photographs, providing detailed information on the damage caused by the iceberg that sank the Titanic.
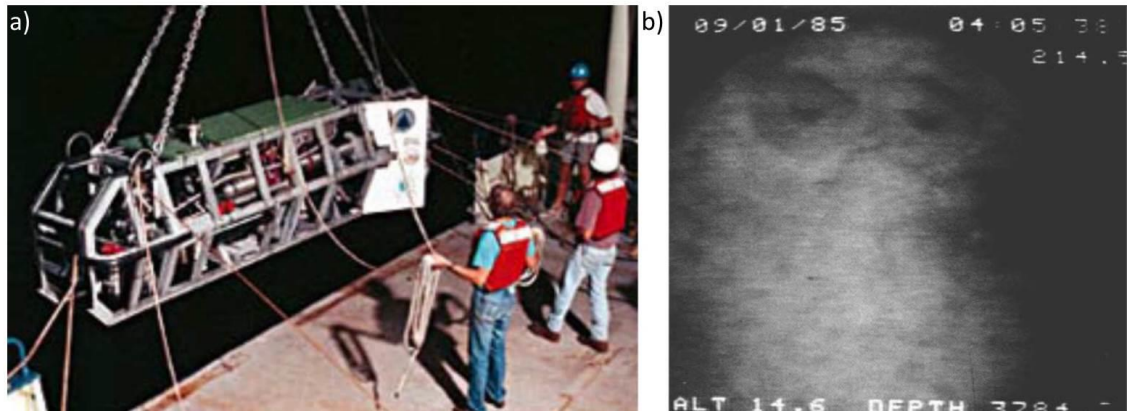
Figure 2.2. a) Photograph of the ARGO system. b) First image of the boilers of the Titanic, obtained with a video taken in 1985. Both from [8].

Over the last few decades, advances in silicon CMOS focal plane arrays has seen a shift from film cameras to digital cameras, greatly improving achievable range and resolution. Under ideal illumination conditions, digital cameras are able to image up to 3 attenuation lengths [9] whilst maintaining an acceptable level of image resolution and contrast. However, advances in solid-state lasers have allowed further progress to be made in underwater imaging systems and techniques. These technological advances have enabled some of the most difficult challenges in the underwater environment to be tackled, as discussed in the next section.

2.3. Active systems

Since Boutan's pioneering work, many of the complications of the underwater environment have been identified, including water and pressure resistant camera enclosures, suitable power supplies, lighting, and several other problems related to scattering underwater still experienced by the most modern systems.

The invention of the laser permitted the exploration of new techniques, which sought to improve the resolution, contrast, and range achievable with an underwater optical system. Indeed, significant improvements in image quality at longer distances can be obtained with active systems, in particular with systems that use a laser as their light source. However, adding a light source to an imaging system can significantly reduce the image contrast and resolution due to scattering of light in water. In this case further considerations on the propagation of light in water have to be discussed.

Although a more in-depth overview of the attenuation of light in water will be given in Chapter 4, it is important to say that absorption is strongly dependent on the wavelength. Hence, to mitigate the effect of absorption of light in water, the wavelength of the laser source can be selected to correspond to a minimum of absorption, typically towards the blue-green region of the visible spectrum. However, scattering events should also be considered at the same time. Scattering comprises several contributions, which are shown schematically in Figure 2.3. Multiple backscatter is light scattered back to the receiver because of the turbidity of the medium, and has not interacted with the target. Volume backscatter is caused by the overlap of the outgoing light and the receiver field of view. These two contributions act as clutter returns, causing a reduction in the contrast of the image. The last contribution is forward scattered light, which is caused by small angle scattering events that slightly deviate the light while travelling from the source to the target and on the way back to the receiver. Forward scattered light causes the image to be blurred, reducing the resolution.
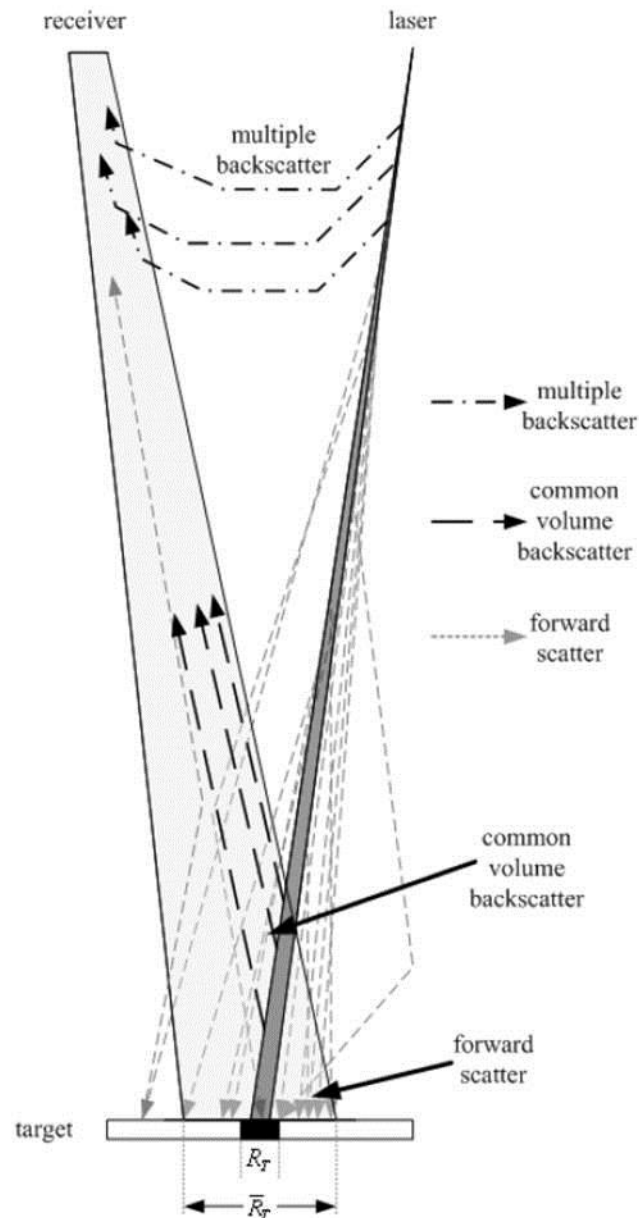
Figure 2.3. Schematic representation of scattered light. From [10].

Several techniques were developed in order to limit the effect of scattering. They can be summarised in three main categories: temporal discrimination, spatial discrimination, and modulation discrimination. Each technique will be discussed in the subsequent sections alongside a few examples of active systems based on laser techniques.

2.4. Temporal discrimination

Several methods have been devised to reduce the limiting effect of scattered light when imaging in underwater environments. An example is time-gated imaging, where the receiver is time-gated to only allow a detected signal in correlation with the expected return of the pulsed illumination from the target, hence removing much of the

backscattered light whilst maintaining the full return signal. A schematic of this approach is shown in Figure 2.4. In Figure 2.4a), the system emits a laser pulse, which propagates to the target (Figure 2.4b). The gating is maintained closed while the light pulse travels to the target and from the target to the system. In Figure 2.4c), the light pulse reflected by the target reaches the system, the gating is open and the receiver is able to collect the signal from the target.
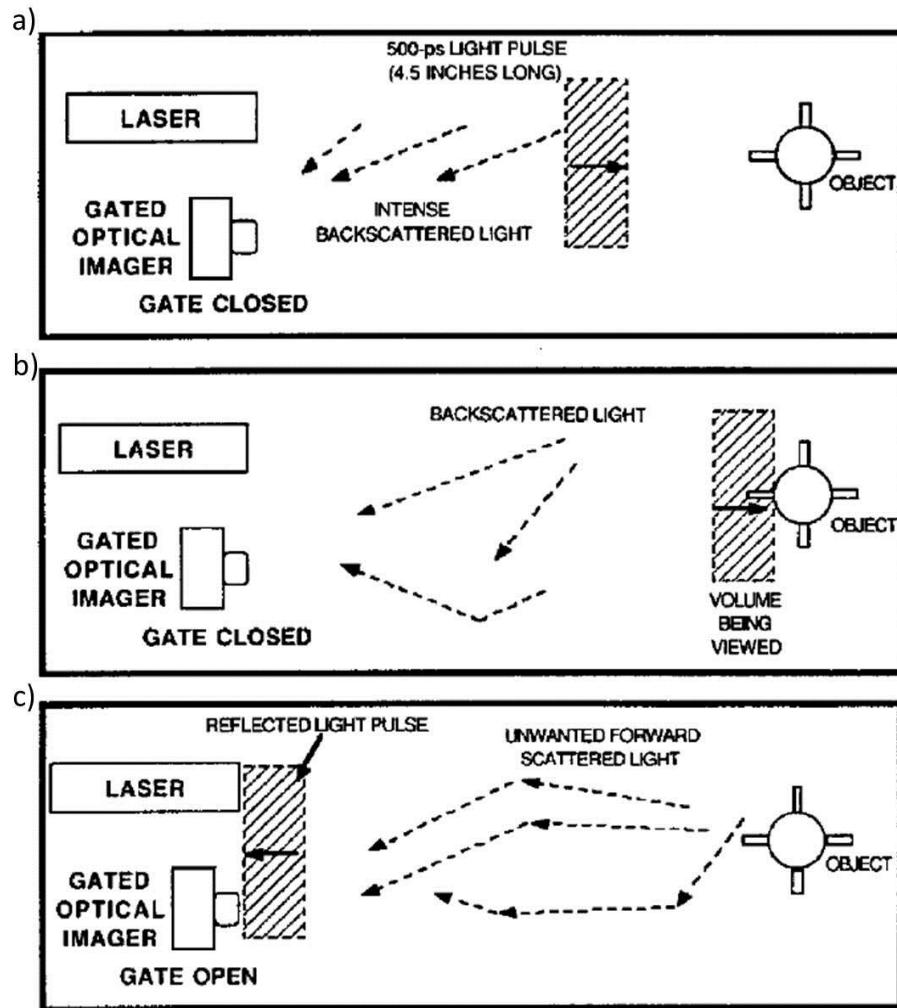
Figure 2.4. Schematic of the principle of the time-gated technique in underwater imaging. (a) The system emits a laser pulse, (b) which propagates to the target. The gate of the imager is closed in a) and b), while in (c) it is open in correspondence with the reflected light pulse arriving back at the system. From [11].

To the best of the author's knowledge, the first example of time-gated experiment was performed by *Heckman et al.* in 1967 [12]. The experimental setup comprised a laser source, yielding a 20 ns duration pulse at the wavelength $\lambda = 530$ nm and optical power of approximately 500 μW. The receiver was a film image-converter camera gated by

means of a wire grid, controlled by an external voltage. The schematic of the experimental setup is shown in Figure 2.5.
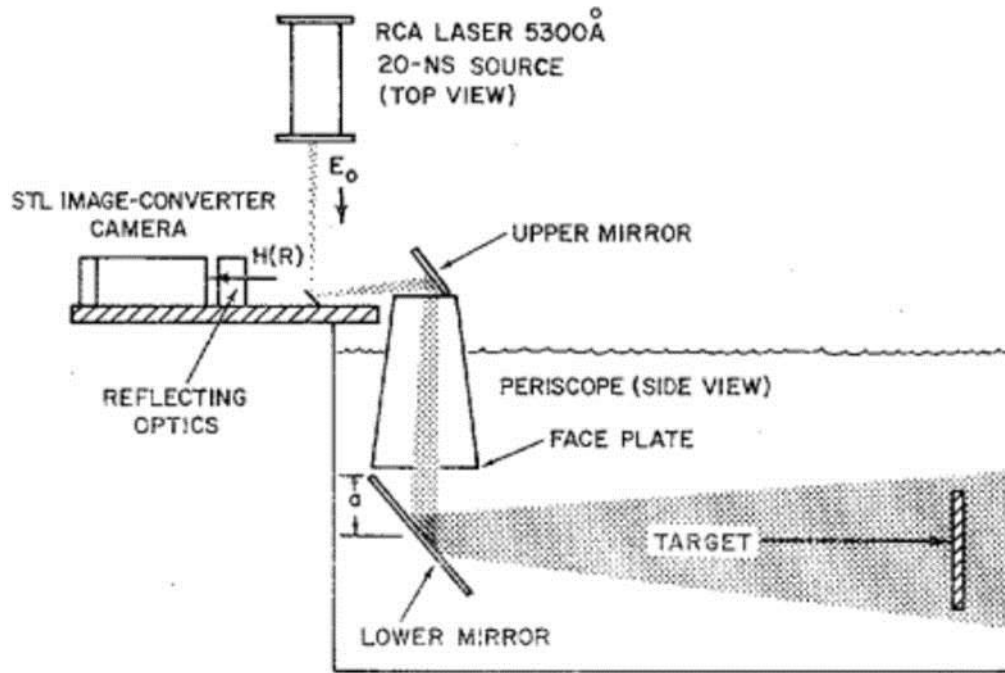
Figure 2.5. Schematic of the experimental setup developed by Heckman et al. in 1967. The system comprised a pulsed laser source with wavelength λ = 530 nm, and average optical power of approximately 500 μW. The receiver was a gated film image converter camera. From [12].

With this setup, *Heckman et al.* demonstrated the advantages of the gated technique with respect to non-gated techniques, taking several photographs of a target consisting of a black tape cross on a reflective material. The improvement in the image is evident in the example shown in Figure 2.6. The figure shows two photographs of the black tape cross target placed at a stand-off distance of 3.5 attenuation lengths. The photograph in Figure 2.6a) is taken with the gated technique and it is possible to discern the target. While Figure 2.6b) shows the non-gated photograph of the target under the same conditions. In this case, the target is not visible due to the strong effect of the backscattered light.
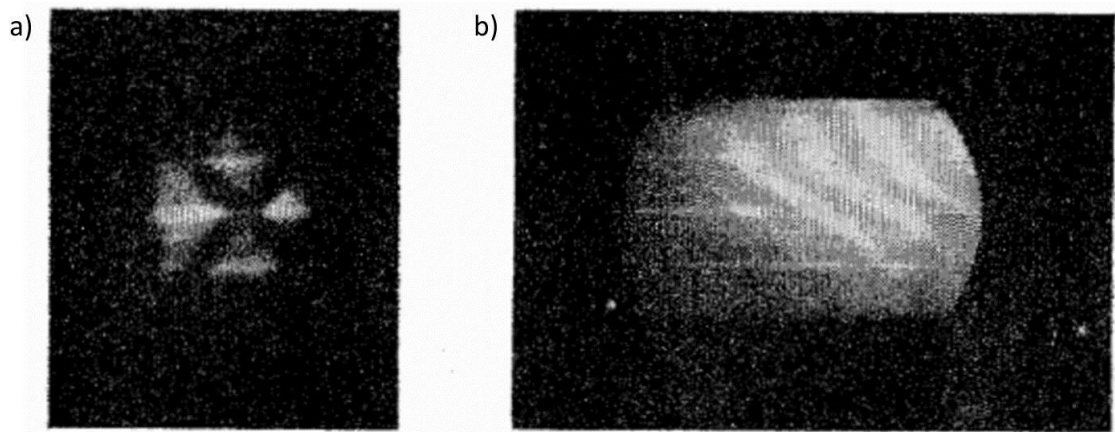
Figure 2.6. Photograph of the black cross target taken with (a) a gated and (b) non-gated configuration. The system comprised a pulsed laser source with wavelength λ = 530 nm, and average optical power of approximately 500 μW. The receiver was a film image converter camera. The target was at a stand-off distance of 3.5 attenuation lengths. The target is visible in the photograph shown in a), while in b) it is not possible to discern the target because of the effect of backscattering.

Another example of an underwater range gated system was developed by *Fournier et al.* in 1993 [13]. In its first version, the Laser Underwater Camera Image Enhancer (LUCIE system) comprised a gated CCD camera and a pulsed laser source with 532 nm central wavelength at a repetition rate of 2 kHz, and an average optical power of 80 mW. The system was mounted on a remotely operated vehicle (ROV) designed to dive to a maximum depth of 200 m. With this technique, *Fournier et al.* were able to increase the operational range by a factor 3 when compared to passive vision, meaning an achievable operational range of approximately 3-4 attenuation lengths. At a later stage, they improved the original system to include a larger field of view, an illumination field matched to camera field of view, and an improved user interface. In addition, the system was placed in a more compact ROV, making the manoeuvrability easier for the user. The improved system was called LUCIE II, and allowed for images up to approximately 5 attenuation lengths [14, 15]. A third version of the same system was developed between 2006 and 2009, and in this case the improvements were dedicated mostly to the ROV. Reduced weight, size, and power consumption allowed the construction of a handheld system, which could be used by divers [16]. Photographs of the three systems are shown in Figure 2.7.
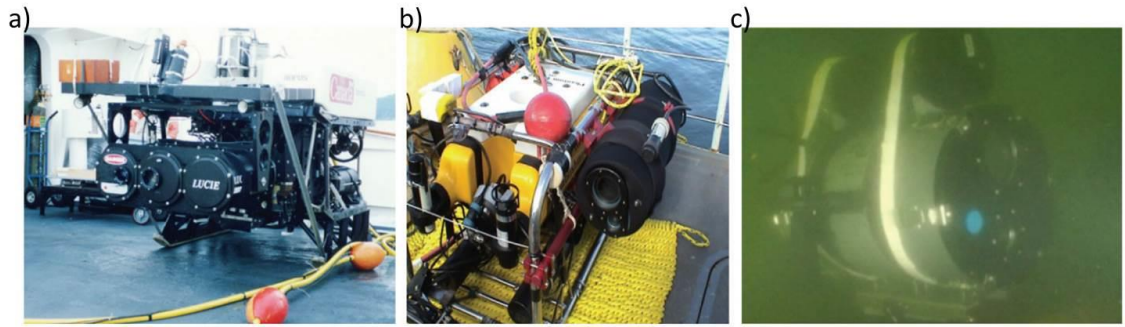
Figure 2.7. Three generations of the LUCIE system. a) Photograph of LUCIE (1990-1996). b) Photograph of LUCIE II (1998-2006). c) Photograph of LUCIE (2009). From [17].

However, LUCIE systems obtained only 2-D images by gated-viewing. A system based on similar hardware was developed by *Busck* in 2005, with the addition of an algorithm to construct an underwater 3-D image. The system recorded a sequence of 2-D images with different gating windows. The gating width was increased with a known regular step, which allowed the algorithm to return 3-D underwater profiles, at the same operational range [18]. Figure 2.8 shows few examples of depth profiles obtained with this system. The target was a cone section 5 cm high, with top diameter equal to 6 cm, and bottom diameter equal to 12 cm. The target was camouflaged with sand and placed on a sandy floor, meaning a low contrast scenario, as shown in the photograph in Figure 2.8a). Figure 2.8b) shows the depth profile of the target placed in sea water at a stand-off distance of 5 metres from the system. The graphs in c) and d) show the depth profiles obtained at 4 metres of stand-off distance in sea water and tap water, respectively. No information was given about the attenuation coefficient of the sea water, hence it was not possible to estimate the stand-off distances of the target in attenuation lengths. However, 4 metres in unfiltered tap water was typically equivalent to approximately a half attenuation length, when the laser source uses a wavelength in the green region.
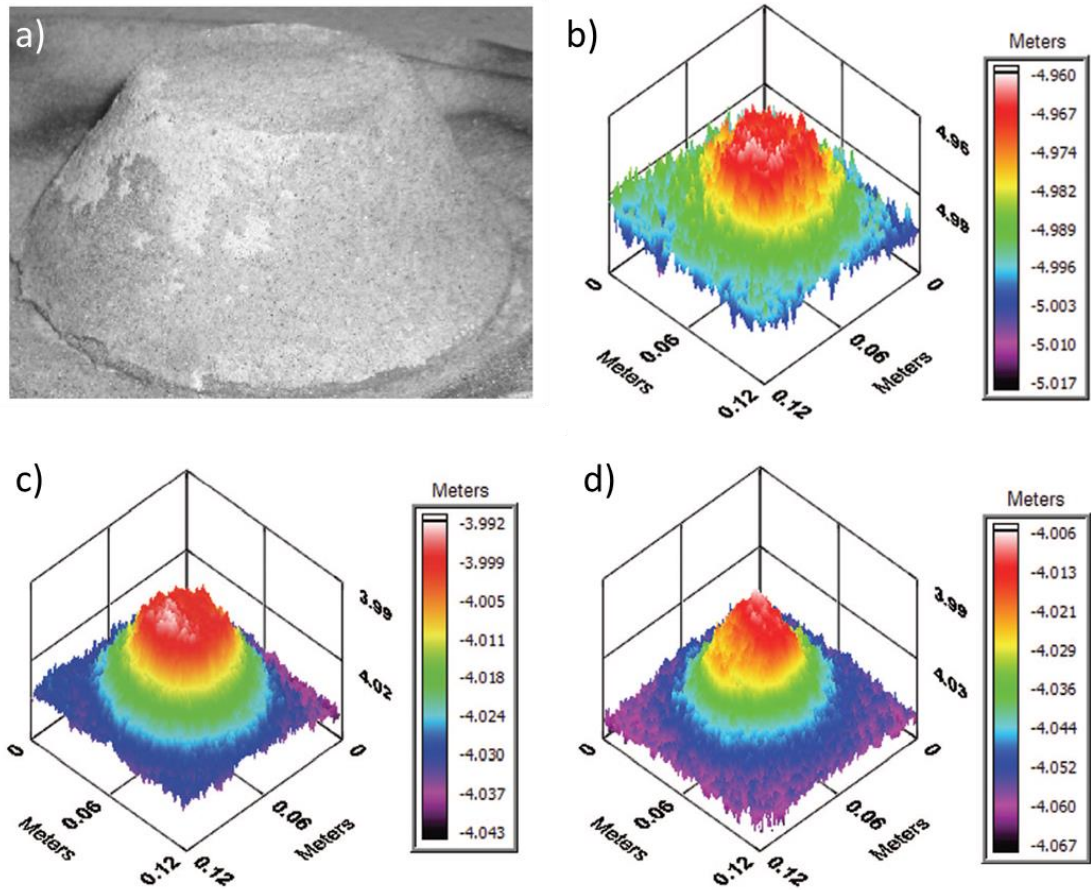
Figure 2.8. The photograph in a) shows the target (6 cm and 12 cm are the top and the bottom diameters, and 5 it is cm high) camouflaged by sand on a sandy back-ground, hence the contrast between the target and the background was very low. The system used to obtain 3D profiles of the target comprised a gated CCD camera and a pulsed laser source of wavelength λ = 532 nm. In b), the graph shows the depth profile of the target placed in sea water at stand-off distance of 5 metres from the system. The graphs in c) and d) show the depth profiles obtained at 4 metres of stand-off distance in sea water and tap water, respectively. All from [18].

2.5. Spatial discrimination

Another technique used to reduce the effect of backscattering is based on spatial discrimination, which consists of minimising the overlap between the transmitted light and the field of view of the receiver. The most intuitive way of achieving this is to separate the source and receiver. This technique may improve the performance of the conventional camera-strobe systems because the light backscattered in the water volume

common to the field of view of the receiver and the illumination source is reduced, and only the weak side-scattered photons can reach the receiver, as shown in Figure 2.9.
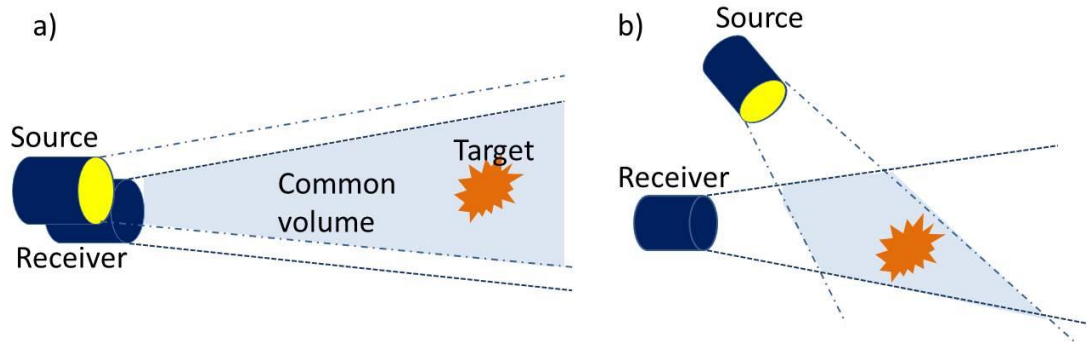
Figure 2.9. Separating the source (S) and the receiver (R) reduces the common volume of the field of view of the receiver and the illumination source, hence reducing the backscattered light.

This method permits imaging at distances of up to 3-4 attenuation lengths, but then the effect of the backscattered light reduces drastically the contrast of the image [19].

This technique was commonly adopted on small submarines or underwater robots (3-5 metres) [20]. However, once unmanned underwater vehicles (UUV) became available it was not always possible to separate the receiver and source due to the limited space. Thus, more complex configurations were needed.

To further reduce the overlap between the field of view of the receiver and the volume illuminated by the source, different combinations of source and receiver can be used, as shown schematically in Figure 2.10. From the schematic, it can be seen that the choice of a receiver with a narrow field of view, or a narrow source (i.e. collimated or focused light), results in a smaller overlap between transmitted light and field of view of the receiver (Figure 2.10b) and c)). Ultimately, the overlap is minimised when both narrow source and narrow field of view are selected, as shown in Figure 2.10d). The latter case is known as synchronous scan imaging, and can achieve from 3 to 7 attenuation lengths [19].
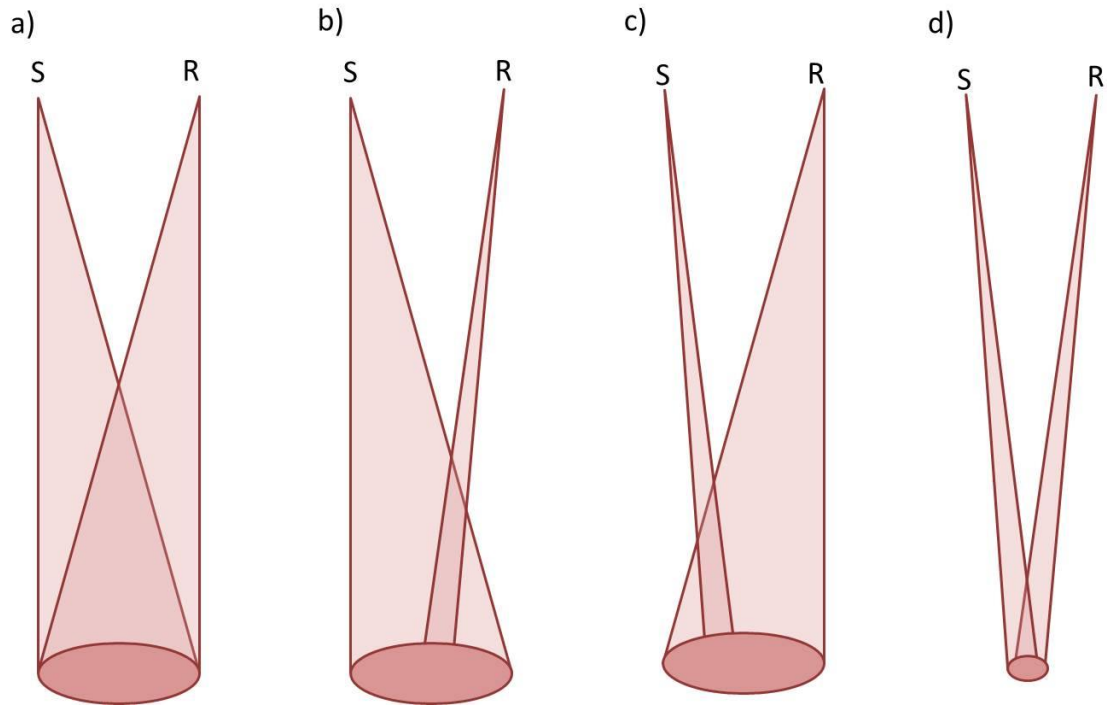
Figure 2.10. Different combinations of receiver field of view, and illumination source. a) Wide source and wide receiver field of view. b) Wide source and narrow receiver field of view. c) Narrow source and wide receiver field of view. d) Narrow source and receiver field of view. Adapted from [8].

In synchronous scan imaging, the target is generally scanned with a highly collimated source and the receiver has a narrow field of view. Several variations of this method have been developed in the last three decades. One of these is the laser line scan (LLS) approach, where a highly collimated laser beam is used. This method allows for 3D image acquisition by triangulation or time-of-flight.

Triangulation uses the geometric relation between the receiver, the source, and the target. The principle is shown schematically in Figure 2.11 for a basic laser scanning system.
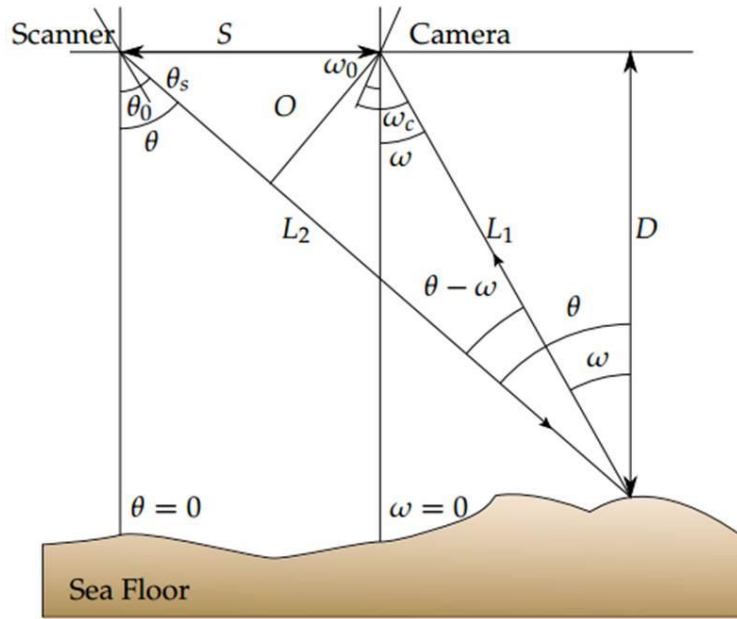
Figure 2.11. Triangulation geometric principle for a basic laser scanning system. From [21].

The depth D of the target is calculated as [21]

$$D = L_1 \cos(\omega) = \frac{S \cos(\theta)\cos(\omega)}{\sin(\theta - \omega)} = \frac{S}{\tan(\theta) - \tan(\omega)} \qquad \text{Equation 2.2}$$

where S is the distance between the centre of the light source and the centre of the receiver, while θ and ω are the scanning and viewing angles, respectively. From Figure 2.11, it can be seen that

$$\theta = \theta_0 + \theta_S \quad \text{and} \quad \omega = \omega_0 + \omega_c \qquad \text{Equation 2.3}$$

where the angles θ_0 and ω_0 are the offset mounting angles for the source and the receiver, respectively. θ_S is the laser beam angle, generally with respect to a galvanometer mirror of the optical setup, and ω_c is the pixel viewing angle with respect to the receiver housing. Therefore,

$$D = \frac{S}{\tan\left(\theta_0 + \theta_S\right) - \tan\left(\omega_0 + \omega_c\right)} \qquad \text{Equation 2.4}$$

Both angles θ_0 and ω_0 have to be calculated by calibration, otherwise the depth of the target cannot be evaluated. This is the main disadvantage of the triangulation technique, as the calibration process has to be done before every measurement. Calibration techniques have been studied for years, and several routines were developed and optimised on the basis of the optical configuration of the systems in free-space [22, 23] and in underwater environments [24, 25].

The time-of-flight approach relies on measuring the distance of a target surface by the round-trip time of an optical pulse, typically a short laser pulse. If the light spends the time *ToF* to travel from the system to the target and back, then the distance *d* of the target is evaluated as

$$d = \frac{c}{n}\frac{ToF}{2} \qquad \text{Equation 2.5}$$

where *c* is the speed of light in vacuum, and *n* is the refractive index of the propagation medium. This method is particularly suitable for underwater environments, as it allows temporal discrimination between back-scattered light and signal from the target. In addition, it can be used in both monostatic and pseudo-monostatic systems.

2.6. Laser line scan systems

Laser line scan systems were the most studied and developed systems for underwater imaging, and this section will give a brief review of these systems.

Initially, continuous wave lasers at a blue-green wavelength were used, however the contrast of the images obtained was still limited by both multiple backscatter and common volume backscatter [15]. One solution which could be employed to further limit the effect of the backscattered light was increasing the distance between source and receiver. However, this introduced additional problems such as the requirement of bulky systems, often not compatible with UUV, as previously mentioned. Furthermore, one of the disadvantage of many basic LLS is the small depth of field (DOF) over which the receiver

and the source can be scanned synchronously. In such systems, a small DOF can lead to frequent image drop-out which prevents image acquisition. In LLS systems DOF depends on several factors, including distance system-to-target, source-receiver distance, beam divergence, and field of view of the receiver [26]. Using an increased distance between source and receiver reduces the common volume back-scattering, but decreases the DOF, as schematically shown in Figure 2.12.
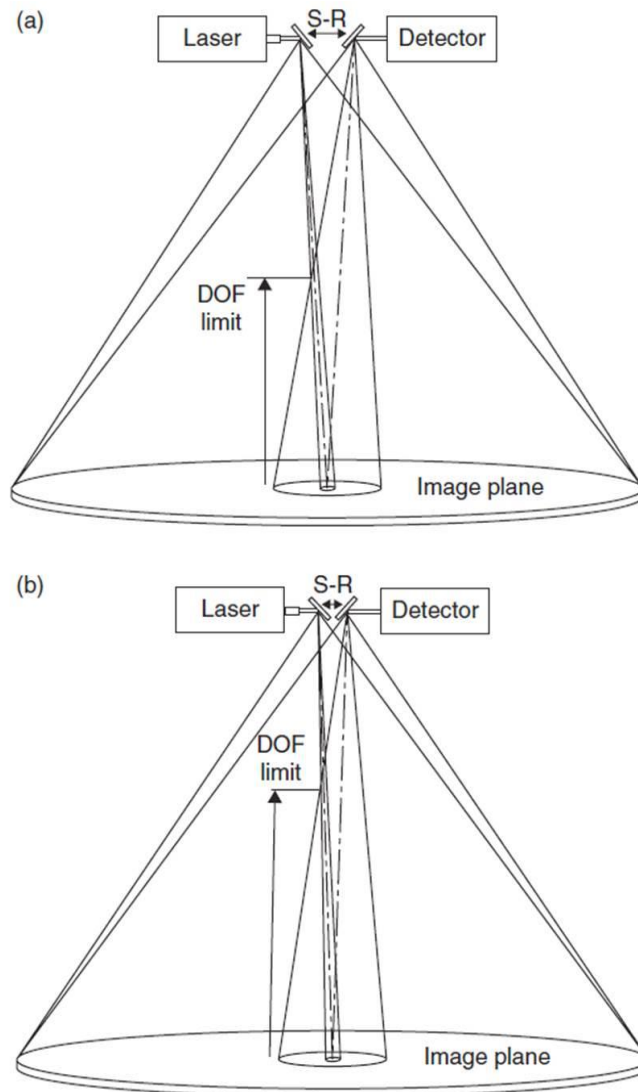
Figure 2.12. Effect of source-receiver separation on the DOF of an LLS system. a) A wide separation between source and receiver reduces the common volume backscattering but leads to a small DOF. b) A small separation between source and receiver leads to an improved DOF but more common volume backscattering. From [6].

In the same way, a narrow receiver field of view reduces the common volume backscattering, but decreases the DOF, as schematically shown in Figure 2.13.
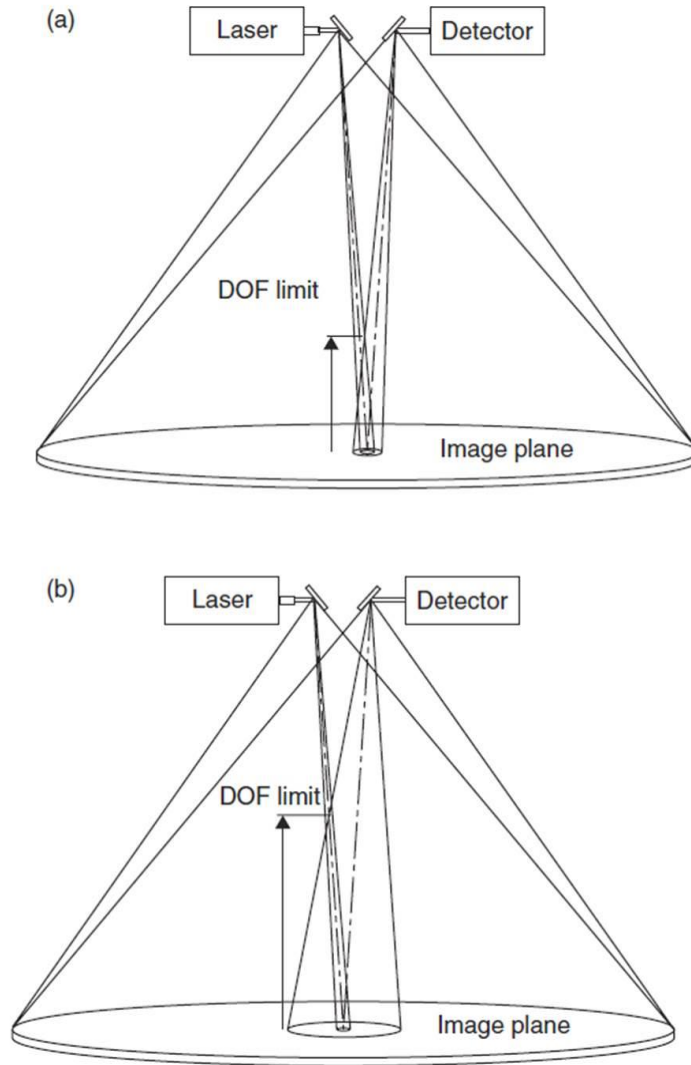
Figure 2.13. Effect of receiver field of view on the DOF of an LLS system. a) A narrow field of view of the receiver reduces the common volume backscattering but leads to a small DOF. b) A narrow field of view of the receiver leads to an improved DOF but more common volume backscattering. From [6].

In 1993 *Kulp et al.* developed a synchronous scanning underwater system that employed a continuous laser line to scan the target, and a photomultiplier tube (PMT) to collect the return signal from the target [27]. With such a system the achievable range was approximately 4 attenuation lengths. For several years, research groups developed computational models of LLS, predicting an achievable range up to 6 attenuation lengths

[28]. These results were demonstrated by *Caimi et al.* with laboratory-based experiments in the early 2000s [29]. For example, Figure 2.14 shows three scans of a white on black USAF resolution chart performed with a LLS system using a 1.5 W continuous wave laser at a green wavelength. The receiver was a photomultiplier tube (PMT), placed at a few centimetres from the light source. The target was placed at a stand-off distance of 7 metres from the system, equivalent to a stand-off distance of 1.85 attenuation lengths (Figure 2.14a), 5.68 attenuation lengths (Figure 2.14b), 6.46 attenuation lengths (Figure 2.14c). The results showed that for distances longer than 6 attenuation lengths, the contrast and resolution of the scans were greatly affected by scattering in water.
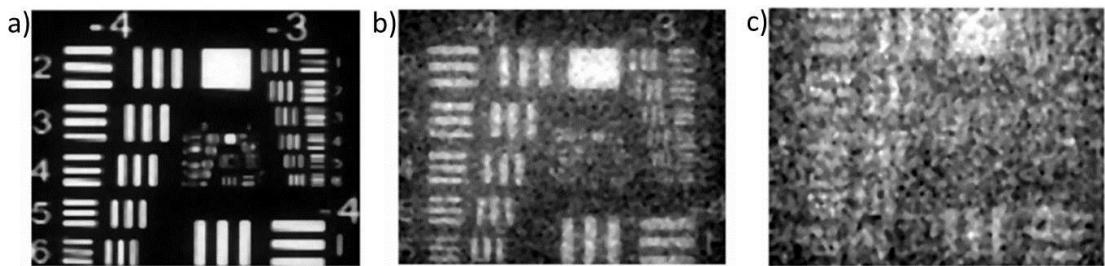
Figure 2.14. Scans of a white on black USAF resolution chart target placed at a stand-off distance of (a) 1.85 attenuation lengths, (b) 5.68 attenuation lengths, and (c) 6.46 attenuation lengths. The scans were performed with a LLS system using a 1.5 W continuous wave laser at a green wavelength, and a PMT receiver placed few centimetres apart from the light source. From [29].

At the same time, the same research group demonstrated with computational models that the use of a pulsed laser source and a gated receiver could improve the contrast of the images [30]. The use of spatial and temporal discriminations on the same system made it possible to exclude most of the back-scattering contributions, increasing the achievable range up to more than 7 attenuation lengths. For example, Figure 2.15 shows the comparison performed by *Dalgleish et al.* [31] between the results obtained with a continuous wave laser source (CW-LLS) and a pulsed laser source (PG-LLS), both at the wavelength $\lambda = 532$ nm. CW-LLS used a power of 2.2 W, while the PG-LLS used an average optical power of 1.3 W. In both cases, the receiver was a PMT placed a few centimetres apart from the light source, and in the PG-LLS system it was used in a gated configuration. The experiments validated the computational model, demonstrating an

achievable range up to 7 attenuation lengths. At longer distances, the effect of scattered light did not allow the target to be discerned.
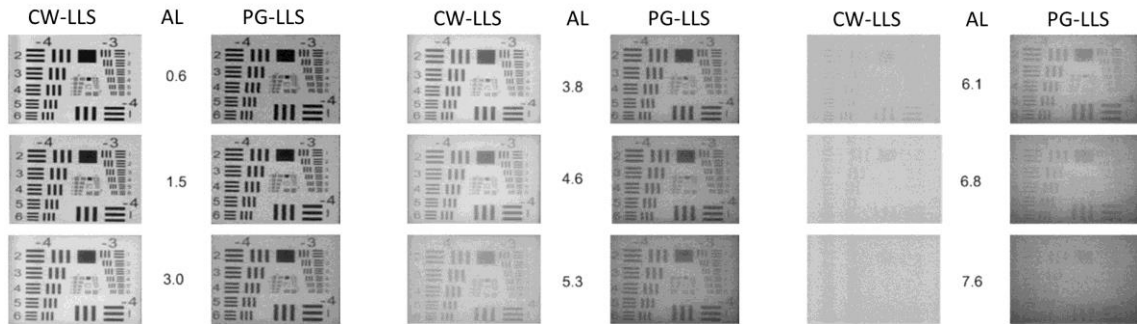
Figure 2.15. Images sequence of a black on white USAF resolution chart target, performed with two LLS systems with wavelength λ = 532 nm: a continuous wave LLS system (CW-LLS) with a power of 2.2 W, and a pulsed laser and gated receiver LLS system (PG-LLS), with average optical power of 1.3 W. The scans were performed at several attenuation lengths (AL). From [31].

It is worth noting that the techniques summarised so far allowed for the rejection of multiple backscattering and common volume backscattering, but no considerations were given to the forward scattering component. A narrow instantaneous field of view (IFOV) of the receiver can spatially filter out the forward scattered signal, improving the resolution of the images.

Therefore, in addition to the comparison between CW-LLS and PG-LLS, *Dalgleish et al.* performed another set of experiments considering two different IFOVs of the receiver, 15 mrad and 30 mrad, and a few examples are shown in Figure 2.16 [31]. The target was a white on black USAF resolution chart placed at a stand-off distance of 7 metres, and the scans were performed with the PG-LLS system. The results show that for a wider IFOV the images are more blurred, resulting in a lower resolution. However, they performed a quantitative study based on the contrast-signal-to-noise ratio, defined as [31]

$$CSNR = \frac{WhiteMean - BlackMean}{\sqrt{WhiteSTD^2 + BlackSTD^2}}$$

Equation 2.6.

The results showed that the CSNR was higher for CW-LLS and a wider IFOV for stand-off distances less than 3 attenuation lengths, and non-dependent on the IFOV for stand-off distances between 3 and 5 attenuation lengths. For stand-off distances longer than 5 attenuation lengths, the PG-LLS with a narrower IFOV showed the best performance, as characterised by the highest CSNR. For completeness, the graph of the CSNR versus the number of attenuation lengths is shown in Figure 2.17.
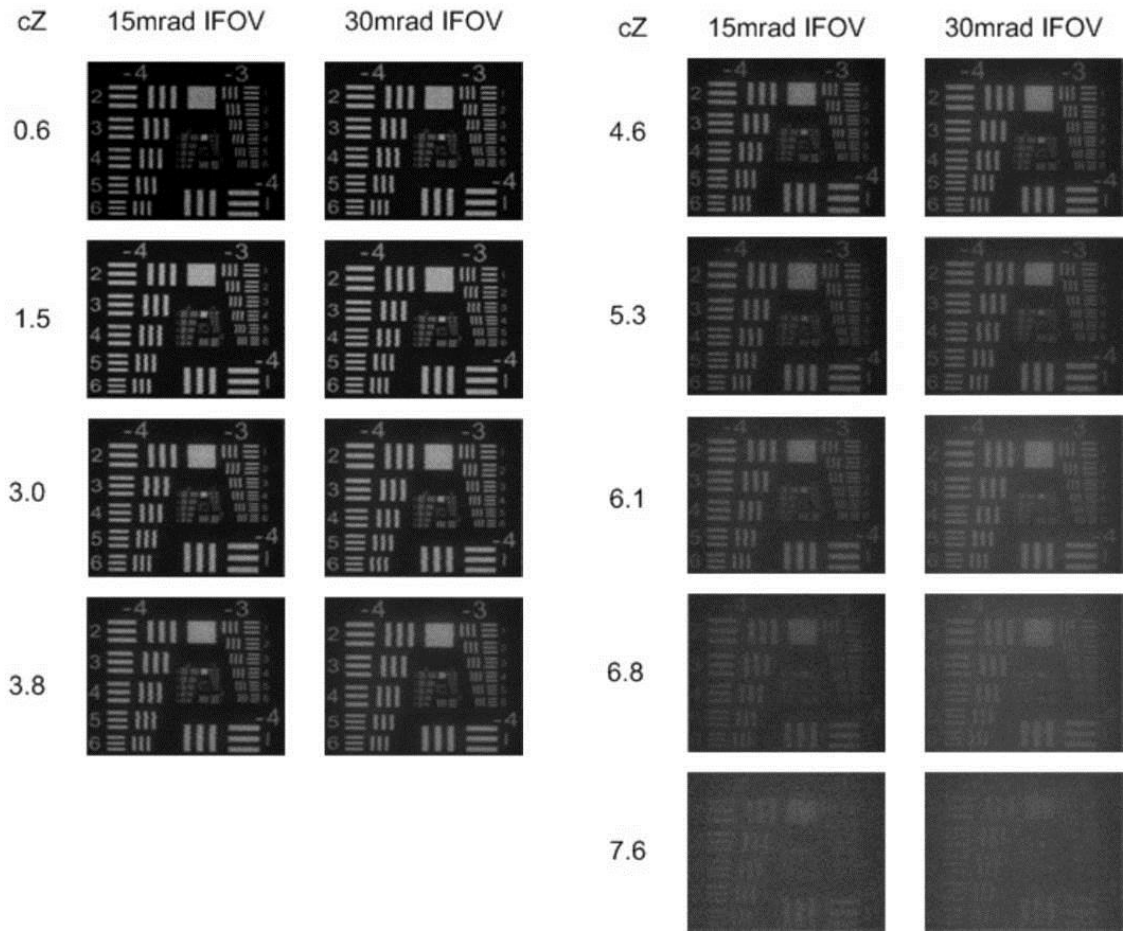

Figure 2.16. Image sequence of a white-on-black USAF resolution chart target, performed with a PG-LLS system with wavelength λ = 532 nm and 1.3 W average optical power, for two different IOFVs of the receiver: 15 mrad on the left column, and 30 mrad on the right column. The comparison was performed at different values of attenuation lengths. From [31].
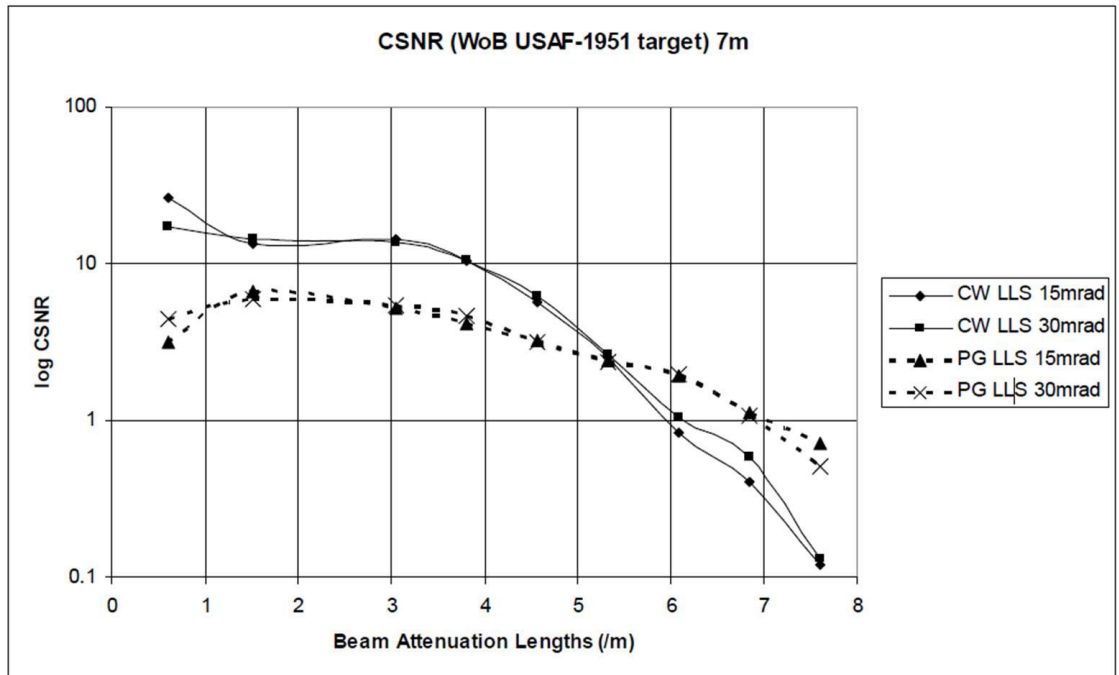
Figure 2.17. Evaluation of CSNR versus the number of attenuation lengths for different configurations of LLS systems: continuous and pulsed LLS when two different instantaneous field of view are considered, 15 and 30 mrad. From [31].

The work performed by *Dalgleish et al.*[31] aimed to improve the achievable range of an underwater optical system, while other systems were developed with the aim of high-resolution 3D imaging. Thanks to the wide FOV achieved by LLS systems, the synchronous scan technique is preferred for topography [32] and bathymetry [33]. However, it is also a well-established technique for subsea equipment inspection, as it allows high-resolution images at short ranges. For example, *McLeod et al.* in 2013 developed a LLS system based on the time-of-flight approach [34]. The system uses a pulsed laser source at the wavelength $\lambda = 532$ nm, but no information about the average power is provided. The system was tested in different water conditions, obtaining images of a custom calibration target (Figure 2.18a) in a clear water test tank, at stand-off distances up to 20 metres. Figure 2.18a) shows the photograph of the target, which is 2.1 metres wide, 0.5 metres high on the right side and 1 metre high on the left side. Figure 2.18b) shows the target in the water tank at a stand-off distance of approximately 8 metres, and the processed scan is shown in Figure 2.18c). In addition, Figure 2.19 shows a zoomed-in scan demonstrating that the system was able to resolve smaller details of the target. For example, the black writing was only 8 mm deep, while the fins were 20.5 cm apart and 17.8 deep.
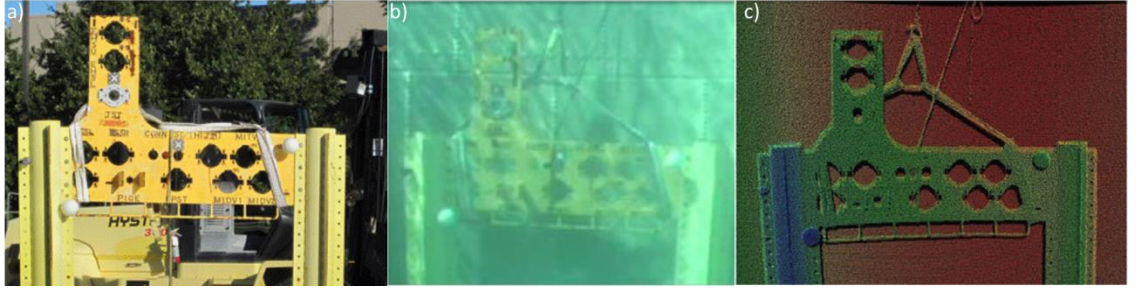
Figure 2.18. (a) Photograph of the target in air; (b) photograph of the target in a fresh water test tank; (c) processed point cloud image of the target. The system used for the scan was a PG-LLS system with wavelength λ = 532 nm based on the time of flight approach. From [34] and[35].
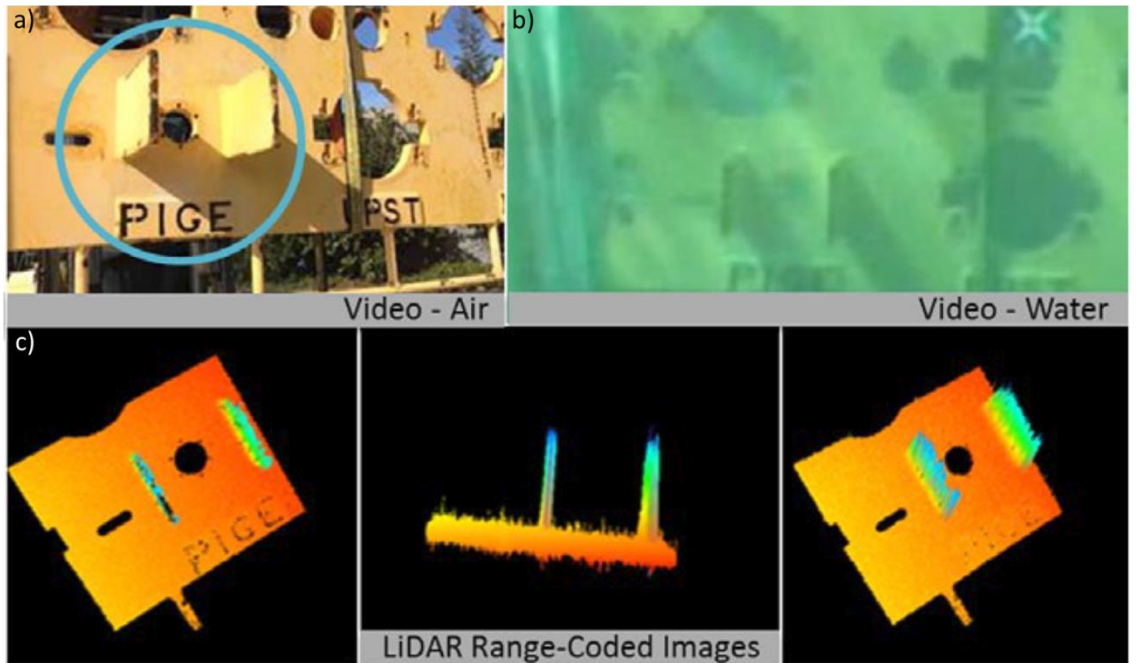
Figure 2.19. (a) Photograph of the target section in air; (b) photograph of the target in a fresh water test tank; (c) processed point cloud image of the target at different projections. The system used for the scan was a PG-LLS system with wavelength λ = 532 nm based on the time of flight approach. From [35].

This research has allowed commercially available systems to be marketed [36, 37], which allow extended range in comparison to systems based on triangulation approach, although the latter show a superior resolution. Figure 2.20 shows an example of scan performed with a commercially available LLS based on triangulation [38], in this case the resolution

varies between 0.01 millimetre at a stand-off distance of 0.13 metre, to 0.3 millimetre at a stand-off distance of 1 metre, as stated by the manufacturer [39].
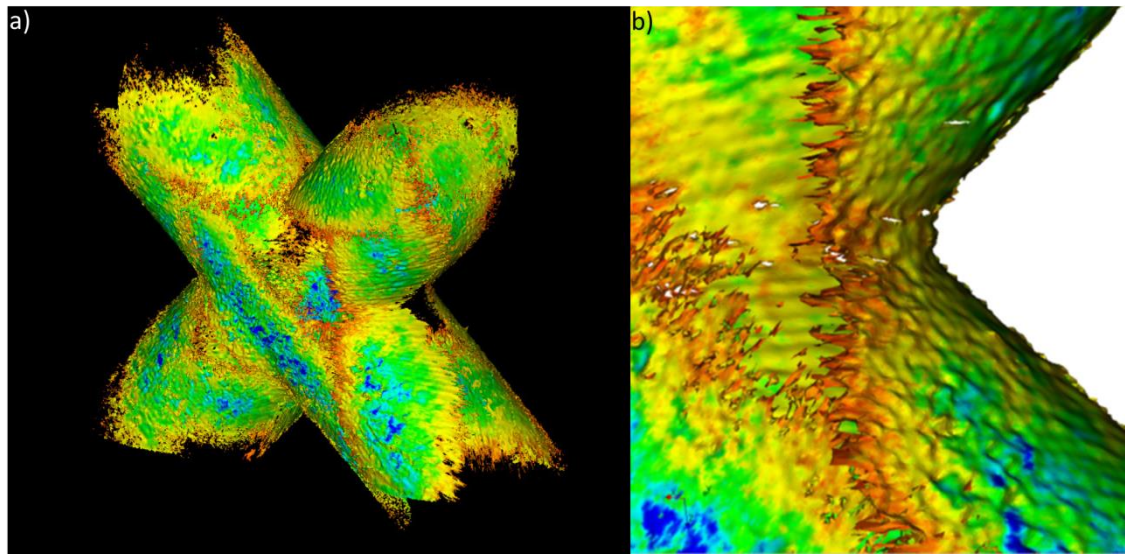
Figure 2.20. (a) 3D point cloud map of an underwater jacket joint. (b) Detail of the jacket joint. The system used for the scan was the ULS-100 by 2G Robotics, a LLS system with wavelength λ = 532 nm based on the triangulation approach. From [38].

In this section, particular attention was dedicated to systems using highly collimated light sources. However, different light source configurations can be considered, as discussed in the next section.

2.7. Structured light

In order to reduce the acquisition time for a 3D image, a different light source configuration can be used. For example, structured light is a technique based on triangulation, and consists of projecting a known light pattern on to the target. Then, with appropriate signal processing techniques, 3D images can be obtained studying the deformation of the original pattern [40, 41].

Commonly, systems based on structured light comprise a digital light projector and a camera, placed at a known distance apart. The light patterns can be manifold, and several examples can be found in the literature [42]. However, small patterns are preferable in order to limit the effect of back-scattering. For example, *Narasimhan et al.* in 2005 used a projector to illuminate the target with a stripe of white light [43], as shown schematically

in Figure 2.21. The receiver was a CCD camera, placed at a known distance from the light source.
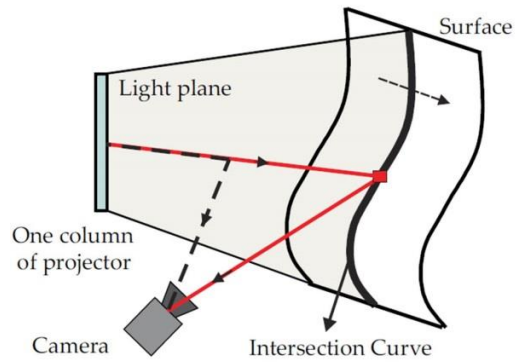
Figure 2.21. Schematic of stripe structured light. The light stripe was swept across the target surface through a light projector, and a CCD camera was placed at a known distance from the light source. From [43].

This system was used to obtain images of two objects in water, under different scattering conditions, and a few image examples are shown in Figure 2.22. The scattering was varied by adding milk to tap water, and no attenuation coefficients were provided.
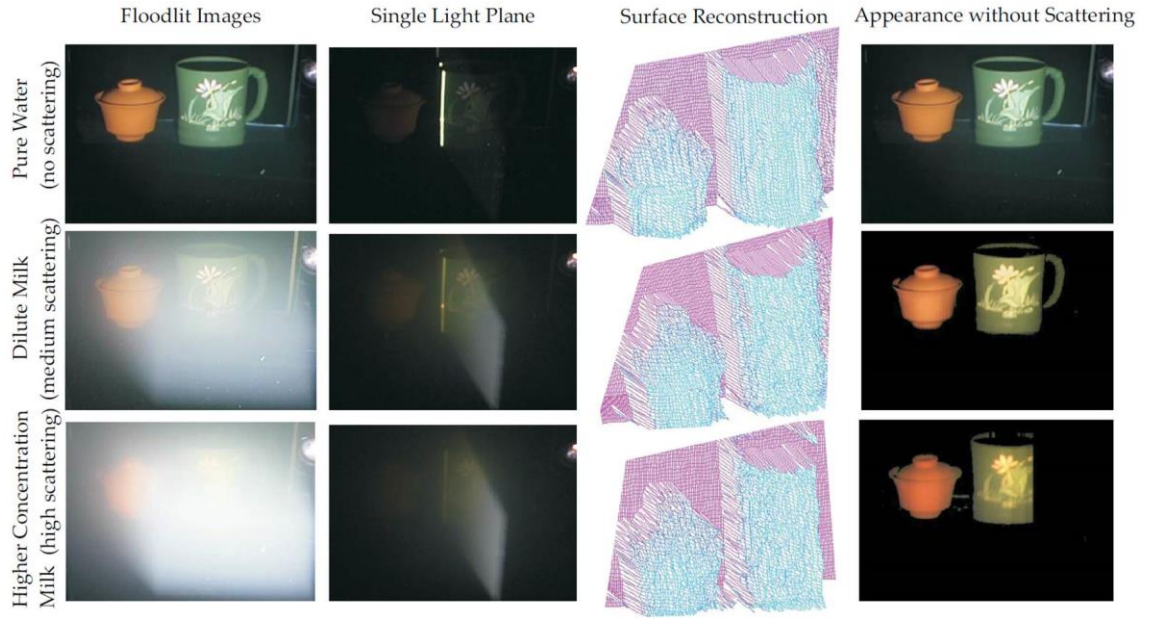
Figure 2.22. Target scene in water at different concentrations of milk. The first column shows the projector illuminating the wide field scene. The second column shows the projector illuminating the targets with a single light stripe. The third column shows the depth of the target scene, obtained scanning the targets with a single light stripe and detecting the light scattered back from the target with a camera. The last column shows the reconstruction of the target reflectance. From [43].

The results show that the system was able to identify the targets also in highly scattering conditions (last row of Figure 2.22), and the reconstructed surface is shown in the point cloud graph in the third column. In addition, *Narasimhan et al.* developed an algorithm to recover the reflectance of the targets at different colour channels [43], and the results are shown in the last column of Figure 2.22. It is interesting to note that in highly scattering conditions, they were able to recover the depth and reflectance of most of the target scene, although the handle of the cup is missing because of the low signal detected due to the high level of attenuation. However, no details about the resolution were provided in the reference.

Structured light techniques can be improved by adding more receivers to the system, and in this case several configurations can be considered. For example, *Bruno et al.* in 2011 used two CCD cameras in conjunction with a projector, which illuminates the entire target with a programmable light pattern [44]. However, despite each pattern covering the entire target scene at once, the 3D image acquisitions required the projection of 50 patterns.

With this system, *Bruno et al.* were able to obtain images at stand-off distances up to approximately 4 attenuation lengths, and few results are shown in Figure 2.23. The figure shows in column a) the photographs of the target illuminated by one light pattern, in three different water conditions. While column b) in Figure 2.23 shows the point cloud graphs obtained by structured illumination technique.
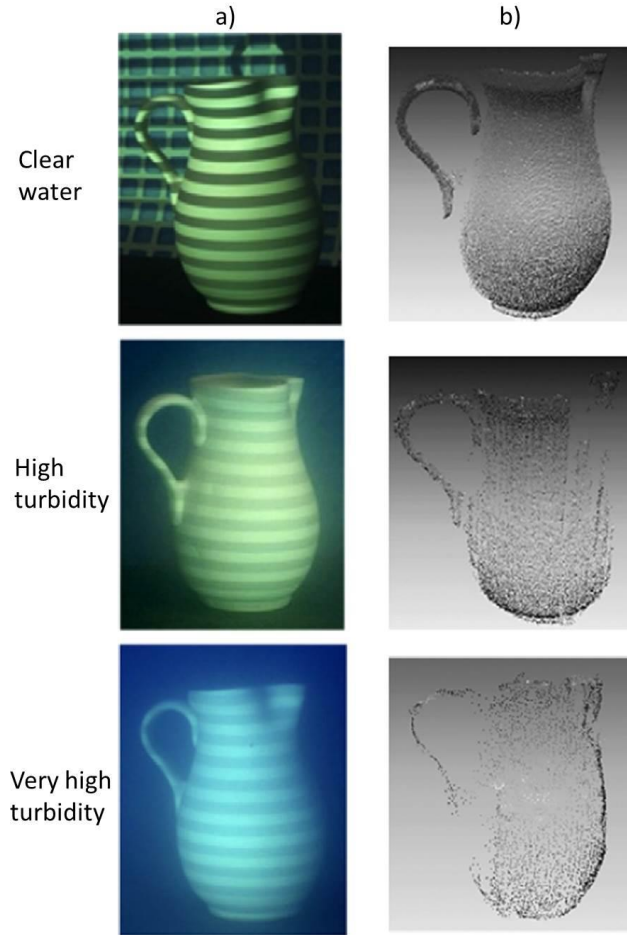
Figure 2.23. (a) Photographs of one pattern projected on the target at different turbidity levels. (b) Point cloud graphs of the reconstructed target. The system comprised two CCD cameras and a light projector, programmed to project different light patterns. Adapted from [44].

Alternatively, a different source can be considered for structured light. For example, *Massot-Campos et al.* in 2014 used a CCD camera in conjunction with a green continuous wave laser and a diffractive optical element in front of the laser beam [45]. This system allowed for the use of multiple laser lines at the same time in order to form a structured illumination, as shown schematically in Figure 2.24. The laser used a wavelength of $\lambda = 532$ nm and 5 mW optical power, and it is shown in Figure 2.25a). The photograph

shows the laser in the white housing, while the camera is in the black housing. The system was tested in unfiltered tap water in the tank of the Ocean Systems Laboratory at Heriot-Watt University. The tank was 4 metres long, 3 metres wide, and 2 metres deep (Figure 2.25b).
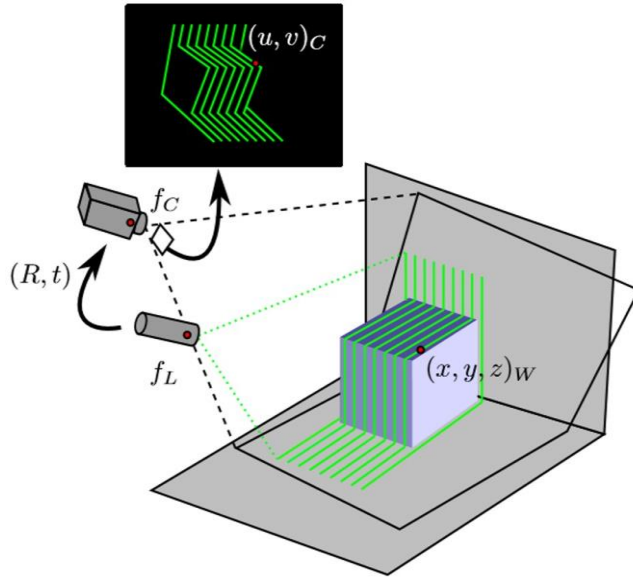
Figure 2.24. Schematic of single frame structured light system based on triangulation. A light pattern is projected on the target, which deforms the original pattern. Studying the deformations, it is possible reconstruct a 3D map of the target. From [45].
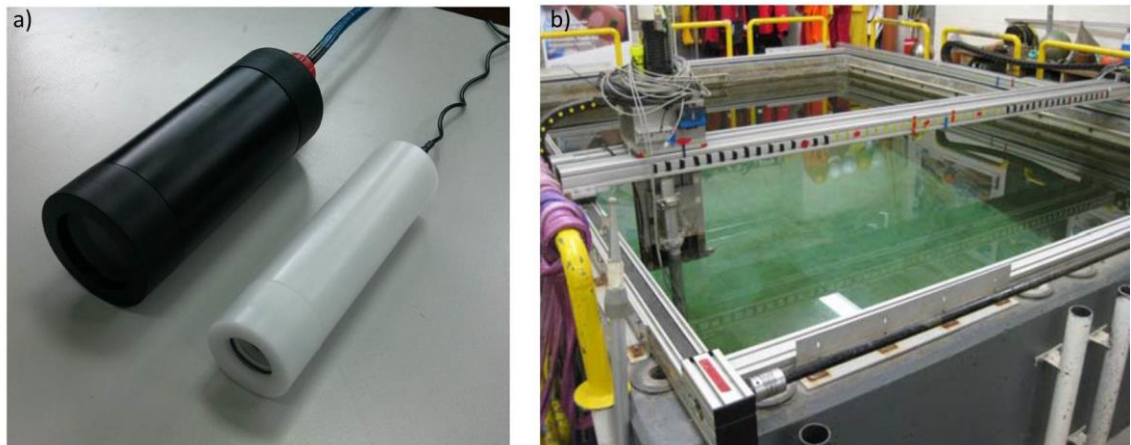
Figure 2.25. (a) Photograph of the system, the black housing comprised a CCD camera, while the white housing comprised a laser with wavelength λ = 532 nm and 5 mW optical power. (b) The system was tested in the water tank of the Ocean Systems Laboratory at Heriot-Watt University. From [46].

Figure 2.26 shows an example of a non-processed 3D reconstruction of a 15 cm plastic weight plate in unfiltered tap water, (b) front view and (c) bottom view [45]. Preliminary tests showed that the laser based structured light system allowed sharp and clear details [46]. However, a quantitative study in clear and turbid water conditions was not yet performed and is part of future work.
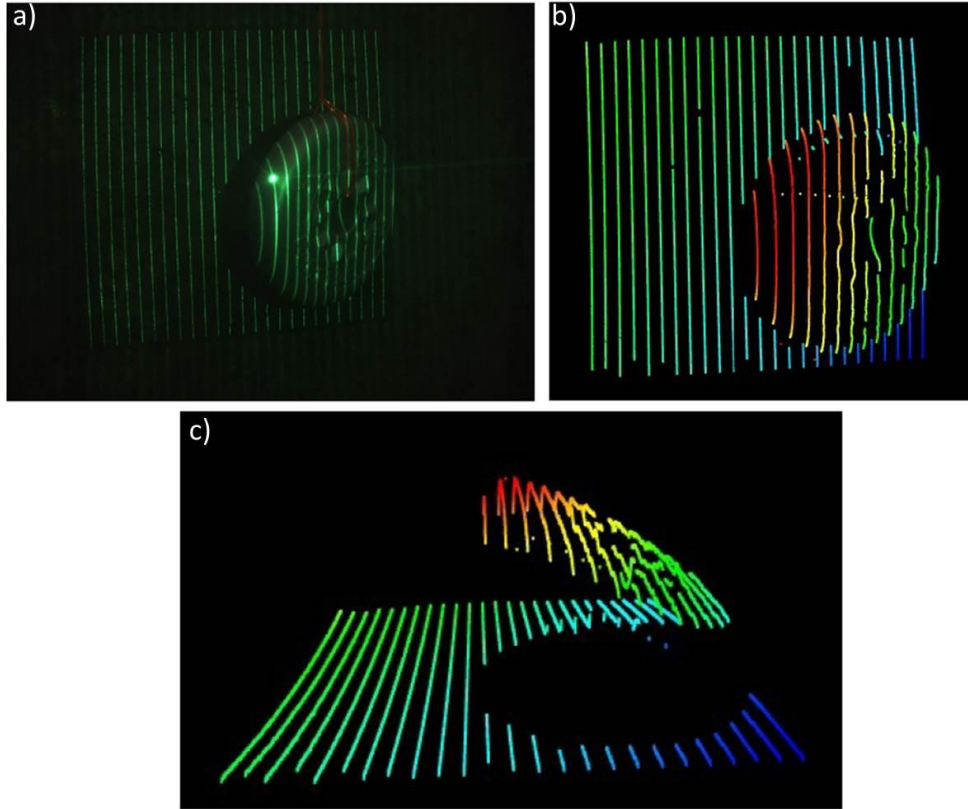
Figure 2.26. (a) Laser input frame obtained with the system in Figure 2.25 illuminating a 15 cm plastic weight plate. (b) Front view of the 3D reconstruction of the weight plate. (c) Bottom view of the 3D reconstruction of the weight plate. From [45].

2.8. Modulation discrimination

The frequency domain provides another way to discriminate between the backscattering component and the target signal using the modulation technique. This approach uses light modulated in the microwave range. Transmitted and received light experiences multiple scattering events in the transmission medium and then sums incoherently at the receiver. At the same time, un-scattered light reaching the target will fully retain the modulation characteristic [47]. By filtering the received signal, the modulated return from the target can be distinguished from the backscattered light [48]. In addition, the target signal is

characterised by a phase term which is directly proportional to the target distance. Therefore, target range information is obtained by the measurement of the phase difference between the transmitted and the reflected signals simultaneously for each pixel, allowing for the construction of the 3D profile of the target [49].

This technique was implemented in several configurations, including the use of pseudo-monostatic or bi-static platforms, continuous wave or pulsed lasers, and different receivers, typically CCD cameras or PMTs.

The potential of a system based on the modulation technique was initially investigated by *Mullen et al.* for airborne LiDAR systems [47, 50, 51]. In 2004, *Mullen et al.* demonstrated the technique for underwater imaging at different target stand-off distances [49]. They used a pseudo-monostatic system, with a CCD camera and a continuous wave laser, at the wavelength $\lambda = 532$ nm and 5 W optical power. Different modulation frequencies were investigated in the range 10 to 100 MHz, and target images were obtained at stand-off distances equivalent to up to 6.7 attenuation lengths [49].

A similar system was developed by *Bartolini et al.* in 2005 [52]. In this case, the authors were more interested in clear water, hence they used a laser at the wavelength $\lambda = 405$ nm, which is closer to the minimum of absorption of pure water, and an optical power of 20 mW. The receiver was a PMT, which was placed in a pseudo-monostatic configuration with the laser source. The system allowed for the estimation of the target depth at a stand-off distance of approximately 1.5 m in unfiltered tap water, and an example is shown in Figure *2.27*. The target was a steel surface 10 cm wide and 3.8 cm high, with 1 cm steps, coated with a high-reflectivity paint. The authors performed a synchronous scan of the target using a pixel format of 80×40 and an acquisition time of 10 ms per pixel, meaning an overall acquisition time of approximately 32 seconds. Figure 2.27a) shows a set of data reporting the phase versus the range, which shows the profile (i.e. the depth) of the target. Figure 2.27b) shows the 3D reconstruction of the target, from four different perspectives [52].
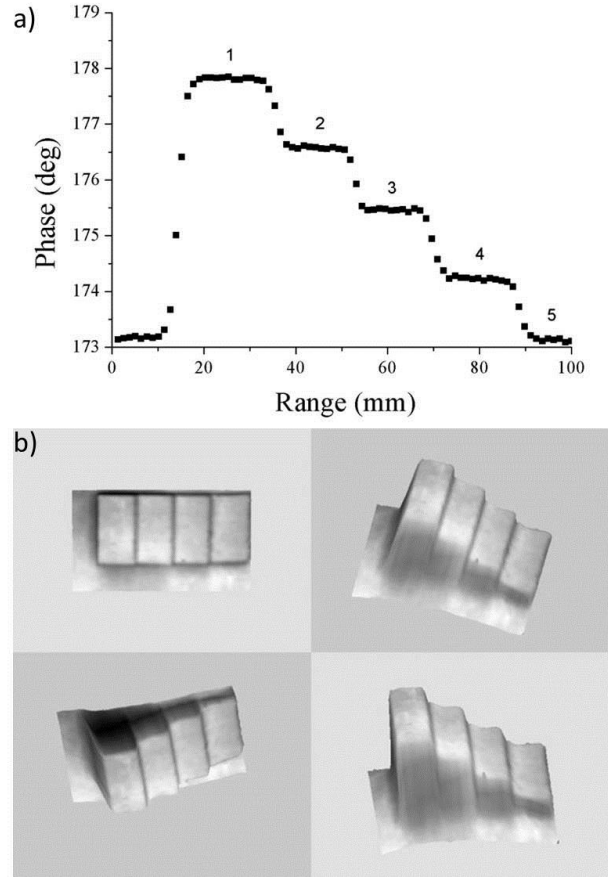
Figure 2.27. (a) Phase versus the range for one row of pixels, showing the target profile. (b) 3D reconstruction of the target, from four different perspectives. The system comprised a laser at the wavelength λ = 405 nm and optical power of 20 mW, and a PMT to detect the backscatter signal from the target. From [52].

Since 2008, *Bartolini et al.* studied the contrast and the SNR as function of the modulation frequency, suggesting that given the water attenuation coefficient and the required target range window, optimal working modulation frequencies may be selected in order to optimise SNR and contrast [53, 54]. In addition, in 2014 *Mullen et al.* demonstrated that the modulation discrimination technique can be used to suppress the forward scattered light if high modulation frequencies (of the order of 1 GHz) are used [55].

It is worth saying that the modulation technique was implemented also on bi-static configurations, where the source was placed close to the target and the receiver was in a different platform at several metres from the laser source [56, 57]. This configuration has the advantage of avoiding multiple and back-scattering events, and minimising attenuation of light between the source and the target, allowing for imaging at stand-off

distances of more than 10 attenuation lengths. However, it is important to note that this configuration requires a priori knowledge of where the source can be placed, making the implementation of this configuration in a real environment extremely difficult.

2.9. Conclusions

This chapter presented a brief review of the main systems developed to image man-made objects underwater. Optical imaging systems can be divided in to two main classes, passive and active systems. Passive systems use natural light for illumination while active systems employ an artificial light source. Passive systems can image up to approximately 3 attenuation lengths under ideal illumination conditions. However, significant improvements in image quality at longer distances can be obtained with active systems, in particular with systems that use laser-based techniques. Generally, using a light source can significantly reduce the image contrast due to scattered light, which is often a major issue in turbid media. Several methods have been devised to reduce the limiting effect of back and forward-scattered light when imaging in underwater environments. The main techniques used to limit backscattered light are based on temporal discrimination, spatial discrimination, or modulation discrimination.

In temporal discrimination, the receiver is time-gated to only allow a detected signal in correlation with the expected return of the pulsed illumination from the target, hence removing much of the backscattered light whilst maintaining the full return signal.

Spatial discrimination consists of minimising the overlap between the transmitted light and the field of view of the receiver, for example by separating the source and receiver. However, this task can also be performed by narrowing the field of view of the receiver, the source, or both. The latter case is known as synchronous scanning, which is on the basis of laser line scan systems.

The modulation technique uses light modulated in the microwave range. While propagating from the source to the target and back to the receiver, modulated transmitted light experiences multiple scattering events in the transmission medium, and will sum incoherently at the receiver. At the same time, un-scattered light reaching the target will fully retain the modulation characteristic, allowing for discrimination between target

signal and backscattered signal. In addition, if high modulation frequency is used, the forward scattered component can also be discriminated by the target return.

Each technique allows 2D imaging to stand-off distances of up to 5-6 attenuation lengths. A combination of these techniques allows for imaging of up to more than 7 attenuation lengths. In addition, it is important to note that all the systems considered in this chapter use average optical power in the range from few milli-watts to several Watts, which are likely to exceed eye-safety thresholds, as well as requiring high electrical power consumption.

These techniques can be implemented in different configurations: monostatic, pseudo-monostatic, and bi-static. In a monostatic configuration, the source and the receiver are in the same platform and share one or more optical elements. While in a pseudo-monostatic configuration, source and receiver are on the same platform but have dedicated optical setups. A bi-static configuration generally uses two separated platforms for the source and receiver. Particular attention was given to monostatic and pseudo-monostatic configurations, as a bi-static configuration requires a priori knowledge of where the source should be placed, which is a difficult condition to satisfy in a real underwater environment.

A 3D profile can be obtained if additional techniques are used. For example, temporal and spatial discrimination can be used in conjunction with triangulation or time-of-flight approaches. The triangulation approach estimates the depth of the target on the basis of the known system baseline. However, this technique requires appropriate calibration techniques before each measurement. The time-of-flight approach measures the distance of a target surface by the round-trip time of an optical pulse. Usually, triangulation provides a higher resolution with respect to the time-of-flight approach, but at the cost of a shorter range.

Modulation discrimination allows for 3D target profiles, as the target signal is characterised by a phase term which is directly proportional to the target distance. Therefore, target range information is obtained by measurement of the phase difference between a reference signal and the reflected signal simultaneously for each pixel of the receiver.

In conclusion, the selection of the technique and the development of the system are strictly related to the final application and involve several considerations, including achievable range, absorption and scattering properties of the environment, resolution requested, and platform available.

References

1.   S. Reed, Y. Petillot, and J. Bell, "An automatic approach to the detection and extraction of mine features in sidescan sonar," IEEE J. Oceanic Eng. **28**, 1, 90-106 (2003).

2.   J. S. Jaffe, M. D. Ohman, and A. De Robertis, "OASIS in the sea: measurements of the acoustic reflectivity of zooplankton with concurrent optical imaging " Deep-Sea Research II **45**, 1239-1253 (1998).

3.   M. Evangelidis, L. Ma, and M. Soleimani, "High definition electrical capacitance tomography for pipeline inspection," Prog. Em. Res. **141**, 1-15 (2013).

4.   S. Q. Duntley, "Light in the sea," J. Opt. Soc. Am. **53**, 214-234 (1963).

5.   D. Alley, B. Cochenour, and L. Mullen, "Remotely operated compact underwater temporally encoded imager – CUTEI," in *Proc. of SPIE Vol. 9827, Ocean Sensing and Monitoring VIII, 982708* (SPIE, Baltimore, USA, 2016).

6.   J. Watson, and O. Zielinski, *Subsea optics and imaging* (Woodhead Publishing Limited, 2013).

7.   S. E. Harris, W. M. Marquet, and R. D. Ballard, "ARGO: Capabilities for deep ocean exploration," in *OCEANS '86* (Washington DC, USA, 1986).

8.   J. S. Jaffe, "Underwater optical imaging - The past, the present, and the prospects," IEEE J. Oceanic Eng. **40**, 1-18 (2015).

9.   J. R. V. Zaneveld, and W. S. Pegau, "Robust underwater visibility parameter," Opt. Express **11**, 23, 2997-3009 (2003).

10.   F. M. Caimi, and F. R. Dalgleish, "Performance considerations for continuous-wave and pulsed laser line scan (LLS) imaging systems," J. Eur. Opt. Soc. **5**, 10020S (2010).

11.   E. A. McLean, H. R. J. Burris, and M. P. Strand, "Short-pulse range-gated optical imaging in turbid water," Appl. Opt. **34**, 21, 4343-4351 (1995).

12.   P. J. Heckman, and R. T. Hodgson, "Underwater Optical Range Gating " IEEE J. Quantum Electron. **3**, 11, 445-448 (1967).

13. G. R. Fournier, D. Bonnier, J. L. Forand, and P. W. Pace, "Range-gated underwater laser imaging system," Opt. Eng. **32**, 9, 2185-2190 (1993).

14. A. D. Weidemann, G. R. Fournier, J. L. Forand, P. Mathieu, and S. McLean, "Using a Laser Underwater Camera Image Enhancer for Mine Warfare Applications: What is Gained?," in *5th Int. Symposium on Technology and the Mine Problem* (Monterey, CA, 2002).

15. D. M. Kocak, F. R. Dalgleish, F. M. Caimi, and Y. Y. Schechner, "A focus on recent developments and trends in underwater imaging," Mar. Technol. Soc. J. **42**, 52-67 (2008).

16. G. R. Fournier, J. L. Forand, and P. Mathieu, "Laser underwater camera image enhancer," (Her Majesty the Queen as represented by the Minister of National Defence of Her Majesty's Canadian Government, Canada, 2009).

17. W. Hou, *Ocean Sensing and Monitoring* (SPIE, USA, 2013).

18. J. Busck, "Underwater 3-D optical imaging with a gated viewing laser radar," Opt. Eng. **44**, 11, 116001 (2005).

19. J. S. Jaffe, K. D. Moore, J. McLean, and M. P. Strand, "Underwater optical imaging: status and prospeccts," Oceanography **14**, 3, 64-75 (2001).

20. J. S. Jaffe, "Computer modeling and the design of optimal underwater imaging systems," IEEE J. Oceanic Eng. **15**, 2, 101-112 (1990).

21. M. Massot-Campos, and G. Oliver-Codina, "Optical sensors and methods for underwater 3D reconstruction," Sensors **15**, 31525-31557 (2015).

22. Q. Zhang, and R. Pless, "Extrinsic calibration of a camera and laser range finder (improves camera calibration) " in *IEEE/RSJ International Conference on Intelligent Robots and Systems* (IEEE, Sendai, Japan, 2004).

23. H. Yang, X. Liu, and I. Patras, "A simple and effective extrinsic calibration method of a camera and a single line scanning LiDAR," in *21st International Conference on Pattern Recognition* (Tsukuba, Japan, 2012).

24. J. Liu, A. Jakas, A. Al-Obaidi, and Y. Liu, "Practical issues and development of underwater 3D laser scanners," in *IEEE Conference on Emerging Technologies and Factory Automation (ETFA)*(IEEE, Bilbao, Spain, 2010).

25.   C. Bräuer-Burchardt, M. Heinze, I. Schmidt, P. Kühmstedt, and G. Notni, "Underwater 3D surface measurement using fringe projection based scanning devices," Sensors **16**, 13 (2016).

26.   F. R. Dalgleish, F. M. Caimi, C. H. Mazel, and J. M. Glynn, "Extended range underwater optical imaging architecture," in *OCEANS 2006* (IEEE, Boston, USA, 2006).

27.   T. J. Kulp, D. Garvis, R. Kennedy, T. Salmon, and K. Cooper, "Development and testing of a synchronous-scanning underwater imaging system capable of rapid two-dimensional frame imaging," Appl. Opt. **32**, 19, 3520-3530 (1993).

28.   T. E. Giddings, J. J. Shirron, and A. Tirafat-Gefen, "EODES-3: An electro-optic imaging and performance prediction model," in *OCEANS 2005*(Washington DC, USA, 2005).

29.   F. M. Caimi, D. M. Kocak, F. R. Dalgleish, and J. Watson, "Underwater imaging and optics: recent advances," in *OCEANS 2008*(IEEE, Quebec City, Canada, 2008).

30.   F. M. Caimi, F. R. Dalgleish, T. E. Giddings, J. J. Shirron, C. Mazel, and K. Chiang, "Pulse versus CW laser line scan imaging detection methods: simulation results," in *OCEANS 2007*(IEEE, Aberdeen, United Kingdom, 2007).

31.   F. R. Dalgleish, F. M. Caimi, W. B. Britton, and C. F. Andren, "Improved LLS imaging performance in scattering-dominant waters," in *Proc. in SPIE Vol. 7317, Ocean sensing and monitoring, 73170E* (2009).

32.   K. D. Moore, and J. S. Jaffe, "Time-evolution of high-resolution topographic measurements of the sea floor using a 3-D laser line scan mapping system," IEEE J. Oceanic Eng. **27**, 3, 525-545 (2002).

33.   K. D. Moore, J. S. Jaffe, and B. L. Ochoa, "Development of a new underwater bathymetric laser imaging system: L-bath," J. Atmos. Oceanic Technol. **17**, 1106-1117 (2000).

34.   D. McLeod, J. Jacobson, M. Hardy, and C. Embry, "Autonomous Inspection using an Underwater 3D," in *OCEANS 2013* (San Diego, USA, 2013).

35.   S. Hannon, "Underwater mapping," LiDAR Magazine **3**, 1 (2013).

36.   3D at Depth, "SL 1 High Resolution Subsea Laser Scanner - Data sheet (2016)," (http://www.3datdepth.com/?page_id=143 (Accessed on 08/07/2016)).

37.   3D at Depth, "SL2 High Resolution Subsea Laser Scanner - Data sheet (2016)," (http://www.3datdepth.com/?page_id=1386 (Accessed on 08/07/2016)).

38.   2G Robotics, "Offshore jacket inspection," (http://www.2grobotics.com/wp-content/uploads/2014/11/Jacket_Inspection.pdf (Accessed on 11/08/2016), 2016).

39.   2G Robotics, "http://www.2grobotics.com/products/underwater-laser-scanner-uls-100/ (Accessed on 11/08/2016)," (2016).

40.   J. Batlle, E. Mouaddib, and J. Salvi, "Recent progress in coded structured light as a technique to solve the correspondence problem: a survey," Pattern Recognit. **31**, 7, 963-982 (1998).

41.   J. Salvi, J. Pages, and J. Batlle, "Pattern codification strategies in structured light systems," Pattern Recognit. **37**, 827-849 (2004).

42.   J. Salvi, S. Fernandez, T. Pribanic, and X. LLlado, "A state of the art in structured light patterns for surface profilometry," Pattern Recognit. **43**, 2666-2680 (2010).

43.   S. G. Narasimhan, S. K. Nayar, B. Sun, and S. Koppal, "Structured light in scattering media," in *Tenth IEEE International Conference on Computer Vision (ICCV'05)*(2005).

44.   F. Bruno, G. Bianco, M. Muzzupappa, S. Barone, and A. V. Razionale, "Experimentation of structured light and stereo vision for underwater 3D reconstruction," ISPRS J. Photogramm. Remote Sens. **66**, 508-518 (2011).

45.   M. Massot-Campos, and G. Oliver-Codina, "One-shot underwater 3D reconstruction," in *IEEE Emerging Technology and Factory Automation (ETFA)*(IEEE, Barcelona, Spain, 2014).

46.   M. Massot-Campos, G. Oliver-Codina, H. Kemal, Y. Petillot, and F. Bonin-Font, "Structured light and stereo vision for underwater 3D reconstruction," in *OCEANS 2015* (IEEE, Genova, Italy, 2015).

47.   L. Mullen, A. J. C. Vieira, P. R. Herczfeld, and V. M. Contarino, "Application of RADAR technology to aerial LIDAR systems for enhancement of shallow underwater target detection," IEEE Trans. Microwave Theory Tech. **43**, 9, 2370-2377 (1995).

48.   L. Mullen, A. Laux, B. Cochenour, E. P. Zege, I. L. Katsev, and A. S. Prikhach, "Demodulation techniques for the amplitude modulated laser imager," Appl. Opt. **46**, 30, 7374-7383 (2007).

49.   L. Mullen, A. Laux, B. Concannon, E. P. Zege, I. L. Katsev, and A. S. Prikhach, "Amplitude-modulated laser imager," Appl. Opt. **43**, 19, 3874-3892 (2004).

50.   L. J. Mullen, P. R. Herczfeld, and V. M. Contarino, "Hybrid LIDAR-radar ocean experiment," in *CLEO '96*(1996).

51.   V. M. Contarino, P. R. Herczfeld, and L. J. Mullen, "Modulator LIDAR System," (United States of America, 1998).

52.   L. Bartolini, L. De Dominicis, M. Ferri de Collibus, G. Fornetti, M. Guarneri, E. Paglia, C. Poggi, and R. Ricci, "Underwater three-dimensional imaging with an amplitude-modulated laser radar at a 405 wavelength," Appl. Opt. **44**, 33, 7130-7135 (2005).

53.   L. Bartolini, L. De Dominicis, M. Ferri de Collibus, G. Fornetti, M. Francucci, M. Guarneri, M. Nuvoli, E. Paglia, and R. Ricci, "Experimental evidence of signal-optical noise interference like effect in underwater amplitude-modulated laser optical radar systems," Opt. Lett. **33**, 22, 2584-2586 (2008).

54.   R. Ricci, M. Francucci, L. De Dominicis, M. Ferri de Collibus, G. Fornetti, M. Guarneri, M. Nuvoli, E. Paglia, and L. Bartolini, "Techniques for effective optical noise rejection in amplitude-modulated laser optical radars for underwater three-dimensional imaging," EURASIP J. Adv. Signal Process. **2010**, 958360 (2010).

55.   B. Cochenour, S. O'Connor, and L. Mullen, "Suppression of forward-scattered light using high-frequency intensity modulation," Opt. Eng. **53**, 5, 051406 (2014).

56.   D. Alley, B. Cochenour, A. Laux, and L. Mullen, "Multistatic optical imaging system," in *Proc. of SPIE Vol. 9111, Ocean Sensing and Monitoring, 91110L* (SPIE, Baltimore, USA, 2014).

57.   J. Nash, R. Lee, and L. Mullen, "Wide bandwidth optical signals for high range resolution measurements in water," in *Proc. of SPIE Vol. 9827, Ocean Sensing and Monitoring, 98270A* (SPIE, Baltimore, USA, 2016).

Chapter 3

Time-correlated single-photon counting and single-photon detection

3.1. Introduction

The time-correlated single-photon counting technique is a particularly effective optical detection approach for applications where a very low photon return is expected, offering high sensitivity and a temporal resolution of a few picoseconds. This chapter will give an overview of the time-correlated single-photon counting technique, as well as a brief introduction to the most important single-photon detector technologies currently available. Due to the wide range of applications that require the capability of measurement of fast optical signals, it is important to understand the physics underlying the operation of single-photon detectors and their key performance characteristics. Specific attention is given to silicon single-photon detectors, which are the detectors used in the experiments reported in this Thesis. However, single-photon detectors for the infrared wavelength range will also be introduced for comparison and completeness.

3.2. Time-correlated single-photon counting

The time-correlated single-photon counting (TCSPC) technique relies on the measurement of the time difference between an optical input pulse, typically a repetitive pulsed laser signal, and a photon event recorded by a single-photon detector. If the pulsed laser signal provides the start of the measurement and the detector provides the stop signal, the operating mode is called forward mode, and this is shown schematically in Figure 3.1. A schematic of a typical experimental implementation of the technique is shown in Figure 3.2. When a photon is detected, the timing difference between the corresponding laser pulse and the detection event is recorded and added to a timing histogram. Repeated over many pulses, the timing histogram can be a highly accurate representation of the optical transient signal being measured. An example of timing histograms recorded in a time-of-flight measurement is shown in Figure 3.3. The width of each timing histogram bin can be set before the measurement, and it can be as short as one picosecond using the data acquisition hardware employed for the experiments reported in this Thesis [1].
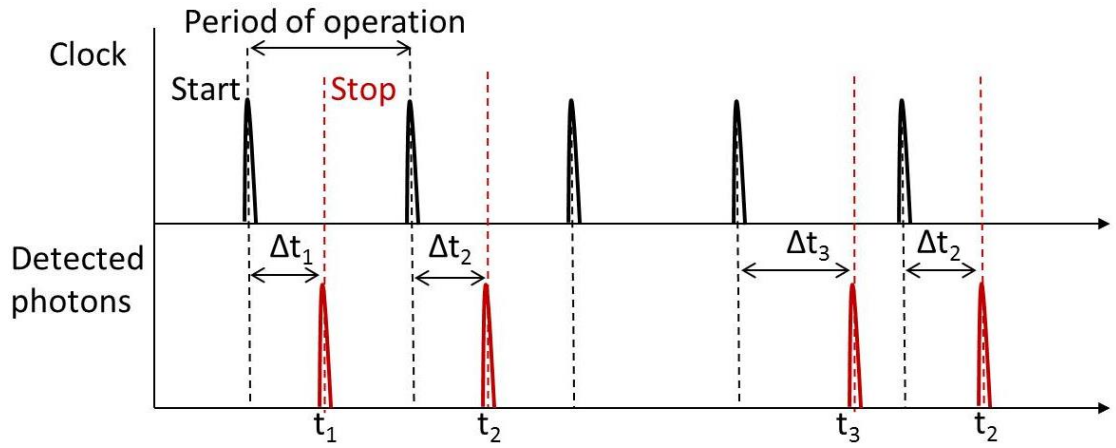
Figure 3.1. Timing diagram of start-stop time measurements. If used in forward mode (as shown here), the start signal is provided by an external clock pulse, the stop signal corresponds to an electrical output pulse provided by the detector for each detected photon. Reverse mode starts on a detector pulse and ends on a laser pulse.   Δt represents the difference between the start and the stop pulses.
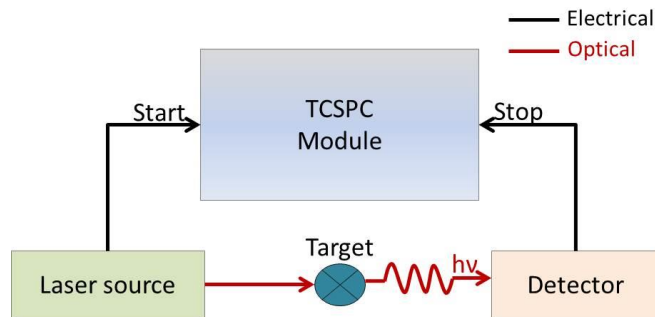
Figure 3.2.   Schematic of a typical time-correlated single-photon experiment operated in forward mode [2]. The laser source provides the start signal while the detector provides the stop.
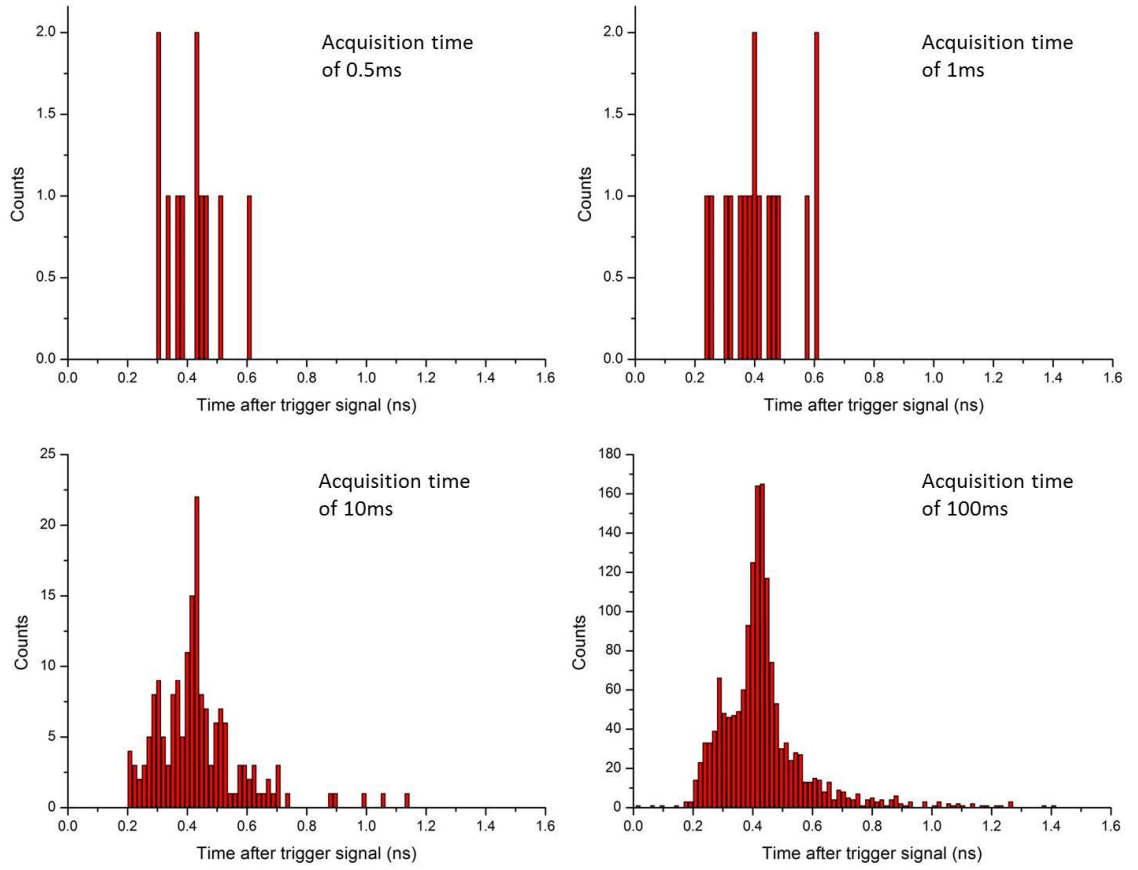
Figure 3.3. Examples of histograms in a time-of-flight measurement for different acquisition times. For longer acquisition times, the timing histogram gives a highly accurate representation of the time of flight information. Due to latency and delays from electronic components, an arbitrary zero was chosen for the displayed time-scale.

To obtain accurate results, the probability of detecting one photon per start signal has to be much less than one [2]. This means that the likelihood of two or more photons being incident after a given pulse is kept very small. If this condition is not satisfied, then the probability distribution across the timing window is skewed, leading to a distortion in any timing measurement. This effect is known as "pulse pile-up", and it is shown schematically in Figure 3.4. The figure shows also the dead time, which is the time spent by the electronics to reset after a detection event, and during this time no more events can be detected. Therefore, when more than one photon event occurs within one period of the clock signal (pulse pile-up), just one of these photons can be detected. Typically, only early events are recorded and, as a result, the timing histogram is skewed toward the start of the timing window, as shown in Figure 3.5 for the case of

fluorescence decay measurements. To avoid pulse pile-up, the count rate of the TCSPC system must not exceed 5% of the excitation rate [2].
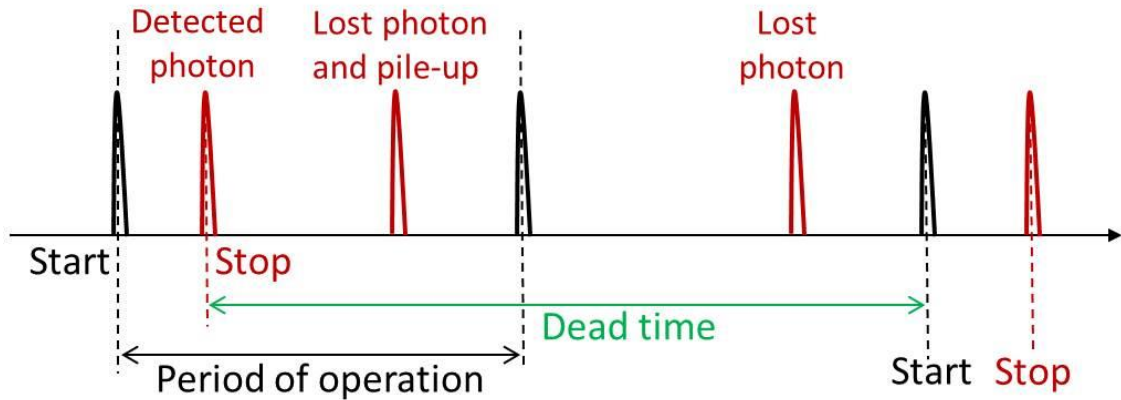
Figure 3.4. Diagram of the pile-up effect over one period of operation. The dead time starts when the first photon is detected.
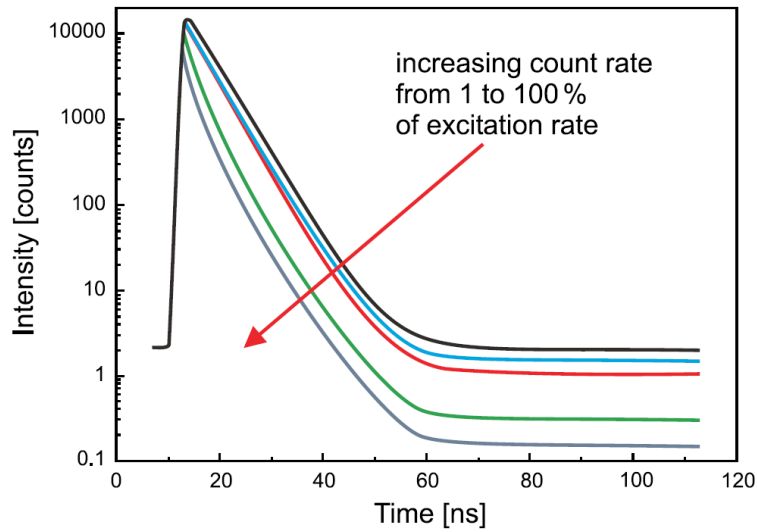
Figure 3.5. Distortion of a fluorescence decay histogram due to pulse pile-up. From [1].

Since photon detections can be treated as independent events, they follow Poissonian statistics. Therefore, the probability to detect N number of photons over an interval time Δt is [3]

$$P(N=k) = \frac{e^{-\lambda \Delta t} (\lambda \Delta t)^k}{k!}$$

Equation 3.1

where λ is the number of events expected in the unit time interval, such that $\lambda\Delta t$ represents the number of events expected in the time interval Δt. The uncertainty associated with this distribution is known as photon noise, and its standard deviation corresponds to $\sigma_{\Delta t} = \sqrt{\lambda\Delta t} = \sqrt{N}$. Hence, to improve the accuracy of a measurement, the number of counts has to be high with respect to the background, meaning that the measurements should be recorded at the highest count rate possible within the limitations discussed before. One source of background noise is non-correlated photons from ambient light sources. Another source of noise is given by the dark counts of the detector, discussed in more detail in section 3.4.3. The detector dark counts generate a background that limits the sensitivity of the system, and the parameters of this particular contribution to the background are a characteristic of the type of detector used. However, a mean background level can be subtracted from the recorded histogram.

A useful parameter used to compare the signal to the background level is the signal-to-background ratio (SBR), defined as

$$\text{SBR} = \frac{n_p}{n_b} \qquad\qquad \text{Equation 3.2}$$

where n_p is the number of photons in the highest bin in the peak (shown in red in Figure 3.6), and n_b is the average background photons per bin.
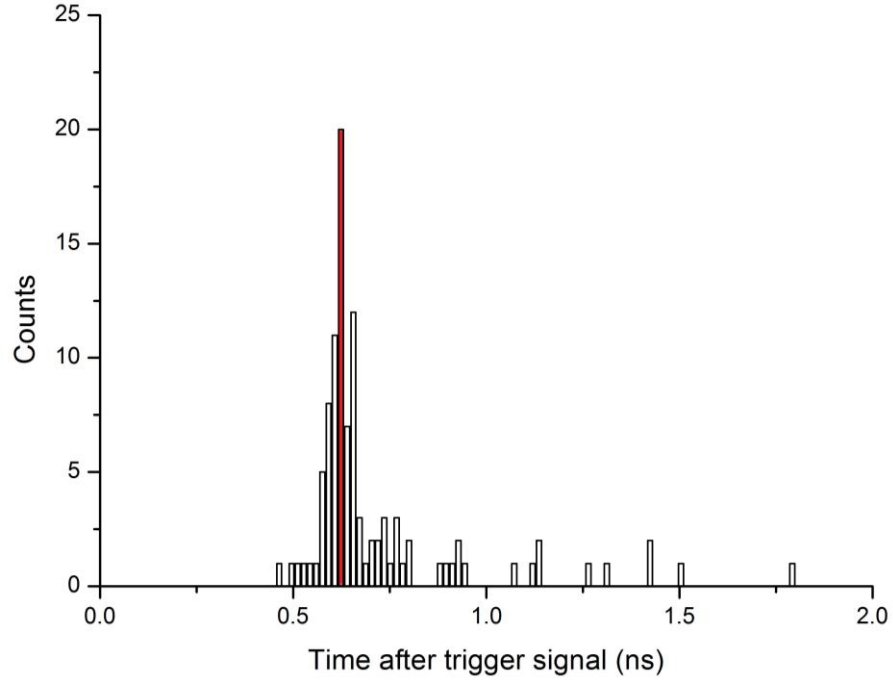
Figure 3.6. Example of histogram showing in red the number of photons in the highest bin in the peak, n_p. An arbitrary zero was chosen for the displayed time-scale.

However, the SBR does not depend on the acquisition time chosen and consequently it does not take into account that the shape of the instrumental response converges asymptotically to the convolution of the instrumental responses of all components. A parameter that considers the shape of the instrumental response is the signal-to-noise ratio (SNR), defined as [4]:

$$\text{SNR} = \frac{n_p}{\sqrt{n_p + n_b}} = \sqrt{n_p}\sqrt{\frac{\text{SBR}}{\text{SBR} + 1}} \qquad \text{Equation 3.3}$$

This difference is explained in Figure 3.7, where three simulated histograms with different acquisition times are shown. The SBR is approximately 15 in all three cases while the SNR decreases for shorter acquisition times.
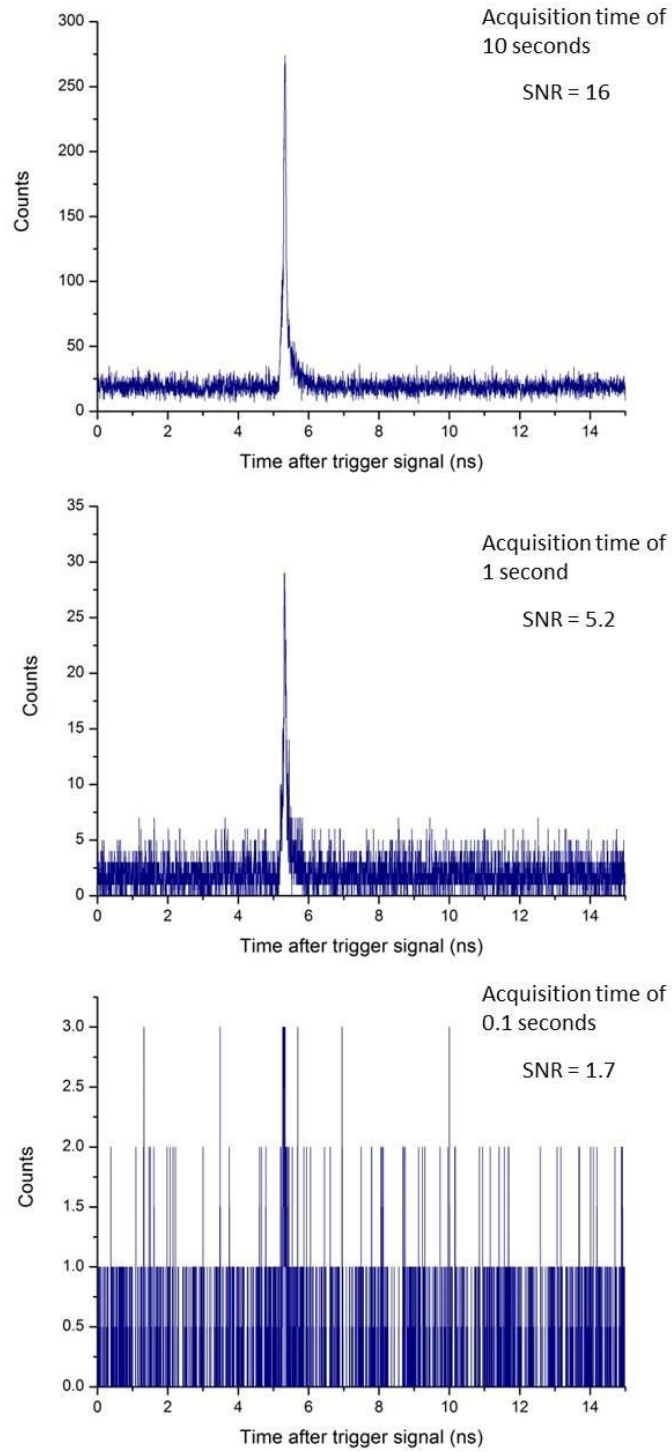
Figure 3.7. Simulated histograms for three different acquisition times, 10 seconds, 1 second, 0.1 seconds. Apart from acquisition times, the simulations are made under identical conditions. The histograms present the same SBR (SBR = 15) but different SNR, which decreases for shorter acquisition times.

3.3. TCSPC hardware

Figure 3.8 shows the block diagram of a conventional forward mode TCSPC system. The level trigger adapts the sync signal so that it is accepted by the TCSPC system. The timing information (the stop signal) is provided via a Constant Fraction Discriminator (CFD), which compares the detector signal with a copy of it, delayed by a constant, inverted, and amplified by a constant fraction. The signal obtained from the comparison changes polarity at the height of the detector signal constant fraction. This zero crossing point gives the timing information, which is independent of the amplitude of the detector signal. Figure 3.9 provides a diagram of the operation of a CFD.
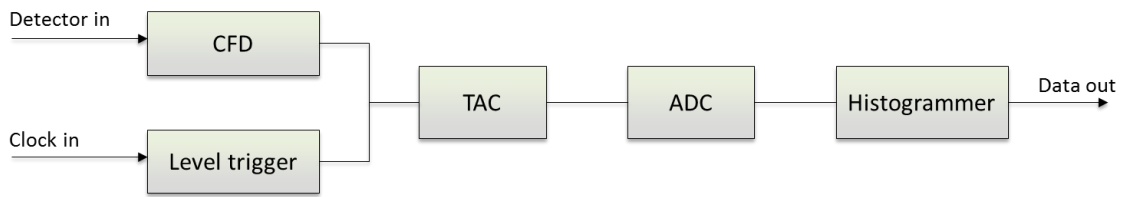
Figure 3.8. Block diagram of a conventional TCSPC system. The system comprises a Constant Fraction Discriminator (CFD), a Time to Amplitude Converter (TAC), an Analogue to Digital Converter (ADC), and a Histogrammer.
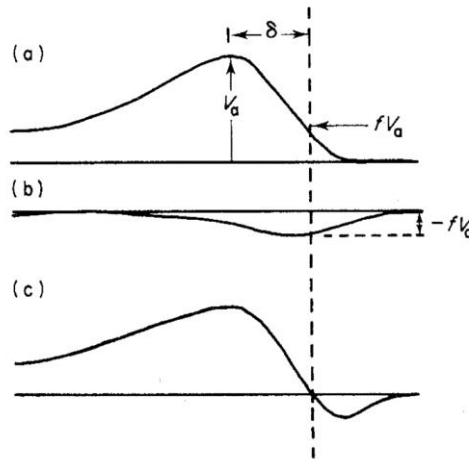
Figure 3.9. Diagram of a CFD operation. (a) The detector signal is delayed by a constant time δ, (b) attenuated by the factor f and inverted. The sum of (a) and (b) is shown in (c), and where the curve changes polarity provides the zero crossing point that gives the timing information. From [5].

51

The signals from the trigger level and the CFD are sent to a Time to Amplitude Converter (TAC), which generates a voltage ramp that starts with the sync signal and stops with the CFD signal, as shown in Figure 3.10. The output voltage is proportional to the time difference between the start and the stop signals, and it is sent to an Analog to Digital Converter (ADC) that provides the digital timing value to be used by the histogrammer [1]. The amplitude of the voltage ramp when the stop signal occurred is used as a record of the time at which the stop signal occurred. The ADC measures that amplitude to some precision and records it as a numeric value that is taken as a measure of the time difference between start and stop signals.
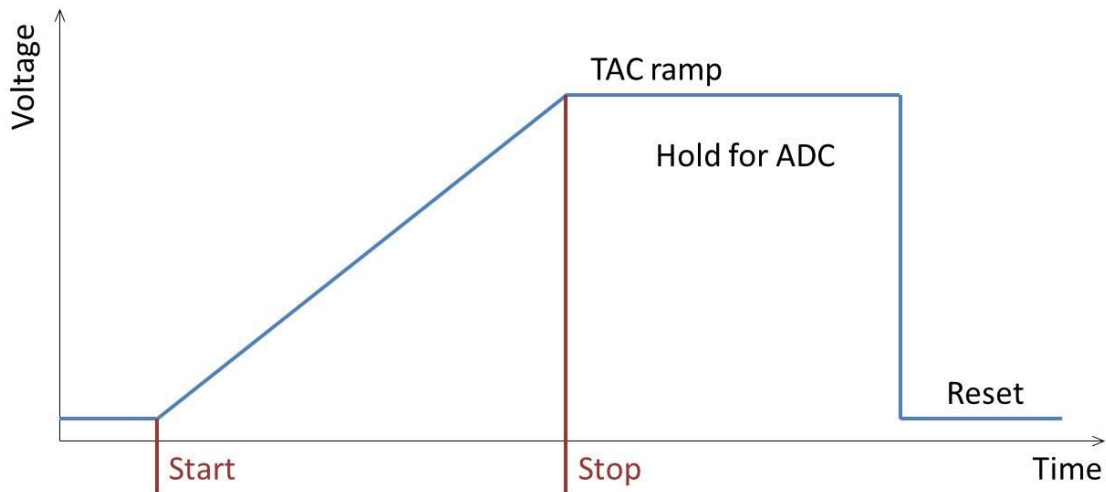
Figure 3.10. Principle of operation of a Time to Amplitude Converter.

As discussed before, the probability of detecting a photon per clock period is much less than unity, meaning that the TAC has to be restarted every time a clock period has elapsed without a recorded event. A dedicated circuit can be included in the system to reset the TAC, but this solution works well only when the sync signal repetition rate is low. When high repetition rates are used, the dead time of the system has to be considered. If the period of the clock signal is shorter than the dead time of the TAC and ADC, the system is not able to record events that may occur for laser pulses that take place during the reset process. This problem can be solved by using a reverse start-stop configuration, where the start signal is provided by the detector event while the stop is provided by the next clock signal [1].

In modern TCSPC systems, the function of the TAC and ADC can be performed by a Time to Digital Converter (TDC), a crystal clock digital counter based on high-speed all-digital technology. A TDC measures the time differences between signals in logic gates, offering high-speed time measurements with picosecond-resolution. This configuration permits retention of temporal information about the photon arrival, thanks to a coarser timing performed on each event with respect to the clock signal [6]. This acquisition mode is called Time-Tagged Time-Resolved data collection [7], and it will be discussed more in detail in Chapter 5.

3.4.   Single-photon detectors

Several parameters can be defined to evaluate the performance of single-photon detectors based on different technologies. Each parameter will be briefly defined here, and then considered in greater detail later.

Dead time is the time spent by the detection system to reset itself after a detection event. During this time the detector is not able to detect any other event, hence long dead times can affect the total count rate. The detector dead time can be considerable, depending on the type of detector. In many cases, the reset time of other components in the acquisition chain can be greater than the detector dead time, for example, the dead time of the ADC or TDC is often greater than the time spent by the detector for the reset

Detection efficiency is defined as the probability that an incident photon generates a measurable current pulse, assuming that the time between photon arrivals is greater than the dead time of the detection system [8]. This is an overall efficiency that includes several contributions: coupling efficiency (probability that the photon is incident on the active area of the detector), absorption efficiency (probability that a photon is absorbed by the detector), and the triggering efficiency (probability that a photon absorbed in the active volume of the detector produces a readable output pulse).

Timing jitter can be defined as an estimation of the error in the timing of the detection response. When considering the histogram of the studied optical signal, the timing jitter is typically described in terms of the Full Width at Half Maximum (FWHM) of the distribution, as shown in Figure 3.11.
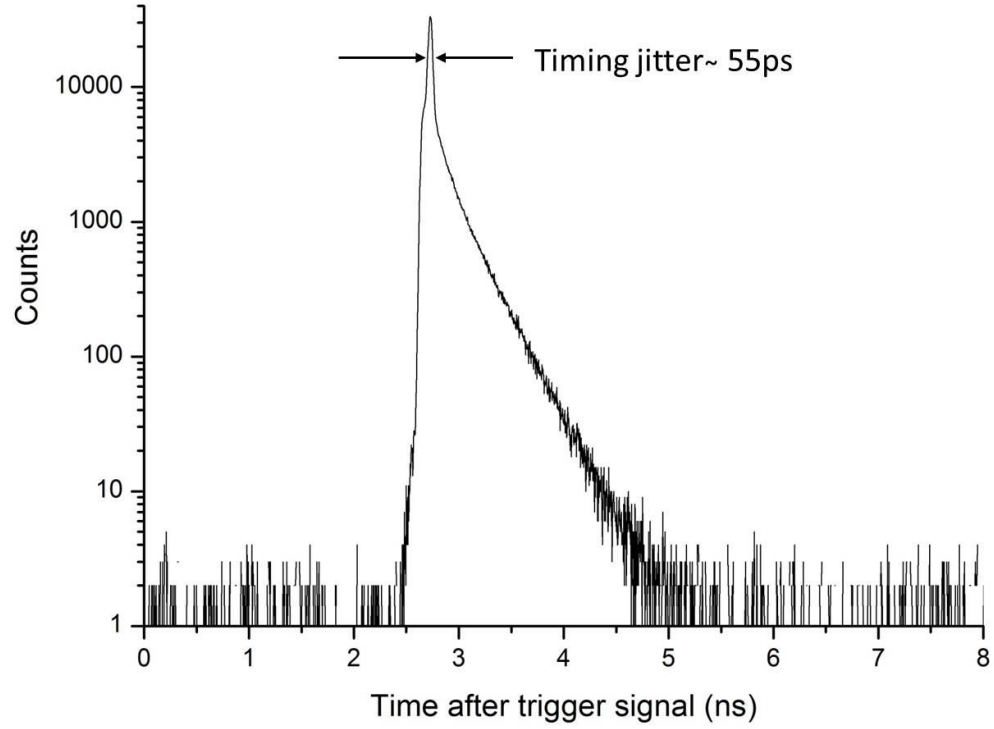
Figure 3.11. Timing histogram showing the timing jitter of a Micro Photon Devices (MPD) PDM series Si-based single-photon detector at λ = 670 nm.

Some events can be recorded by the detector even in the absence of incident light. These events are called "dark events". They represent the internal noise of a single-photon detector and are typically expressed in counts/sec, the average number of times the detector is triggered in 1 second by events that cannot be attributed to external photons. Dark events can be caused by several mechanisms, which will be discussed in more detail in section 3.4.3. Since false events contribute to the total count rate in the measurement, the dark count rate has to be as low as possible in order to optimise the SNR.

Every detector works in a specific range of wavelengths. This depends on the absorption efficiency of the detector, and on the probability that the absorption leads to a self-sustaining avalanche which can be detected. It is therefore useful to have a single parameter that can compare different detectors across different architectures, material compositions, and operational wavelengths. One potential comparative figure of merit for single-photon detectors is the noise equivalent power (NEP). This depends on the single-photon detection efficiency (η) and the dark count rate (DCR), and it is defined as

$$NEP = \frac{hc}{\lambda \eta} \sqrt{2DCR}$$ Equation 3.4

where λ is the wavelength of the incident light. The NEP is defined as the signal power required to attain a unity signal-to-noise ratio within 1 second of integration time [8]. The lower the NEP, the more sensitive is the detector.

3.4.1.   Photomultiplier Tubes

A photomultiplier tube (PMT) is the first example of a single-photon detector considered here. It was first demonstrated in 1935 [9] and used in a wide range of application. Figure 3.12 shows a diagram of the device. PMTs use a photocathode placed at the incident end of a vacuum tube, and a series of dynodes placed before an anode, which is at the far end. When a photon is absorbed in the photocathode, an electron is emitted because of the photoelectric effect. The electron is accelerated in an electric field toward the first dynode. When it hits the dynode more electrons are released via secondary emission and subsequently accelerated toward the next dynode. Each dynode is biased with a higher positive voltage than the previous, resulting in an increasing number of electrons propagating through the vacuum tube until the electron cascade reaches the anode creating a current pulse of typically 10^6 or more electrons [8]. PMTs have a high internal gain, compared to the silicon semiconductor single-photon detectors employed in the experiments reported in this Thesis. When N dynodes are used, the multiplication factor M is

$$M = \alpha^N$$ Equation 3.5

where α is the secondary electron coefficient. Typical values $\alpha = 5$ and $N = 10$ gives a multiplication factor of 10^7 [10].
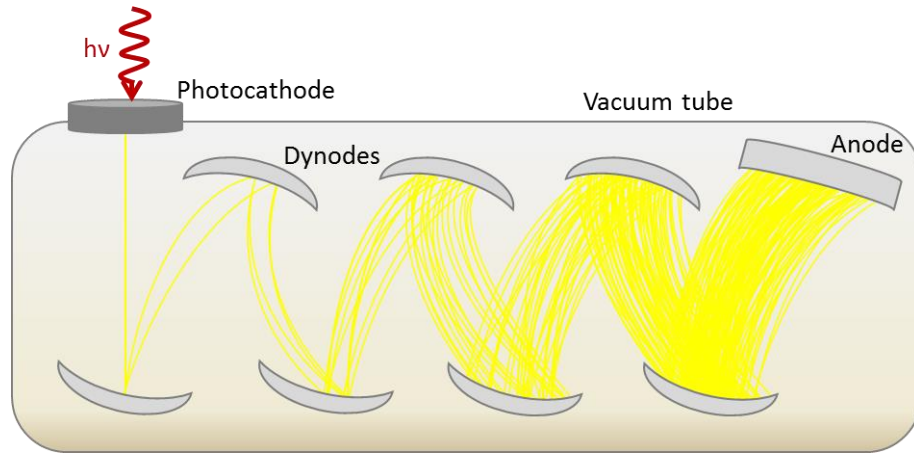
Figure 3.12. Schematic of a photomultiplier tube.

Compared to the detector described later in this chapter, PMTs have a large collecting area (i.e. a large photocathode) – typically a few mm in diameter. However, PMTs typically show NEP values of the order of 10^{-16} WHz$^{-1/2}$[11], low to moderate single-photon detection efficiency, and the timing jitter is approximately in the range of 1 ns, because of the transit time spread between photocathode and anode [8]. Hence in an application where high detection efficiency and low timing jitter are required, detectors based on different technologies are preferred.

3.4.2. Microchannel plates

Another example of a photocathode based detector is the microchannel plate (MCP). An MCP consists of a two-dimensional array of thousands of channels composed of thin glass tubes with a diameter typically of the order ~ 10 μm. The inner wall of each channel is made with a photo-emissive material that serves as an emitter of secondary electrons. The first input electron is accelerated along the channel. When this collides with the walls, a secondary electron cascade is started. The process is repeated for each secondary electron, resulting in an exponential multiplication of the electron flux along the channel [12]. A schematic of an MCP structure is shown in Figure 3.13. Compared with PMTs, the gain of MCPs is lower and limited to approximately 10^4 [13]. However, the timing jitter of MCPs is of the order of $20 - 30$ ps thanks to the short electron transit times and very low transit time spread in these devices [14]. In addition, the large 2D array configuration makes the MPCs particularly suitable for being used as an image intensifier, an X-ray diagnostic tool and for non-destructive imaging [12].
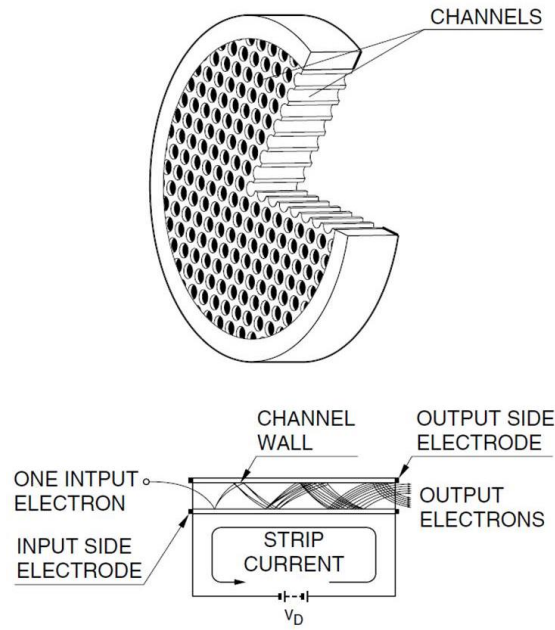
Figure 3.13. Schematic structure of an MCP. From [13].

3.4.3.   Single-photon avalanche photodiodes

A more efficient alternative to dynode-based detectors is given by single-photon avalanche diodes (SPADs). These devices convert an optical signal into an electrical signal, exploiting the conductive properties of semiconductors. When a photon is absorbed, an electron is promoted from the valence band to the conduction band, leaving a hole in the valence band that will act as a positive charge. In this way, an electron-hole pair is formed, which generates a measurable photocurrent when accelerated by an electric field [15]. The most basic detector uses a p-n junction, formed by two semiconductors, one with an excess of holes (p-type) and the other with an excess of electrons (n-type). In equilibrium, the difference in doping concentrations leads to a diffusion of the carriers: holes diffuse toward the n-type semiconductor leaving ion acceptors, and electrons diffuse toward the p-type semiconductor leaving ion donors [16]. Due to the diffusion of the carriers, a small charged region is formed at the interface, known as depletion region because it is depleted of charge carriers [17]. As a result, an electric field E_0 is created in proximity of the junction, causing the holes to drift toward the p-type semiconductor, and the electrons to drift in opposite direction. At the equilibrium, the diffusion current due to the different doping concentration balances the drift current due to the electric field, meaning that the total current in the junction is zero. This process is shown schematically in Figure 3.14.
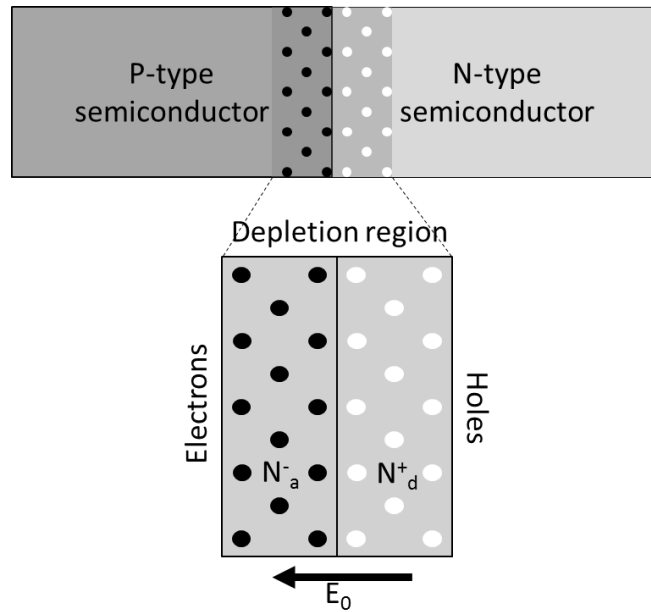
Figure 3.14. P-n junction in equilibrium conditions. The depletion region is enlarged in the figure. In equilibrium, the difference in doping concentrations leads holes to diffuse toward the n-type semiconductor leaving ion acceptors N_a^-, and electrons to diffuse toward the p-type semiconductor leaving ion donors N_d^+.

If an external potential difference is applied to the junction, the potential across the junction can be lowered (forward bias) or increased (reverse bias), as shown in Figure 3.15. When the junction is forward biased, the charge carriers move to re-establish an equilibrium condition, creating a current across the junction. If reverse biased, the diffusion of the charge carriers is inhibited because the holes in the p-type semiconductor move away from the depletion region increasing the number of negative acceptor ions, and at the same time the electrons in the n-type semiconductor move away from the depletion region increasing the number of positive donor ions. This results in a wider depletion region in both the p-side and the n-side.
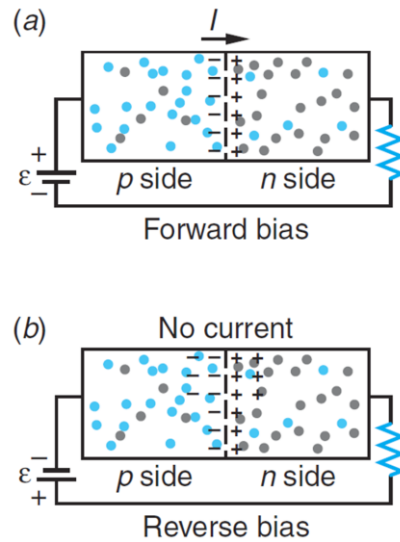
Figure 3.15. A p-n junction diode forward biased in (a) and reverse biased in (b). When the junction is forward biased, the charge carriers move across the junction, resulting in a current in the device. When the junction is reverse biased, the charge carriers are inhibited from moving. From [17].

When a photon with energy greater than the band gap of the material is absorbed in the depletion region of a reverse biased p-n junction, it creates an electron-hole pair. The electron and the hole will drift in opposite directions, producing a measurable current in the device, called photocurrent and often denoted by I_{ph}. However, the photon can be absorbed outside the depletion region. In this case, the charge carriers will contribute to the photocurrent just after they diffuse into the depletion region. In general, the diffusion is a slow process and it should be avoided for fast detector operation. This can be accomplished changing the width of the depletion region to increase the likelihood of photons being absorbed within the depletion region. If a layer of intrinsic (not doped) semiconductor is grown between the p-side and n-side, a wider depletion region can be achieved. When reverse biased, the intrinsic layer is depleted and the electric field is extending over the thickness of the intrinsic region. Such a device is called p-i-n junction, and in Figure 3.16 it is compared to a reverse biased p-n junction. The advantages of the p-i-n photodiode are increased detection efficiency, and higher carrier mobility in the i-region allowing faster carrier transport in this lower capacitance design.
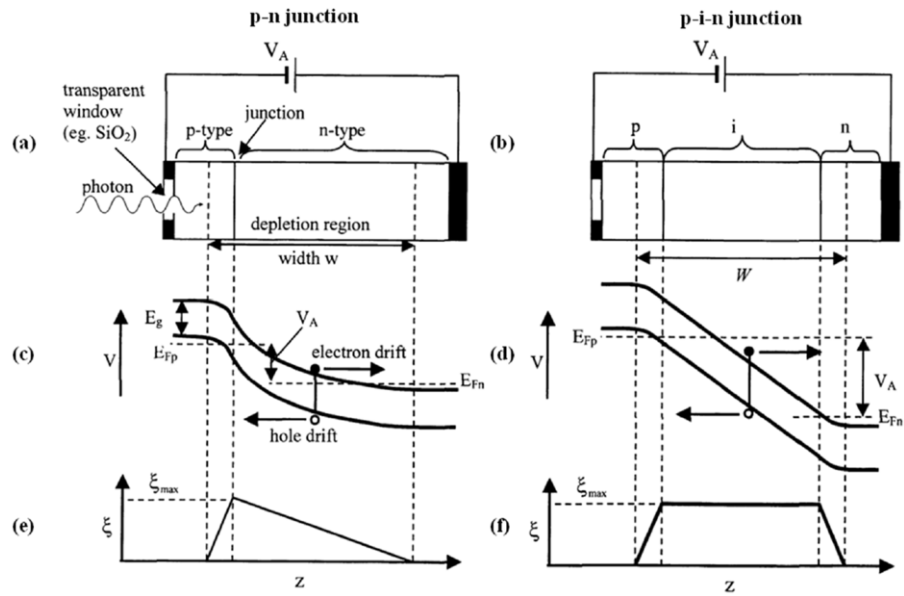
Figure 3.16. Reverse biased p-n junction (on the left) and p-i-n junction (on the right). From [18].

Figure 3.17 shows an example of an I-V characteristic curve for a photodetector. The graph shows that increasing the magnitude of the reverse bias leads to the breakdown region. In this case, the electric field is high enough to let a drifting electron gain sufficient kinetic energy to impact on atoms of the crystal lattice and promote a bound electron from the valence band to the conduction band. This electron will go through the same process, resulting in an avalanche multiplication. This process is called impact ionisation and it is shown schematically in Figure 3.18. Devices operating in this mode are known as Avalanche Photo-Diodes (APDs), and the operation mode is called "linear multiplication mode".
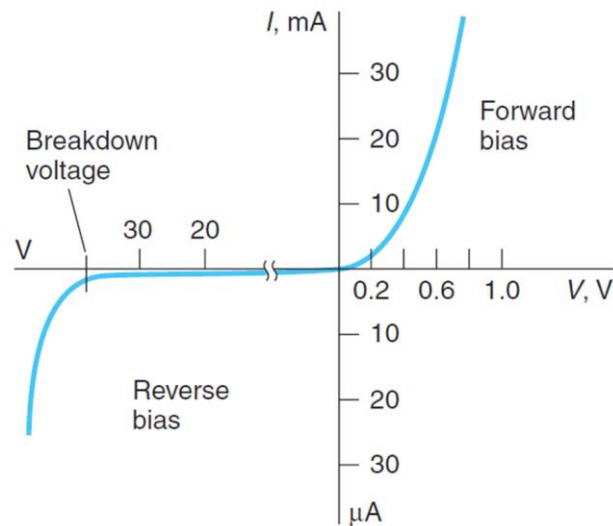
Figure 3.17.   Example of I-V characteristic curve for a photodetector.
From [17].
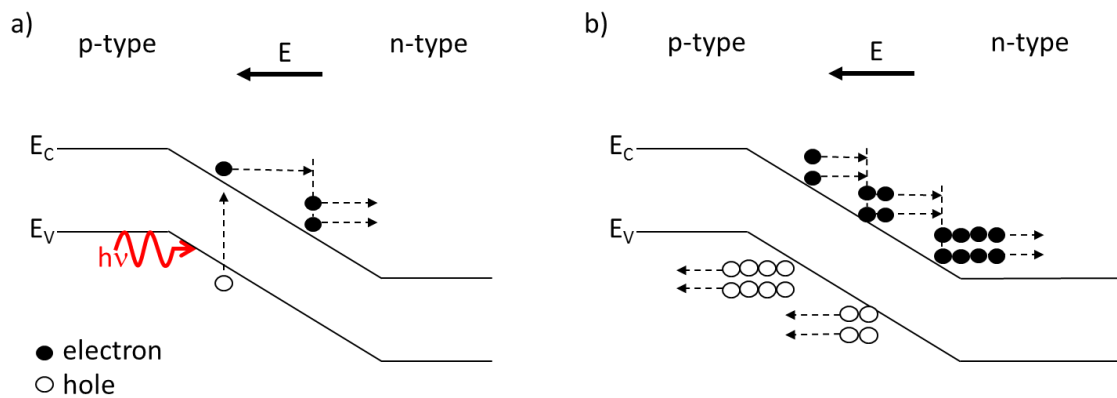
Figure 3.18.   (a) If a photon is absorbed in the depletion region of the
junction and its energy is high enough, an electron is promoted to the
conduction band, leaving a hole in the valence band. (b) If the electric
field in the junction is high enough, the charge carriers can gain
sufficient kinetic energy to cause more impact ionisation events colliding
with the lattice, resulting in an avalanche effect.

If the device is biased beyond the avalanche breakdown region, it operates in "Geiger mode". In this case, a very high electric field drifts all the free charge carriers and no current flows in the depletion region. When a photon is absorbed, it creates an electron-hole pair that will be induced to drift by the electric field, and impact ionisation will take place. However, this process is self-sustaining due to the high electric field [19], and the avalanche current will flow until externally quenched. Avalanche photodiodes operating in this mode are referred to as Single-Photon Avalanche-Diodes (SPADs).

61

To stop the avalanche current, three types of quenching can be applied: passive, active, and gated. In passive quenching, most of the external bias drops across a high impedance load, connected in series with the SPAD [20]. However, this configuration requires long recovery times, typically of the order of 1 μs [21]. Shorter recovery times (of the order of a few nanoseconds) can be obtained with active quenching, where a negative pulse is superimposed to the external bias quenching the avalanche process [22, 23]. A different approach is used for the gated quenching, in this case the device is biased above the breakdown level just for a small temporal interval when the photon is expected. Hence, the knowledge of the arrival time of the photon is required, making this technique unsuitable for an application like time-of-flight ranging, where the distance to the target is, in general, unknown.

As mentioned before, the dark count rate represents the internal noise of a SPAD and can limit the performance of the device. Dark events in SPADs can be due to different mechanisms such as, for example, carriers thermally generated in the active area of the detector or generated by tunnelling processes [24]. These two mechanisms cause avalanche events even in the absence of incident photons. Thermally generated carriers can be significantly reduced by reducing the operating temperature of the device. However, charge carriers can also be generated by tunnelling processes, which are not dependent on temperature. These processes depend on the electric field in the device, setting a lower limit to the dark count rate because the electric field has to be high enough to ignite avalanche multiplication. Dark counts can also be due to the effect of afterpulsing, caused by carriers emitted from trapping levels that were previously populated, for example when a previous dark count or an incident photon triggered an avalanche process in the detector [25]. Defects and impurities in the crystal generate local levels at intermediate energies between the band edges, which act as traps that hold carriers during an avalanche multiplication. When the device is quenched, the traps release the carriers, which can trigger another avalanche multiplication if the quenching is stopped before all the traps are empty. This effect is mainly dependent on the bias voltage: at high voltage more carriers are free to move, increasing the probability that a trap holds a carrier. Hence, the afterpulsing can be effectively reduced limiting the carriers in the detector and using appropriate quenching circuits [21]. However, this comes at the cost of a lower photon detection efficiency, which increases with the excess bias voltage applied [26].

3.4.3.1.   Silicon single-photon avalanche diodes

Silicon (Si) based SPADs operate in the wavelength range 400-1000 nm, and they are widely used in several applications including time-of-flight ranging [27], and quantum communication [28, 29].   The main designs of Si-SPADs in use at present are sometimes referred to as "thick junction" and "thin junction", and examples of device design schematics are shown in Figure 3.19.   The difference between the two junctions is in the depletion region, which leads to different performances of the devices.   In thick junctions the depletion region is 10-100 μm wide [30], and due to the long interaction length these devices have a single-photon detection efficiency of the order of ~65% at $\lambda = 700$ nm [31]. The timing jitter is of the order of 400 ps in devices with active area of approximately 200 μm [31], however it is possible to optimise the detector timing response by up to 40% using external timing circuitry [32].   In thin junction detectors the depletion region is a few μm wide [33], resulting in a lower detection efficiency of ~50% at $\lambda = 550$ nm [34].   However, the timing jitter in this case is greatly improved, and it can be up to 50 ps when the active area is ~50 μm diameter [34].
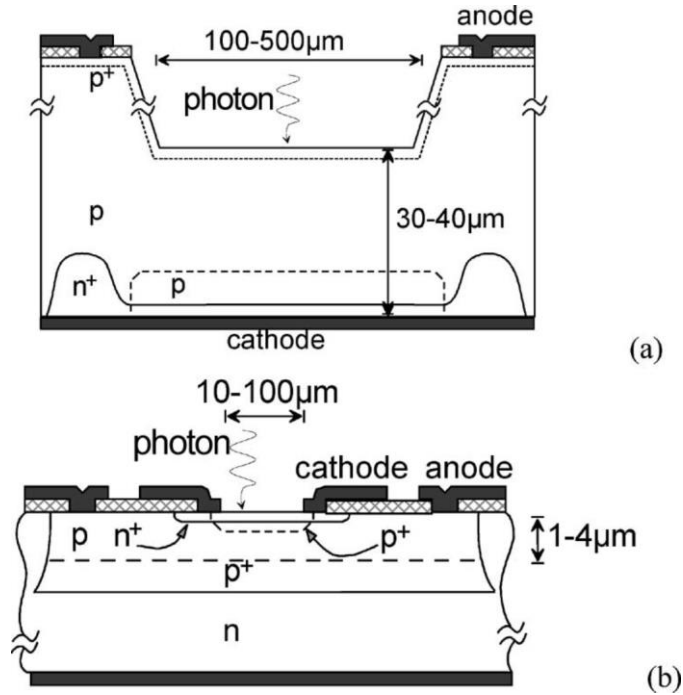
Figure 3.19.   (a) Schematic of a thick junction silicon single-photon avalanche diode, and (b) a thin junction silicon single-photon avalanche diode.   From [30].

The first practical design of a Si-SPAD was implemented by *Cova et al.* in 1981 [23], using thin junction geometry.   However, the early devices exhibited a long diffusion

tail, caused by carriers absorbed in the substrate and diffusing more slowly towards the depletion region [35], as shown in Figure 3.20. Over the years, improvements in the design of thin junctions allowed the suppression of diffusion tails [36, 37], also achieving a temporal resolution of a few hundreds of picoseconds at $1/100^{th}$ of the maximum of the detector response [38, 39].
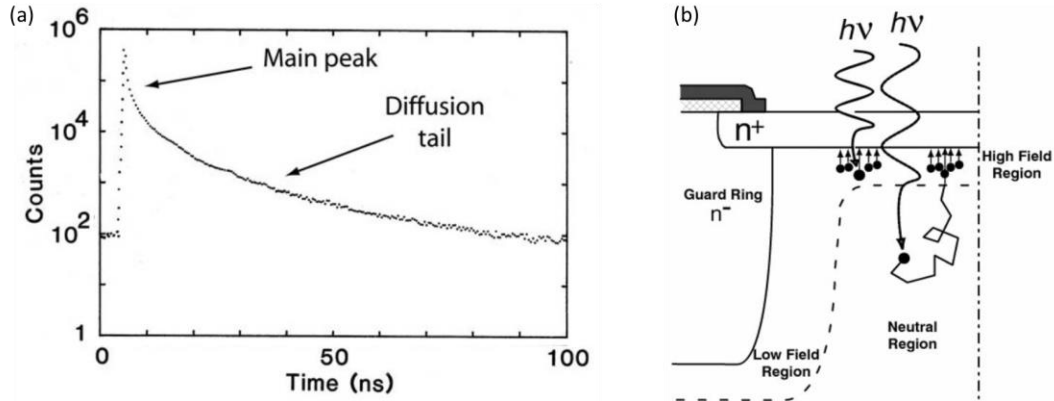
Figure 3.20. (a) Timing histogram showing the response of a planar Si-SPAD. (b) Avalanche process when a photon is absorbed in the depletion layer and in the substrate. Both from [39].

While the photon detection efficiency is not dependent on the active area of the device [28], the dark count rate increases for larger active areas. An example is shown in Figure 3.21, where the dark count rate is shown for devices with three different active areas, in the temperature range from -50°C to 20°C [40]. At room temperature, typical values are ~900 cps for 50 μm active area, ~4000 cps for 100 μm active area, and ~40000 cps for 200 μm active area [40]. As the temperature decreases, the probability of thermally generated events drastically reduces and the dark count rate decreases exponentially.
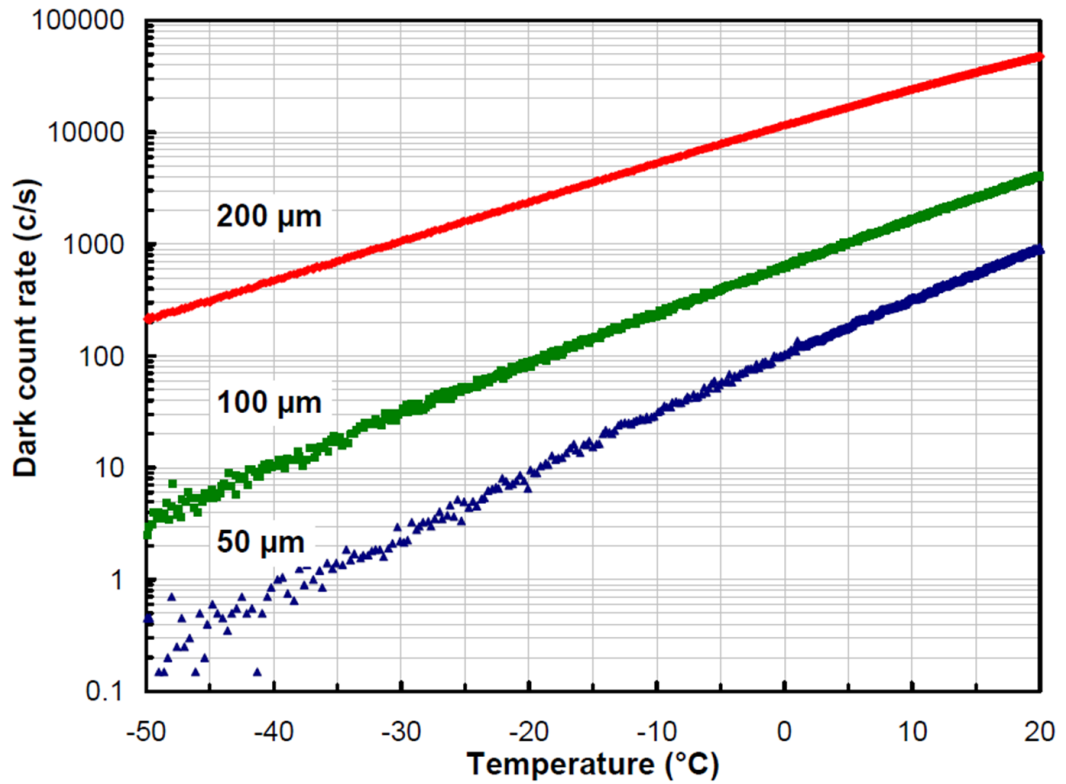
Figure 3.21. Dark count rate versus temperature for three Si-SPADs with different active areas [40].

It is worth noting that values of NEP of the order of 10^{-17} WHz$^{-1/2}$ were demonstrated for a 50 μm diameter thin junction Si-SPAD, operating at room temperature using an incident wavelength of $\lambda = 850$ nm [40]. While typical NEP values of the order of 10^{-18} WHz$^{-1/2}$ for thick junction are achievable at a temperature of approximately -25 °C, and at room temperature, the NEP can be also of the order of 10^{-16} WHz$^{-1/2}$ [8].

Silicon devices were selected to perform the experiments reported in this Thesis, as they offer high detection efficiencies in the visible wavelength range, corresponding to a low attenuation for water (refer to Chapter 4). Semiconductor devices were chosen since they are relatively compact, Peltier cooled modules with low timing jitter compared to alternatives such as PMTs. Three silicon-based single-photon detectors were used, a thick junction Si-SPAD manufactured by Perkin Elmer (Canada), and two different thin junction Si-SPADs manufactured by Micro Photon Devices (Italy).

The Perkin Elmer SPCM-AQR series (SPCM – CD 2882) offers single-photon detectors based on the thick junction Slik silicon avalanche photodiode [32, 33, 41]. The model available for this project had an active area of 180 μm. The photon detection

efficiency was approximately 65% at the wavelength $\lambda = 700$ nm, with a maximum dark count rate of 500 cps, as specified by the manufacturer. A typical curve of photon detection efficiency versus the wavelength is reported in Figure 3.22b).
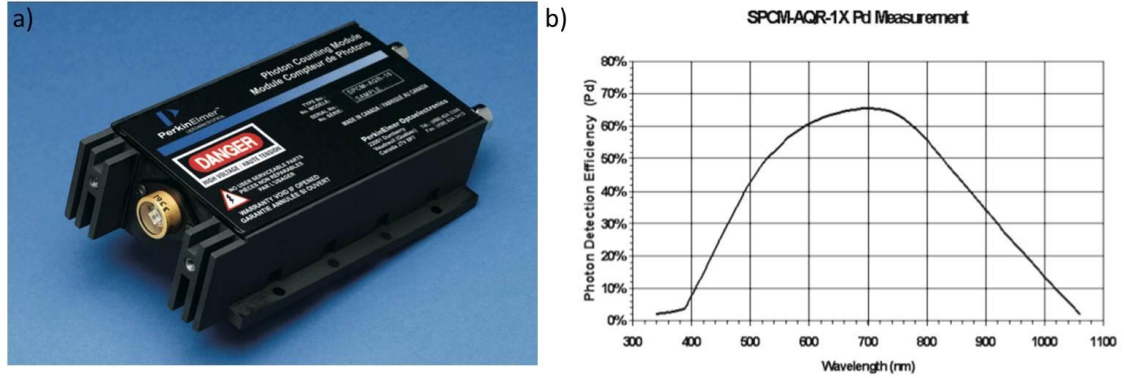
Figure 3.22. (a) Photograph of the thick junction Perkin Elmer Si-SPAD SPCM – CD 2882. (b) Photon detection efficiency of the same SPAD versus the wavelength. Both from [31].

When an event was detected, the module provided a differential TTL positive electrical pulse. The pulse was re-shaped using an inverter and several attenuators to meet the input requirements of the TCSPC module. The temporal response of the Perkin Elmer module stated by the manufacturer was approximately 350-400 ps. However, during the experiments the overall temporal response of the system is a combination of the jitter of all the components, resulting in an overall jitter of approximately 530 ps.

The detectors mainly used during this PhD project were two Micro Photon Devices (MPD) PDM series Si-based thin junction single-photon detectors. One of the modules had an "FC" fibre-receptacle pre-aligned to the optical detector, the other was pigtailed with a multi-mode fibre of 62.5 μm diameter core. In general, the specifications of the two modules are similar, however under the same conditions they exhibited a different response, showing different SNR, gating window width, and background events detected, as will be discussed in Chapter 5. The nominal active area of both detectors was 50 μm diameter. These detectors had a low jitter, which was stated by the manufacturer to be less than 50 ps. However, this came at the cost of lower detection efficiency compared to the thick-junction Si SPADs, as shown in Figure 3.23. The graph shows a peak single-photon detection efficiency of 48% at the wavelength $\lambda = 550$ nm, with the efficiency reducing to approximately 30% at $\lambda = 700$ nm.
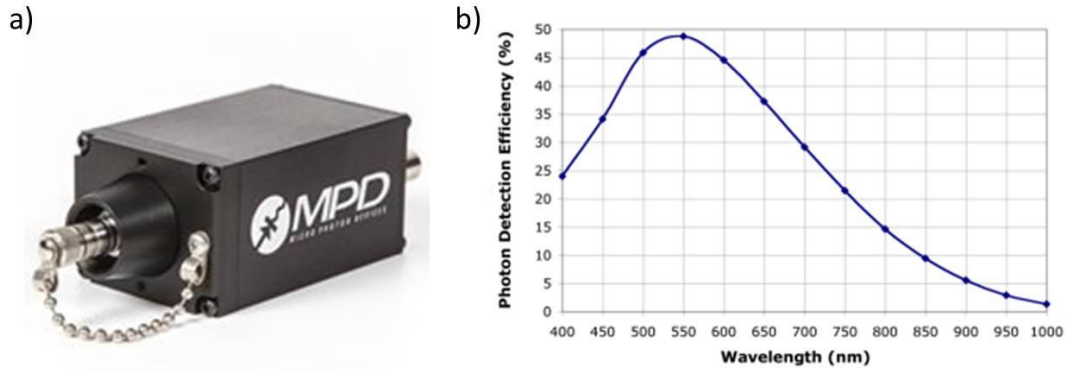
Figure 3.23. (a) Photograph of the fibre receptacle version of the Si-SPAD manufactured by Micro Photon Devices. (b) Photon detection efficiency of the same SPAD versus the wavelength. Both from [34].

The MPD Si-SPADs are thermoelectrically cooled, meaning that they are ready to collect events after only a few seconds of being powered on. The integrated active quenching circuit includes a built-in fast gating function that requires an external TTL signal to gate the detector on for a temporal window up to a few nanoseconds. This gives the advantage that the single-photon detector can be used to study weak optical signals, whilst gating out the undesired counts that occur at times outside the timing window of interest.

In the early 2000s, Si-SPADs were integrated into complementary metal oxide semiconductor (CMOS) technology [42], opening the way to the fabrication of compact high pixel density SPAD arrays. Early implementations of SPAD arrays did not integrate a time-to-digital converter (TDC) on chip, meaning that only one pixel per time was active [43, 44]. However, in 2008 *Niclass at el.* developed a 128×128 array with a bank of 32 integrated TDCs and a fast parallel readout circuitry [45]. A group of 4 pixels shared a TDC allowing one to activate an entire row at once, resulting in the first row-wise parallel acquisition array. Ideally, the integration of one TDC per detector is preferable in order to achieve a fast data acquisition over the entire array. The first example of such a design, as well with its characterisation, was presented in 2009 by *Gersbach et al.* [46]. They designed and characterised a 32×32 TDC array, demonstrating a timing jitter of approximately 120 ps. However, the design of the array showed non-uniform performance in the detection efficiency and in the measured arrival time, limiting the timing resolution [47]. In addition, when in-pixel circuitry is included in the array design, the detector photo-sensitive area available is compromised.

A useful parameter to quantify this issue is the geometric fill-factor, defined as the ratio of photo-sensitive area to total pixel area. For example, in reference [46] a fill-factor of 2.3% is reported, meaning a low overall active area available despite the large number of pixels. In 2014, *Villa et al.* reported a 32×32 array made of fully independent pixels operating in parallel [47]. In this case, each pixel had a SPAD detector with an active area of 30 μm diameter, fabricated in a 0.35 μm CMOS technology, which provides a better SPAD performance [48] than the standard deep-sub-micron CMOS technology used in the previously mentioned references. A micrograph of the array is shown in Figure 3.24a), while Figure 3.24b) shows the block diagram of a single pixel.

Figure 3.24. (a) Micrograph of the SPAD array. (b) Block diagram of a single pixel. Both from [47].

This design presented a fill factor of 3.14%, which was later improved with the integration of diffractive microlens arrays [49]. Recently, a fill-factor of almost 20% was achieved by *Parmesan et al.* basing the sensor on sample and hold Time-to-Amplitude Converter (TAC) pixels [50]. For each pixel a 2 bit column-parallel flash ADC was designed, and the histogram time generation is schematically shown in Figure 3.25. Each column comprised 4 comparators, which sampled 4 voltage references generated by a single ramp. The two reference voltages V_+ and V_- can be adjusted by the user, allowing to zoom into the time region of interest. This means that the TCSPC time bin range can be matched to the optical signal to be observed, contrary to the previous cases where the time bin range was fixed.

Figure 3.25. Column-parallel flash ADC digital readout. From [50].

3.4.3.2. InGaAs/InP single-photon avalanche diodes

SPAD detectors have been developed for near-infrared light detection. Generally, these detectors are not suitable for the underwater environment because of the high attenuation of infrared wavelengths in water. Below is a short discussion of available near-infrared SPAD detectors for comparison.

Indium gallium arsenide/indium-phosphide (InGaAs/InP) SPADs are the established technology for infrared single-photon counting at near-room and room temperature. In this case, separate absorption and multiplication layers are used to improve the performance of the device, in particular to reduce the effects of tunnelling on the narrow gap InGaAs region which will contribute to increased dark noise and reduced efficiency. An example of a cross-section of an InGaAs/InP SPAD is given in Figure 3.26, in which is shown that the absorption takes place in the InGaAs region, and impact ionisation takes place in the wide-gap InP layer.

Figure 3.26.   Schematic of a diffused-junction planar-geometry InGaAs/InP SPAD.   On the right of the figure, the behaviour of the electric field is reported for the centre of the device (in red) and for the edge of the diffused region (in grey).   From [51].

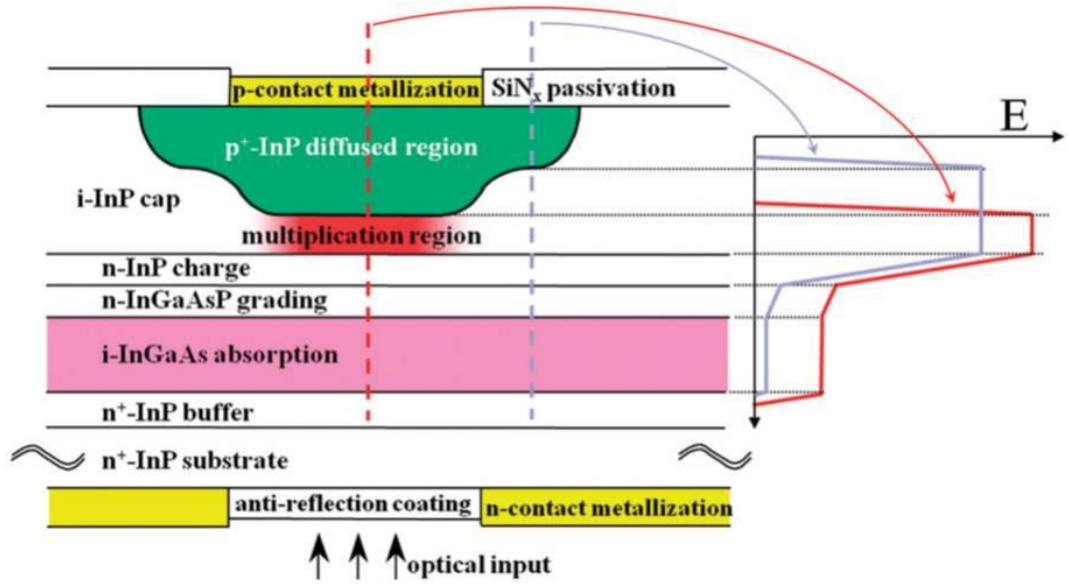The major issue for these devices is afterpulsing, which is reduced by using the detector in electrically gated mode. Gating the detector off allows the traps to empty and helps avoid further secondary avalanches caused by carriers emitted by the traps. In addition, more rapid quenching techniques have been developed to reduce the afterpulsing effect in these SPADs, allowing detection efficiencies up to 10.8% at $\lambda = 1550$ nm, and afterpulsing probability down to 2.8%, in rapid gated mode of up to 1.5 GHz [52, 53].

In recent years, advances in the growth and design of InGaAs/InP SPADs led to devices with single-photon efficiencies of up to 45% at $\lambda = 1550$ nm, 3 kcps dark count rate at 200 K operation, and 30 ps timing jitter, as reported by *Itzler et al.* in 2007 [54, 55]. In 2012, *Tosi et al.* designed and fabricated an InGaAs/InP SPAD working in gated mode at 225 K, exhibiting a detection efficiency of more than 25% at $\lambda = 1550$ nm and 40% at $\lambda = 1000$ nm, with a dark count rate below 100 kcps [56]. A number of references report also several techniques to operate an InGaAs/InP SPAD [57-60], however several researches are still ongoing on this field, in order to minimise dark count rate and afterpulsing with good efficiency.

As before, a wide range of NEP values can be found in the literature. To give an example, a value of the order of 10^{-17} WHz$^{-1/2}$ was demonstrated at room temperature,

with the device operating in free-running mode [61]. However, improvements can be obtained at low temperature, and NEP of the order of 10^{-16} W Hz$^{-1/2}$ at the temperature 77 K can be achieved [25].

3.4.3.3. Germanium based single-photon avalanche diodes

Due to the promising absorption properties at a wavelength of ~1500 nm of germanium (Ge) at room temperature [62], commercially available Ge-APDs were investigated in Geiger mode for the first time for photon-counting applications in 1994 [24, 63]. However, these devices were shown to have large dark count rate, low detection efficiency, and high afterpulsing probability compared to Si-SPADs at shorter wavelengths. However, subsequent studies demonstrated that using separate Ge absorption and Si multiplication layers improves the performance of the device [64]. In this case, the photon is absorbed in the Ge layer, creating an electron-hole pair. The electron is accelerated towards the interface between the two layers, before entering the Si multiplication layer. Here, impact ionisation takes place, and if the electric field is above the avalanche breakdown value, more impact ionisations can create a self-sustaining current. An example of a Ge-on-Si SPAD structure is shown in Figure 3.27.
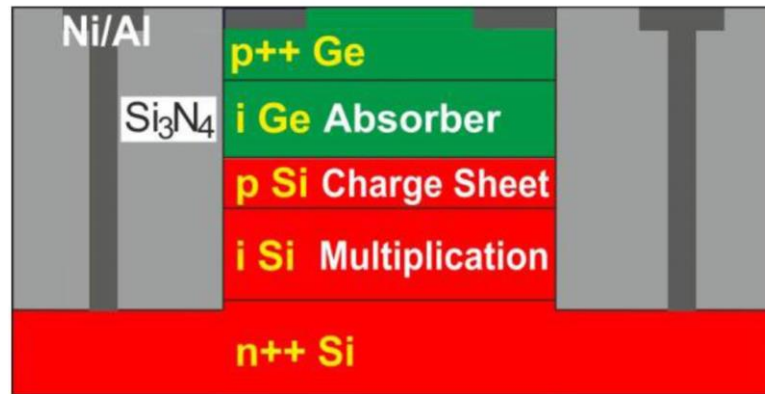
Figure 3.27. Schematic cross-section of a Ge-on-Si APD. From [65].

The main challenges in this field are concerned with the growth and the fabrication [66, 67], and several designs were developed in order to improve the detection efficiency and reduce the dark count rate and the afterpulsing effect [68]. Several research groups characterised Ge-on-Si SPADs based on different designs [69-71], presenting improvements in the detection efficiency (up to 14% at $\lambda = 1310$ nm in [69]) or the operating temperature (100 K in [71]). However, these devices presented high dark count rates (DCR > 10^8 Hz), which limited the performance of the devices.

In the literature, the reported values of the NEP vary in a wide range, however, as an example, values of less than 10^{-17} WHz$^{-1/2}$ at a wavelength of $\lambda = 1550$ nm have been demonstrated at room temperature [72].

3.4.4.   Superconducting single-photon detectors

Another class of detectors is based on superconducting materials. Superconductivity was discovered by Kamerlingh Onnes in 1911 while he was studying the electrical resistance behaviour of pure metals at low temperature. He observed that the resistance of some metals suddenly dropped down to zero at a particular temperature, called the critical temperature T_C, characteristic of the metal under study [73]. This discovery started a new research field, which has seen several landmarks over the years.

The absorption of a photon perturbs the electrical properties of the superconducting material, and these properties were exploited to create high sensitivity single-photon detectors for the infrared wavelength range.

3.4.4.1.   Superconducting transition-edge sensors

Transition-edge sensors (TES) are built with a film of superconducting materials, kept at a temperature just below the transition-edge from superconducting to non-superconducting state. The absorption of an incident photon heats the material, causing a change in the resistance. If the detector is biased with a constant voltage, a current can be read out using a superconducting quantum interference device (SQUID) amplifier [74]. The current pulse is proportional to the energy of the photon absorbed or to the photon number when a fixed wavelength is used [75]. These detectors offer high single-photon detection efficiency, of the order of 95% at $\lambda = 1550$ nm. However, they exhibit timing jitter in the region of 100 ns. Thanks to their capability in resolving photon number, these detectors are widely used for quantum optics experiments [76].

3.4.4.2.   Superconducting nanowire single-photon detectors

Superconducting nanowire single-photon detectors (SNSPDs) were developed for the first time in 1991 by *Gol'tsman et al.* [77]. The operation of an SNSPD is shown schematically in Figure 3.28. The material is kept at a temperature below its critical temperature. When an incident photon with energy greater than the superconducting energy gap is absorbed, it creates a local resistive hotspot with an average temperature

above T_C. The hotspot grows as hot electrons move away from the centre. At the same time, the supercurrent is perturbed and expelled from the hotspot, being concentrated between the hotspot and the edge of the wire. If the bias current is greater than the critical current, a non-superconducting region is rapidly formed, which creates a resistive strip on the wire, leading to a measurable voltage pulse.
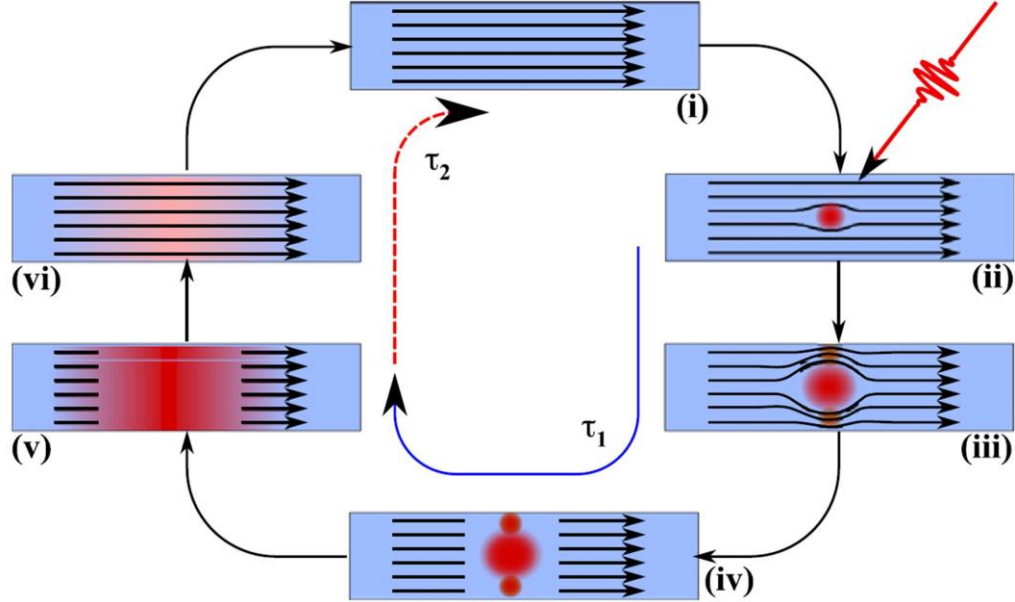
Figure 3.28. Schematic of the operating principle of a superconducting nanowire single-photon detector (SNSPD). The time constants τ_1 and τ_2 represent the rise time and decay of the voltage pulse. From [78].

Wires have to be narrow so that the resistive strip can form across the wire. However, such a narrow wire represents a small area for the absorption of a photon. Usually, the superconducting wire is arranged in a meander design that covers an area of up to 20 μm × 20 μm [79], as shown schematically in Figure 3.29, to increase the active area. Small area SNSPDs (3 μm × 3 μm) offer a detection efficiency of up to 20% at λ = 1550 nm and a timing jitter of 30 ps [80], while large area SNSPDs have detection efficiencies of approximately 1% at λ = 1550 nm and a timing jitter of 65 ps [74]. However, the detectors need to be cooled below the critical temperature in order to reach the superconducting state. Hence, the use of refrigerators or cryogens is essential, making SNSPDs highly expensive and difficult to employ in many applications where space, mass and power consumption are critical factors.
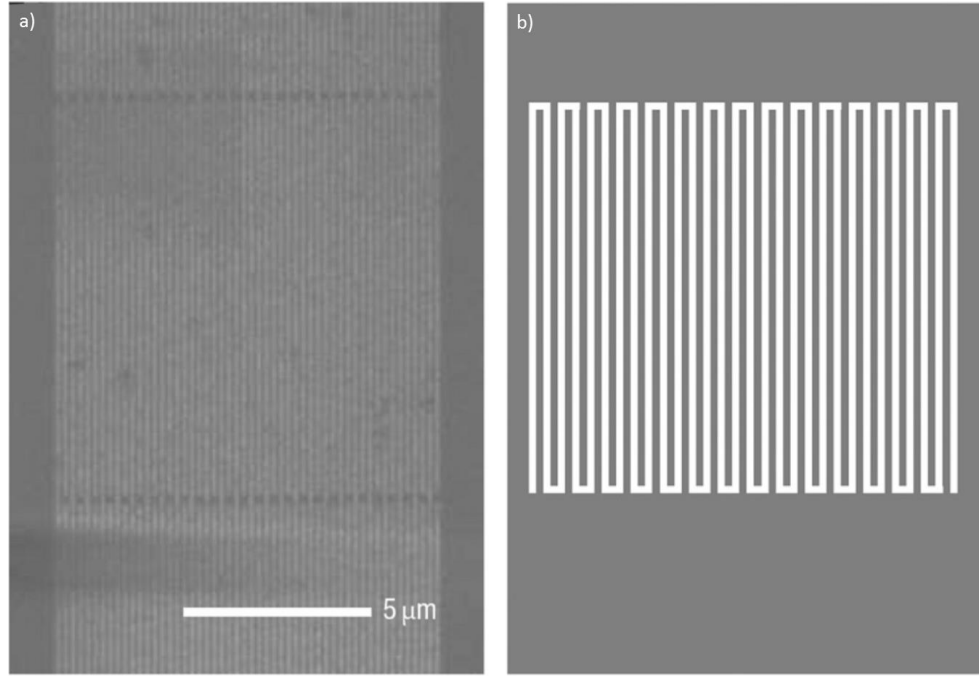
Figure 3.29. (a) Scanning electron microscope image of a superconducting nanowire single-photon detector [81]. (b) schematic of the meander design of a superconducting nanowire single-photon detector. From [8].

3.5. Conclusions

This chapter presented a brief review of the TCSPC technique and explained how picosecond optical transients can be measured in photon-starved regimes. This technique is used in several applications like time-resolved fluorescence [82], quantum communication [83], and long-range depth imaging [84]. The extension of this technique to underwater depth imaging will be investigated in this thesis, showing how the high sensitivity and precise temporal resolution of the TCSPC technique can be used to provide high spatial and depth resolution imaging also in highly scattering environments.

Appropriate considerations have to be made of the single-photon detection technologies available in order to choose the most suitable detector for implementation in the optical experiments. Hence, an overview of the main single-photon detectors was reported in this chapter, with particular attention to their key figures of merit, advantages, and limiting factors.

Si-SPADs are the best candidates for underwater imaging, as at room temperature they offer high detection efficiencies in the visible wavelength range, which corresponds to a low attenuation for clear water and scattering environments. Si-SPADs are relatively compact, Peltier cooled modules with low timing jitter compared to alternatives such as PMTs. Two different technologies of silicon detectors were used during this PhD project, a thick junction Si-SPAD by Perkin Elmer, and two thin junctions Si-SPADs by MPD.

The Perkin Elmer SPCM-AQR series thick junction exhibited a photon detection efficiency of approximately 65% at the wavelength $\lambda = 700$ nm, with a maximum dark count rate of 500 cps, as specified by the manufacturer. However, despite the high detection efficiency, the temporal response observed during the experiments was of the order of 530 ps.

In order to improve the temporal response of the system, two thin junctions by MPD were tested during this project. MPDs thin junctions offered a temporal response in the range $60 - 120$ ps, but this came at the cost of a lower detection efficiency. The two thin junctions had a photon detection efficiency up to 49% at the wavelength $\lambda = 550$ nm, as stated by the manufacturer.

In addition, the thin junctions MPD detectors include in the modules the appropriate circuitry to be gated. Gated detectors offer the opportunity to temporarily deactivate the detector in order to exclude unwanted optical signals, as back-reflections in the system or backscattering events which may occur in highly scattering envirnments.

For completeness, a brief review of the SPADs for infrared single-photon detection was given in this chapter, including InGaAs/InP SPAD, Ge-on-Si SPAD, and SNSPD. However, these detectors are not suitable for the underwater environment because of the high attenuation of infrared wavelengths in water.

References

1.   M. Wahl, "Time-Correlated Single Photon Counting," (PicoQuant, 2014).

2.   W. Becker, *Advanced Time-Correlated Single Photon Counting Techniques* (Springer, 2005).

3.	G. S. Buller, and A. M. Wallace, "Ranging and three-dimensional imaging using time-correlated single-photon counting and point-by-point acquisition," IEEE J. of Sel. Top. Quantum Electron. **13**, 1006-1015 (2007).

4.	S. Pellegrini, G. S. Buller, J. M. Smith, A. M. Wallace, and S. Cova, "Laser-based distance measurements using picosecond resolution time-correlated single-photon counting," Meas. Sci. Technol. **11**, 712-716 (2000).

5.	D. V. O'Connor, and D. Phillips, *Time-Correlated Single Photon Counting* (Academic, London, 1984).

6.	M. Wahl, H.-J. Rahn, I. Gregor, R. Erdmann, and J. Enderlein, "Dead-time optimized time-correlated photon counting instrument with synchronized, independet timing channels," Rev. Sci. Instrum. **78**, 033106 (2007).

7.	M. Wahl, H.-J. Rahn, T. Röhlicke, G. Kell, D. Nettels, F. Hillger, B. Schuler, and R. Erdmann, "Scalable time-correlated photon counting system with multiple independent input channels," Rev. Sci. Instrum. **79**, 123113 (2008).

8.	G. S. Buller, and R. J. Collins, "Single-photon generation and detection," Meas. Sci. Technol. **21**, 012002 (2010).

9.	H. Iams, and B. Salzberg, "The secondary emission phototube," Proceedings of the Institute of Radio Engineers **23**, 1, 55-64 (1935).

10.	G. F. Knoll, *Radiation detection and measurement* (John Wiley & Sons, Inc., 2000).

11.	https://www.hamamatsu.com/resources/pdf/etd/R9110_R9110P_TPMS1080E.pdf, Accessed 02-06-2016.

12.	A. Woodhead, and R. Ward, "The channel electron multiplier and its use in image intensifiers," Radio Electron. Eng. **47**, 12, 545-553 (1977).

13.	https://www.hamamatsu.com/resources/pdf/etd/MCPassy_TMCP0001E.pdf, Accessed 01-02-2016.

14.	W. Becker, and A. Bergmann, "Detectors for High-Speed Photon Counting," (Becker and Hickl GmbH, Berlin, 2002).

15.	C. Kittel, *Introductuion to solid state physics* (John Wiley & Sons, Inc., 2005).

16.	J. Millman, and C. C. Halkias, *Integrated electronics: Analog and digital circuits and systems* (McGraw-Hill Kogakusha, Ltd., 1972).

17.   P. A. Tipler, and R. A. Llewellyn, *Modern Physics* (Clancy Marshall, United States of America, 2008).

18.   C. E. Webb, and J. D. Jones, *Handbook of Laser Technology and applications: LAser design and laser systems* (2004).

19.   A. Lacaita, M. Mastrapasqua, M. Ghioni, and S. Vanoli, "Observation of avalanche propagation by multiplication assisted diffusion in p-n junctions," Appl. Phys. Lett. **57**, 5, 489-491 (1990).

20.   R. G. W. Brown, K. D. Ridley, and J. G. Rarity, "Characterization of silicon avalanche photodiodes for photon correlation measurements. 1: Passive quenching," Appl. Opt. **25**, 22, 4122-4126 (1986).

21.   S. Cova, M. Ghioni, A. Lacaita, C. Samori, and F. Zappa, "Avalanche photodiodes and quenching circuits for single-photon detection " Appl. Opt. **35**, 12, 1956-1976 (1996).

22.   P. Antognetti, S. Cova, and A. Longoni, "A study of the operation and performances of an avalanche diode as a single-photon detector," in *2nd ISPRA Nuclear Electronics Symposium* (Stresa, Italy, 1975).

23.   S. Cova, A. Longoni, and A. Andreoni, "Towards picosecond resolution with single-photon avalanche diodes," Rev. Sci. Instrum. **52**, 3, 408-412 (1981).

24.   A. Lacaita, P. A. Francese, F. Zappa, and S. Cova, "Single-photon detection beyond 1 μm: performance of commercially available germanium photodiodes," Appl. Opt. **33**, 30, 6902-6918 (1994).

25.   P. A. Hiskett, G. S. Buller, A. Y. Loudon, J. M. Smith, I. Gontijo, A. C. Walker, P. D. Townsend, and M. J. Robertson, "Performance and design of InGaAs/InP photodiodes for single-photon counting at 1.55 mm," Appl. Opt. **39**, 36, 6818-6829 (2000).

26.   W. G. Oldham, R. R. Samuelson, and P. Antognetti, "Triggering phenomena in avalanche diodes," IEEE Trans. Electron Devices **19**, 9, 1056-1060 (1972).

27.   A. McCarthy, R. J. Collins, N. J. Krichel, V. Fernandez, A. M. Wallace, and G. S. Buller, "Long-range time-of-flight scanning sensor based on high-speed time-correlated single-photon counting," Appl. Opt. **48**, 32, 6241-6252 (2009).

28.   S. Cova, M. Ghioni, I. Rech, A. Gulinatti, A. Giudice, and P. Maccagnani, "Silicon Single Photon Avalanche Diodes for Quantum Key Distribution," SECOQC Review (2008).

29.   P. J. Clarke, R. J. Collins, V. Dunjko, E. Andersson, J. Jeffers, and G. S. Buller, "Experimental demonstration of quantum digital signatures using phase-encoded coherent states of light," Nat. Commun. **3**, 1174 (2012).

30.   F. Zappa, S. Tisa, S. Cova, P. Maccagnani, D. Bonaccini Calia, R. Saletti, R. Roncella, G. Bonanno, and M. Belluso, "Single-Photon Avalanche Diode Arrays for Fast Transients and Adaptive Optics," IEEE Trans. Instrum. Meas. **55**, 1, 365-374 (2006).

31.   "SPCM-AQR Single Photon Counting Module Datasheet," (Perkin Elmer, 2005).

32.   I. Rech, I. Labanca, M. Ghioni, and S. Cova, "Modified single photon counting modules for optimal timing performance," Rev. Sci. Instrum. **77**, 033104 (2006).

33.   H. Dautet, P. Deschamps, B. Dion, A. D. MacGregor, D. MacSween, R. J. McIntyre, C. Trottier, and P. P. Webb, "Photon counting techniques with silicon avalanche photodiodes," Applied Optics **32**, 21, 3894-3900 (1993).

34.   "MPD - PDM Series Datasheet," (Micro Photon Devices, 2013).

35.   A. Lacaita, M. Ghioni, and S. Cova, "Double epitaxy improves single-photon avalanche diode performance," Electron. Lett. **25**, 13, 841-843 (1989).

36.   A. Lacaita, S. Cova, M. Ghioni, and F. Zappa, "Single-photon avalanche diode with ultrafast pulse response free from slow tails," IEEE Electron Device Lett. **14**, 7, 360-362 (1993).

37.   S. Cova, A. Lacaita, M. Ghioni, G. Ripamonti, and T. A. Louis, "20-ps timing resolution with single-photon avalanche diodes," Rev. Sci. Instrum. **60**, 6, 1104-1110 (1989).

38.   A. Spinelli, M. Ghioni, S. Cova, and L. M. Davis, "Avalanche detector with ultraclean response for time-resolved photon counting," IEEE J. Quantum Electron. **34**, 5, 817-821 (1998).

39.   M. Ghioni, A. Gulinatti, I. Rech, F. Zappa, and S. Cova, "Progress in silicon single-photon avalanche diodes," IEEE J. Sel. Top. Quantum Electron. **13**, 4, 852-862 (2007).

40.   M. Ghioni, A. Gulinatti, I. Rech, P. Maccagnani, and S. Cova, "Large-area low-jitter silicon single photon avalanche diodes," in *Quantum Sensing and Nanophotonic Devices V*, 6900 (SPIE, San Jose , USA, 2008).

41.   L.-Q. Li, and L. M. Davis, "Single photon avalanche diode for single molecule detection," Rev. Sci. Instrum. **64**, 6, 1524-1529 (1993).

42.   A. Rochas, M. Gani, B. Furrer, P. A. Besse, and R. S. Popovic, "Single-photon detector fabricated in a complementary metal-oxide-semiconductor high-voltage technology," Rev. Sci. Instrum. **74**, 7, 3263-3270 (2003).

43.   C. Niclass, A. Rochas, P. A. Besse, and E. Charbon, "Design and characterization of a CMOS 3-D image sensor based on single photon avalanche diodes," IEEE J. Solid-State Circuits **40**, 9, 1847-1854 (2005).

44.   D. Stoppa, L. Pancheri, M. Scandiuzzo, L. Gonzo, G. Dalla Betta, and A. Simoni, "A CMOS 3-D Imager hased on Single Photon avalanche diode," IEEE Trans. Circuits Syst. I Regul. Pap. **54**, 1, 4-12 (2007).

45.   C. Niclass, C. Favi, T. Kluter, M. Gersbach, and E. Charbon, "A 128 x 128 single-photon image sensor with column-level 10-bit time-to-digital converter array," IEEE Journal of Solid-State Circuits **43**, 12, 2977-2989 (2008).

46.   M. Gersbach, Y. Maruyama, E. Labonne, J. Richardson, R. Walker, L. Grant, R. Henderson, F. Borghetti, D. Stoppa, and E. Charbon, "A parallel 32x32 time-to-digital converter array fabricated in a 130 nm imaging CMOS technology," in *IEEE - 35th European Solid State Circuits Conference (ESSCIRC)*(Athens, Greece, 2009).

47.   F. Villa, R. Lussana, D. Bronzi, S. Tisa, A. Tosi, F. Zappa, A. Dalla Mora, D. Contini, D. Durini, S. Weyers, and W. Brockherde, "CMOS imager with 1024 SPADs and TDCs for single-photon timing and 3-D time-of-flight," IEEE J. Sel. Top. Quantum Electron. **20**, 6, 3804810 (2014).

48.   F. Villa, D. Bronzi, Y. Zou, C. Scarcella, G. Boso, S. Tisa, A. Tosi, F. Zappa, D. Durini, S. Weyers, U. Paschen, and W. Brockherde, "CMOS SPADs with up to 500 um diameter and 55% detection efficiency at 420 nm," J. Mod. Opt. **61**, 2, 102-115 (2014).

49.   G. Intermite, A. McCarthy, R. E. Warburton, X. Ren, F. Villa, R. Lussana, A. J. Waddie, M. R. Taghizadeh, A. Tosi, F. Zappa, and G. S. Buller, " Fill-factor improvement of Si CMOS single-photon avalanche diode detector arrays by integration of diffractive microlens arrays," Opt. Express **23**, 26, 33777-33791 (2015).

50.   L. Parmesan, N. A. W. Dutton, N. J. Calder, N. Krstajic, A. J. Holmes, L. A. Grant, and R. Henderson, "A 256 x 256 SPAD array with in-pixel Time to Amplitude Conversion for Fluorescence Lifetime Imaging Microscopy," in *International Image Sensor Workshop* (Vaals, Netherlands, June 2015).

51.   M. A. Itzler, X. Jiang, M. Entwistle, K. Slomkowski, A. Tosi, F. Acerbi, F. Zappa, and S. Cova, "Advances in InGaAsP-based avalanche diode single photon detectors," J. Mod. Opt. **58**, 3-4, 174-200 (2011).

52.   N. Namekata, S. Sasamori, and S. Inoue, "800 MHz Single-photon detection at 1550-nm using an InGaAs/InP avalanche photodiode operated with a sine wave gating," Opt. Express **14**, 21, 10043-10049 (2006).

53.   N. Namekata, S. Adachi, and S. Inoue, "1.5 GHz single-photon detection at telecommunication wavelengths using sinusoidally gated InGaAs/InP avalanche photodiode," Opt. Express **17**, 8, 6275-6282 (2009).

54.   M. A. Itzler, R. Ben-Michael, C.-F. Hsu, K. Slomkowski, A. Tosi, S. Cova, F. Zappa, and R. Ispasoiu, "Single photon avalanche diodes (SPADs) for 1.5 um photon counting applications," J. Mod. Opt. **54**, 2-3, 283-304 (2006).

55.   M. A. Itzler, X. Jiang, B. Nyman, R. Ben-Michael, and K. Slomkowski, "InP-based Single Photon Avalanche Diodes," in *IEEE LEOS Annual Meeting Conference Proceedings (LEOS '08)*(Newport Beach, California, 2008).

56.   A. Tosi, F. Acerbi, M. Anti, and F. Zappa, "InGaAs/InP Single-Photon Avalanche Diode With Reduced Afterpulsing and Sharp Timing Response With 30 ps Tail," IEEE J. Quantum Electron. **48**, 9, 1227-1232 (2012).

57.   A. Restelli, J. C. Bienfang, and A. L. Migdall, "Single-photon detection efficiency up to 50% at 1310 nm with an InGaAs/InP avalanche diode gated at 1.25 GHz," Appl. Phys. Lett. **102**, 141104 (2013).

58.   A. Tosi, C. Scarcella, G. Boso, and F. Acerbi, "Gate-Free InGaAs/InP Single-Photon Detector Working at Up to 100 Mcount/s," IEEE Photonics J. **5**, 4, 6801308 (2013).

59.   A. Tosi, N. Calandri, M. Sanzaro, and F. Acerbi, "Low-Jitter, High Detection Efficiency InGaAs/InP Single-Photon Avalanche Diode," IEEE J. Sel. Top. Quantum Electron. **20**, 6, 3803406 (2014).

60.   X. Jiang, M. A. Itzler, K. O'Donnell, M. Entwistle, M. Owens, K. Slomkowski, and S. Rangwala, "InP-Based Single-Photon Detectors and Geiger-Mode APD Arrays for Quantum Communications Applications," IEEE J. Sel. Top. Quantum Electron. **21**, 3, 3800112 (2015).

61.   R. E. Warburton, M. A. Itzler, and G. S. Buller, "Improved free-running InGaAs/InP single-photon avalanche diode detectors operating at room temperature," Electron. Lett. **45**, 19 (2009).

62.   W. C. Dash, and R. Newman, "Intrinsic Optical Absorption in Single-Crystal Germanium and Silicon at 77K and 300K," Phys. Rev. **99**, 4, 1151-1155 (1955).

63.   P. C. M. Owens, J. G. Rarity, P. R. Tapster, D. Knight, and P. D. Townsend, "Photon counting with passively quenched germanium avalanche," Appl. Opt. **33**, 30, 6895-6901 (1994).

64.   M. S. Carroll, K. Childs, R. Jarecki, T. Bauer, and K. Saiz, "Ge–Si separate absorption and multiplication avalanche photodiode for Geiger mode single photon detection," Appl. Phys. Lett. **93**, 183511 (2008).

65.   G. Intermite, R. E. Warburton, M. Myronov, P. Allred, D. R. Leadley, K. Gallacher, D. J. Paul, N. J. Pilgrim, L. J. M. Lever, Z. Ikonic, R. W. Kelsall, and G. S. Buller, "Design and performance of a prototype mesa-geometry Ge-on-Si single-photon avalanche diode detector at 1310 nm and 1550 nm wavelengths," in *IEEE 10th International Conference on Group IV Photonics (GFP)*(Seoul, Korea, 2013).

66.   V. A. Shah, A. Dobbie, M. Myronov, and D. R. Leadley, "Effect of layer thickness on structural quality of Ge epilayers grown directly on Si(001)," Thin Solid Films **519**, 7911-7917 (2011).

67.   V. A. Shah, A. Dobbie, M. Myronov, and D. R. Leadley, "High quality relaxed Ge layers grown directly on a Si(0 0 1) substrate," Solid State Electron. **62**, 189-194 (2011).

68.   J. Osmond, G. Isella, D. Chrastina, R. Kaufmann, M. Acciarri, and H. von Känel, "Ultralow dark current Ge/Si(100) photodiodes with low thermal budget," Appl. Phys. Lett. **94**, 201106 (2009).

69.   Z. Lu, Y. Kang, C. Hu, Q. Zhou, H. Liu, and J. C. Campbell, "Geiger-Mode Operation of Ge-on-Si Avalanche Photodiodes," IEEE J. Quantum Electron. **47**, 5, 731-735 (2011).

70.   M. Aminian, A. Sammak, L. Qi, L. K. Nanver, and E. Charbon, "A Ge-on-Si single-photon avalanche diode operating in Geiger mode at infrared wavelengths," in *Advanced Photon Counting Techniques VI*(SPIE, 2012).

71.   R. E. Warburton, G. Intermite, M. Myronov, P. Allred, D. R. Leadley, K. Gallacher, D. J. Paul, N. J. Pilgrim, L. J. M. Lever, Z. Ikonic, R. W. Kelsall, E. Huante-Cerón, A. P. Knights, and G. S. Buller, "Ge-on-Si Single-Photon Avalanche Diode Detectors: Design, Modeling, Fabrication, and Characterization at Wavelengths 1310 and 1550 nm," IEEE Trans. Electron Devices **60**, 11, 3807-3813 (2013).

72.   Z. Yan, D. R. Hamel, A. K. Heinrichs, X. Jiang, M. A. Itzler, and T. Jennewein, "An ultra low noise telecom wavelength free running single photon detector using negative feedback avalanche diode," Rev. Sci. Instrum. **83**, 073105 (2012).

73.   H. K. Onnes, "Investigation into the properties of substances at low temperatures, which have led, amongst other things, to the preparation of liquid helium," (Nobel Lecture, 1913).

74.   R. H. Hadfield, "Single-photon detectors for optical quantum information applications," Nat. Photonics **3**, 696-705 (2009).

75.   A. J. Miller, S. W. Nam, M. Martinis, and A. V. Sergienko, "Demonstration of a low-noise near-infrared photon counter with multiphoton discrimination," Appl. Phys. Lett. **83**, 4, 791-793 (2003).

76.   D. Rosenberg, J. W. Harrington, P. R. Rice, P. A. Hiskett, C. G. Peterson, R. J. Hughes, A. E. Lita, S. W. Nam, and J. E. Nordholt, "Long-distance decoy-state quantum key distribution in optical fiber," Phys. Rev. Lett. **98**, 010503 (2007).

77.   G. N. Gol'tsman, A. D. Semenov, Y. P. Gousev, M. A. Zorin, I. G. Godidze, E. M. Gershenzon, P. T. Lang, W. J. Knott, and K. F. Renk, "Sensitive picosecond NbN detector for radiation from millimetre wavelengths to visible light " Supercond. Sci. Technol. **4**, 453-456(1991).

78.   C. M. Natarajan, M. G. Tanner, and R. H. Hadfield, "Superconducting nanowire single-photon detectors: physics and applications," Supercond. Sci. Technol. **25**, 063001 (2012).

79.   S. Miki, M. Fiujiwara, M. Sasaki, B. Baek, A. J. Miller, R. H. Hadfield, S. W. Nam, and Z. Wang, "Large sensitive-area NbN nanowire superconducting single-photon

detectors fabricated on single-crystal MgO substrates," Appl. Phys. Lett. **92**, 061116 (2008).

80.   K. M. Rosfjord, J. K. W. Yang, E. A. Dauler, A. J. Kerman, V. Anant, B. M. Voronov, G. N. Gol'tsman, and K. K. Berggren, "Nanowire Single-photon detector with an integrated optical cavity and anti-reflection coating," Opt. Express **14**, 2, 527-534 (2006).

81.   H. Takesue, S. W. Nam, Q. Zhang, R. H. Hadfield, T. Honjo, K. Tamaki, and Y. Yamamoto, "Quantum key distribution over a 40-dB channel loss using superconducting single-photon detectors," Nat. Photonics **1**, 343-348 (2007).

82.   N. R. Gemmell, A. McCarthy, B. Liu, M. G. Tanner, S. D. Dorenbos, V. Zwiller, M. S. Patterson, G. S. Buller, B. C. Wilson, and R. H. Hadfield, "Singlet oxygen luminescence detection with a fiber-coupled superconducting nanowire single-photon detector," Opt. Express **21**, 4, 5005-5013 (2013).

83.   R. J. Collins, R. J. Donaldson, V. Dunjko, P. Wallden, P. J. Clarke, E. Andersson, J. Jeffers, and G. S. Buller, "Realization of Quantum Digital Signatures without the Requirement of QuantumMemory," Phys. Rev. Lett. **113**, 040502 (2014).

84.   A. McCarthy, X. Ren, A. Della Frera, N. R. Gemmell, N. J. Krichel, C. Scarcella, A. Ruggeri, A. Tosi, and G. S. Buller, "Kilometer-range depth imaging at 1550 nm wavelength using an InGaAs/InP single-photon avalanche diode detector," Opt. Express **21**, 19, 22098-22114 (2013).

Chapter 4

Attenuation of light in water

4.1. Introduction

This section describes the experiments performed to obtain transmittance and attenuation spectra of the water samples subsequently used for the depth profile measurements. These preliminary results permitted selection of an appropriate operational wavelength for each of the different scattering levels of the environments considered in this Thesis. Section 4.2 will give a few considerations about attenuation of light in water. Section 4.3 will explain the experiments performed to characterise the water sample selected, and it will provide some considerations about the settling times of the scattering agent used.

4.2. Propagation of light in water

To understand how the performance of an underwater imaging system may be improved, it is important to consider the physical properties of the propagation medium. In water, the light is attenuated mainly by absorption and scattering. Absorption includes all the irreversible thermodynamic processes, typically the transformation of photon energy into thermal kinetic energy of the propagation medium [1], and it can be described through the absorption coefficient a. Scattering events take place because of particles with feature sizes comparable to the wavelength of light. All the events can be described with the total scattering coefficient, b, defined as the superposition of many scattering events that occur in all directions. Indicating with $\beta(\vartheta, \varphi)$ the scatter per unit metre and per unit steradian in the direction (ϑ, φ), the scattering coefficient b can be expressed as [2]

$$b = \int_0^{2\pi}\int_0^{\pi} \beta(\vartheta, \varphi)\sin\vartheta\, d\vartheta\, d\varphi = 2\pi\int_0^{\pi} \beta(\vartheta)\sin\vartheta\, d\vartheta \qquad \text{Equation 4.1}$$

Both effects can be considered through a single attenuation coefficient $\alpha=a+b$, which can be related to the optical power level, $P(r)$, after propagation of a distance r in the medium [3]:

$$P(r) = P_0 e^{-\alpha r}$$

Equation 4.2

where P_0 is the initial power.

The attenuation coefficient of water exhibits a strong dependence on wavelength [4], with the attenuation minimum typically in the visible range [5]. For example, Figure 4.1 shows the optical absorption coefficient of pure water. The minimum of absorption is approximately in the blue range of the visible spectrum, where transitions between energy states in the water molecule are not induced.
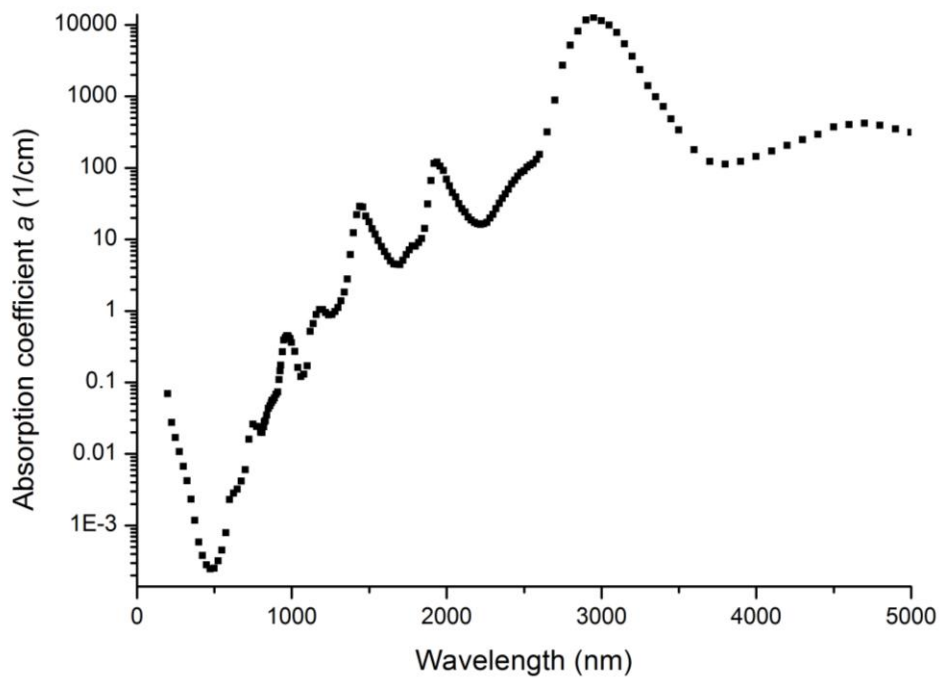

Figure 4.1. Optical absorption coefficient of pure water. Data from [5].

As the water becomes more turbid, the attenuation coefficient increases and the attenuation minimum shifts to longer wavelengths [6]. In general, the optical properties of naturally occurring water vary significantly, as they depend on different factors including temperature, salinity [7], and the nature of the dissolved organic matter and suspended sediments present in the water [8, 9]. Hence, spectral transmittance

measurements were performed on a number of different water samples across the wavelength range 500-900 nm, in order to characterise the water types used in the experiments reported in this Thesis. More specifically, the transmittance spectra of unfiltered tap water and coastal seawater were obtained to study natural waters. In addition, different volumes of Maalox were added to a tank of tap water to simulate the effects of scattering. Maalox is a commercially available antacid medicine that strongly affects scattering without inducing significant optical absorption [10]. The main ingredients of the agent were dried aluminium hydroxide gel 220 mg / 5 ml, and magnesium hydroxide 195 mg / 5 ml, which had an average particle size of approximately 40 μm. This scattering agent permitted to simulate real conditions, as its volume scattering function is similar to the volume scattering function of sea water [11].

4.3. Characterisation of water samples

In these measurements, a supercontinuum laser source, SuperK EXTREME – EXW12 (NKT Photonics, Denmark), was used in conjunction with an acousto-optic tunable filter (AOTF), SuperK Select multi-line tunable filter (NKT Photonics, Denmark), in order to select a single wavelength, whose spectral width was approximately 5 nm FWHM. Both of these components will be described in more detail in Chapter 5. As shown schematically in Figure 4.2, the monochromatic laser light emitted from a 50 μm diameter multi-mode optical fibre was collimated into a beam of approximately 6 mm in diameter and directed with into an 110 litre capacity tank (1750 mm long, 250 mm high, 250 mm wide). A mirror was placed in the tank of water at an angle of 45° to the beam and directed the light out through the side wall of the tank. To determine the transmittance of the water samples, optical powers were recorded with a silicon detector (Newport Power Meter 1830C and 818-UV detector head). First, the optical power readings were taken at Position 1, as shown in Figure 4.2. For each optical power measurement, two separated irises were aligned in front of the detector 21 cm apart. This configuration of spatial filtering allowed the laser beam to efficiently pass but blocked most of the forward-scattered light that could cause an over-estimation of the power of the transmitted light. The optical power was then measured with another mirror in Position 2 and the transmittance over one metre of propagation within the transmission medium was calculated from the ratio of these two power values. The medium's attenuation coefficient for that wavelength was then calculated using Equation 4.2. By repeating these optical power measurements at a series of different discrete wavelengths, the

transmittance and attenuation length spectra were ascertained. Figure 4.3 reports a photograph of the experimental setup.
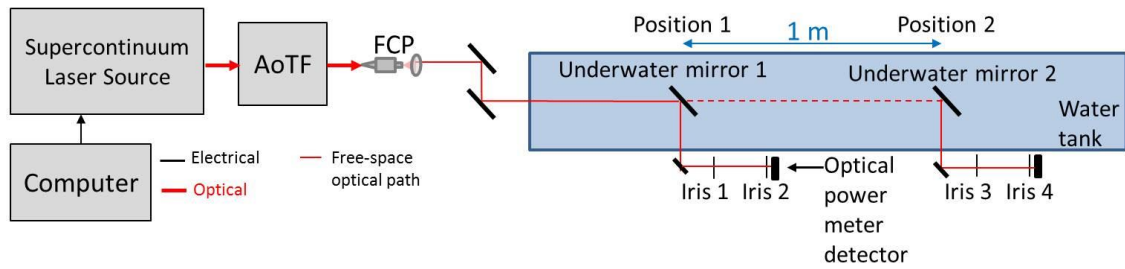

Figure 4.2. Schematic of the experimental setup used for the water transmittance measurements. The setup comprised a supercontinuum laser source, an acousto-optic tuneable filter (AOTF), an optical fibre collimation package (FCP), a tank, six mirrors, four irises and a silicon optical power meter.
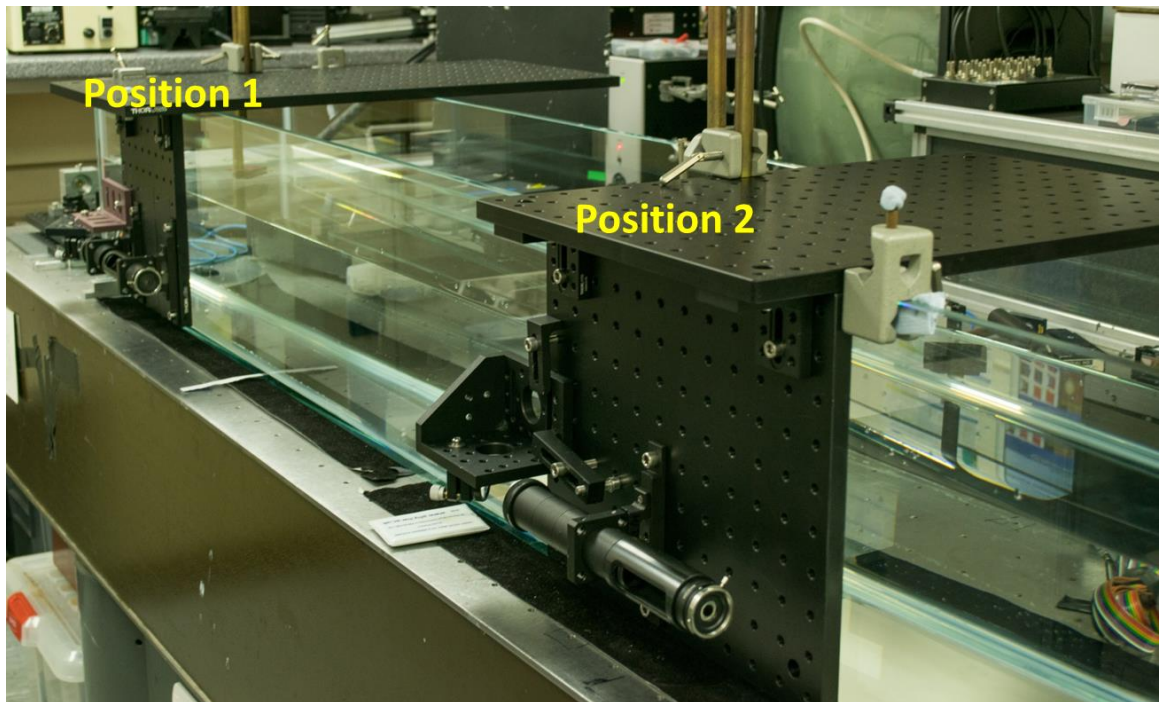

Figure 4.3. Photograph of the setup used for the transmittance measurements. The mirrors inside the tank are 1 metre apart, in order to measure the transmittance of the medium in the tank over 1 metre.

Several volumes of Maalox in unfiltered tap water [12] were investigated and the main results are reported in Table 4.1.

	Water sample	Attenuation length (m)	Optimum wavelength (nm)
1	**Unfiltered tap water**	**8.90**	**525**
2	Water + 0.0007% of Maalox	2.18	565
3	Water + 0.0015% of Maalox	1.40	565
4	**Water + 0.003% of Maalox**	**0.70**	**585**
5	Water + 0.006% of Maalox	0.40	690
6	**Water + 0.01% of Maalox**	**0.28**	**690**
7	Water + 0.0123% of Maalox	0.22	695
8	**Water + 0.0125% of Maalox**	**0.21**	**695**
9	**Water + 0.016% of Maalox**	**0.18**	**695**
10	**Water + 0.018% of Maalox**	**0.17**	**695**
11	Water + 0.021% of Maalox	0.15	695
12	Water + 0.025% of Maalox	0.12	700
13	Water + 0.026% of Maalox	0.11	700

Table 4.1. The table shows a list of all the concentrations of scattering agent in water investigated. The attenuation length and the optimum wavelength for transmission are reported for each water sample. The water types in bold (1, 4, 6, 8, 9 and 10) are the water sample used for the scans reported in this Thesis.

The attenuation length for unfiltered tap water is reported in Figure 4.4, which shows that the attenuation length decreases for longer wavelengths. The turning points at approximately $\lambda = 600$ nm and $\lambda = 740$ nm correspond to the major absorption shoulders in the visible range examined and the first absorption peak in the near infrared [13]. Secondary turning points are visible also at approximately $\lambda = 555$ nm and $\lambda = 650$ nm, corresponding to the secondary absorption shoulders in the visible range [13]. Figure 4.4 shows also the attenuation length spectra of tap water from Heriot-Watt University with different low concentrations of Maalox while Figure 4.5 reports the attenuation length of

high concentrations of Maalox in tap water. From Figure 4.4 and Figure 4.5, it is evident that as the concentration of Maalox is increased, the attenuation increases at all wavelengths. However, the maximum of attenuation length shifts towards longer wavelengths because the scattering is more pronounced at shorter wavelengths.
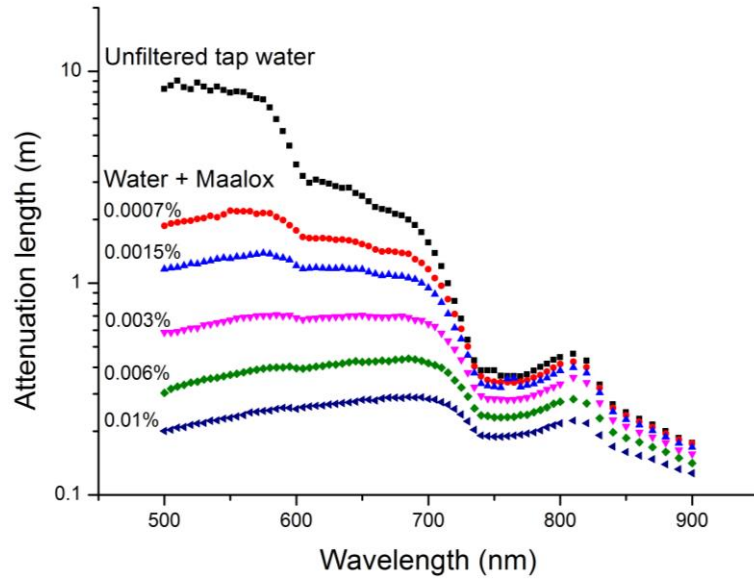

Figure 4.4. Plots of attenuation length versus wavelength for tap water and different concentrations of Maalox simulating low levels of scattering.
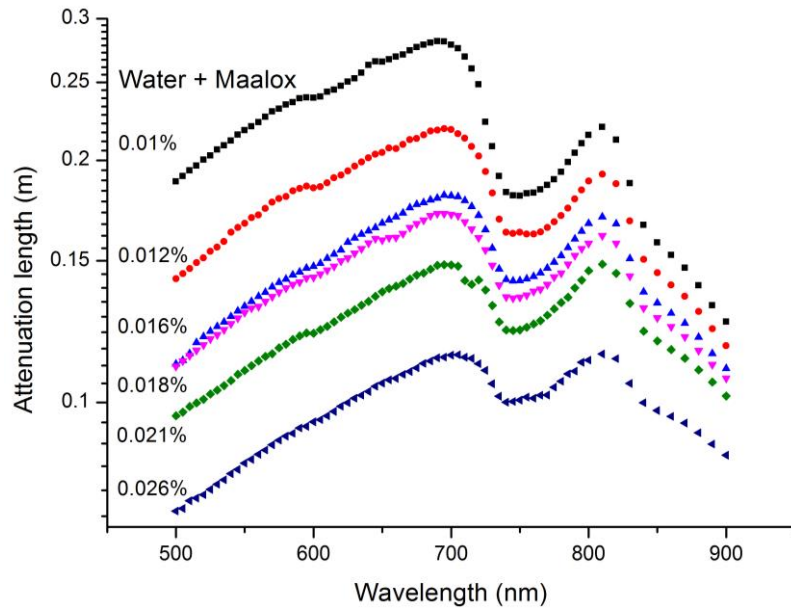

Figure 4.5. Plots of attenuation length versus wavelength for unfiltered tap water and different concentrations of Maalox simulating high levels of scattering. Unfiltered tap water and 0.01% of Maalox is reported in this graph as a comparison.

The same measurements of the attenuation length spectra for coastal sea water (collected at North Berwick 56°3′2N, 2°43′W) are reported in Figure 4.6. This naturally occurring water contains a mixture of varying particle size, and some of the particles settle if left undisturbed. Hence, attenuation length spectra were measured at different settling times. The "stirred" set was done by mixing the water and waiting few seconds for the ripples to settle before every optical power measurement. In this case, a narrower wavelength range was investigated because of the high level of scattering, and the attenuation length spectrum was obtained from $\lambda = 500$ nm to $\lambda = 750$ nm, therefore including the main attenuation shoulder. Additionally, sets of measurements were performed after the water had settled for 1 hour, 2 hours, and 15 hours. From the measured transmission spectra the wavelength for which the minimum attenuation occurs was determined for each sample of water.
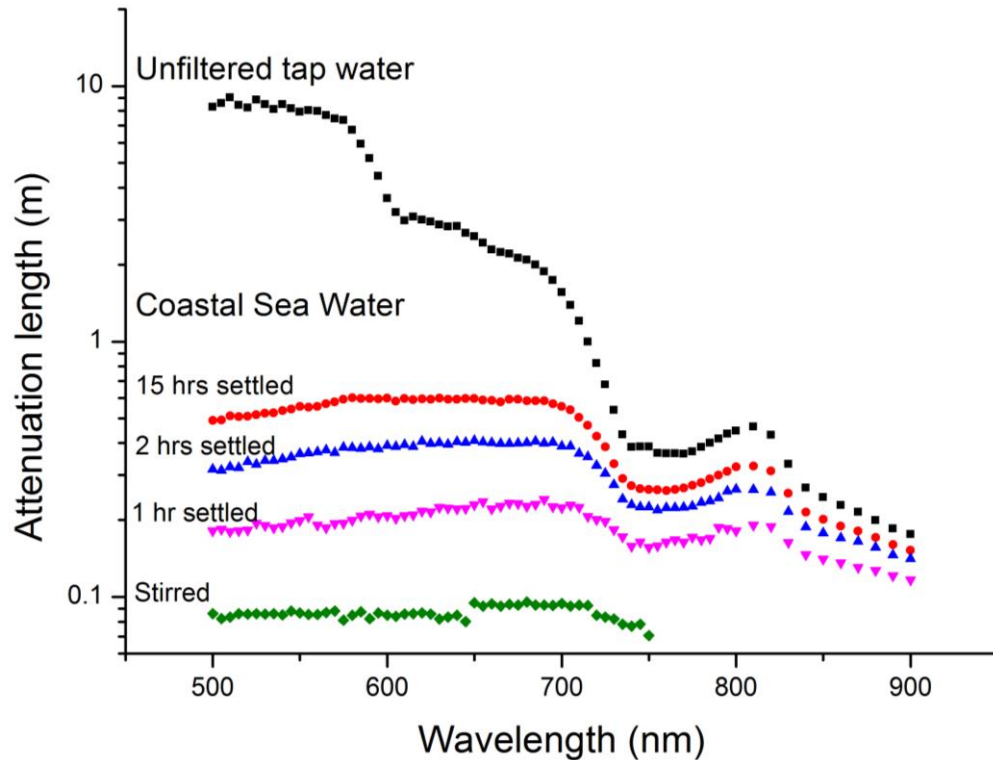

Figure 4.6. Plots of attenuation length versus wavelength for coastal sea water. Since the sea water was collected close to the coast and contained a range of different sized scattering particles, the attenuation spectra were measured at different settling times. Unfiltered tap water is reported as a comparison.

Based on these characterisation measurements, a small subset of the water samples investigated were selected for the depth profiles discussed in this Thesis. Unfiltered tap water without Maalox contamination was used as the reference sample, with an attenuation length of 8.9 m at the optimum wavelength $\lambda = 525$ nm. Water with 0.003% of Maalox was chosen because its attenuation length spectrum is comparable with sea water after 15 hours of settling, as shown in Figure 4.7. This concentration of Maalox corresponds to an attenuation length of 0.7 m at the optimum wavelength $\lambda = 585$ nm. To simulate a highly attenuating environment, water with 0.01%, 0.012%, and 0.016% of Maalox was used to characterize the system. For these last three concentrations the transmission peak is at $\lambda = 690$ nm, corresponding to attenuation lengths of 0.30 m, 0.21 m, and 0.18 m respectively.
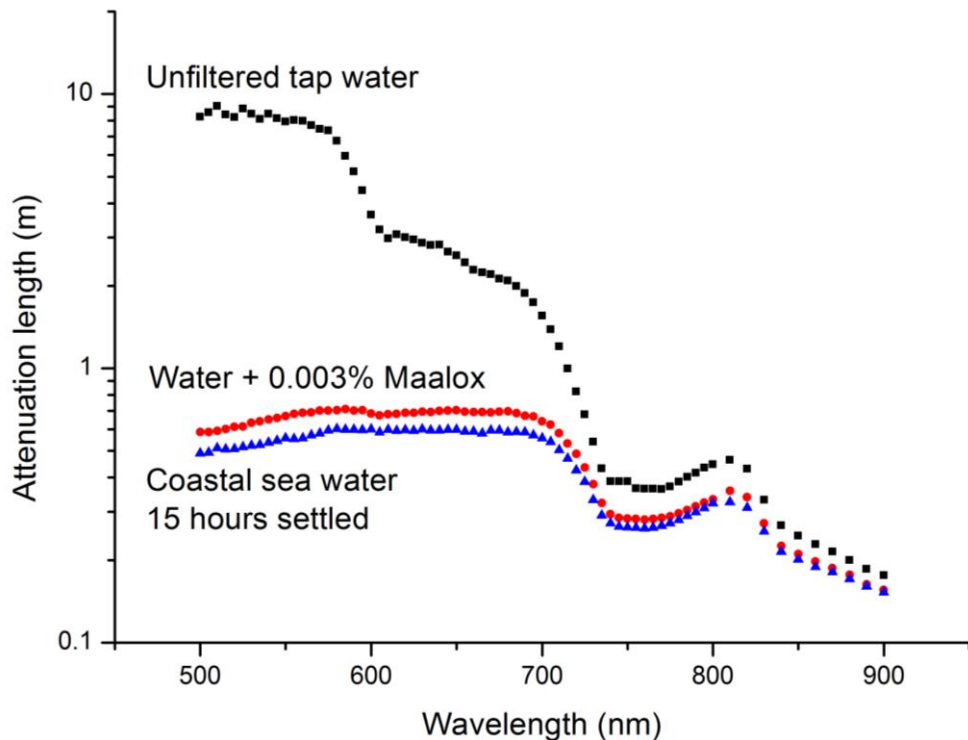

Figure 4.7. Comparison between attenuation length spectra of water with 0.003% of Maalox and coastal sea water settled for 15 hours.

In addition to sea water, two other natural waters were investigated. Figure 4.8 shows the attenuation length spectrum of water collected in Loch Earn (56°23′N 4°14′W), a freshwater lake with a rocky coast. Even if the lake bed close to the coast was covered by stones instead of sand, and the water therefore did not present a high level of scattering due to suspended material, the water was allowed to settle for 2 hours before the measurements. In this case, the maximum of transmittance occurs at the wavelength

$\lambda = 645$ nm, although it worth noting that the curve is flat in the entire wavelength range 640 – 700 nm. Two concentrations of Maalox are reported in the same graph for comparison with the water sample under study. Figure 4.8 shows that in the first part of the spectrum the attenuation length is between that of unfiltered tap water with 0.0015% and 0.003% of Maalox. While in the wavelength range 700 – 900nm, the attenuation length spectrum of loch water follows the same behaviour as unfiltered tap water with 0.0015% of Maalox.
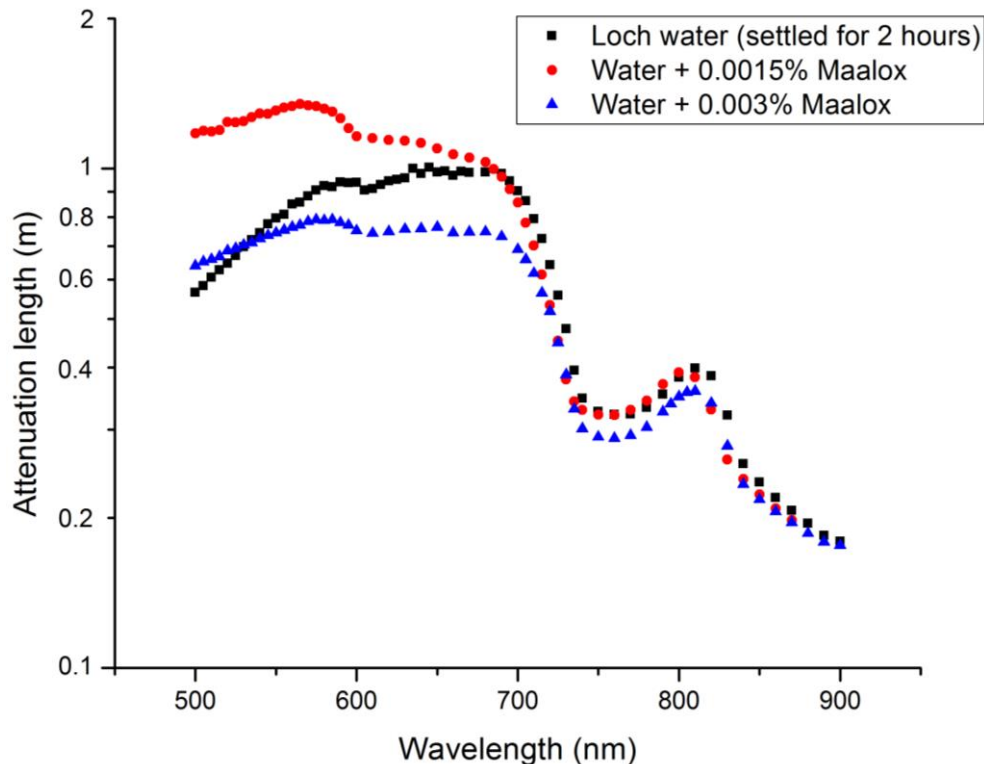

Figure 4.8. Plot of attenuation length versus wavelength for loch water. Since the water was collected close to the coast, the water settled for 2 hours before the measurements. Water with 0.0015% of Maalox and water with 0.003% of Maalox are reported as a comparison.

Another water sample was collected in Harlaw reservoir (55°52′10″N 3°18′40″W), a reservoir with a fine sandy floor. In this case, the measurements were performed in the wavelength range 500 - 740 nm, and the results are reported in Figure 4.9. Because of the fine sand contained in this water sample, the water was allowed to settle for 2 hours before the measurements. Due to the higher level of scattering, the optimum wavelength shifted to $\lambda = 685$ nm. In the graph, the attenuation length curve of unfiltered tap water with 0.01% of Maalox is shown as a comparison.
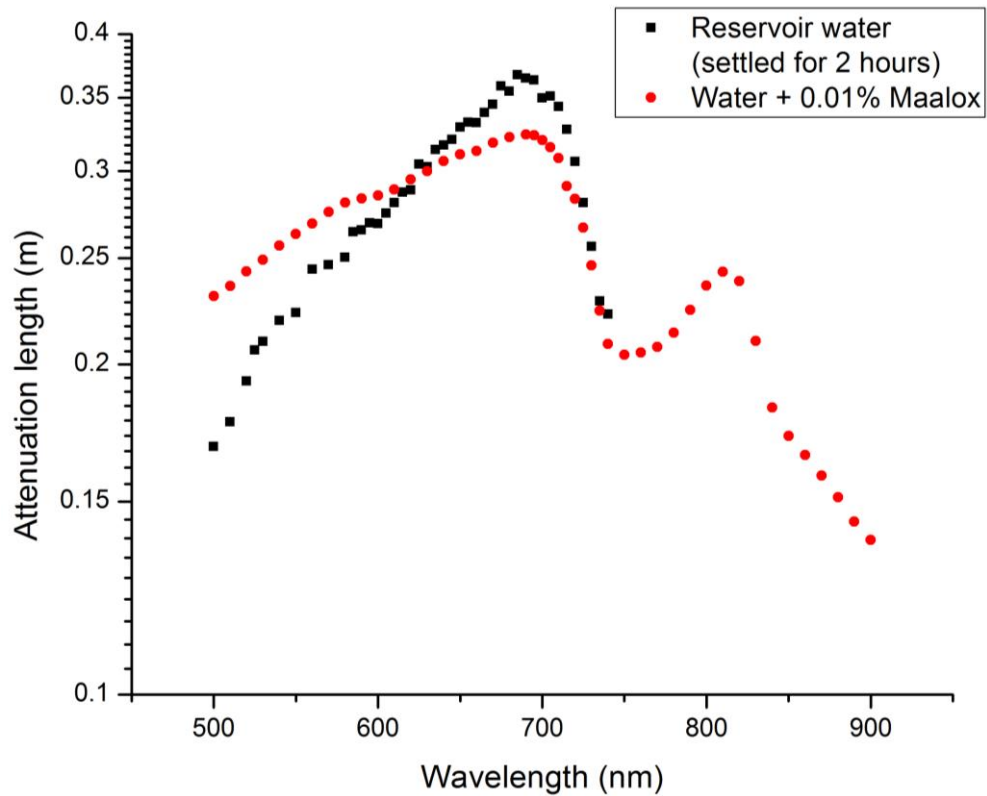
Figure 4.9. Plot of attenuation length versus wavelength for reservoir water. Since the water was collected close to the coast, the water settled for 2 hours before the measurements. Unfiltered tap water with 0.01% of Maalox is reported as a comparison.

From the results it is evident that lake water samples strongly attenuate the light in the wavelength range 500 – 600 nm, resulting in a maximum of transmittance contained in the narrow range between $\lambda = 640$ nm and $\lambda = 690$ nm. As the scattering increases, the maximum of transmittance shifts towards longer wavelengths, and the attenuation length curve shows a pronounced peak around $\lambda = 690$ nm.

In order to investigate the settling time of Maalox in water, power measurements were recorded over one hour in water with 0.012% of Maalox, at the optimum wavelength ($\lambda = 690$ nm). Power readings were recorded as previously described in Figure 4.2, approximately every 5 minutes without stirring the water sample. The transmittance over one metre was calculated for each measurement, and the results are shown in Figure 4.10. The graph shows how the transmittance slightly increases during the first quarter and then linearly increases over the time. Hence, for the scans reported in this Thesis, overall acquisition times of approximately 20 - 30 minutes were chosen when concentrations of 0.012% of Maalox or higher were used, meaning that the target distance expressed in

attenuation lengths changed less than 5% during a scan. For concentrations of up to 0.01% of Maalox in water, the target distance expressed in attenuation lengths varied less than 5% over approximately one hour, and overall acquisition times up to one hour were suitable for high-resolution scans.
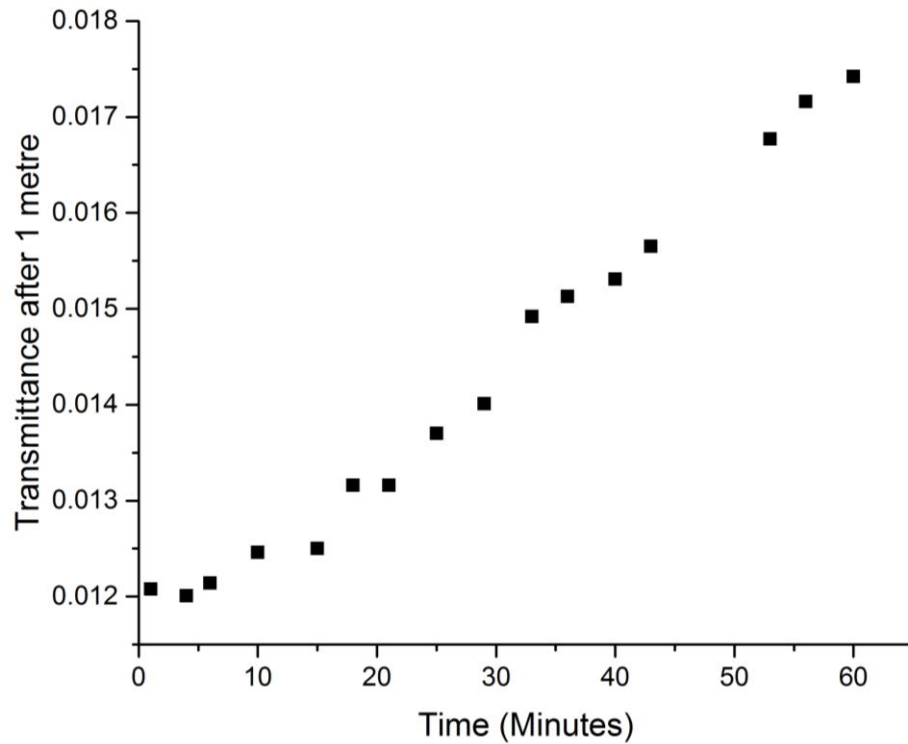

Figure 4.10. The graph reports the transmittance of water with 0.012% of Maalox, recorded over one hour at the wavelength λ = 690 nm.

Due to the relatively quick settling times of Maalox, the setup was modified in order to permit simultaneous 3D depth profile scanning and verification of the stand-off distance of the target. This came at the cost of using two supercontinuum systems, one for the 3D depth profile scans and one to verify the transmittance. A schematic of the revised setup is shown in Figure 4.11. The setup was modified by including a moving stage on the support in Position 1, which permitted the mirror to be lifted in the water so that the beam could propagate to Position 2, 50 cm further along the tank. The two mirrors were placed closer to the side wall of the tank, in order to not block the beam for the 3D depth profile scan. The transmittance of the medium in the tank was ascertained at the operational wavelength through Equation 4.2, before and after each scan when highly scattering environments were used.
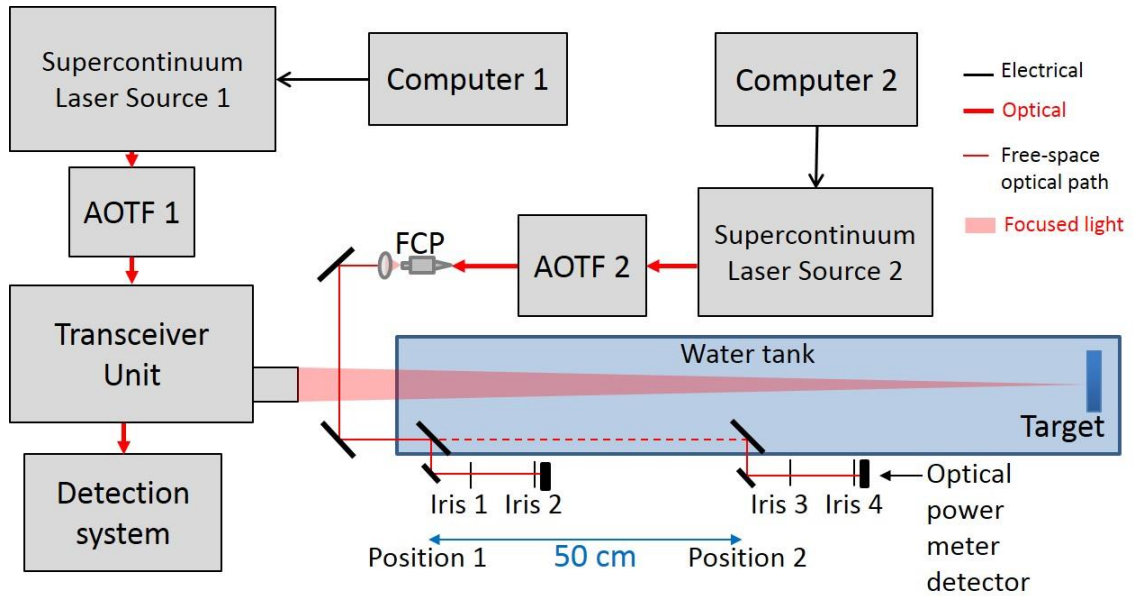
Figure 4.11. Schematic of the experimental setup used to verify the target distance in attenuation length. The setup comprises two supercontinuum laser sources and two acousto-optic tuneable filters (AOTF), the supercontinuum "source 1" is used to perform the scans, and the supercontinuum "source 2" is used for power readings in two positions 0.5 metres apart. The "Transceiver Unit" is the 3D depth profiling system described and used in subsequent chapters of this thesis.

4.4. Conclusions

The measurements reported in this chapter permitted to ascertain the attenuation length spectra for a number of water samples. The minimum of attenuation was determined for all the samples, allowing to select the most appropriate environments in which to investigate the potential of the depth imaging system, as described in the following chapters. From the results it can be seen that the minimum of attenuation is in the wavelength range 525 – 690 nm, showing a shift towards longer wavelengths of this range as the scattering level is increased. The main advantage of this approach is that it permits optimal adaptation of the operating wavelength to the scattering level of the environment where the scan is performed. Therefore, both transmitted and received signals are optimised, even in highly scattering environments.

In addition, the settling times of the scattering agent was studied for all the water samples selected. The study showed that for concentrations above 0.012%, the target distance in attenuation lengths changed significantly over 30 minutes. This put a limit to the overall

acquisition time for the scans in highly scattering environments, allowing for the selection of appropriate parameters for the depth imaging experiments, including acquisition time per pixel and pixel format.

References

1.   S. Q. Duntley, "Light in the sea," J. Opt. Soc. Am. **53**, 214-234 (1963).

2.   J. S. Jaffe, "Computer modeling and the design of optimal underwater imaging systems," IEEE J. Oceanic Eng. **15**, 2, 101-112 (1990).

3.   J. S. Jaffe, "Enhanced extended range underwater imaging via structured illumination," Opt Express **18**, 12, 12328-12340 (2010).

4.   R. C. Smith, and K. S. Baker, "Optical properties of the clearest natural waters (200-800 nm)," Appl Optics **20**, 2, 177-185 (1981).

5.   G. M. Hale, and M. R. Querry, "Optical Constants of Water in the 200-nm to 200-μm Wavelength Region," Appl Optics **12**, 3, 555-563 (1973).

6.   E. Y. S. Young, and A. M. Bullock, "Underwater-airborne laser communication system: characterization of the channel," in *Free-Space Laser Communication Technologies XV* (SPIE, San Jose, CA, 2003).

7.   W. S. Pegau, and J. R. V. Zaneveld, "Temperature-dependent absorption of water in the red and near-infrared portions of spectrum," Limnol. Oceanogr. **38**, 1, 188-193 (1992).

8.   L. Prieur, and S. Sathyendranath, "An optical classification of coastal and oceanic waters based on the specific spectral absorption curves of phytoplankton pigments, dissolved organic matter, and other particulate materials," Linnol. Oceanogr. **26**, 19 (1981).

9.   W. Hou, *Ocean Sensing and Monitoring* (SPIE, USA, 2013).

10.   B. Cochenour, L. Mullen, and J. Muth, "Effect of scattering albedo on attenuation and polarization of light underwater," Opt. Lett. **35**, 12, 2088-2090 (2010).

11.   F. Hanson, and S. Radic, "High bandwidth underwater optical communication," Appl. Opt. **47**, 2, 277-283 (2008).

12.   S. water, "Annual report: Marchbank B - Sample period: 01-01-2015 to 31-12-2015," (2015).

13.   R. M. Pope, and E. S. Fry, "Absorption spectrum (380-700nm) of pure water. II. Integrating cavity measurements," Appl. Opt. **36**, 33, 8710-8723 (1997).

Chapter 5

Underwater depth imaging using TCSPC

5.1 Introduction

This chapter will describe an active depth imaging system based on the single-photon time of flight approach. The system can be used to measure depth profiles of objects placed underwater. Firstly, a detailed description of the system will be provided in sections 5.2 to 5.7, as well as an illustration of the targets used during the experiments. Then in section 5.8 and 5.9, the potential of the system is investigated at low and medium levels of scattering, while highly scattering environments are considered in section 5.10 to 0. In addition, the spatial and depth resolutions were investigated for different configurations of the system, and the results are reported in sections 5.13 and 5.14.

5.2 Scanning system

The scanning transceiver used to obtain the results in this Thesis was designed and built by the Single-Photon group at Heriot-Watt University for single-photon depth imaging over long distances in free-space [1]. With appropriate reconfiguration, the transceiver unit has been used with a range of different detectors and laser sources. The system has been used over a range of wavelengths from 500nm to 1550nm, and has also been used with several wavelengths operating simultaneously [2-4]. In the transceiver assembly, the optical components are arranged on a slotted base-plate, which allows the optical alignment to be optimised for the experiment [5], and maintain long-term stability in field trial situations. The transceiver assembly was made of black anodised aluminium, in order to reduce the stray light inside the transceiver. The unit was then covered with a black anodised aluminium lid to further minimise the background light during the experiments. Figure 5.1 is a schematic representing the optical configuration, while Figure 5.2 shows a photograph of the transceiver unit.

The transmit and receive channels in the transceiver system were coaxial and therefore most of the optical components were common to both channels. The light from the laser was collimated using an optical fibre collimation package in the transmit channel (FCP-Tx in Figure 5.1). The transmit beam was overlapped to the receive channel via a

polarising beam splitter (PBS). The light was reflected by the first scanning mirror (y-axis), passed through two telecentric relay lenses and reflected by the second scanning mirror (x-axis). The light was then focused by a third relay lens before passing through the objective lens. The objective lens was used to focus the transmitted light to the target and collect the back-scattered light from the target. The return photons followed the same path up to the polarising beam splitter, where the receive and transmit channels are separated. Then, the return signal is coupled into an optical fibre with a collimation package (FCP-Rx), and then onto the detector.
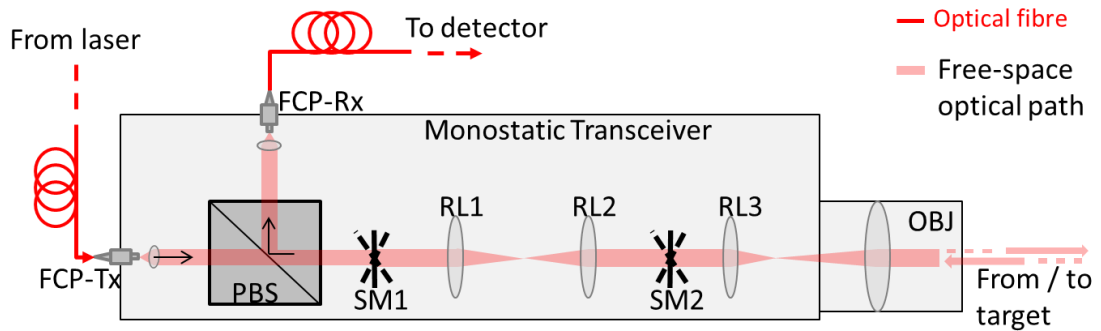

Figure 5.1. Schematic of the transceiver unit. The optical components shown in the transceiver unit included two optical fibre collimation packages, for the transmit channel (FCP-Tx) and receive channel (FCP-Rx). A polarising beam splitter (PBS) was used to overlap and separate the transmit and receive channels. Three relay lenses (RL1, RL2, RL3) were used in conjunction with two galvanometer mirrors (SM1, SM2) to perform the raster scan of the target. A camera objective lens (OBJ) was used to focus the transmitted laser light onto the target surface and collect the scattered return signal.
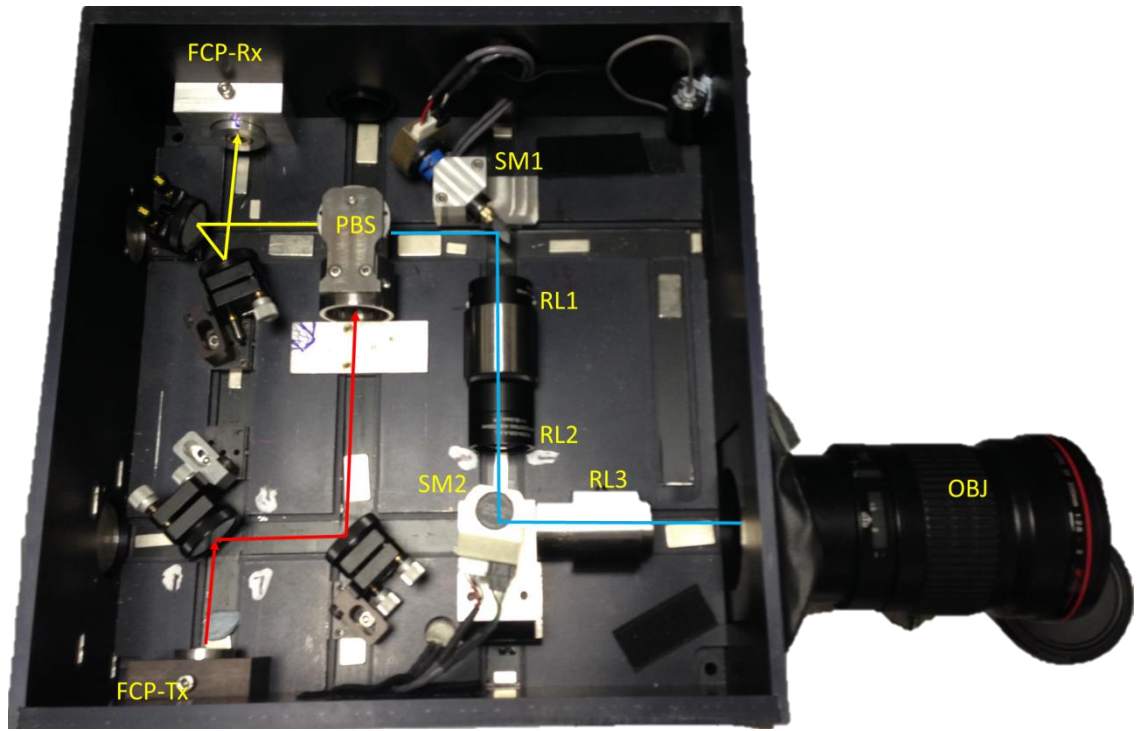
Figure 5.2. Photograph of the transceiver unit. The input light was fibre-coupled into the transmit channel, shown in red, via a fibre-collimation package (FCP-Tx). The path in yellow is the receive channel, which was fibre-coupled to the detector via the fibre-collimation package FCP-Rx. The two channels were overlapped at a polarising beam splitter (PBS), and the common optical path is highlighted in blue. The common channel comprised three relay lenses (RL1 - RL3), which relayed the image operating at infinite conjugates. Two galvanometer scanning mirrors (SM1 and SM2) were used to perform a raster scan of the target. A camera objective lens (OBJ) was used to focus the light on the target and collect the light scattered by the target.

The telecentric configuration was needed to guarantee that the beam was always on-axis, independent of the deflection angle. At the same time, the relay lens RL3 was used as a scan lens, forming an image on the image plane of the objective lens. This limited the field of view of the transceiver, imposing a lower limit on the f-number of the entire system of approximately f/4. The transceiver unit was optimised and aligned before every experiment, and the optical components were selected on the basis of their performance at the wavelength range to be used in the experiment. In general, the optical elements were chosen with a high performance anti-reflective coating in order to minimise the back-reflections, which can find their way into the detection channel in

this monostatic configuration. If the wavelength during the experiment was varied over a wide range, the alignment was performed at a weighted intermediate wavelength to take into account the chromatic characteristics of the system. The same alignment procedure was followed for all the optical configurations reported in this Thesis.

The two scanning mirrors were placed at conjugate planes of the system, and the relay lenses were chosen so that the distance between the mirrors was twice the sum of their focal lengths. In order to perform the alignment, the light was delivered from the laser source (described in section 5.3) to the transmit channel via a polarisation maintaining optical fibre. The PBS was placed in the transceiver unit to overlap the transmit and receive channels, and the light transmitted by the PBS was maximised rotating the optical fibre collimation package FCP-Tx. A more precise overlap of the two channels was performed after all the optical components were aligned. Two temporary lenses were used to place the relay lenses in the right position. As shown in Figure 5.3a), a temporary lens with appropriate focal length was used to focus the light on the SM2 galvo-mirror, while this was moving. An image was formed on a CCD camera using a concave mirror with focal length 505 mm to allow the relay lens RL3 to be placed at a distance equal to its focal length from SM2. The relay lenses RL1 and RL2 were pre-aligned in a lens tube, on a separate setup, to set them at a distance equal to the sum of their focal lengths. Then, the block with the two lenses was placed between SM1 and SM2, as well with a temporary lens with appropriate focal length before SM1 (Figure 5.3b). Through this configuration a spot was imaged on the CCD camera, and the focus was adjusted varying the distance of the pair from SM1.
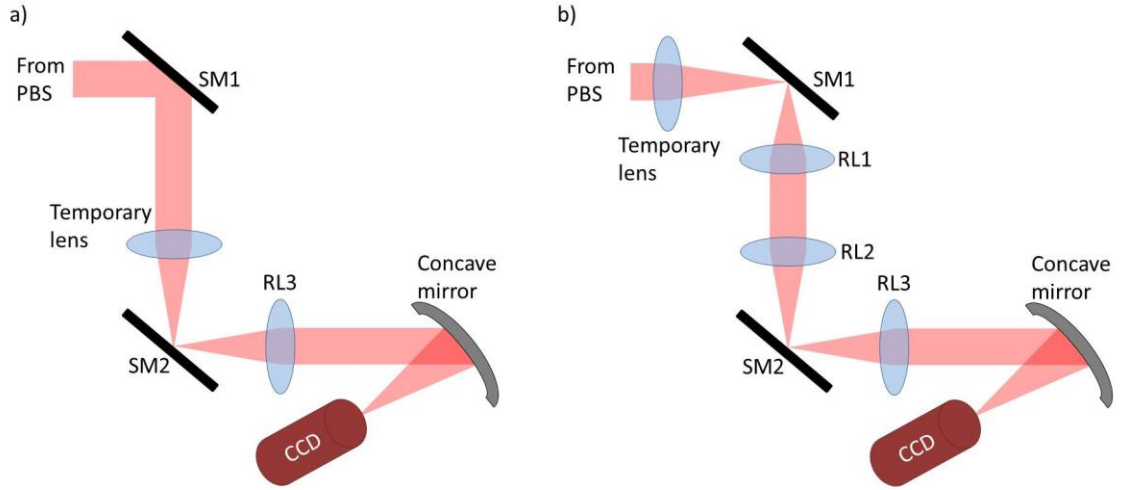
Figure 5.3. Setup for the alignment of the relay lenses RL1, RL2, and RL3 with the two galvanometer mirrors SM1 and SM2. The focus was adjusted using two temporary lenses, in (a) to adjust the position of RL3, and in (b) to adjust the position of the pair RL1 and RL2.

The last step was the optimisation of the coaxial overlapping of the transmit and receive channels. This was achieved by delivering the laser light from both channels through optical fibres, and collimated in free space. Then, light was focused on the CCD camera by the concave mirror, showing the light spots from the two channels. To perform an efficient coaxial alignment, the overlapping of the transmit and receive spots needs to be verified in two different positions. Hence, the camera was moved forward and backward to inspect the images formed in focus and de-focus positions, as shown schematically in Figure 5.4. For a more precise adjustment of the overlap between transmit and receive channels, a microscope objective lens was mounted on the camera to magnify the image, and better highlight small mis-alignments.
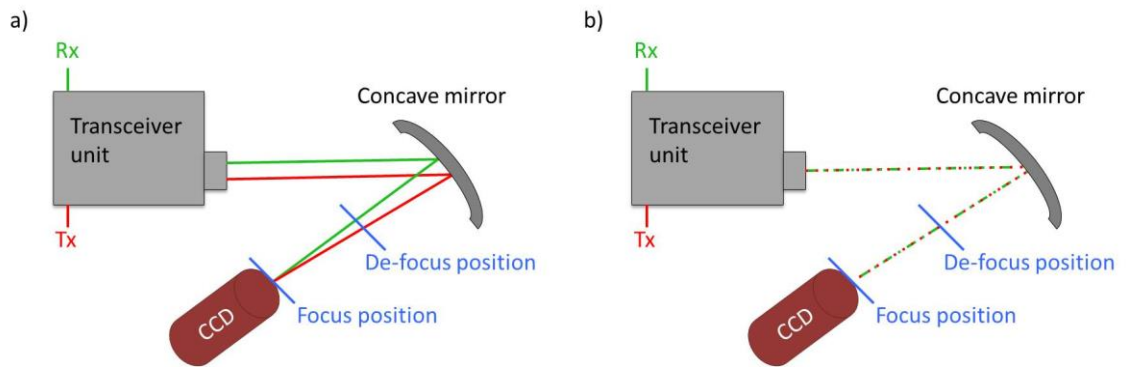
Figure 5.4. Coaxial overlapping of transmit and receive channels. In a) the two channels are not overlapped, hence moving the CCD camera away from the focus position two separate spots will be visible (de-focus position in the figure). In b) the two channels are coaxial, and the spots imaged are overlapped for different positions of the CCD camera.

The two galvanometer mirrors were controlled by an electrical driver system, schematically shown in Figure 5.5. The voltage ranges required to scan the target area in x and y-axes were manually set through custom software, as well with the overall acquisition time of the scan and the pixel format. These parameters were used by a digital-to-analogue converter (DAC), which provided the control voltage to drive the galvanometer mirrors, and the trigger signal to mark a new pixel. The servo controllers and the motors for the mirrors were located beneath the slotted base-plate.
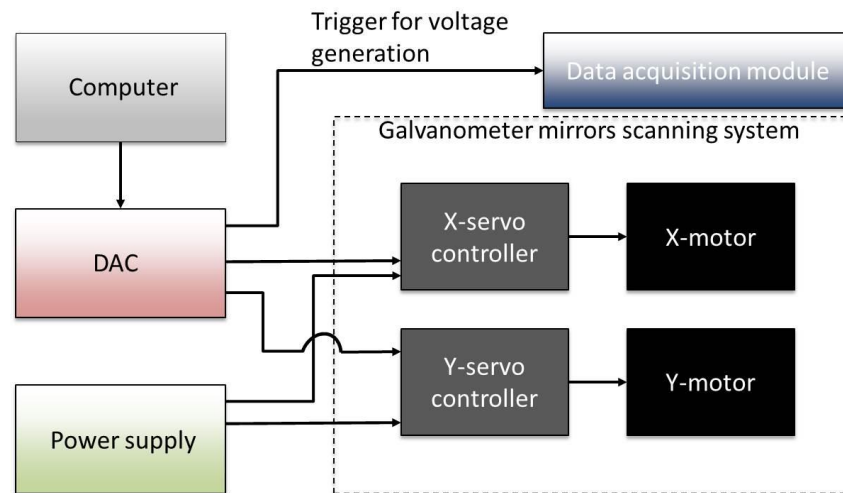

Figure 5.5. Schematic of galvanometer mirrors scanning system. A digital-to-analogue converter provided control voltages (preset by computer) to the servo controllers to move the X and Y mirrors, performing the raster scan of the target. At the same time, the DAC provides the trigger signal to the TCSPC module to mark a new pixel.

5.3 Supercontinuum laser systems

The laser source used was a supercontinuum source, which provided a high power broadband white-light spectrum. In particular, two supercontinuum sources were used, SuperK Extreme EXW-6 and EXW-12 (NKT Photonics, Denmark), both photonic crystal fibre (PCF) based, meaning that their spectra are generated by sending a pulsed master seed laser pulse into a PCF [6, 7]. The master seed laser source was a diode-pumped Nd:YAG laser of wavelength $\lambda = 1064$ nm with a pulse width of approximately 5 ps FWHM, for both supercontinuum lasers. The range covered was 485 nm – 2400 nm for the EXW-6, and 460 nm - 2400 nm for the EXW-12.
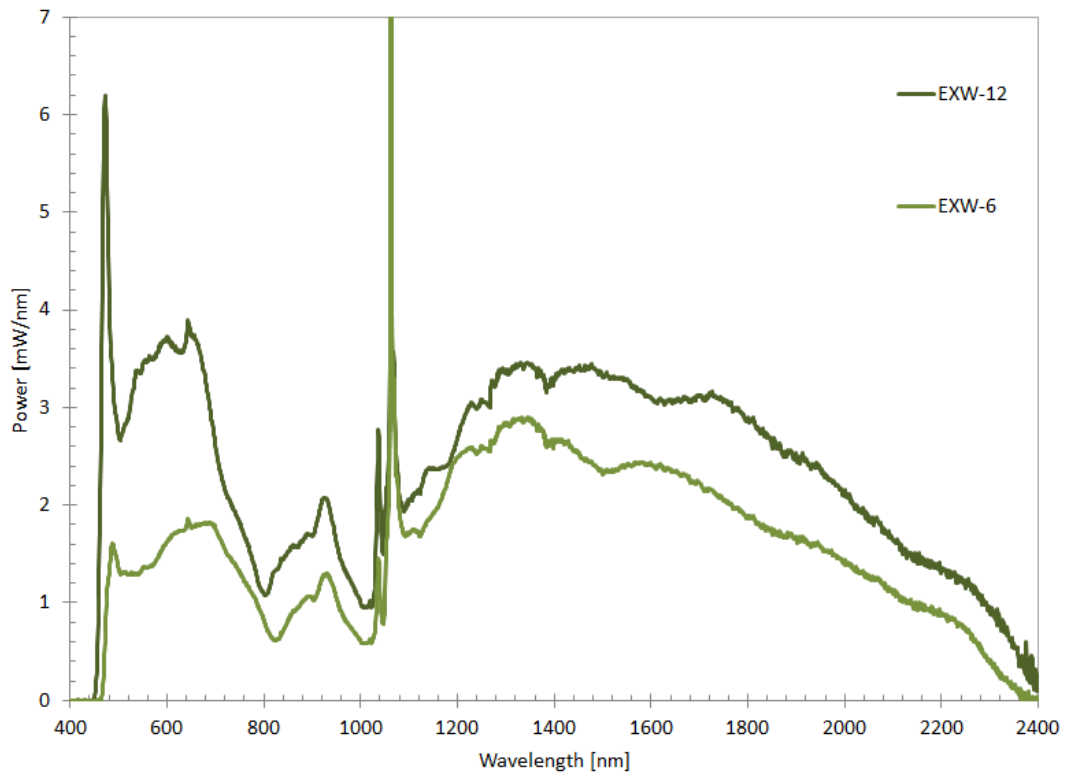

Figure 5.6. Spectra of the two supercontinuum sources used for the experiments. From [8].

The master seed laser source had a repetition rate of 80 MHz, with lower repetition rates up to approximately 300 kHz being enabled by a pulse picker option, which divided the seed repetition rate by a number of discrete ratios. The output from both supercontinuum sources was collimated and delivered via an armoured fibre. Each supercontinuum laser source could be used in conjunction with an acousto-optic tunable filter (AOTF) (SuperK SELECT multi-line tunable filter, NKT Photonics, Denmark) able to select up to 8 wavelengths at the same time over a wide spectral range, thanks to

the integration of two AOTF crystals. For all the measurements presented in this Thesis, the AOTF crystal VIS-nIR was chosen, allowing the selection of the operational wavelength in the range 500 nm – 900 nm. When the AOTF was connected to the source, the light was delivered to a polarisation maintaining fibre through a fibre delivery system (SuperK CONNECT, NKT Photonics, Denmark), with the output light power being maximised using the two mirrors included in the delivery system. Particular attention needed to be given to this step because when the AOTF was not properly aligned, the spectral peak corresponding to a single wavelength was shifted, giving an incorrect value of the central wavelength and with a wider spectral response than expected. An example of 7 spectral peaks after a full alignment procedure is shown in Figure 5.7. The data were collected with a spectrometer (USB Serie HR2B805 by Ocean Optics, USA), and the optical power in each case was adjusted in order to not saturate the detector of the spectrometer. As expected, from the results it can be seen that the FWHM slightly increases for longer wavelengths.
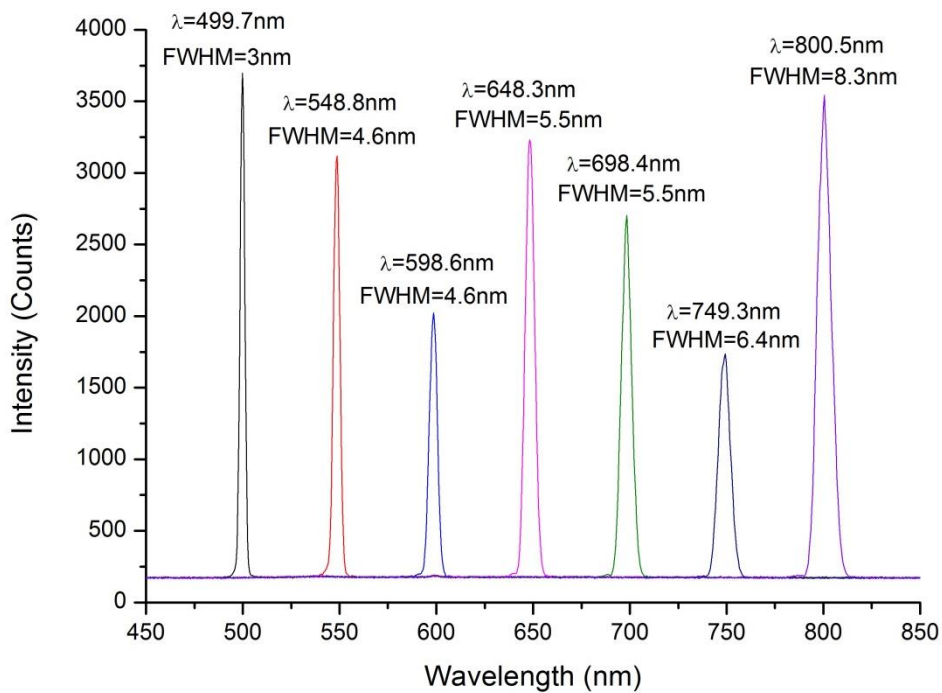

Figure 5.7. Spectral lines for seven different wavelengths after the alignment of the AOTF. In each case, the optical power level of the laser was adjusted in order to not saturate the detector of the spectrometer.

As an alternative to the AOTF, a combination of coated optical filters was used for wavelength selection from the supercontinuum spectrum, which had the advantage of

allowing higher average optical power levels due to the reduced optical loss and a choice of wider operational spectrum.

5.4 TCSPC modules and data acquisition modes

Two TCSPC modules were used during this project: the PicoHarp 300 and HydraHarp 400, both manufactured by PicoQuant GmbH, Germany. Both modules offered two time-tagged-time-resolved (TTTR) acquisition modes, called T2 and T3 modes. In general, the main difference between the two modes is that in T3 mode one channel is dedicated to the synchronisation signal and the times of all detector events are measured relative to the last synchronisation signal (known as micro-time), while in T2 mode all timing inputs of the TCSPC module are identical, with no dedication of a channel to a synchronisation signal, and all times are recorded relative to the start of the measurement (macro-time) [9]. This means that in T2 mode every occurrence of a repetitive synchronisation signal will be recorded with full timing precision.

There are major differences between the operation of each of these modes in the two modules considered. Although both of the operating modes use 32 bit records on each device, the structure of the data within these 32 bits is different in each case. When data are recorded with T2 mode in the PicoHarp 300, 28 bits are used to record the time of each event on both the detector and the synchronisation channel [10]. However, a limitation of the TCSPC hardware module meant that the frequency of its clock input could not exceed 10 MHz, meaning that higher synchronisation signal frequencies had to be divided externally. In addition, the size of the recorded file could be extremely large, significantly increasing the memory requirements and the time required for the data analysis after the measurement. When the 28 bits used to record the time "overflow" (after 2^{28} "ticks" of the internal clock) then a special "overflow-reset" marker is injected into the data and the 28 bits of the time record are reset to 0 to start again.

The T3 mode of the PicoHarp 300 includes an internal dividing function, allowing the use of higher laser repetition rates, by only synchronising on the divided frequency. In this case, 12 bits are used to record the timing of an event on just the detector channel relative to the time of the last synchronisation channel event. The event times of the repetitive synchronisation signal are not stored and, hence, the file size is reduced. However, fewer bits are dedicated to the timing precision of the measurement of the

time from the start signal, resulting in a maximum histogram length of up to 2^{12} bins since overflow markers are not injected into the data. This limitation can be overcome using short synchronisation periods, which fit within the maximum number of bins.

The PicoHarp 300 can be replaced with the more advanced HydraHarp 400. T3 mode in the Hydraharp 400 uses 15 bits to record the time of the event on just the detector channel. This allows a histogram of 32768 bins with a timing precision of up to 1 ps bin width [11], depending on the synchronisation signal period, still with compact and efficient data file sizes. It is worth noting that T2 mode is also available in HydraHarp400. In this case, T2 mode allows the use of identical input channels and recording the macro-time for both channels independently, with no need for a synchronisation signal. This makes the T2 mode on the HydraHarp 400 particularly useful in applications where non-periodic signals are studied.

The data presented in this Thesis were acquired using T2 mode in Picoharp 300 and T3 mode in HydraHarp 400. When T2 mode was used with the PicoHarp 300, a histogram for each pixel was built by the TCSPC module and then recorded in an independent file, streamed by custom software from the TCSPC module to the storage memory. When T3 mode in Hydraharp 400 was used, each pixel was identified with a marker, which is an electrical signal from the galvanometer mirror driver being sent to the "Marker" input of the TCSPC module. The raw data consist of only one file including the time-tag information for each event detected. The file was streamed by custom software from the TCSPC module to the storage memory, and the histograms were reconstructed for each pixel with a custom script in MatLab. This allows for the extraction of time tagged events in order to replicate histograms with shorter acquisition times from a long acquisition time measurement, meaning that there was no need to make multiple measurements of same scene when shorter acquisition times had to be investigated. In addition, larger pixel formats could be considered thanks to the smaller size of the recorded file, greatly increasing flexibility of the system.

The custom software was initially developed by Dr. Nils J. Krichel and Dr. Robert J. Collins, it was then modified for the T3 acquisition mode by Dr. Ximing Ren, who also modified the MatLab script to reconstruct the histograms.

5.5 Analysis method for histograms

Once the histograms were obtained for each pixel, a cross-correlation was performed between each histogram and a normalised instrumental response. The instrumental response was measured using a reference Lambertian scatterer, a Spectralon target (SRT-99-020 Spectralon Diffuse Reflectance Target, Labsphere), which will be described in more detail in section 5.7.1. The target was placed approximately at normal incidence to the beam, and a single pixel measurement was performed using an acquisition time of 100 seconds. Generally, the instrumental responses were recorded using unfiltered tap water as the transmission medium in order to have a well defined peak return from the target. A different instrumental response was recorded for each configuration presented in this Thesis, taking into consideration any change in the optical or electrical component. If R denotes the normalised instrumental response with r timing bins, and H the histogram recorded with h timing bins, the cross-correlation C performed for each pixel is

$$C_i = \sum_{j=1}^{r} H_{i+j} \times R_j \qquad \text{Equation 5.1}$$

with i varying in $[-r, h]$. The highest value of the cross-correlation reveals the time-of-flight to the target with respect to the reference for that individual pixel. By collecting this time-of-flight information for all of the pixels, a depth image for the scanned field of regard was then estimated.

At the same time, a range of 30 bins was used to collect the number of events around the highest value of the cross-correlation for each pixel. This allowed an intensity map to be produced in order to represent the number of counts per pixel, to form an image of the area scanned. When the return from the target is sufficiently high with respect to the background, the intensity map provides valuable additional information about the target.

5.6 Specifications of the water tank

The experiments reported here were conducted in a custom-designed water tank on an optical bench, in an air-conditioned laboratory. The tank was 1750 mm long, 250 mm high, 250 mm wide, hence, it has a capacity of approximately 110 litres. It was made of 10 mm thick Optiwhite glass from Pilkington that has, according to the datasheet, a

transmittance of 91% in the visible part of the spectrum, significantly higher than the standard float glass typically used in the construction of aquariums. A hole in bottom corner of each end of the tank facilitated emptying the tank when needed. In the experiments described in this chapter, the tank was placed at a slight angle with respect to the incident beam thereby avoiding unwanted back-reflections in the scanning system.

5.7 Summary of the Targets

Several targets were used to perform the experiments in order to investigate the potential of the system, and a detailed description is given below.

5.7.1 Spectralon targets

Reference targets were used during the experimental work to investigate the instrumental response of the system and to calibrate the intensity distribution for different optical configurations. The reference targets were made of Spectralon reflectance material, a thermoplastic resin with known reflectance $\rho = 99\%$. This material is highly hydrophobic, which makes it particularly suitable for measurements underwater. The surface and subsurface structure of Spectralon exhibit highly Lambertian behaviour in a wide wavelength range, from 300 nm up to 2400 nm [12]. When the material is doped with black pigment, different reflectance values can be available maintaining the Lambertian behaviour over the same wavelength range. In the experiments performed during this PhD project, four Spectralon targets were used. Figure 5.8 shows three targets of area 5×5 cm^2, with reflectance equal to (a) 2%, (b) 10%, (c) and 99%. Another Spectralon target with $\rho = 99\%$ and area 13×13 cm^2 was used for wide area scans.

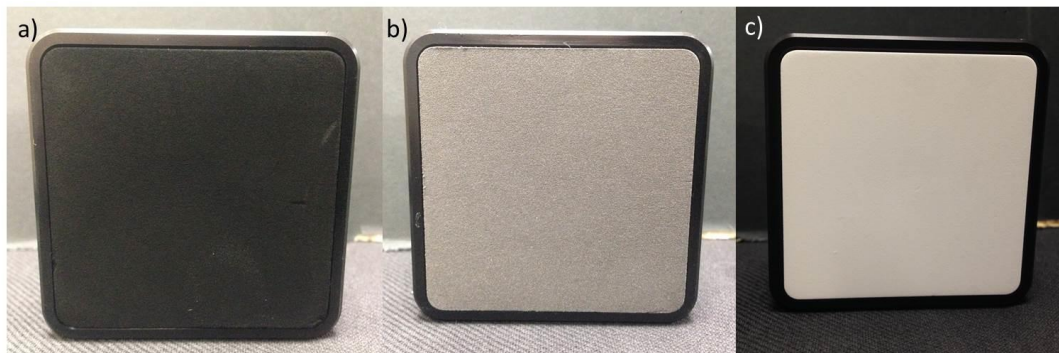*Figure 5.8. Photographs of Spectralon targets of area 5 × 5 cm² and different reflectance values, (a) 2%, (b) 10%, (c) and 99%.*

5.7.2   Plastic and copper pipe connections

The target mainly used for the scans underwater was a commercially available plastic pipe connection. This is an elbow connection with millimetre and sub-millimetres depth features at both ends. The target was approximately 8 cm wide, 5 cm high, and 3.5 cm deep and is shown in Figure 5.9a). In addition, some scans were performed with a commercially available copper T-connection of the same dimensions as the plastic pipe, in order to investigate materials with lower reflectivity than the white plastic pipe target. The photograph of the copper pipe target is shown in Figure 5.9b).
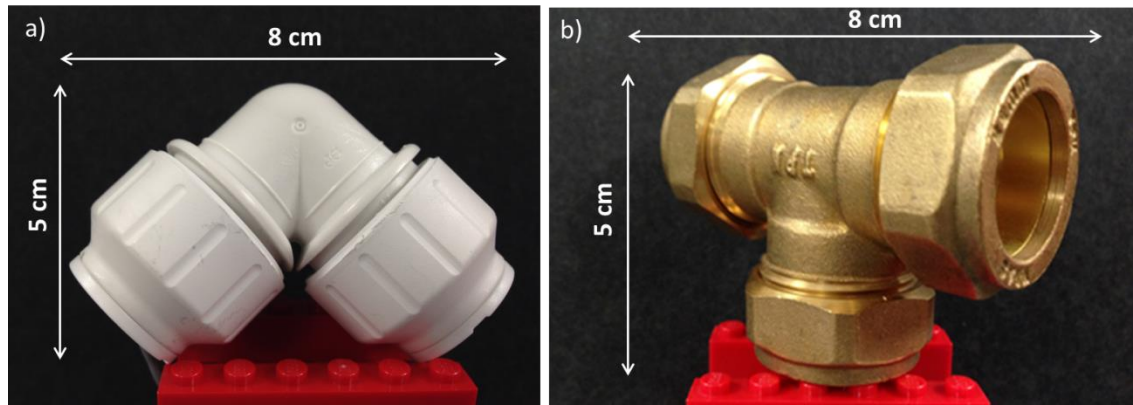

Figure 5.9.   These photographs show the targets used for the depth profile measurements, (a) a plastic pipe and (b) a copper pipe, both approximately 8 cm wide, 5 cm high, and 3.5 cm deep.

5.7.3   Tennis ball

Preliminary measurements were performed using a tennis ball (Figure 5.10) as a target. The diameter of the tennis ball was approximately 6.5 cm, suitable for the limited dimensions of the tank. However, the target was made of white rubber covered by yellow fibrous felt, and mono-material targets were preferred to investigate the potential of the system. The case of the multi-material target will be discussed in Chapter 8.

Figure 5.10. Photograph of the tennis ball. The target had a diameter of approximately 6.5 cm.

5.8 Preliminary measurements

A number of preliminary scans were performed with the experimental setup schematically shown in Figure 5.11. It is important to note that the system was optimised for a different free-space, multi-spectral experiment to be performed using simultaneously the wavelengths $\lambda_1 = 531$ nm, $\lambda_2 = 570$ nm, $\lambda_3 = 670$ nm, $\lambda_4 = 780$ nm, as detailed in [4]. Hence, the wavelengths used to obtain the results reported in this section differ only slightly from the optimum wavelengths established in Chapter 4, so we took advantage of an existing set-up for these preliminary measurements.

The SuperK Extreme EXW-6 supercontinuum source was used in conjunction with the AOTF, and fibre-coupled to the transceiver unit with a photonic crystal fibre, an armoured optical fibre of 9 μm diameter core. The repetition rate used for this experiment was 2 MHz, and the average optical power range was varied from a few nanowatts up to 520 nW. For all the scans presented in this Thesis, the optical power measurements were performed with a silicon detector (Newport Power Meter 1830C and 818-UV detector head), in the transceiver unit just before the objective lens, unless otherwise specified in the text. The TCSPC module was the PicoHarp 300, which received the electrical clock signal from the laser source, and the stop signal from the Perkin Elmer Si-SPAD. The receive channel of the transceiver unit was fibre-coupled via an armoured 9 μm diameter core single mode fibre to a wavelength routing system based on a diffraction grating [13]. At the same time, the detector was fibre-coupled to a single wavelength channel of the routing unit through a 50 μm diameter core multi-mode fibre.

The transceiver unit was configured and aligned to work in the visible wavelength range. The relay lenses were chosen with anti-reflection coatings with reflectance less than 0.4% in the wavelength range 400 nm – 700 nm, providing high light transmission in the wavelength range of interest and minimising the back-reflection within the transceiver unit. In addition, the selected polarising beam splitter provided a transmittance of p-polarised light above the 95% in the wavelength range 420 nm – 800 nm. The objective lens was a single-lens reflex camera lens (Canon EF 200mm f/2.8L II USM), which was used for all the measurements presented in this chapter.
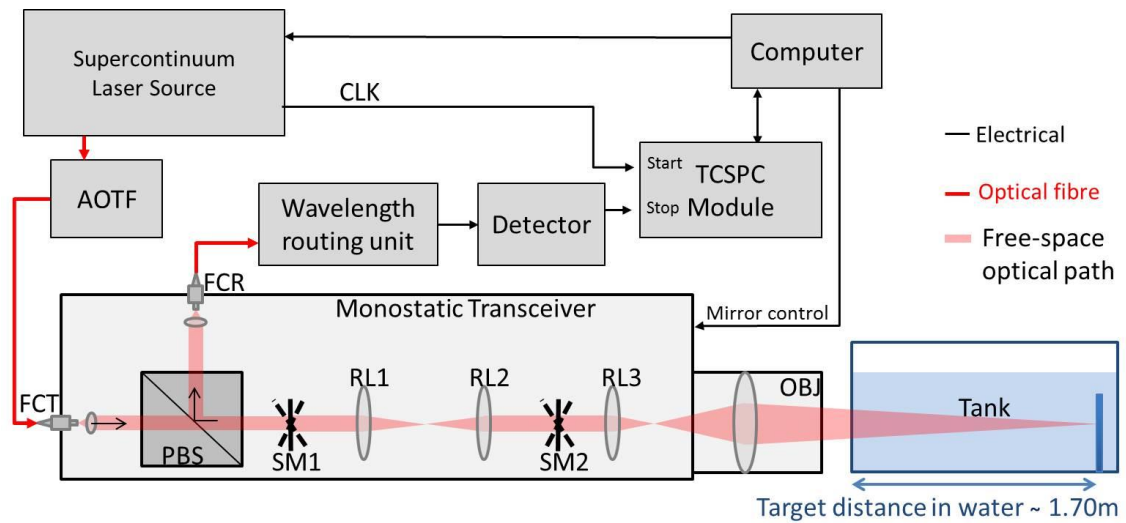

Figure 5.11. Schematic of the single-photon depth imaging system. It comprised the pulsed supercontinuum laser source SuperK Extreme EXW-6, the monostatic scanning transceiver unit, with alignment optimised for the wavelength range 500 nm – 780 nm. The scanning transceiver was fibre-coupled to a wavelength routing unit, fibre-coupled to an individual thick junction Si-SPAD detector by Perkin Elmer.

The instrumental response is reported in Figure 5.12. The histogram was recorded using a 16 ps bin width, the wavelength $\lambda = 670$ nm, an average optical power of approximately 20 nW, and an acquisition time of 30 seconds. The target used was the Spectralon with 99% reflectance, placed at a stand-off distance of approximately 1.7 metres in clear water. The timing jitter of the system is shown in the histogram, and it was approximately 500 ps. Due to the optical configuration used in the transceiver and the high sensitivity of the single-photon detector, the optical back-reflections in the system can be significant, contributing to the overall dead-time of the detection system and reducing the transceiver effectiveness. If high optical powers are used, the back

reflections can saturate the single-photon detector and prevent detection of the returns from the target. With detectors operating in free running mode, optical powers must therefore be selected to ensure that the detector is not saturated and the target can still be resolved, when this is possible. The effect of these back-reflections is apparent in the histogram, showing their relevant contribution to the total count rate.
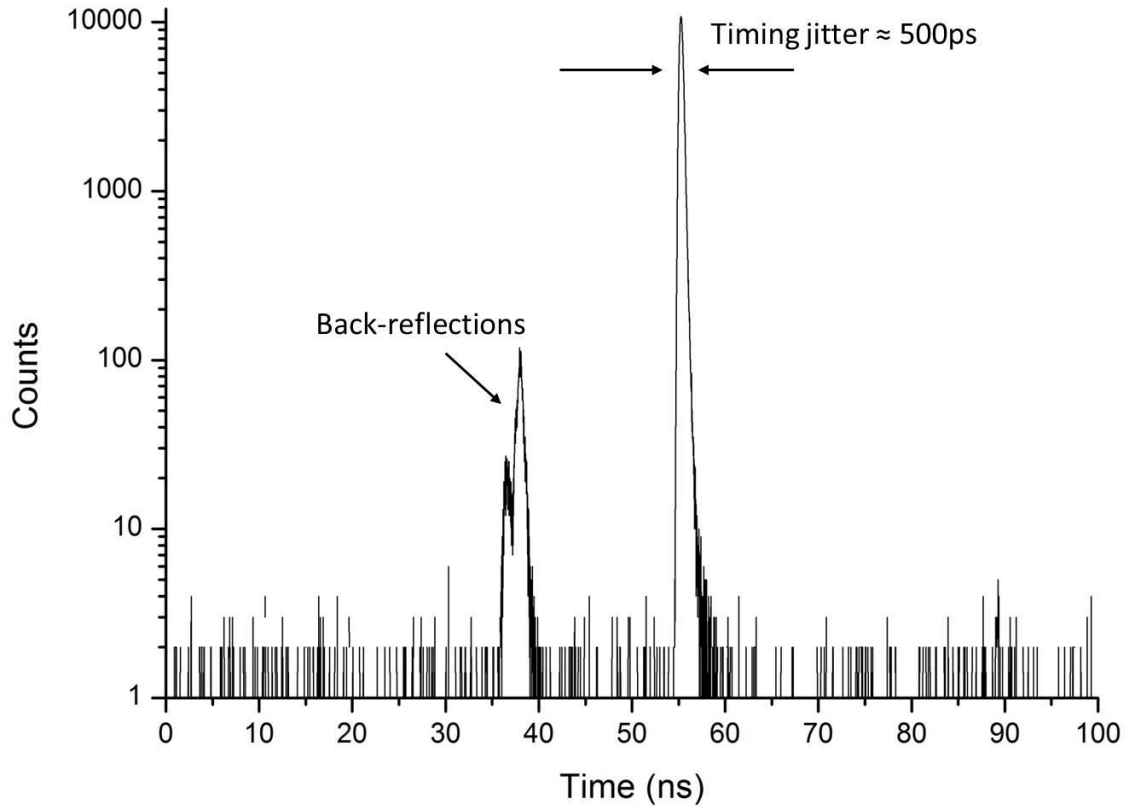

Figure 5.12. The instrumental response of the system. The first peak is due to the back-reflections from optical components in the monostatic configuration, while the second peak is the return signal from the target. The histogram was recorded using the 99% reflectance Spectralon target, placed at a stand-off distance of approximately 1.7 metres in unfiltered tap water. The laser repetition rate was 2 MHz, using the wavelength λ = 670 nm, and an acquisition time of 30 seconds.

5.8.1. 3D depth profile results

One example of depth profile performed using the tennis ball as the target is shown in Figure 5.13a). The target was placed in unfiltered tap water, at a stand-off distance of approximately 1.7 metres, equivalent to 0.2 attenuation lengths between target and system. The measurement was performed using a 60×60 pixel format, 100 ms acquisition time per pixel, and an average optical power of 450 nW at the single

wavelength $\lambda = 531$ nm. The light was focused on a middle plane of the half target scanned. From the results, it can be seen that the entire surface of the target is well resolved in the depth profile, even on the edge of the target despite the spherical shape. However, little information can be deduced from the intensity map, shown in Figure 5.13b). In this case, just the two strips of white rubber can be distinguished, while the return from the yellow fibrous felt is not enough to identify the target.
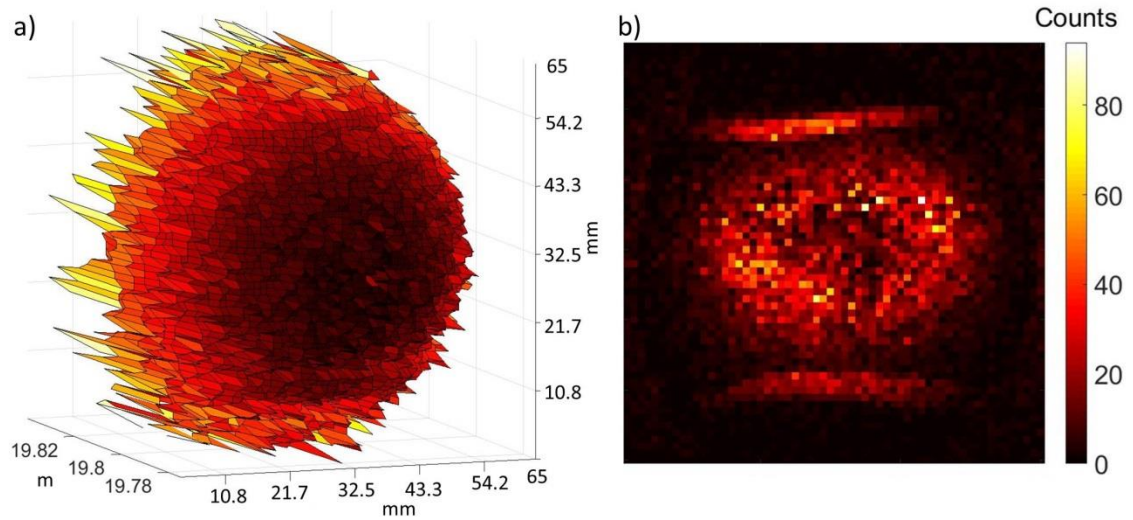

Figure 5.13. (a) Depth displayed in a 3D graph. (b) The number of counts per pixel is displayed in. The colour scale shown in the inset displays the number of counts per pixel. The scan was performed in clear water, at the wavelength λ = 531 nm. The average optical power was approximately 450 nW, and the acquisition time per pixel was 100 ms, with a 60 × 60 pixel format.

The scan of the same target was repeated in water with 0.01% of Maalox, meaning a stand-off distance of 5.7 attenuation lengths between target and system. In this case, the wavelength was $\lambda = 670$ nm and the average optical power was set to 520 nW. This was the highest average optical power possible since the return peak due to the back-reflections increased the detector count rate to such an extent that this put an upper limit to the power range that could be used. If a higher optical power was used, then the measurement would be subject to the deleterious effects of pulse pile-up described previously in the thesis. The pixel format used was 60 × 60 also in this case, but the acquisition time per-pixel was increased to 300 ms because of the very low return from the target at this low power level. The results are shown in Figure 5.14.
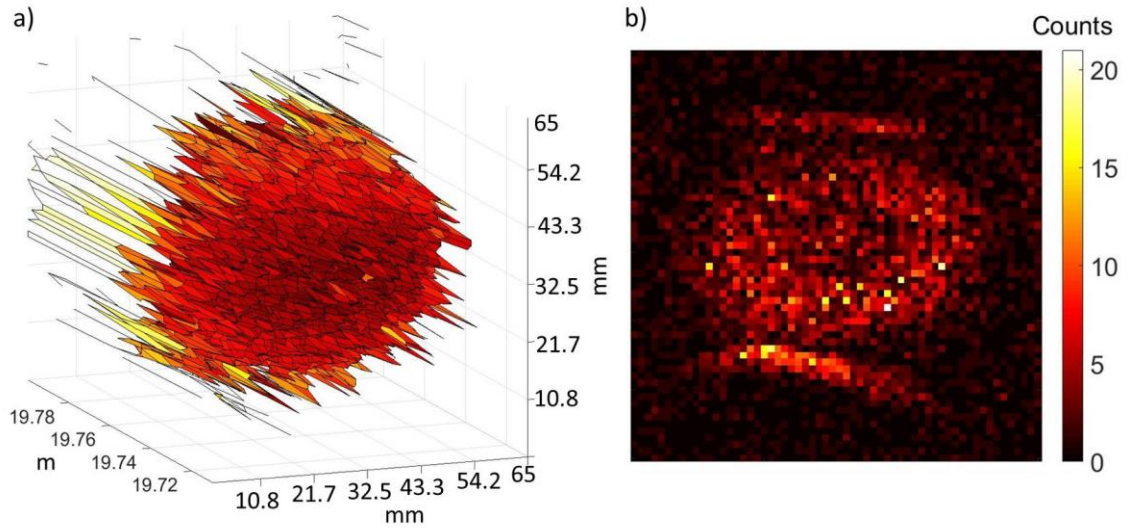
Figure 5.14. A scan of the tennis ball performed in water with 0.01% of Maalox, at the wavelength λ = 670 nm. The average optical power was approximately 520 nW, and the acquisition time per pixel was 300 ms, with a 60 × 60 pixel format. The depth is displayed in a 3D graph in figure (a), and figure (b) shows the intensity map. The depth and the number of photons are displayed in the colour scales shown in the insets.

From the results, the effect of scattering is evident in both depth profile and intensity map. In the depth profile, the return from the edge of the target is not high enough for the cross-correlation to determine the time of flight for those pixels. Compared to the case of clear water, there is a reduction of almost 8% in target-pixels, i.e. those pixels reporting the depth of the target. This lack of target-pixels is particularly evident on the top and bottom of the profile, resulting in an apparent alteration of the shape and size of the target. As in the case of unfiltered tap water, the intensity map does not provide enough information to distinguish the target.

These preliminary measurements show promise from the point of view of measuring depth profiles of targets in highly attenuating environments. However, some major issues with the system were highlighted. For example, if high optical powers are used, the back-reflections in the monostatic system can saturate the single-photon detector and prevent detection of the returns from the target. Electrically gated detectors offer the opportunity to temporarily deactivate the detector during the expected arrival time for photons from the back-reflections, allowing higher optical powers to be used.

The next section explains how such a configuration can be implemented, allowing the use of higher average optical powers, which can significantly improve the performance of the system.

5.9 Underwater depth profiles in low and medium levels of scattering

Several modifications were made to the system in order to improve its performance. Firstly, the wavelength routing unit was removed and the transceiver unit was fibre-coupled to the detector. This allowed avoiding additional coupling losses in the system, as the routing system introduced an attenuation factor in the range 5 dB to 9 dB, depending on the wavelength channel [14]. Secondly, a higher repetition rate for the laser was used in order to increase the average optical power and obtain a higher return signal from the target. However, this also meant greater back-reflections in the transceiver unit, contributing to the overall dead-time of the system, and limiting the overall power possible prior to the onset of pulse pile-up. By using an electrically gated detector, the back-reflections could be excluded by disabling the detector at the expected return time of the back-reflections, allowing a greater average power to be used to examine targets in highly scattering media.

In order to implement these system improvements, a different detection scheme was adopted, as shown schematically in Figure 5.15. The pulsed laser source was the SuperK Extreme EXW-12 fibre-coupled to the AOTF, and the light was delivered from the AOTF to the transmitting channel of the scanning transceiver unit with an armoured photonic crystal fibre with a 5 μm diameter core. The transceiver unit was reconfigured to work in the wavelength range 500 nm – 700 nm. The Perkin Elmer detector was replaced with the pigtailed version of the MPD module. This allowed to use the detector in a time-gated detection scheme, meaning that the detector was temporarily deactivated during the expected arrival time for photons from the back-reflections, so that the detection of the internal back-reflections was avoided and higher optical powers could be used. The detector was activated for a temporal window of 6 ns in correspondence with the approximate expected return time from the target, gating out these unwanted back-reflections. The gating scheme was implemented by applying an external TTL signal from a Pulse Pattern Generator (PPG) (Agilent 81110A) with the same frequency as the clock signal. The laser source provided an electrical synchronization signal to trigger both the TCSPC module (PicoHarp 300) and the detector gating. In these experiments, a 19.5 MHz laser repetition rate was used.

However, a limitation of the TCSPC hardware module meant that the frequency of its clock input could not exceed 10 MHz and as a result the synchronization signal was divided by a factor of 10 with a Constant Fraction Discriminator (CFD). Consequently, this modified the number of optical pulses per start signal to 10, and hence, every histogram had 10 return peaks from the target, as shown in Figure 5.16. In the timing histograms, a bin width of 16 ps was chosen to record the data. This configuration allowed to increase the average optical power to approximately 120 µW, allowing more rapid data acquisition. This compared with a maximum of only ~ 520nW using the free-running thick junction Si-SPAD detector. During the course of the measurements the laboratory was kept in dark conditions, to avoid ambient light contributing to the background level of the detector. Under these conditions, the detector background level was approximately 10 counts per second.
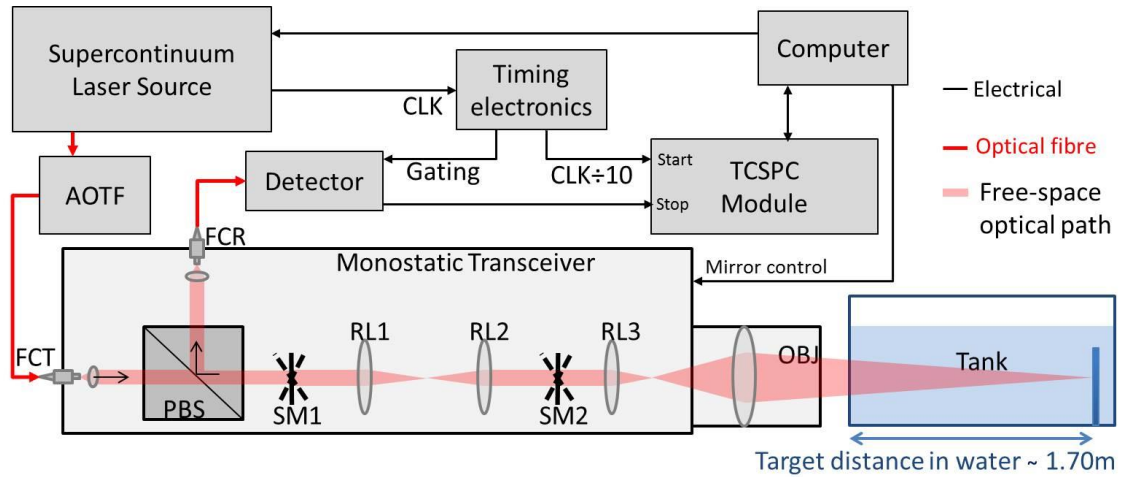

Figure 5.15. Schematic of the single-photon depth imaging system. It comprised the pulsed supercontinuum laser source SuperK Extreme EXW-12, the monostatic scanning transceiver unit, with alignment optimised for the wavelength range 500 nm – 750 nm, was fibre-coupled to an individual thin junction MPD Si-SPAD detector. A time-gated configuration was used, with the single-photon detector being gated on for a 6 ns temporal window in correspondence with the return signal from the target.
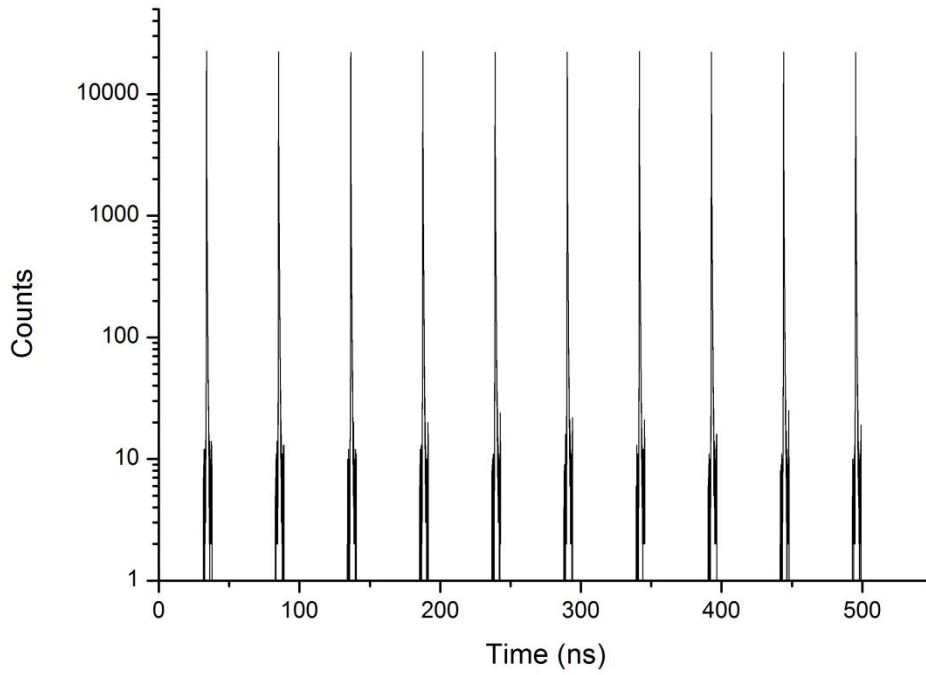
Figure 5.16. An example of timing histogram recorded with the system described. The use of an external frequency divider of the clock signal caused several optical pulses per start signal.

This configuration had an overall system temporal jitter of approximately 100 ps FWHM, and an example of the timing distribution in the recorded histogram is shown in Figure 5.17.   This compares to a timing jitter of ~400ps from the previous configuration using the free-running detector. The use of such low timing jitter means better timing resolution and depth estimation, as the uncertainty $\overline{\sigma}$ in the depth estimation depends on the number of integrated counts N and the timing jitter of the system σ by means of [15]

$$\overline{\sigma} = \frac{\sigma}{\sqrt{N}}$$

Equation 5.2

However, it is worth noting that the improvement in the timing jitter of the system came at the cost of a small decrease in detection efficiency. In this case, the photon detection efficiency of the thin junction Si-SPAD was approximately 48% at the wavelength $\lambda = 550$ nm and decreases down to approximately 30% at $\lambda = 700$ nm, as stated by the manufacturer. While in the case of the thick junction Si-SPAD, the photon detection efficiency was approximately 55% $\lambda = 550$ nm, and up to 65% at the wavelength $\lambda = 700$ nm.
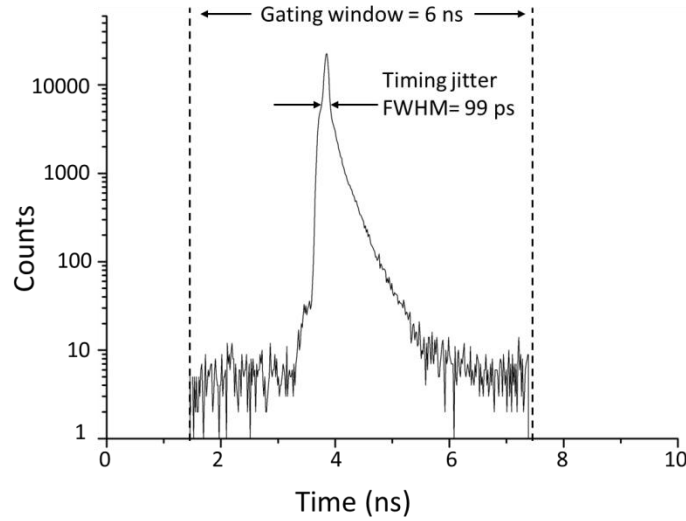
Figure 5.17. An enlarged view of one of the 10 peaks in a timing histogram recorded with the depth imaging system described in the text. The timing jitter of the system (99 ps FWHM in this case) and the gating window are shown in the figure. Due to latency and delays from electronic components, an arbitrary zero was chosen for the displayed time-scale.

5.9.1. 3D depth profile results from the modified scanning system

Initially, the detector was fibre-coupled to the receive channel with a single mode fibre of 5 µm diameter core. The scan of the tennis ball was performed again in water with 0.01% of Maalox, at the operational wavelength $\lambda = 690$ nm, using an average optical power of approximately 115 µW, and a 60×60 pixel format. In this case, the light was focused approximately on a middle plane of the target, hence slightly further away from the system compared to the previous experiment. In addition, the return from the target was high enough to use a shorter acquisition time of 100 ms per pixel. The results are shown in Figure 5.18, where it can be seen that the depth profile obtained with the pixel-wise cross-correlation approach resolves more pixels than the previous experiment (Figure 5.14), covering the entire area of the target and restoring the spherical shape of the tennis ball. It is interesting to note that there is a reduction of only 1% in target-pixels, with respect to the case of unfiltered tap water (refer to Figure 5.13). Most of the un-resolved pixels are in the centre of the scan, where there is a fewer number of counts. It is likely that the lower number of counts in the centre of the profile is due to the light being focused on a middle plane of the target, therefore the focus is not well optimised for the pixels in the centre of the scan. Improvements are

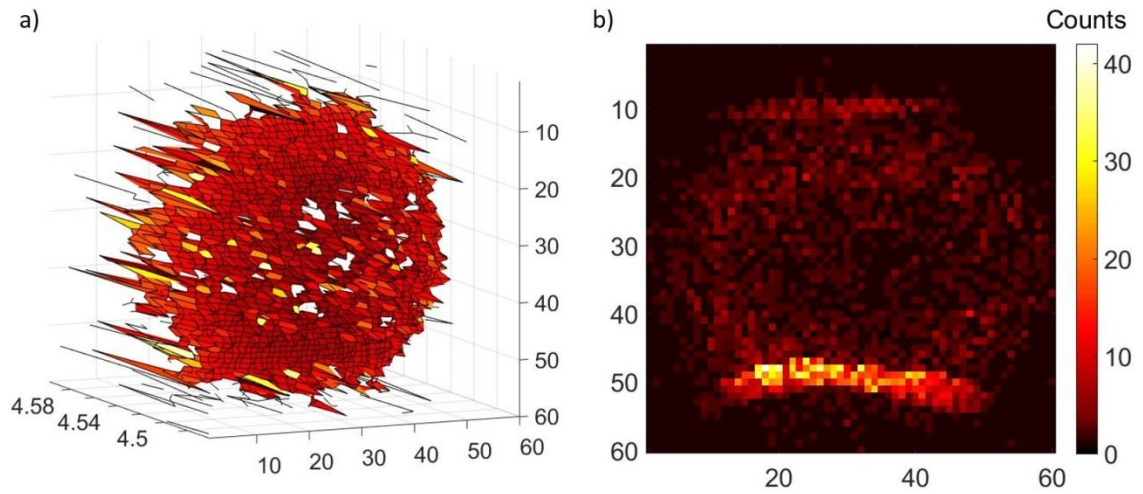visible also in the intensity map, where it is possible to recognise the target despite the low return.

Figure 5.18. Scan of the tennis ball performed in water with 0.01% of Maalox, at the wavelength λ = 690 nm. The average optical power was approximately 115 µW, and the acquisition time per pixel was 100 ms, with a 60 × 60 pixel format. Figure (a) shows the depth profile of the target, while Figure (b) shows the intensity map. The number of photons is displayed in the colour scale shown in the inset.

From Figure 5.18b) it is evident the gap between the returns from the two target materials, due to their different reflectance. From now on, targets made of a single material were used to investigate the potential of the system. The specific case of targets composed of a number of different materials will be studied in Chapter 8.

The level of surface detail recovered from the depth profile depends on a number of factors, including the spacing of the illuminated pixels at the target and the number of photon events recorded at each pixel, which is dependent on the acquisition time, the reflectance of the target, and the diameter of the fibre collecting the return photons in the receive channel. Hence, different pixel formats and acquisition times per pixel were investigated for two different targets and for two different optical fibres coupled to the receive channel. For example, Figure 5.19 shows the depth profiles of the plastic pipe connection performed in unfiltered tap water, at a stand-off distance equivalent to 0.2 attenuation lengths between target and system, at an operational wavelength λ = 525 nm, at four different acquisition times per pixel. To obtain the results shown in

column a), the detector was fibre-coupled to the transceiver unit with a 5 µm diameter core single mode fibre, and the average optical power used was approximately 120 nW. In column b), the displayed profiles were recorded by coupling the receive channel to the detector via a 50 µm core multimode fibre, and using an average optical power of ~ 8 nW. The results obtained in the two cases are equivalent when the optical power is properly adjusted, therefore, just one fibre was chosen to perform the next experiments. In particular, the multimode fibre was selected in order to use very low optical powers necessary in low scattering water, and maximising the photon return when the scans were performed in highly scattering environments.
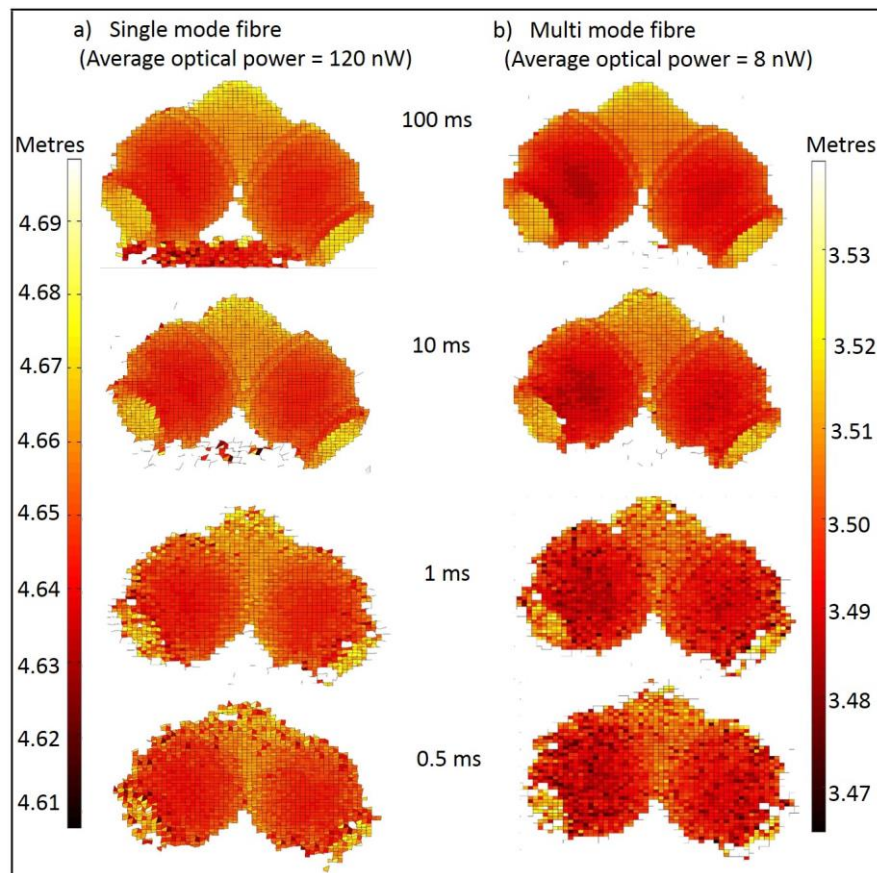

Figure 5.19. Depth profile images of the plastic pipe target performed in clear water at λ = 525 nm, when the detector was fibre-coupled to the transceiver via a single mode fibre (column a), and a multimode fibre (column b). The target was at a stand-off distance equivalent to 0.2 attenuation lengths, and a pixel format of 60 × 60 was used for each scan. The results in column a) were obtained using an average optical power of approximately 120 nW, while an average power of 8 nW was used in column b). Different per-pixel acquisition times are shown in both cases (0.5 ms, 1 ms, 10 ms and 100 ms).

Figure 5.20 reports results from measurements of the plastic pipe connection in order to illustrate how the depth profile is affected by the use of different acquisition times. The results are shown for the case of unfiltered tap water in column (a) at the operational wavelength, $\lambda = 525$ nm. The target was placed at a stand-off distance of 1.7 m, equivalent to 0.2 attenuation lengths in unfiltered tap water. Four different per-pixel acquisition times were used, 0.5, 1, 10, 100 ms, with a very low average power, 8 nW. The same target was measured in water with 0.003% of Maalox ($\lambda = 585$ nm), at a stand-off distance of 1.2 attenuation lengths, using the same average power and acquisition times, and the depth profiles for this case are shown in column (b). From these results, it is evident that even at the shortest acquisition times of 0.5 ms per pixel it is possible to resolve the shape of the target in unfiltered tap water, although some pixels have insufficient returns for a distinct time-of-flight measurement to be determined from the pixel-wise cross-correlation procedure. When the scattering level was increased, the depth profile degrades significantly as the per-pixel acquisition time is reduced, and at 0.5 ms acquisition time the shape of the pipe cannot be discerned from the depth image when using this pixel-wise data analysis approach.
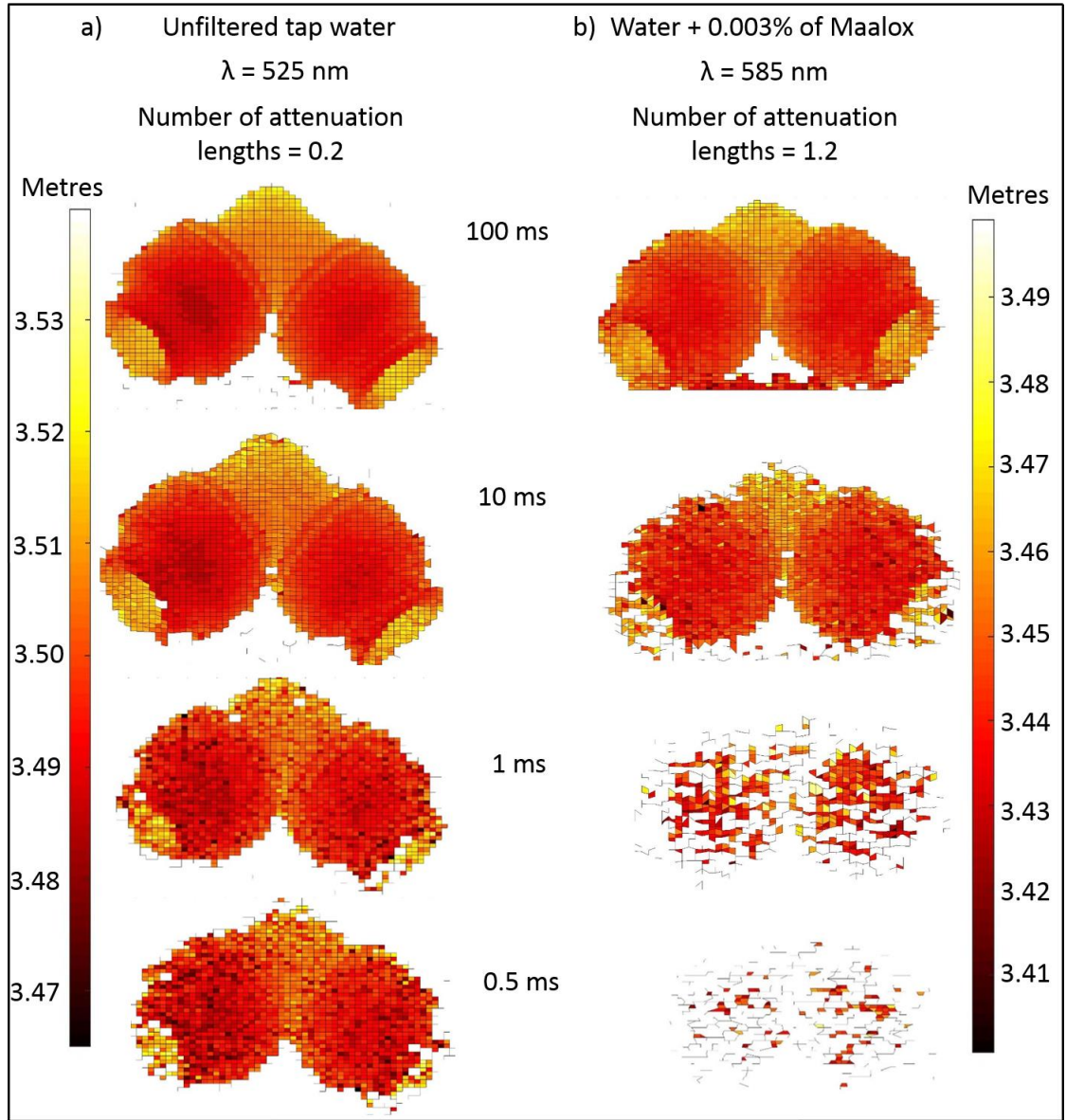
Figure 5.20. Depth profile images of the plastic pipe target performed in clear water at λ = 525 nm (column a) and water with 0.003% of Maalox at λ = 585 nm (column b) using 60 × 60 pixels in all cases. Clear water (column a) corresponded to 0.2 attenuation lengths from transceiver to target, whilst column (b) corresponded to 1.2 attenuation lengths. An average power of just 8 nW was used in all measurements, and different per-pixel acquisition times are shown (of 0.5 ms, 1 ms, 10 ms and 100 ms) in order to investigate how the depth profile obtained with cross-correlation approach changes using different acquisition times.

The same scans were performed with the copper pipe in order to study a target with low reflectance. In Figure 5.21, the case of unfiltered tap water is shown in column (a) at the operational wavelength λ = 525 nm, and the case of water with 0.003% of Maalox at

the operational wavelength $\lambda = 585$ nm is in column (b). As before, four acquisition times were investigated, 0.5, 1, 10, 100 ms, and the target was placed at a stand-off distance of 1.7 metres, equivalent to 0.2 attenuation lengths in unfiltered tap water and 1.2 attenuation lengths in water with 0.003% of Maalox. Due to the low reflectance of the target, the average optical power was increased to approximately 235 nW. Also, in this case, the target is resolved even at the shortest acquisition time in unfilterd tap water. While at a higher level of scattering, the analysis performed with the pixel-wise cross-correlation approach does not allow sufficient pixels to provide enough depth information such that the target can be distinguished from the noise clutter. These scans suggest that the results obtained for the plastic and copper pipes are equivalent as long as the average optical power is properly adjusted, in accordance with the target reflectance. However, a more detailed study on target reflectance will be reported in Chapter 7.
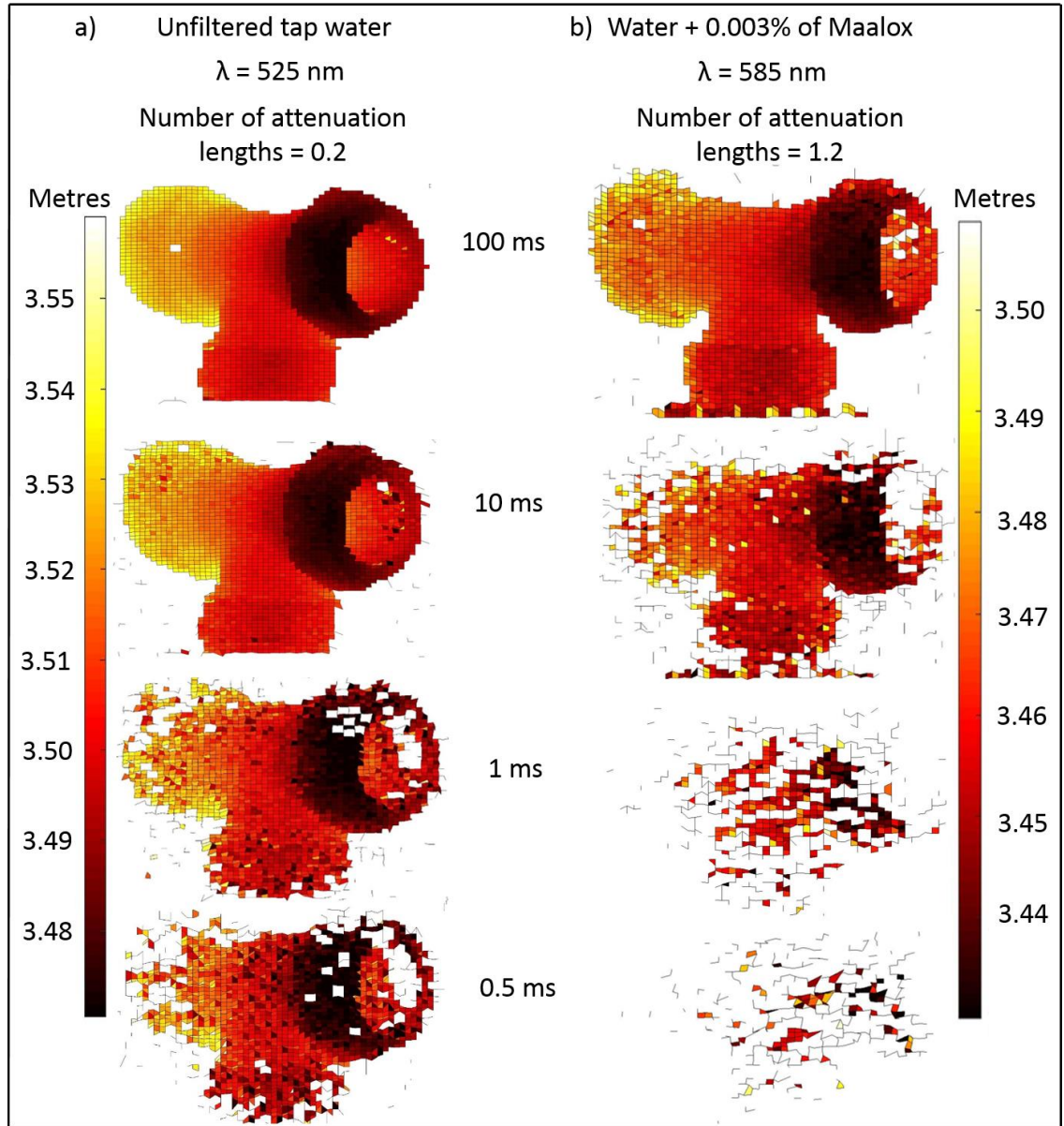
Figure 5.21. Depth profile images of the copper pipe target performed in clear water at λ = 525 nm (column a) and water with 0.003% of Maalox at λ = 585 nm (column b) using 60 × 60 pixels in all cases. Unfiltered tap water (column a) corresponded to 0.2 attenuation lengths from transceiver to target, whilst column (b) corresponded to 1.2 attenuation lengths. An average power of 234 nW was used in all measurements, and different per-pixel acquisition times are shown (of 0.5 ms, 1 ms, 10 ms and 100 ms) in order to investigate how the depth profile changes using different acquisition times.

More scans were performed with a greater pixel format in order to increase the level of detail of both the depth profile and intensity map. Figure 5.22 reports a 256 × 256 pixel depth scan of the plastic pipe in unfiltered tap water, at an operational wavelength of

λ = 525 nm, performed using an acquisition time per pixel of 30 ms, and an average optical power of approximately 9 nW. From the results high-resolution details of sub-millimetre dimensions can be observed. In particular, in Figure 5.22a) the depth profile shows the couplings of the pipe, which present depth details of approximately 1.5 millimetres. At the same time, the grooves at both ends of the pipe are visible in the intensity map, as reported in Figure 5.22b).
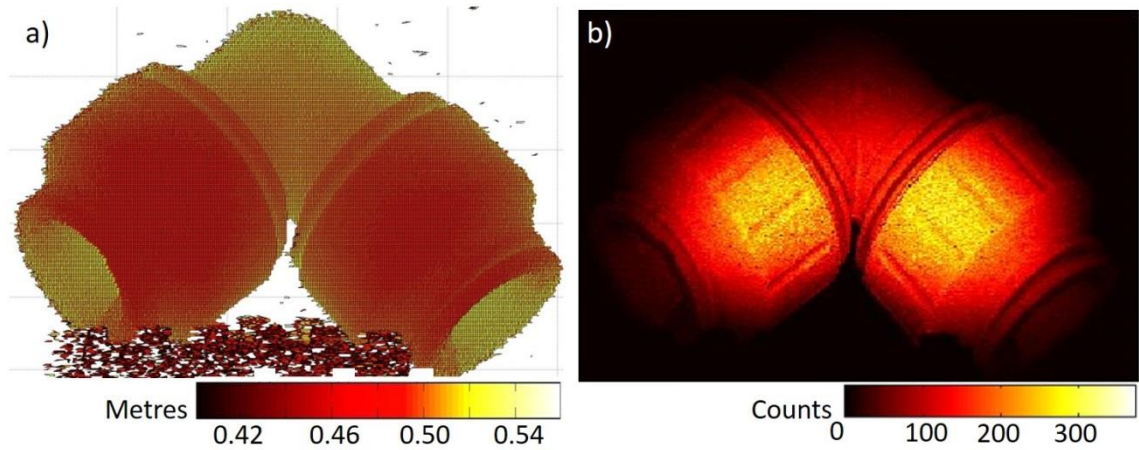

Figure 5.22. Figure (a) shows a 256 × 256 pixel depth scan of the plastic pipe target made in clear water at λ = 525 nm, and a stand-off distance of 1.7 metres, corresponding to 0.2 attenuation lengths between transceiver and target. Each pixel had an acquisition time of 30 ms and an average optical power 8.7 nW. Figure (b) shows the same target displayed with the number of photons returned per pixel, ie the intensity map. The depth and the number of photons are displayed in the colour scales shown in the insets.

Measurements of the same target were then performed in water with a concentration of 0.01% of Maalox. Since the amount of scattering is considerably greater at this concentration, the measurements were taken at the longer wavelength of 690 nm, which corresponds to the minimum attenuation, and the average optical power was increased to 121 μW. This case corresponded to an attenuation of 5.7 attenuation lengths between system and target. A per-pixel acquisition time of 50 ms was used for this measurement. The results of the 256 × 256 pixel depth profile and the intensity map are reported in Figure 5.23a) and Figure 5.23b). Also, in this case, the features on the pipe with sub-millimetre dimensions are clearly evident in the depth profile and intensity map despite the attenuation length being only 30 cm.
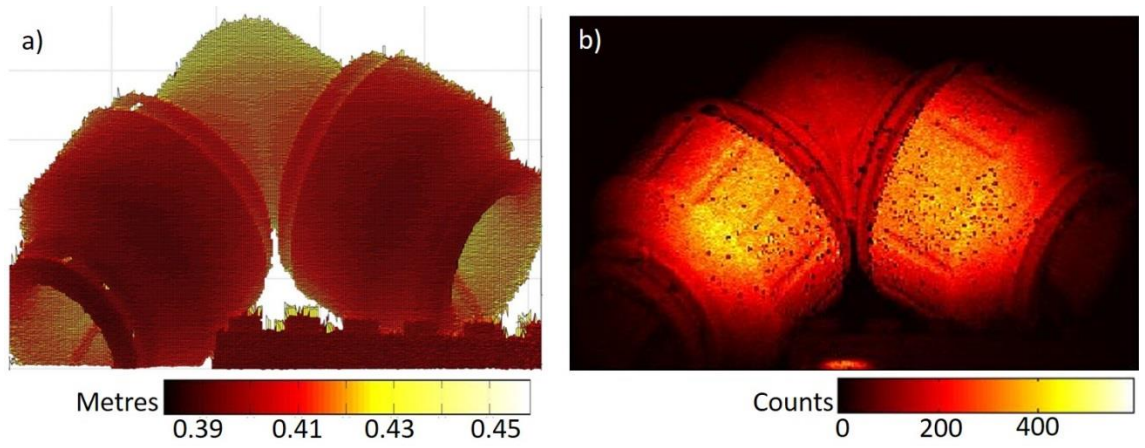
Figure 5.23. Figure (a) shows a 256 × 256 pixel depth scan made in water with 0.01% of Maalox at λ = 690 nm, and a stand-off distance of 1.7 meters, corresponding to 5.7 attenuation lengths between transceiver and target. A per-pixel acquisition time of 50 ms and an average optical power 121 µW was used. Figure (b) shows the same target displayed with the number of photons returned per pixel. The depth and the number of photons are displayed in the colour scales shown in the insets.

The high-resolution scans presented so far show a high level of detail, however, the overall acquisition time was approximately 30 minutes for the scan in Figure 5.22, and more than 50 minutes for the scan in Figure 5.23. A shorter acquisition time per pixel was used in the case of unfiltered tap water, in order to study a more realistic case and avoiding long acquisition times. A 256 × 256 scan was performed in clear water at the operational wavelength λ = 525 nm, with 8 nW average optical power, and 0.5 ms acquisition time per pixel. In this case, the overall acquisition time was less than 1 minute, and from the results (Figure 5.24) it can be seen that the overall shape of the target is still resolved as well as most of the major characteristics, although some of the sub-millimetre details are not visible anymore. However, the analysis performed so far is based just on the cross-correlation approach without additional post-processing of the data, which can greatly improve the image, as will be discussed in Chapter 6.
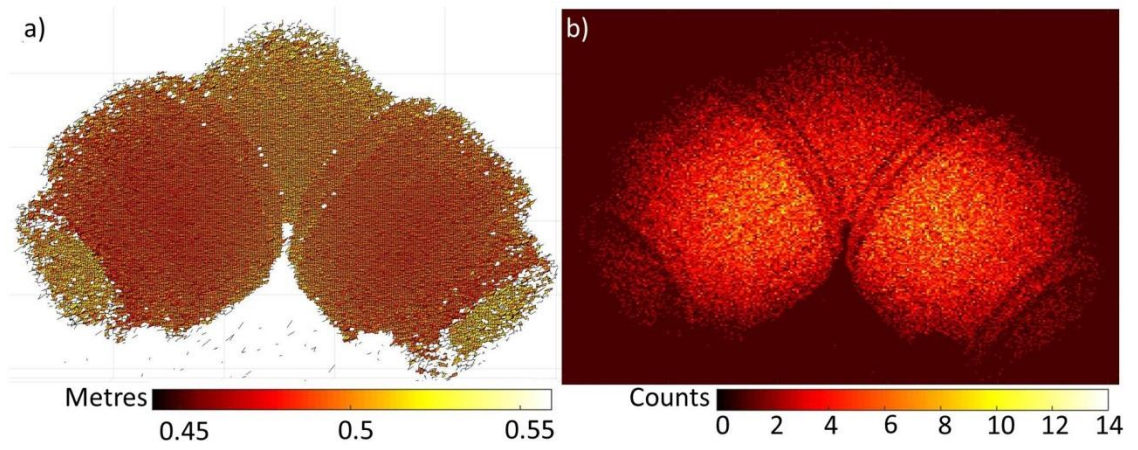
Figure 5.24. Figure (a) shows a 256 × 256 pixel depth scan of the plastic pipe target made in clear water at λ = 525 nm, and a stand-off distance of 1.7 metres, corresponding to 0.2 attenuation lengths between transceiver and target. Each pixel had an acquisition time of 0.5 ms and an average optical power 8 nW. Figure (b) shows the same target displayed in the intensity map. The depth and the number of photons are displayed in the colour scales shown in the insets.

The high-resolution scan of 256 × 256 pixel format was also performed in the reservoir water, in order to have a comparison with a naturally occurring scattering environment. In this case, the operational wavelength was λ = 685 nm, corresponding to 4.6 attenuation lengths between system and target. The average optical power was 120 μW, and the acquisition time per pixel was 10 ms, meaning an overall acquisition time of approximately 10 minutes. The results are shown in Figure 5.25, where sub-millimetre features are clearly visible in both the depth profile and the intensity map.
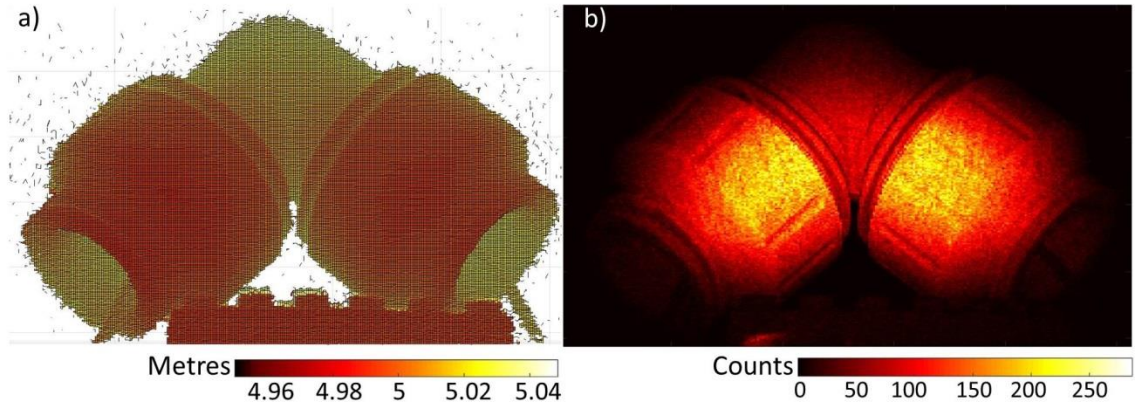
Figure 5.25. Figure (a) shows a 256 × 256 pixel depth scan of the plastic pipe target made in reservoir water at λ = 685 nm, and a stand-off distance of 1.7 metres, corresponding to 4.6 attenuation lengths between transceiver and target. Each pixel had an acquisition time of 10 ms and an average optical power 120 μW. Figure (b) shows the intensity map. The depth and the number of photons are displayed in the colour scales shown in the insets.

5.10   Underwater depth profiles in highly scattering environments

The results presented so far demonstrated the capability of the system to perform depth profiles at stand-off distances equivalent up to 6 attenuation lengths. The potential of the system was then investigated in highly scattering environments, in order to establish the most extreme environments in which the system is capable of obtaining target depth profiles. In order to achieve these objectives, several further changes were made to the system, including: improvements to the output power of the source; improvements to the relay lenses for a more uniform optical field and lower optical loss; the use of the HydraHarp 400 data acquisition module for easier processing and less complex electrical set-up; and the use of an improved shallow-junction Si-SPAD which permitted further reductions in jitter.

To conduct these experiments, a few modifications were made to the electronics and the optical configuration of the transceiver unit, as schematically shown in Figure 5.26. Firstly, the TCSPC module was replaced with the HydraHarp 400, and the data were acquired in T3 mode (described in section 5.4), allowing scans with a greater pixel format. The repetition rate of the laser was kept to 19.5 MHz, and the synchronisation signal frequency was reduced by a factor 8 with the internal synchronisation frequency divider of the HydraHarp 400. In addition, the bin width of the temporal histogram was

changed to 2 ps in order to increase the depth resolution of the system. Since the experiments were performed in highly scattering environments, the optimum wavelength was $\lambda = 690$ nm for most of the water samples investigated, as established in Chapter 4. Therefore, the alignment of the transceiver unit was performed at $\lambda = 690$ nm, and the optical components were chosen to maximise the transmitted light. In particular, the pair of relay lenses RL1 and RL2 was selected with anti-reflection coating characterised by reflectance less than 0.4% in the wavelength range 400 nm – 700 nm, while the relay lens RL3 was a high-performance custom lens [16]. The advantage of using this custom lens was that it permitted obtaining images with fewer distortions and aberrations, and it had a flatter field, with respect to the optical configurations previously considered.
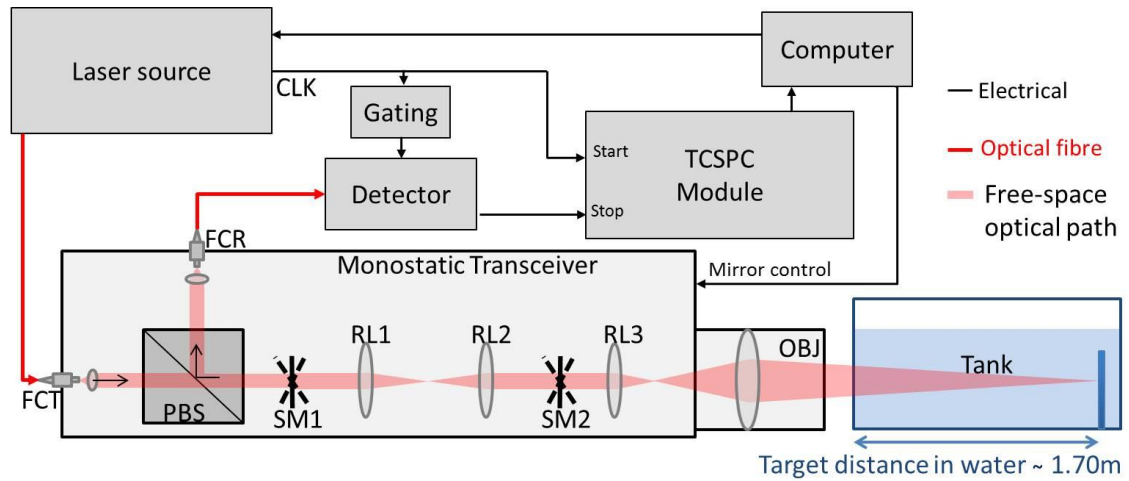

Figure 5.26. Schematic of the single-photon depth imaging system. It comprised the pulsed supercontinuum laser source SuperK Extreme EXW-12, the monostatic scanning transceiver unit, with alignment optimised for the wavelength $\lambda = 690$ nm, was fibre-coupled to an individual thin junction Si-SPAD detector manufactured by MPD. A time-gated configuration was used, with the single-photon detector being gated on for a 9 ns temporal window in correspondence with the return signal from the target.

The laser source was the SuperK Extreme EXW-12, used in conjunction with the AOTF to select the operational wavelength $\lambda = 690$ nm. In this case, a fine optimisation of the transmitted light was achieved acting on the polarising orientation lock ring of the photonic crystal fibre coupling the AOTF to the transceiver unit. This optimised the match between the polarisation plane of the fibre with the polarisation of the output

light from the AOTF, allowing the use of average optical power levels up to approximately 800 µW.

The fibre receptacle version of the MPD Si-SPAD was mainly used in these measurements, and it was fibre-coupled to the receive channel of the transceiver unit via a 50 µm diameter core multi-mode fibre. A time-gated detection scheme was used to avoid detection of the back-reflection in the scanning unit. As before, the detector was gated by applying an external TTL signal from the PPG with the same frequency as the clock signal. For this configuration, the gating window was 9 ns wide, and the timing jitter was approximately 60 ps FWHM. The instrumental response is shown in Figure 5.27.
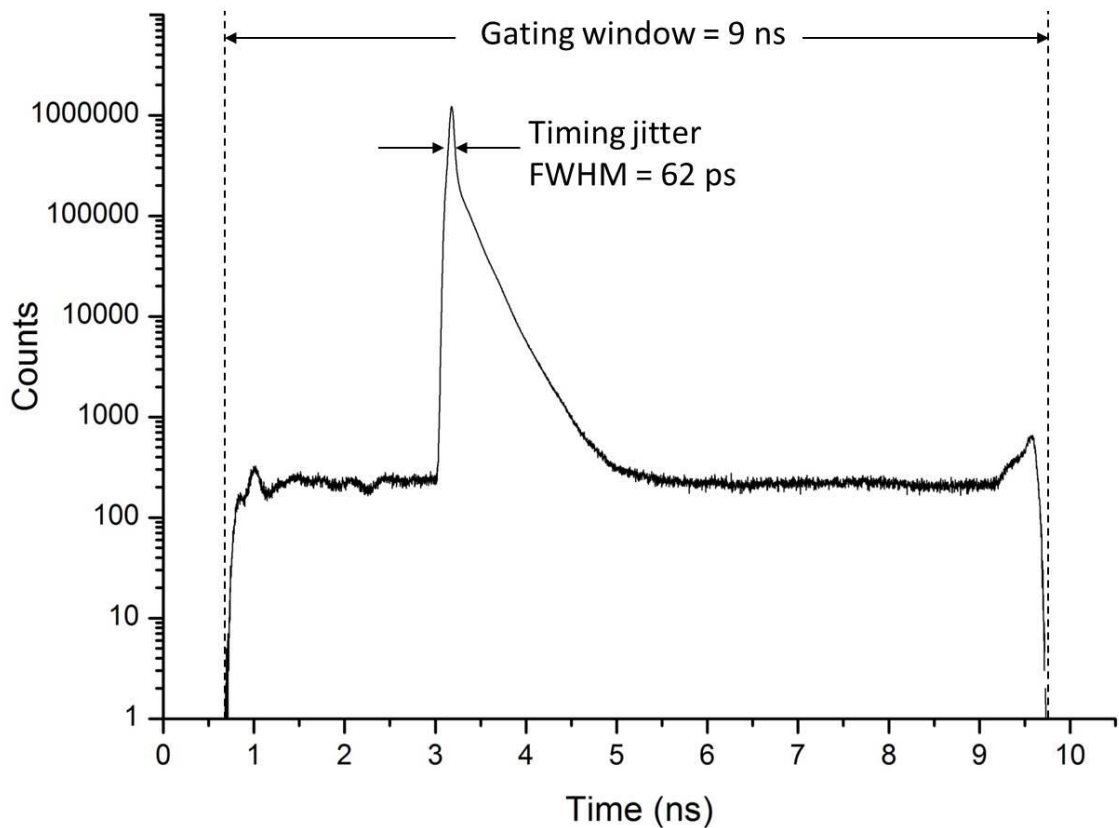

Figure 5.27. Instrumental response recorded with the depth imaging system described in the text. The timing jitter of the system (62 ps FWHM in this case) and the gating window are shown in the figure. Due to latency and delays from electronic components, an arbitrary zero was chosen for the displayed time-scale.

A scan of the plastic pipe target was performed in water with 0.012% of Maalox, equivalent to a stand-off distance of 8 attenuation lengths between system and target. The average optical power was 0.63 mW, while the pixel format was 256×256, with an acquisition time per pixel of 30 ms. The results of the scan are reported in Figure 5.28, where both the depth profile (Figure 5.28a) and the intensity map (Figure 5.28b) still show the sub-millimetre features of the target despite the high level of scattering.
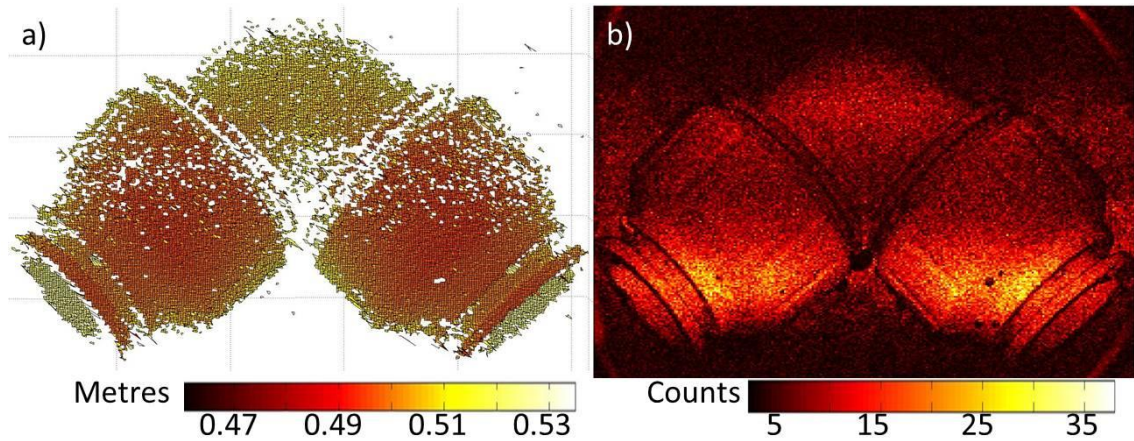

Figure 5.28. Figure (a) shows a 256×256 pixel depth scan of the plastic pipe target at a 0.012% Maalox concentration, and a stand-off distance of 1.7 metres, corresponding to 8 attenuation lengths between transceiver and target. The average optical power used was 0.63 mW. Each pixel had an acquisition time of 30 ms and the analysis used was a pixel-wise cross-correlation approach. Figure (b) shows the same target displayed with the number of photons returned per pixel. The depth and the number of photons are displayed in the colour scales shown in the insets.

The scan of the pipe was performed again in water with 0.016% of Maalox, equivalent to a stand-off distance of 9 attenuation lengths between target and system. The area scanned was reduced to 48×48 mm^2 and just one end of the pipe was used as a target. The pixel format was 120×120, with an acquisition time per pixel of 100 ms. The average optical power was 0.79 mW, and the results are shown in Figure 5.29. In this case, the depth is displayed in a two-dimensional graph (Figure 5.29a), which shows that the target can still be resolved despite the high attenuation level of the environment. However, Figure 5.29b) shows that the target is much less obvious in the intensity map

because of the presence of backscattered light, meaning the weak signal return is not far above the noise level.
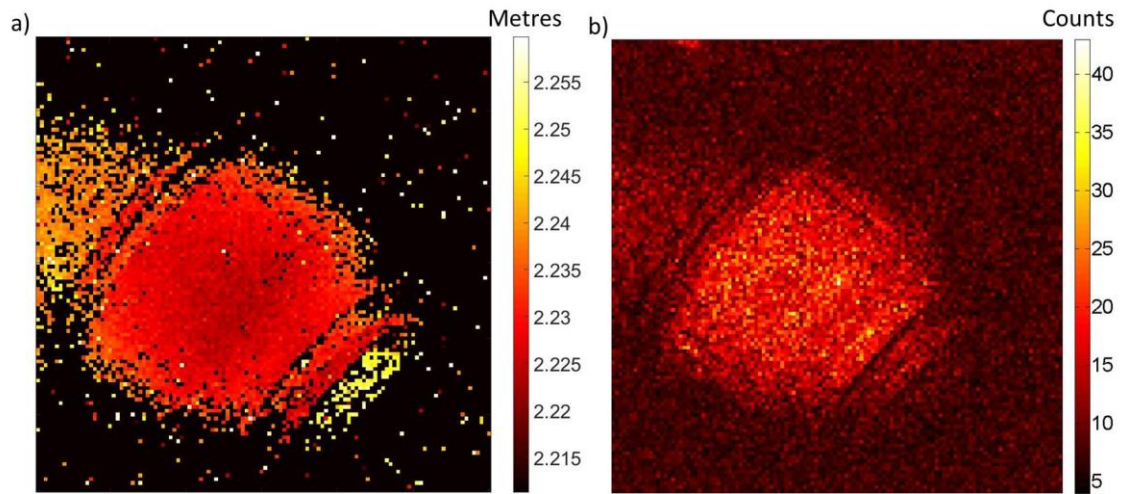

Figure 5.29. (a) Depth map and (b) intensity map of a 120 × 120 pixel scan, with 100 ms acquisition time per pixel, and an average optical power of 0.79 mW. The plastic pipe target was placed at a stand-off distance of 1.7 metres in water with 0.016% of Maalox, equivalent to 9 attenuation lengths.

In general, the intensity map was obtained counting the number of events over a 30 bins range centred on the highest value of the cross-correlation (refer to section 5.5), meaning counting the recorded events over the 15 bins on the left side of the peak and the 15 bins on the right side of the peak. The intensity map of the previous scan was constructed with the same technique, but using different bin ranges in order to improve the image. Figure 5.30 shows the intensity map built counting the number of events over a (a) 10, (b) 40, and (c) 60 bins range centred on the highest value of the cross-correlation. The results suggest that a wider bin range allows the resolution in the intensity map to be improved, allowing the shape of the target to be discerned. It is important to remember that the analysis is based only on the pixel-wise cross-correlation approach with no attempt to apply any spatial correlation, which is likely to improve the results of the scans. A more advanced analysis will be discussed in Chapter 6.
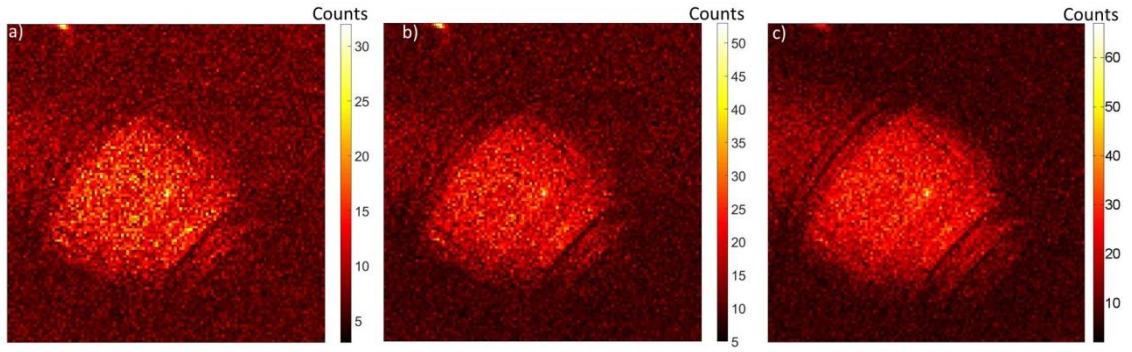
Figure 5.30. Intensity maps of a 120 × 120 scan performed at a stand-off distance of 9 attenuation lengths, using an average optical power of 0.79 mW and an acquisition time per pixel of 100 ms. The intensity maps were obtained identifying the highest value of the cross-correlation between the timing histogram and an instrumental response, and considering all the events in a bin range centred on the highest value of the cross-correlation. The figure shows the case of (a) a 10 bins range, (b) 40 bins range, (c) and 60 bins range.

In order to carry out a comparison between the two thin junction SPADs, the pigtailed version of the Si-SPAD by MPD was fibre-coupled to the receive channel, via the 50 µm core multi-mode fibre. The instrumental response of this case is shown in Figure 5.31 (red curve), where it is also compared to the instrumental response recorded with the fibre receptacle version of the same detector (black curve). From the graph, it can be seen that the two detectors have different responses despite having the same quoted specifications. The two instrumental responses were obtained using an acquisition time of 100 seconds, and an average optical power of 35.8 µW. The target used was the plastic pipe connection, placed at a stand-off distance of approximately 1.7 metres in water with 0.012% of Maalox, equivalent to 8 attenuation lengths. The measurements were recorded at a stand-off distance of 8 attenuation lengths because when the target is 9 attenuation lengths away from the system, the return was too weak to highlight the differences between the two detectors. Under the same conditions, the fibre receptacle version of the thin junction detector presents a signal-to-noise ratio equal to SNR = 20.13, while the pigtailed version has SNR = 16.97. There is clearly a higher peak in the former case, despite the overall integrated counts being approximately the same in each case. The better performance of the fibre receptacle detector can be explained by the reduced jitter of approximately 50 ps, compared to the timing jitter of approximately 75 ps of the pigtailed detector. In addition, there is also

an increased background count level in the latter case, which could be as a result of afterpulsing [17]. This combination of issues means that the fibre-receptacle detector is the better detector for time-of-flight measurements, particularly in highly scattering environments, as it provides the higher value of SNR under identical conditions.
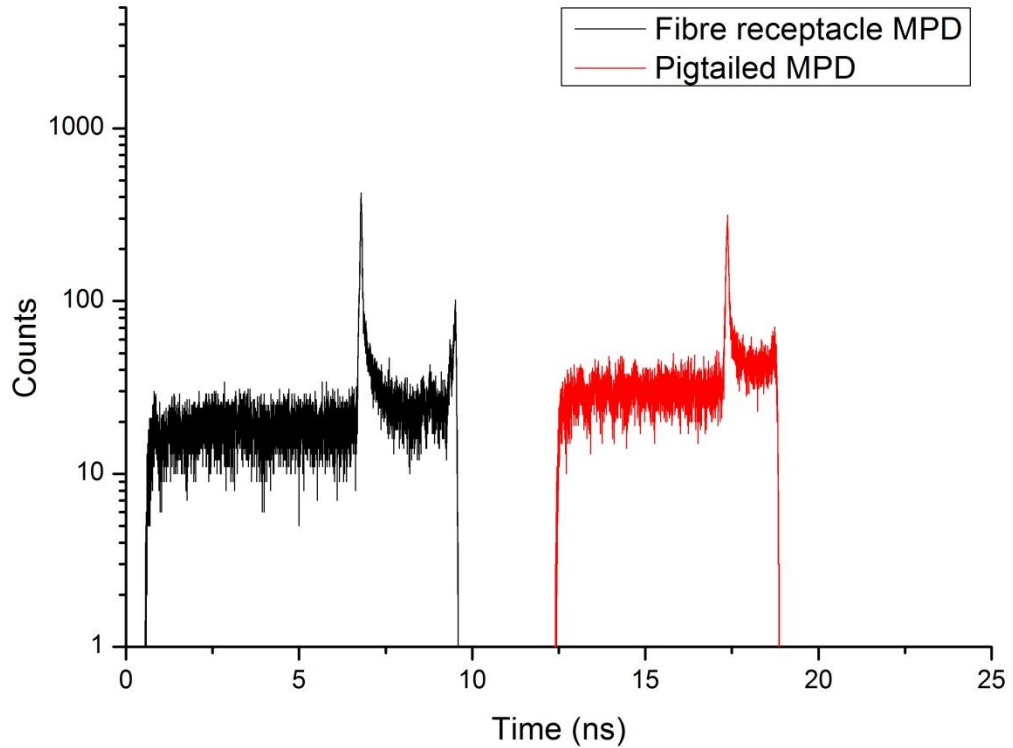

Figure 5.31. Instrumental response when the fibre receptacle version (black) and the pigtailed version (red) of the Si-SPADs by MPD are fibre-coupled to the receive channel of the transceiver unit. The measurements were performed placing the plastic pipe target at a stand-off distance of 1.7 metres in water with 0.012% of Maalox, equivalent to 8 attenuation lengths between system and target. The average optical power used was 35.8 μW, and the integration time was 100 seconds. Under these conditions, the fibre receptacle SPAD shows an SNR = 20.13, while the pigtailed version of the SPAD has SNR = 16.97.

Nevertheless, despite its reduced performance, the pigtailed version of the thin junction MPD detectors was used to perform a scan of the plastic pipe target at a stand-off distance of 9 attenuation lengths, with appropriate analysis. Figure 5.32a) and Figure 5.32b) report the depth and intensity maps, respectively. The scan was performed using an average optical power of approximately 0.78 mW, and 120×120 pixel format, with an acquisition time per pixel of 100 ms, the same conditions as the

scan previously presented in Figure 5.29. In this case, it is not possible to obtain any depth or intensity information with the pixel-wise cross-correlation approach. In these highly scattering conditions and high average optical power, secondary back reflections within the transceiver unit can be visible in the timing histograms recorded, even if the detector is gated. Because of the lower SNR, the return from the target is lower than the secondary back-reflections, leading to the cross-correlation providing the wrong time-of-flight information. However, the results can be greatly improved by software gating the histograms recorded. Software gating consists of performing the pixel-wise cross correlation in a pre-defined time window, which allows the algorithm to ignore any event recorded outside this window. This is different to previous analyses which perform the cross-correlation on all the data, and then evaluate the intensity by counting the recorded events on a selected bin range centred on the highest value of the cross-correlation. By using a narrower timing window in software at around the region of interest permits to isolate the optical return to investigate, when needed.

The effect of software gating is shown in Figure 5.32c) and 5.32d), where the depth and intensity maps, respectively, were obtained performing the cross-correlation over a bin range as narrow as 1200 bins, gating out most of the back-reflections in the system. The results show how the software gating can improve the depth and the intensity maps, allowing recovery of the shape of the target only by narrowing the region of the timing histogram considered by the algorithm.
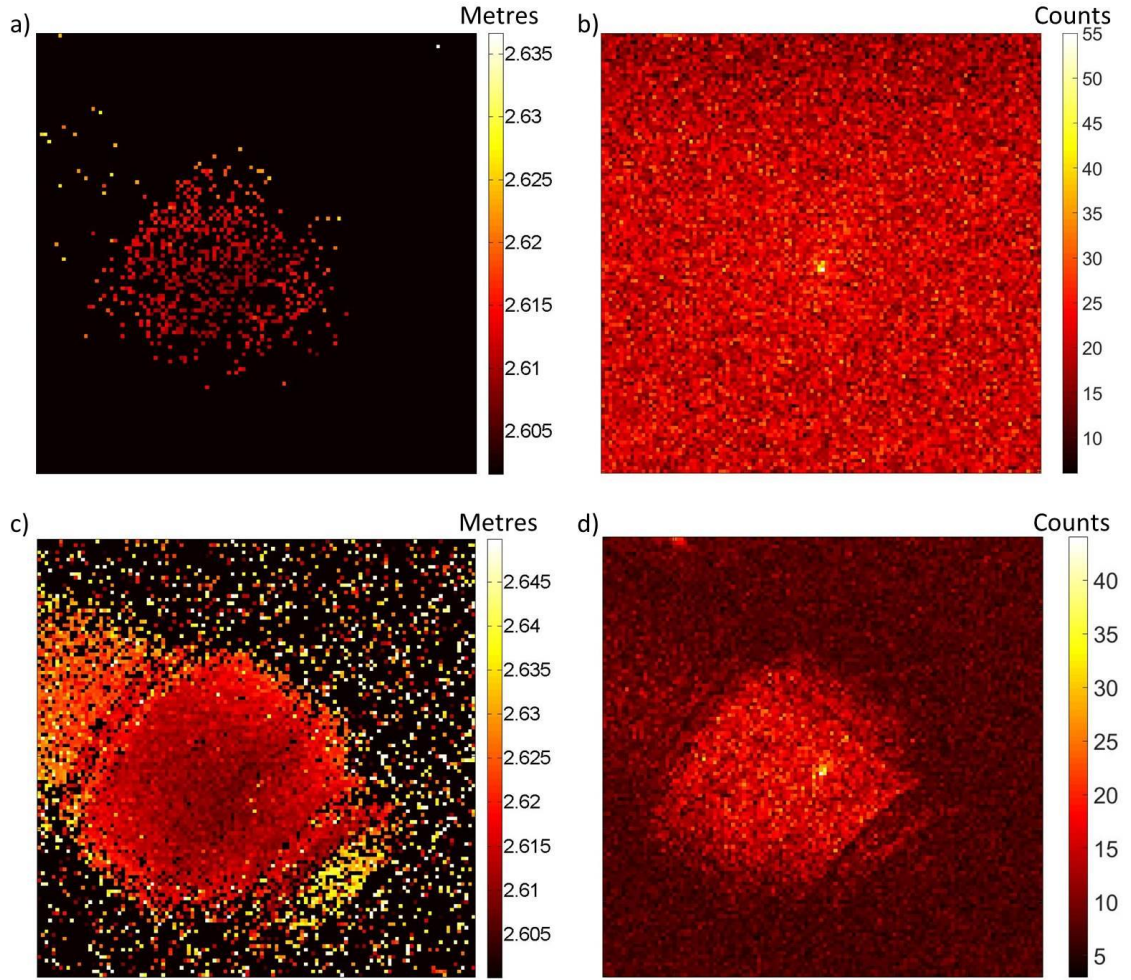
Figure 5.32. 120 × 120 pixel depth map of the right end of the plastic pipe target, placed at a stand-off distance of 9 attenuation lengths. The average optical power used was 776 μW, at the optimum wavelength λ = 690 nm. The detector used for this measurement was the pigtailed version of the thin junction SPADs by MPD. Each pixel used an acquisition time of 100 ms and the analysis used was a pixel-wise cross-correlation approach. Figures a) and b) show the depth and intensity maps respectively, when the entire gating window is used in the algorithm. While Figures c) and d) show the depth and intensity maps obtained considering only a timing window of 1200 bins around the expected return time from the target. The depth and the number of counts are displayed in the colour scales shown in the insets.

The use of software gating helped improve results of a measurement when the detector with a lower SNR was used. However, the next section will show how it can be of great advantage also when the fibre-receptacle thin junction detector (i.e. with a better

performance) is used in conjunction to high average optical power levels, which cause higher secondary back-reflections.

5.11 Underwater depth profiles using high average optical power

In order to investigate higher power levels, the operational wavelength was selected by the use of three optical filters:

- Short pass filter with cut-off wavelength at $\lambda = 700$ nm
- Long pass filter with cut-off wavelength at $\lambda = 600$ nm
- Bandpass filter centred in $\lambda = 700$ nm, 50 nm FWHM

The transmittance of the filters was measured with a spectrophotometer, UV-2550 by Shimadzu, in the wavelength range $450 - 1100$ nm, and the results are shown in Figure 5.33. This allowed selection of a 25 nm wide wavelength range from the supercontinuum spectrum and an increase in the average optical power up to 2.6 mW.
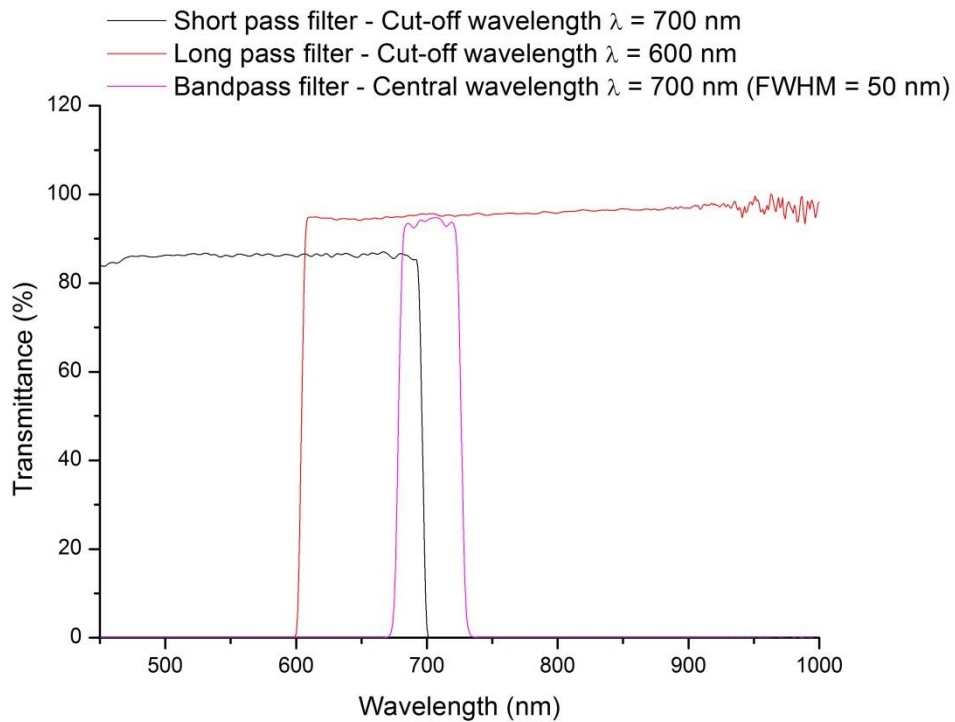

Figure 5.33. Spectra of optical filters used to select a 25 nm wavelength range centred at approximately $\lambda = 690$ nm.

Firstly, a scan of the plastic pipe was obtained in water with 0.012% of Maalox, meaning that the target was at a stand-off distance of 8 attenuation lengths. The measurement was performed using an average optical power of 2.6 mW, 240×240 pixel format, and 30 ms acquisition time per pixel. Figure 5.34a) shows the depth

profile of the target obtained with the pixel-wise cross-correlation approach, while Figure 5.34b) shows the intensity map. In this case, the cross-correlation was performed over the entire timing window, as the return from the target was higher than the secondary back-reflection in the timing histogram. Both graphs show in great detail all the features of the target, allowing the small grooves inside the end of the pipe to be resolved.
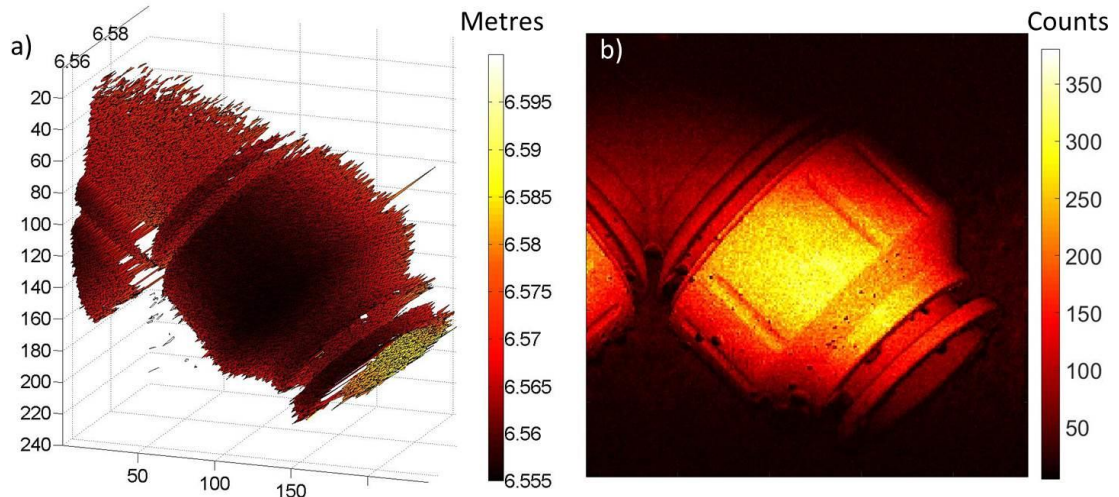

Figure 5.34. Figure (a) shows a 240 × 240 pixel depth scan of the plastic pipe target at a stand-off distance of 8 attenuation lengths between transceiver and target. The average optical power used was 2.6 mW, and each pixel had an acquisition time of 30 ms. Figure (b) shows the same target displayed with the number of photons returned per pixel. The analysis was performed with the pixel-wise cross-correlation approach over the entire timing window. The depth and the number of photons are displayed in the colour scales shown in the insets.

Combining the depth and intensity information together, the scan shows clearly all the sub-millimetre features of the target. This provided a high depth and spatial resolution scan of the plastic pipe target at 8 attenuation lengths, showing how the TCSPC technique can be a useful tool for high-resolution images in photon-starved environments.
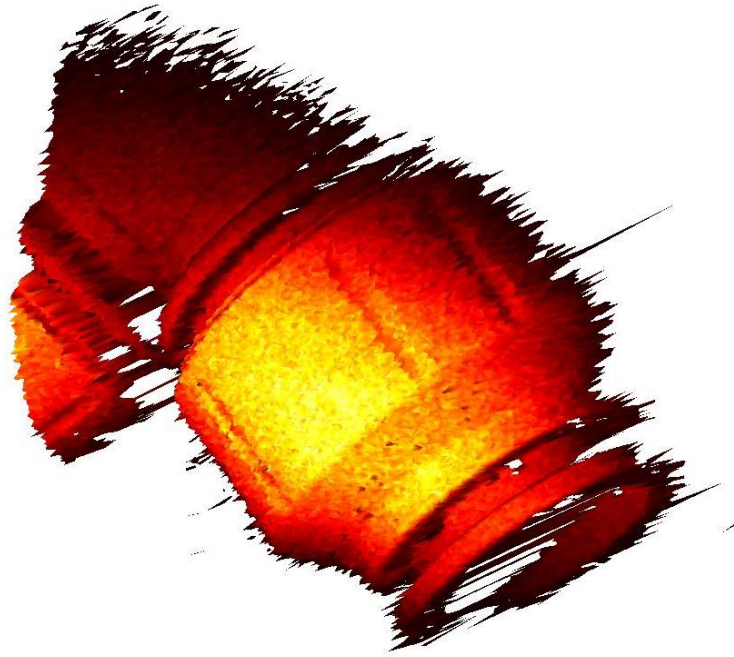
Figure 5.35. Depth estimation combined with intensity information of the plastic pipe at a stand-off distance equivalent to 8 attenuation lengths between transceiver and target.

Then, the scan was obtained in water with 0.016% of Maalox in order to have the target at 9 attenuation lengths. The measurements were performed using 2.6 mW of average optical power and a pixel format of 120×120, while the acquisition time per pixel was increased to 120 ms. Figure 5.36 reports (a) the depth and (b) intensity maps obtained with the cross-correlation approach. In this case, the analysis was performed by software gating the timing window, by selecting 1000 timing bins in correspondence with the return from the target, therefore excluding the optical signal from back reflections. The main features of the target are still visible, in particular in the depth map, while sub-millimetre dimension details cannot be resolved.
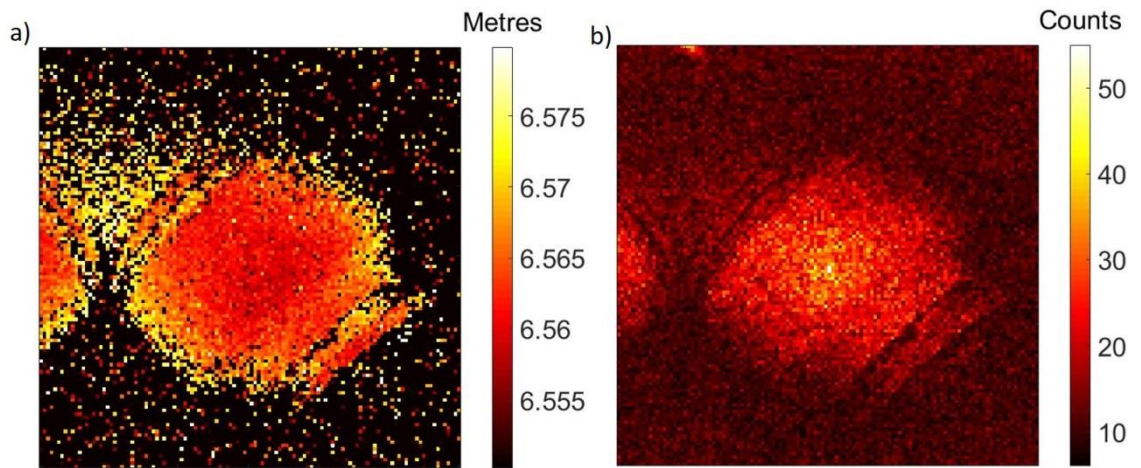
Figure 5.36. Scan of the plastic pipe target at a stand-off distance of 9 attenuation lengths. The scan was performed selecting a 25 nm wavelength range via optical filters. The average optical power was 2.6 mW, the acquisition time per pixel was 120 ms, with a pixel format of 120 × 120. The depth profile is displayed in (a), while the intensity map is shown in (b). The depth and intensity were obtained with the pixel-wise cross-correlation approach performed on a software selected timing window of 1000 bins.

The main limitation that prevents depth imaging in environments with a shorter attenuation length is an unexpected background component. It was observed that the background level increased with the average optical power, reducing significantly the signal to noise ratio. Further studies revealed that this background component was introduced by the detector, and it was dependent on the count rate, and it could be a result of afterpulsing. This effect in conjunction with the background due to the high level of scattering did not allow observation of the return from the plastic pipe target at a stand-off distance of 10 attenuation lengths with the system as described in this Thesis. However, it is worth noting that in this case weak secondary back-reflections could be observed in the histogram, and they were not avoidable with the gating scheme, hence they contributed to the total count rate. A way to avoid the detection of the secondary back-reflections is to move the target to a different position, but it was not possible to investigate this option because of the limited space available in the tank.

5.12   Underwater depth profiles using low average optical power using semiconductor lasers

The advantage of using the supercontinuum laser system is that the operational wavelength can be adapted depending on the scattering level of the environment where the target is placed. However, an implementation of this configuration for field trials would be difficult to realise due to the weight and dimension of this supercontinuum laser system which was designed for laboratory use. Therefore, the supercontinuum laser source was replaced with a PicoQuant PDL800-B pulsed diode laser of wavelength $\lambda = 685$ nm, in order to test the system with a single wavelength source. The wavelength was chosen as a compromise that minimises the attenuation in highly scattering environments, and at the same time provides sufficient transmittance in water with low scattering levels. The repetition rate of the laser source was set to 20 MHz, and it has to be noted that the instrumental response is dependent on the input current settings. For example, Figure 5.37 reports the instrumental response for two values of optical power, 455 µW (black) and 85 µW (red), showing that the timing jitter increases as the input current settings is increased for higher output power levels. Such an increase in the pulse width duration will affect the depth resolution of the system. Hence, low optical power levels were preferred to perform the scans, when possible.
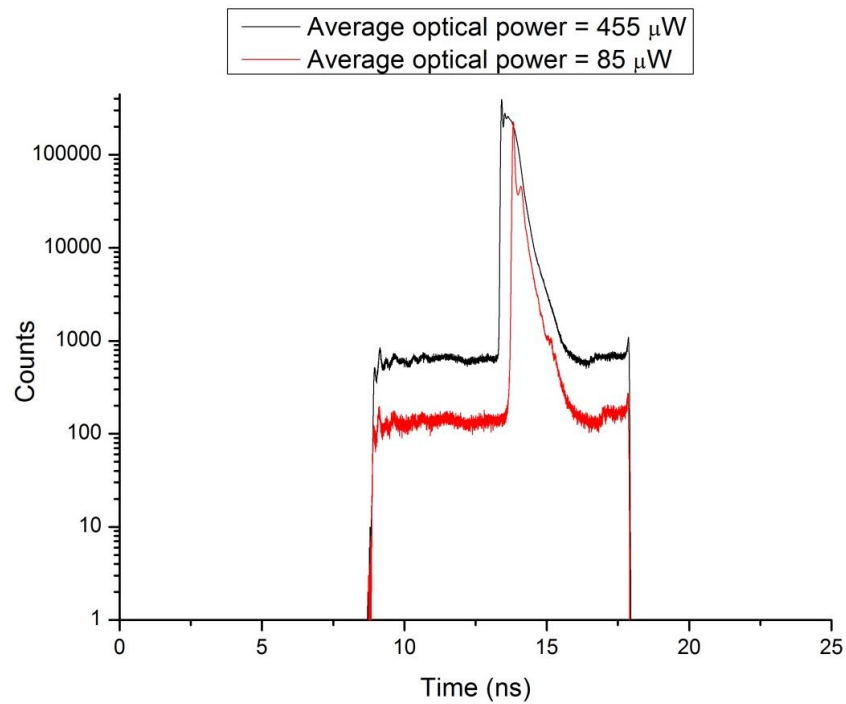
Figure 5.37. Instrumental response of the system for two different average optical power levels of the laser diode source, 455 µW (black), and 85 µW (red). Both measurements were recorded placing the Spectralon target at a distance of 1.7 metres, in water with 0.012% of Maalox, equivalent to 8 attenuation lengths between transceiver and target. The acquisition time used was 100 seconds.

Several scans of the plastic pipe target were obtained with this configuration, and a few examples are shown in Figure 5.38 and 5.39. In all cases, the target was placed at a stand-off distance of 1.7 metres, equivalent to:

- 2.5 attenuation lengths in water with 0.003% of Maalox
- 6 attenuation lengths in water with 0.01% of Maalox
- 8 attenuation lengths in water with 0.012% of Maalox
- 9 attenuation lengths in water with 0.016% of Maalox

The scans were performed with a 120×120 pixel format, while the optical power level and the acquisition time per pixel were adjusted depending on the scattering level. Figures 5.38 a) and b) report the depth profile and intensity map, respectively, in water with 0.003% of Maalox, when an average optical power of 1.3 µW and 1 ms acquisition time per pixel were used. Following the results presented so far, a higher average optical power or a longer acquisition time per pixel can be used to improve the result of the scan, while a greater pixel format can improve the resolution of both the depth profile and intensity map.

The scan of the same target was performed in water with 0.01% of Maalox, increasing the average optical power to 80 μW and the acquisition time per pixel to 10 ms. The depth profile is shown in Figure 5.38c) and the intensity map in Figure 5.38d). In both figures it can be seen that the target is still clearly discernible, despite the lower resolution.
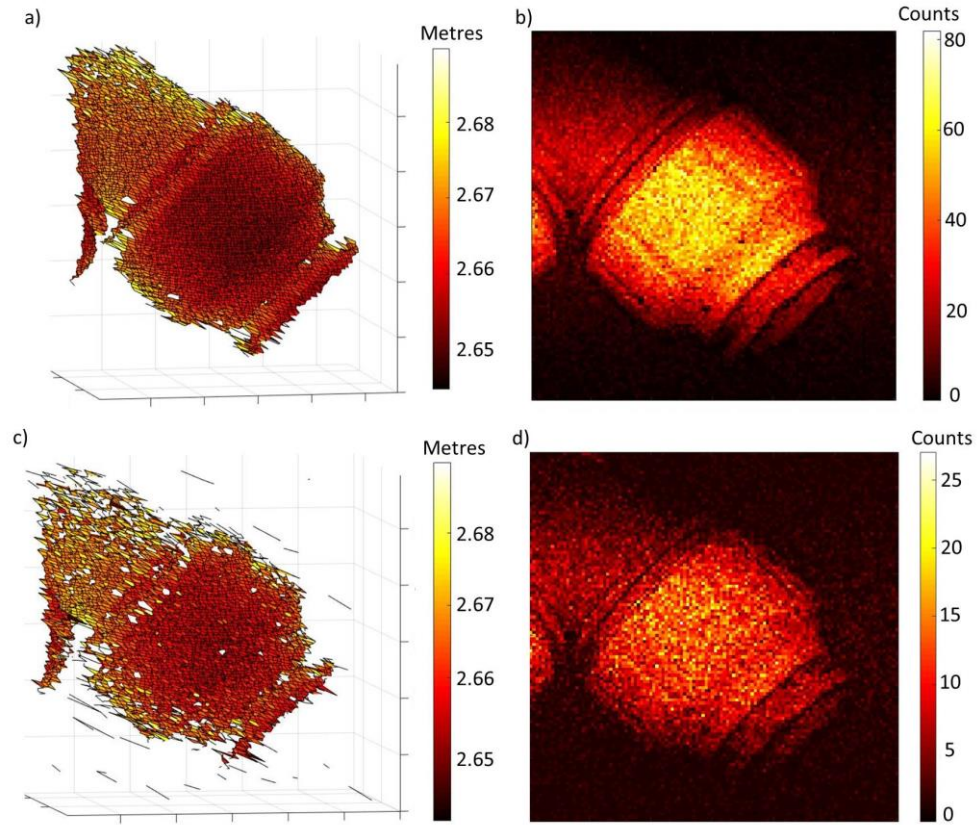

Figure 5.38. (a) Representation of a 120 × 120 pixel depth scan of the plastic pipe acquired in water with 0.003% of Maalox, at a stand-off distance of 1.7 meters, corresponding to 2.5 attenuation lengths between transceiver and target. Each pixel had an acquisition time of 1 ms and an average optical power 1.3 μW was used. (b) The same target displayed with the number of photons returned per pixel. (c) A 120 × 120 pixel depth scan made in water with 0.01% of Maalox, at a stand-off distance of 1.7 metres, corresponding to 6 attenuation lengths between transceiver and target. A per-pixel acquisition time of 10 ms and an average optical power 80 μW was used. (d) Intensity map of the same target displayed with the number of photons returned per pixel. The depth and the number of photons are displayed in the colour scales shown in the insets.

The same conclusions can be drawn from the scan of the same target performed in water with 0.012% of Maalox. In this case, the average power was limited again to 80 µW, while the acquisition time per pixel was increased to 100 ms. This modification was enough to obtain a depth map (Figure 5.39a) sufficiently resolved to distinguish the sub-millimetre features of the target. At the same time, the intensity map (Figure *5.39*b) allows recognition of the shape of the target, although the details are not visible.

When the scan was performed in water with 0.016% of Maalox, the average optical power was increased to approximately 190 µW, with an acquisition time per pixel of 100 ms. Figure 5.39c) reports the depth map, showing clearly the shape of the target despite the high level of scattering. However, the intensity map (Figure 5.39d) makes it difficult to recognise the target because of the low SNR.

It is important to note that all the results presented in this paragraph were obtained using an average optical power of less than 200 µW, showing how this technique allows scans with low optical power levels to be perfomed in highly scattering environments.
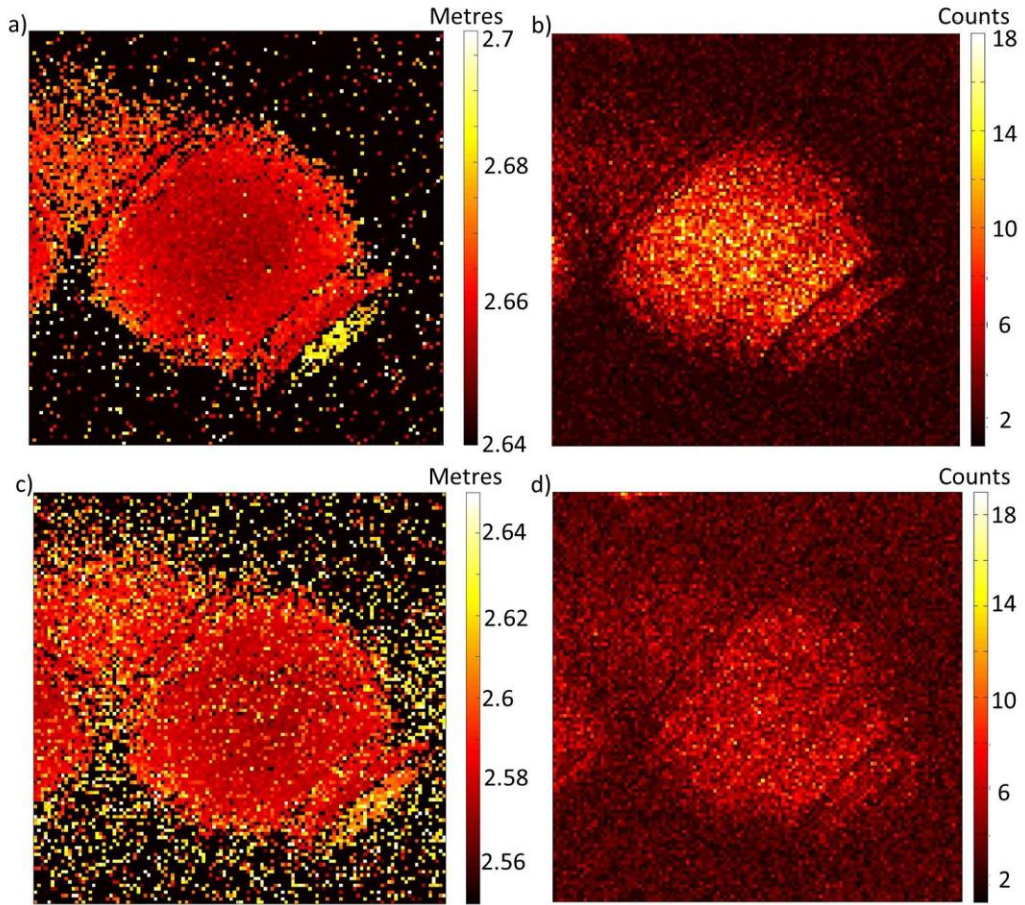
Figure 5.39. (a) Representation of a 120 × 120 pixel depth scan of the plastic pipe acquired in water with 0.012% of Maalox, at a stand-off distance of 1.7 meters, corresponding to 8 attenuation lengths between transceiver and target. Each pixel had an acquisition time of 100 ms and an average optical power 80 μW was used. (b) The same target displayed with the number of photons returned per pixel. (c) A 120 × 120 pixel depth scan made in water with 0.016% of Maalox, at a stand-off distance of 1.7 metres, corresponding to 9 attenuation lengths between transceiver and target. A per-pixel acquisition time of 100 ms and an average optical power 188 μW was used. (d) Intensity map of the same target displayed with the number of photons returned per pixel. The depth and the number of photons are displayed in the colour scales shown in the insets.

5.13 Spatial resolution

To investigate the spatial resolution of the system, a sector star test reference target was scanned in different water types. This target (shown schematically in Figure 5.40) has 36 equally spaced (by 5°) opaque chrome bars on glass radiating out from a shared

centre. The overall diameter is 10 mm, and the clear centre circle has a diameter of 200 μm. The glass substrate measured $25 \times 25 \times 1$ mm. The thickness c of one bar at distance r from the centre is given by the formula

$$c = r \sin\left(\frac{\vartheta}{2}\right)$$ <div style="text-align:right">Equation 5.3</div>

where ϑ is the angle in degrees covered by a pair of bars. The minimum thickness of a bar resolved by the system provides an estimation of the spatial resolution of the system.
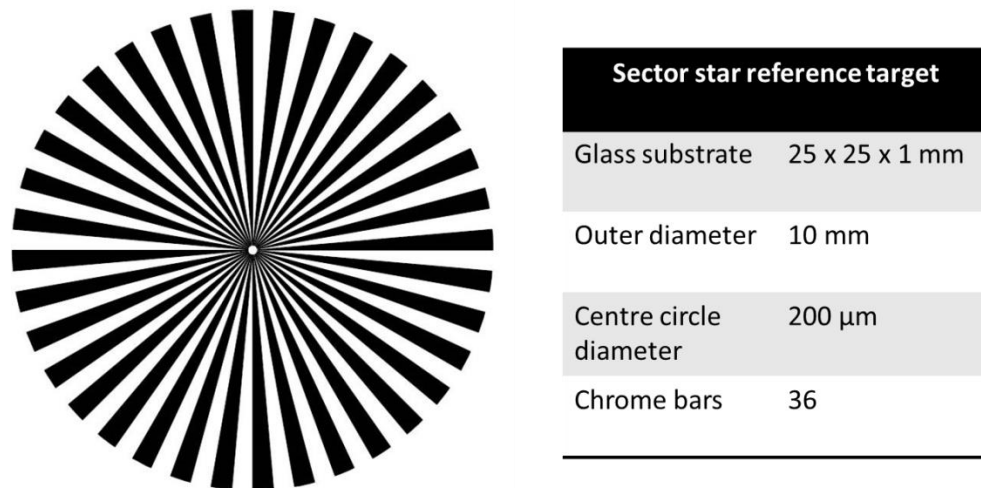

Sector star reference target	
Glass substrate	25 x 25 x 1 mm
Outer diameter	10 mm
Centre circle diameter	200 μm
Chrome bars	36

Figure 5.40. Diagram of the sector star target.

Several scans of the sector star test reference target were performed in different water types. The wavelengths were selected on the basis of the minimum of attenuation for the particular medium used, and the average optical power was increased to take account of the increased scattering. Images of 150×150 pixels with a per-pixel acquisition time of 10 ms were taken, and the results are shown in Figure 5.41, in (a) for clear water ($\lambda = 525$ nm, average power $= 10$ nW), in (b) for water and 0.003% of Maalox ($\lambda = 585$ nm, average power $= 720$ nW), in (c) for water with 0.01% of Maalox ($\lambda = 690$ nm, average power $= 260$ μW), and in (d) for water with 0.012% of Maalox ($\lambda = 690$ nm, average power $= 950$ μW). For each of these environments, Figure 5.41 shows the intensity map and the graph of the number of counts in the pixel line closest to the sector star centre, where distinct peaks are still resolved. Every peak in the graph corresponds to a chrome bar, and this line is shown in light blue in the intensity maps.

Once the distance between this pixel line and the centre of the sector star was determined, the spatial resolution was evaluated as the thickness of one bar at that distance using the Equation 5.2. With this configuration, the spatial resolution was estimated to be approximately 100 µm, corresponding to an angular resolution of approximately 60 µrad, for the target placed over a range between 0.2 and 8 attenuation lengths from the transceiver.
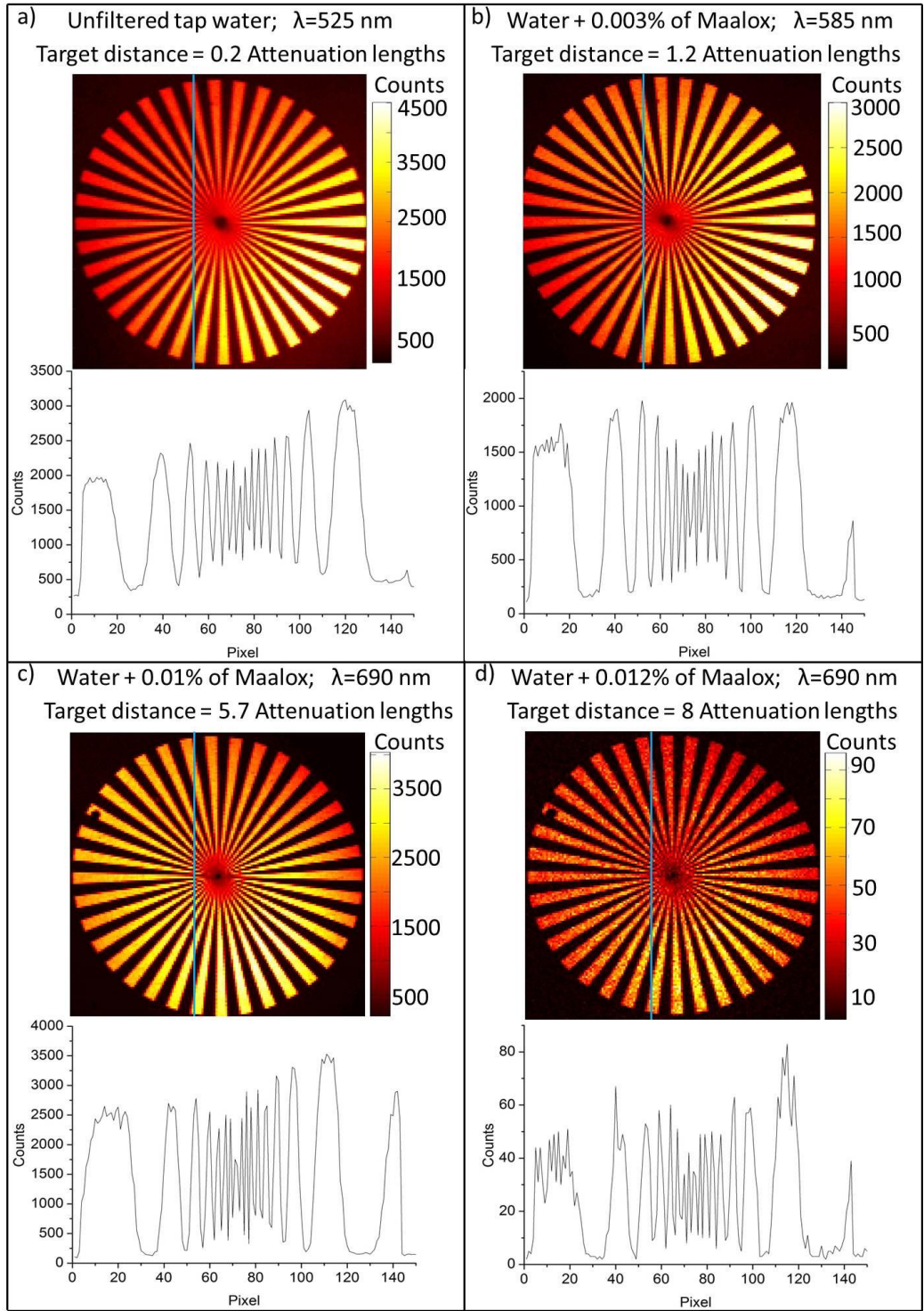
Figure 5.41. The images show 150 × 150 pixel intensity maps of the sector star reference target at the four attenuation lengths of (a) 0.2, (b) 1.2, (c) 5.7 and (d) 8. Below each of these intensity maps is a plot of the number of counts per pixel for the indicated vertical line on the corresponding intensity map. The position of the line was chosen such that the number of counts for the peak corresponding to the narrowest bar width was at least twice that of the adjacent trough i.e. the change between the peak and the trough was still clearly discernible.

The spatial resolution appeared not to be affected by these large changes in scattering level. It is likely that the limited field of view afforded by the transceiver unit allows exclusion of the forward scattered light which is ordinarily expected to degrade the image in scattering media [18, 19].

In the most general case, three contributions to scattering occur in a turbid environment, and a schematic representation is shown in Figure 5.42. The first component is multiple backscattered light, which is light that has not interacted with the target but it is scattered back to the receiver because of the turbidity of the medium. The second contribution is the common volume backscatter, caused by the overlap of the outgoing light and the receiver field of view. The third component is the forward scattered light, which is light slightly deviated while travelling from the source to the target, and on the way back to the receiver. Forward scattered light causes the image to be blurred, reducing its resolution. However, from the figure it can be seen that a narrow field of view limits the detection of forward scattered light, limiting the loss of resolution.
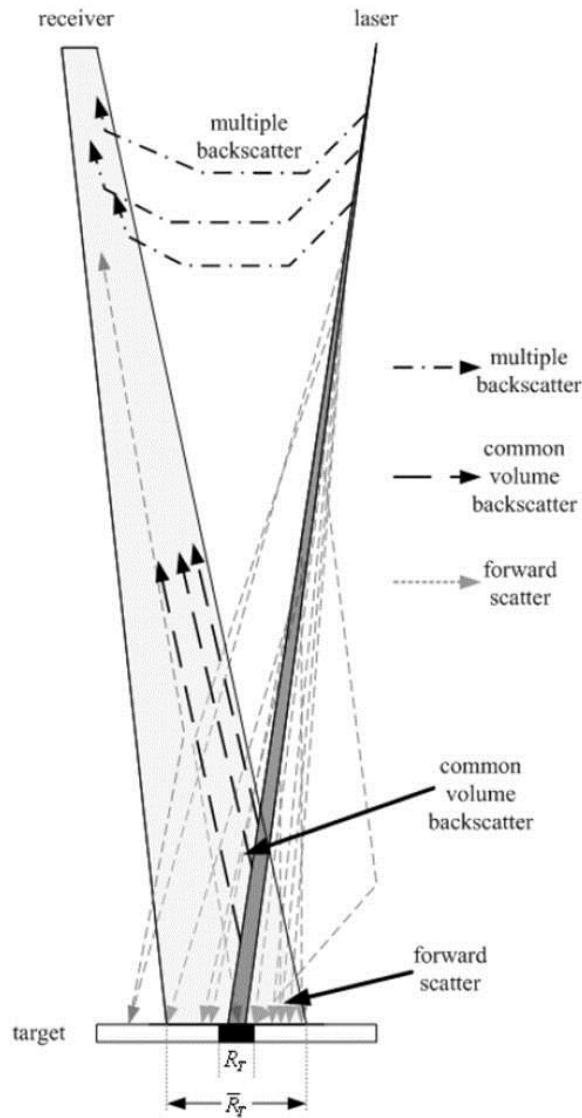
Figure 5.42. Schematic representation of scattered light. From [20].

The system described in this Thesis has coaxial transmit and receive channels, meaning that multiple backscatter and common volume backscatter components coincide. The gated detection scheme prevents most of these events being detected, therefore they do not contribute to the overall count rate of the system. However, the common volume between transmitted light and light scattered by the target is minimised, thanks to the transmitted light being focused on the target and the narrow field of view of the system, reducing even more the backscatter component. In addition, the narrow field of view limits the detection of forward scattered light, resulting in no degradation of the image even in highly scattering environments.

This illustrates a clear advantage of scanning systems of this type which inherently spatially filter out the forward scattered return signal, mainly detecting light scattered by

the target into the system and excluding most of the light scattered by the transmission medium. This allowed high resolution imaging even at stand-off distances of several attenuation lengths.

5.14   Depth resolution

Several scans of a pillar target were performed in different environments in order to investigate the depth resolution of the system. The pillar target is a custom-designed target, which was used to investigate the depth resolution of the system. The design was performed by Dr. Aongus McCarthy and other members of the group, and a CAD model is shown in Figure 5.43. The target consists of a progression of 5 pillars on a radial line, each having the same height but different diameters, as specified in the figure. There are 6 radial lines of pillars, whose height follows the geometrical progression shown in red in Figure 5.43. The same configuration was adopted for the set of holes placed in a specular position in the target. The target was 3D printed and cleaned to remove all the supporting material for the printer. Then it was treated with a plastic primer and painted with a white spray paint for cars, which has a good resistance to water.
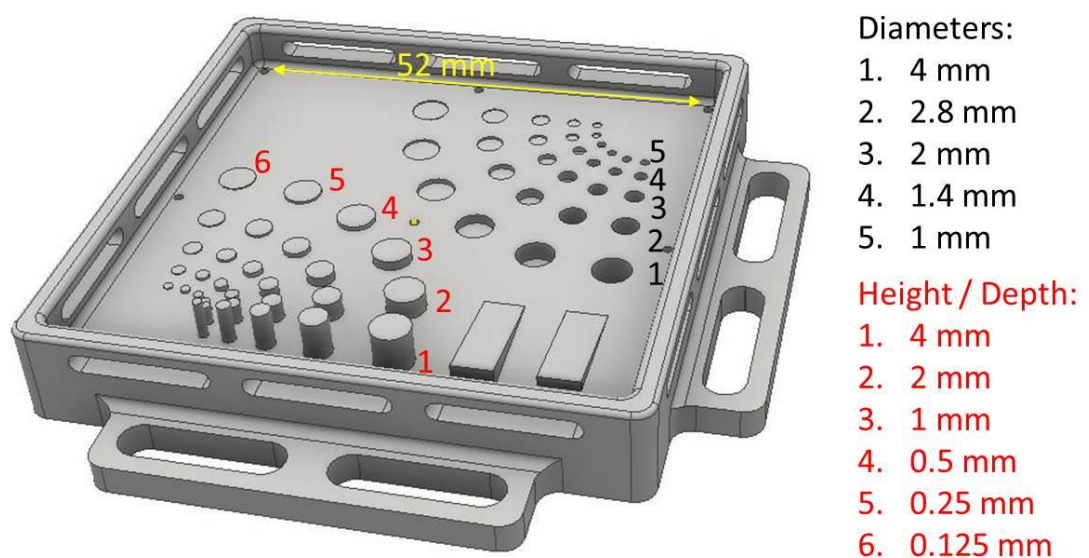

Figure 5.43. CAD model of the pillar target.

The experimental setup presented in section 0 was chosen for this study, since the overall instrumental response of this configuration was greatly affected by the response of the laser source, which can be dependent on the input current settings. Therefore, a

low average optical power was used in order to not increase the pulse width duration, as discussed in section 0. However, a low average optical power meant also a low return from the target. The combination of these issues put a limit to the depth resolution that could be achieved with this configuration, since the uncertainty $\bar{\sigma}$ in the depth estimation depends on the number of integrated counts N and the timing jitter of the system σ by means of [15]

$$\bar{\sigma} = \frac{\sigma}{\sqrt{N}}$$

<div align="right">Equation 5.4</div>

Three examples are reported in Figure 5.44, showing 130×130 pixel depth maps obtained in three environments, when a 2 ps bin width was selected for the timing histogram, meaning a minimum depth resolution of approximately 300 μm can be resolved. In Figure 5.44a), the target was placed at a stand-off distance of approximately 1.7 metres in unfiltered tap water, equivalent to 0.8 attenuation lengths. An average optical power of 24 nW was used with 10 ms acquisition time per pixel. In this case, a depth up to 500 μm can be resolved, which was the smallest target detail that could be resolved using this pillar target and the bin width selected. The scan of the pillar target was performed in water with 0.01% of Maalox, equivalent to a stand-off distance of 6 attenuation lengths, increasing the acquisition time per pixel to 100 ms (Figure 5.44b). The average optical power was 84 μW, meaning that the instrumental response of the system presented only one peak in the histogram. This configuration meant that the depth resolution was preserved at 500 μm, although it came at the cost of a longer acquisition time. The same scan was performed in water with 0.012% of Maalox, equivalent to a stand-off distance of 8 attenuation lengths (Figure 5.44c), showing how the depth resolution is degraded by the attenuation of the environment. A depth up to 2 mm is clearly discernible from the depth map, while the 1 mm high pillars are barely visible.
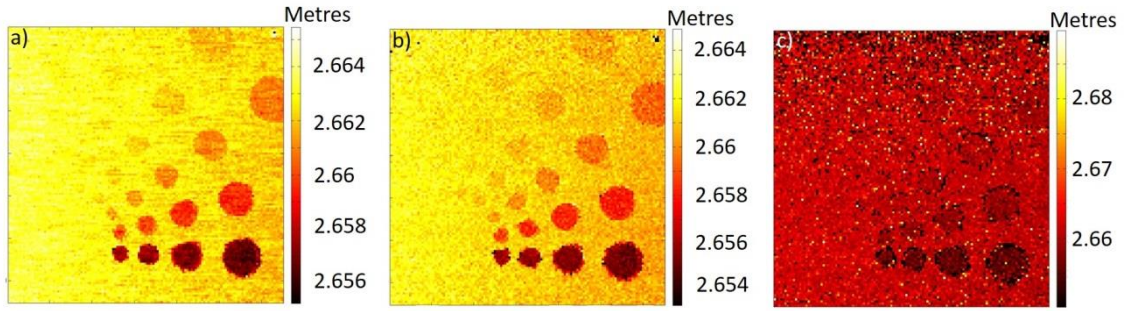
Figure 5.44. 130 × 130 pixel depth maps of the pillar target obtained in unfiltered tap water, equivalent to (a) 0.8 attenuation lengths, using an acquisition time per pixel of 10 ms and an average optical power of 24 nW. The scan was repeated using 100 ms acquisition time per pixel and 84 μW (b) in water with 0.01% of Maalox, equivalent to 6 attenuation lengths, (c) and in water with 0.012% of Maalox, equivalent to 8 attenuation lengths.

These examples established a higher limit to the depth resolution achievable, which is strictly related to the instrumental response of the system, the attenuation of the environment, and the parameters chosen for the scan, therefore, a different configuration may improve the achievable depth resolution.

For completeness, the depth resolution of the system was investigated in water with 0.016% of Maalox, equivalent to a target stand-off distance of 9 attenuation lengths. In this case, a higher average optical power was needed in order to obtain a return from the target high enough to resolve some of the pillars. Hence, the system described in section 5.10 was used for this study, and a 130 × 130 pixel scan was performed using 100 ms acquisition time per pixel and an average optical power of approximately 860 μW. The results are reported in Figure 5.45, where the effect of scattering is clearly visible, causing the return to be insufficient to estimate the depth with the cross-correlation approach for many of the pixels. Because of the sparse photon return, only the 4 mm high pillars were resolved in this case, while the 2 mm high pillars are barely visible.
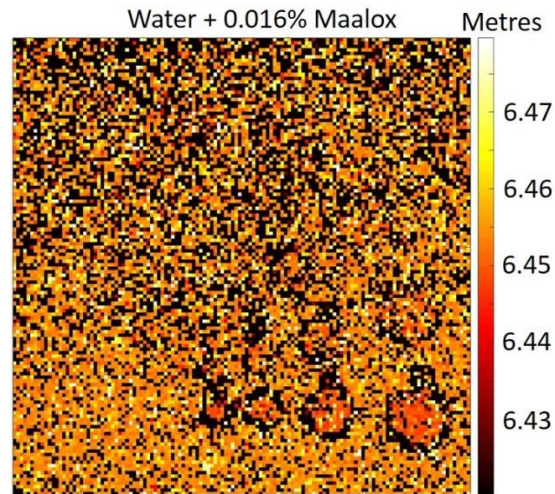
Figure 5.45. 130 × 130 pixel depth maps of the pillar target obtained in water with 0.016% of Maalox, equivalent to 9 attenuation lengths between system and target, using an acquisition time per pixel of 100 ms and an average optical power of 860 µW.

5.15 Conclusions

The investigations reported in this chapter show the potential for depth imaging systems using time-correlated single-photon counting to obtain depth profiles of targets in different underwater environments, in low and high levels of scattering. Lab-based measurements were performed over distances of less than two metres, and several depth profiles were acquired at stand-off distances of up to 9 attenuation lengths. To the best of the author's knowledge, this is the longest stand-off distance achieved underwater with a monostatic optical system.

In all cases, one operational wavelength was selected for each environment, in order to minimize the attenuation of light due to absorption and scattering. The use of a supercontinuum laser source allowed the tuning of the operational wavelength to the environment where the scan was performed.

Several configurations were studied in order to optimise the performance of the system and investigate its limitations. Preliminary measurements were performed using a thick junction SPAD detector in a free-running mode, meaning that back-reflections from the transceiver unit were detected. This limited the average optical power that could be used to the sub-microwatt region. If high optical powers are used when the detector is in free-running mode, the back reflection can saturate the single-photon detector and

prevent detection of the returns from the target. However, these preliminary measurements showed promise from the point of view of measuring depth profiles of targets in highly attenuating environments. Therefore, several modifications were implemented to improve the performance of the system. A gated detection scheme was used in order to avoid the detection of the back-reflections from the transceiver unit and allow higher average optical power. Gated detectors offer the opportunity to temporarily deactivate the detector during the expected arrival time for photons from the back-reflections so that higher optical powers may be used. In order to implement this configuration, the thick junction single-photon detector was replaced with a thin junction SPAD detector, offering a better temporal response even if this came at the cost of a slightly lower detection efficiency. This configuration allowed significantly higher average optical powers to be used, providing a better SNR and faster data acquisition. Several scans were performed placing the target at stand-off distances up to 6 attenuation lengths, and high resolution scans were achieved in several scattering conditions, but at the cost of long overall acquisition times.

More modifications were made to the system to further improve its performance. Firstly, the average optical power was optimised acting on the polarising orientation lock ring of the photonic crystal fibre coupling the AOTF to the transceiver unit, allowing to increase the power up to approximately $800\,\mu W$. Secondly, the data were acquired in T3 mode with the HydraHarp TCSPC module, which meant less complicated electronics and less data storage memory to use, allowing a greater number of pixels to be recorded. In addition, the optical configuration in the transceiver unit was improved including relay lenses with higher performance. These improvements allowed scans of the plastic pipe target to be taken at stand-off distances up to 9 attenuation lengths. In all cases the overall acquisition time was in the range of minutes, which is too long a duration for most applications in the field. In general, appropriate combinations of pixel format, acquisition time per pixel, and average optical power, can be used to minimise the overall acquisition time of the scans. However, the analysis was performed with the pixel-wise cross-correlation approach, without any attempt to perform spatial correlations. Image processing using spatial correlations can help in reconstructing the image with far fewer photons, allowing much reduced acquisition times, as will be discussed in Chapter 6.

In most of the cases, average optical powers in the sub-milliwatt range were used. In addition, higher power levels were investigated and scans were performed using an average optical power of approximately 2.6 mW. This allowed high resolution scans of the plastic pipe to be taken at 8 attenuation lengths, showing detailed features of the target. At 9 attenuation lengths, depth scans were possible but the depth resolution was not preserved due to the high level of scattering which reduced the SNR. For completeness, the scans at 8 and 9 attenuation lengths were performed also using an average optical power up to only $200\,\mu W$. This allowed the depth profiling of the plastic pipe target to be estimated using the pixel-wise cross-correlation approach, at up to 9 attenuation lengths, although in this last case the intensity map does not provide enough information to discern the target. However, these results clearly illustrate that the TCSPC technique allows scans with low optical power levels in highly scattering environments.

Scans were performed also placing the target at 10 attenuation lengths. However, because of the high background and the strong light attenuation, the cross-correlation approach did not recover the shape of the target. The main limitation seemed due to a background component introduced by the detector and dependent on the count rate, which could be related to afterpulsing [17]. This effect in conjunction with the high level of scattering, detected secondary back-reflections which contributed to the overall count rate, and the highly attenuated return from the target, reduced drastically the SNR, meaning that the plastic pipe target could not be imaged at a stand-off distance of 10 attenuation lengths. However, it would be interesting to investigate the case of the target placed at 10 attenuation lengths with no secondary back-reflections detected. Future work will investigate longer range depth images and new transceiver designs which are both likely to reduce the back-reflection issue. In addition, it has to be noted that the number of attenuation lengths between system and target was increased acting only on the scattering properties of the medium, adding Maalox to unfiltered tap water. This means increasing the scattering albedo of the medium, defined as the ratio between the amount of scattering and overall attenuation [21]. As a consequence, the medium glows when high average optical powers and high concentrations of Maalox are used, resulting in a high background level. The scattering albedo of natural sea water is lower than the environments considered in this Thesis. Therefore, it is worth investigating the case of scans performed at 10 attenuation lengths in an environment characterised by a low scattering albedo. This experiment can be performed using the system described in

section 5.11, adding an appropriate dye to unfiltered tap water and Maalox, in order to better simulate open-sea water conditions. In this case, the lower expected background may permit increased SNR at a stand-off distance of 10 or more attenuation lengths. However, in a real underwater environment, ambient light should also be considered as another component which increases the background level. In this case, an appropriate combination of optical filters can be included into the transceiver unit, in order to minimise this ambient background.

Estimations of spatial and depth resolution were performed, and the results show that in unfiltered tap water and medium level of scattering the system allowed estimations of the depth of details up to 500 µm. It is worth noting that because of the timing bin width selected in the TCSPC module corresponded to a depth of approximately 300 µm. The target used for this study was formed by a geometrical progression of pillars, and no pillars with height between 500 µm and 250 µm were included. It is likely that a different geometrical progression in the target may allow the resolution of a pillar of less than 500 µm, under the same conditions. However, increasing the level of scattering of the medium, the achievable depth resolution decreased to few millimetres, mainly due to the low return from the target. It is important to say that this study was performed with the configuration characterised by the lower average optical power investigated in this Thesis. Therefore, the worst case considered in this chapter was investigated, establishing a lower limit for the achievable depth resolution. At the same time, studies of spatial resolution showed that an angular resolution of approximately 60 µrad can be achieved in water samples with a high scattering level. There appeared to be only a little degradation in spatial resolution as a result of increased scattering, most likely due to the limited field of view afforded by the scanning system, effectively excluding the forward scattered return signal, detecting the light scattered by the target and excluding most of the light scattered by the transmission medium.

With appropriate reconfiguration, the transceiver unit can operate with a detector array [14], instead of the individual SPAD detector. This approach may improve the overall acquisition time, as the image of the target can be obtained with a pixel format equal to the array dimensions or by using structured illumination of the target. However, this entails illuminating a wider area of the target, meaning the use of a higher average optical power. In addition, the field of view in this case would be much wider than the case considered in this Thesis, hence it is likely that the forward and backscattered

radiation will degrade contrast and spatial resolution. Therefore, such a configuration may have the advantage of fast acquisition times but at the cost of shorter achievable ranges.

References

1. A. McCarthy, R. J. Collins, N. J. Krichel, V. Fernandez, A. M. Wallace, and G. S. Buller, "Long-range time-of-flight scanning sensor based on high-speed time-correlated single-photon counting," Appl. Opt. **48**, 32, 6241-6252 (2009).

2. N. J. Krichel, A. McCarthy, I. Rech, M. Ghioni, A. Gulinatti, and G. S. Buller, "Cumulative data acquisition in comparative photon-counting three-dimensional imaging," J. Mod. Opt. **58**, 3-4, 244-256 (2011).

3. A. McCarthy, X. Ren, A. Della Frera, N. R. Gemmell, N. J. Krichel, C. Scarcella, A. Ruggeri, A. Tosi, and G. S. Buller, "Kilometer-range depth imaging at 1550 nm wavelength using an InGaAs/InP single-photon avalanche diode detector," Opt. Express **21**, 19, 22098-22114 (2013).

4. A. M. Wallace, A. McCarthy, C. J. Nichol, X. Ren, S. Morak, D. Martinez-Ramirez, I. H. Woodhouse, and G. S. Buller, "Design and evaluation of multispectral LiDAR for the recovery of arboreal parameters," IEEE Trans. Geosci. Remote Sens. **52**, 13 (2014).

5. C. P. Barrett, P. Blair, G. S. Buller, D. T. Neilson, B. Robertson, E. C. Smith, M. R. Taghizadeh, and A. C. Walker, "Components for the implementation of free-space optical crossbars," Appl. Opt. **35**, 8, 4942-4954 (1996).

6. J. M. Dudley, and S. Coen, "Coherence properties of supercontinuum spectra generated in photonic crystal and tapered optical fibers," Opt. Lett. **27**, 13, 1180-1182 (2002).

7. J. M. Dudley, G. Genty, and S. Coen, "Supercontinuum generation in photonic crystal fiber," Rev. Mod. Phys. **78**, 4, 1135-1184 (2006).

8. N.K.T. Photonics, "SuperK EXTREME - Datasheet."

9. M. Wahl, and S. Orthaus-Müller, "Time tagged time-resolved fluorescence data collection in life sciences," (PicoQuant, 2015).

10. PicoQuant, "PicoHarp 300 - User's Manual and Technical Data (Software Version 2.3)."

11. PicoQuant, "HydraHarp 400 - User's Manual and Technical Data - Software Version 2.1."

12. Labsphere, "Technical guide - Reflectance Materials and Coatings."

13. G. S. Buller, R. D. Harkins, A. McCarthy, P. A. Hiskett, G. R. MacKinnon, G. R. Smith, R. Sung, and A. M. Wallace, "Multiple wavelength time-of-flight sensor based on time-correlated single-photon counting," Rev. Sci. Instrum. **76**, 8, 083112 (2005).

14. X. Ren, "Advanced photon counting techniques for long-range depth imaging," in *School of Engineering and Physical Sciences* (Heriot-Watt University, Edinburgh, UK, 2015).

15. S. Pellegrini, G. S. Buller, J. M. Smith, A. M. Wallace, and S. Cova, "Laser-based distance measurements using picosecond resolution time-correlated single-photon counting," Meas. Sci. Technol. **11**, 712-716 (2000).

16. D. T. Neilson, S. M. Prince, D. A. Baillie, and F. A. P. Tooley, "Optical design of a 1024-channel free-space sorting demonstrator," Appl. Opt. **36**, 35, 9243-9252 (1997).

17. P. A. Hiskett, G. S. Buller, A. Y. Loudon, J. M. Smith, I. Gontijo, A. C. Walker, P. D. Townsend, and M. J. Robertson, "Performance and design of InGaAs/InP photodiodes for single-photon counting at 1.55 mm," Appl. Opt. **39**, 36, 6818-6829 (2000).

18. B. Cochenour, S. O'Connor, and L. Mullen, "Suppression of forward-scattered light using high-frequency intensity modulation," Opt. Eng. **53**, 5, 051406 (2014).

19. J. S. Jaffe, "Underwater optical imaging - The past, the present, and the prospects," IEEE J. Oceanic Eng. **40**, 1-18 (2015).

20. F. R. Dalgleish, F. M. Caimi, W. B. Britton, and C. F. Andren, "Improved LLS imaging performance in scattering-dominant waters," in *Ocean sensing and monitoring*, SPIE, ed. (2009).

21. B. Cochenour, L. Mullen, and J. Muth, "Effect of scattering albedo on attenuation and polarization of light underwater," Opt. Lett. **35**, 12, 2088-2090 (2010).

Chapter 6

Image reconstruction and reflectivity restoration using spatial correlations

6.1. Introduction

Several algorithms based on spatial correlations were developed in order to investigate a number of approaches for three-dimensional image reconstruction aimed both to reduce the overall acquisition time of a scan, and improve the results obtained under highly scattering conditions. This chapter will show three different methods which allow for the reconstruction of depth and intensity images by means of exploiting spatial correlations between neighbouring pixels. Section 6.2 describes a model which performed spatial correlations over the depth and intensity maps formed using the pixel-wise cross-correlation approach. Section 6.3 will describe two other approaches that utilise spatial correlations to analyse similar data.

6.2. Image reconstruction with Discrete Cosine Transform method

The results presented in Chapter 5 show the potential for depth imaging using the TCSPC technique and time-of-flight approach to obtain depth profiles of targets at stand-off distances equivalent to up to 9 attenuation lengths. Additionally, it was demonstrated that short overall acquisition times can be obtained by varying the average optical power and pixel format. However, in highly attenuating environments, longer acquisition times are typically required in order to obtain a good reconstruction of the image of a target with the pixel-wise cross-correlation approach, and long acquisition times may be difficult to implement in real underwater environments. In this case, additional analysis may help to restore the degraded image and reconstruct the depth and intensity images.

An algorithm was developed in collaboration with Rachael Tobin and Dr. Abderrahim Halimi from the Single-Photon Group, in order to investigate the effects of shorter measurement acquisition times on image quality. This algorithm was based on the sparseness of the Discrete Cosine Transform (DCT) domain.

In general, the DCT based approach is able to reconstruct an array f of length N as follows [1]:

$$dct_f\left(k\right) = w\left(k\right)\sum_{n=1}^{N} f\left(n\right)\cos\left(\frac{\pi}{2N}\left(2n-1\right)\left(k-1\right)\right), \quad k = 1, 2, ..., N \qquad \text{Equation 6.1}$$

With the coefficients $w(k)$ being

$$w\left(k\right) = \begin{cases} \dfrac{1}{\sqrt{N}}, & k = 1 \\ \sqrt{\dfrac{2}{N}}, & 2 \le k \le N \end{cases} \qquad \text{Equation 6.2}$$

Equation 6.1 and 6.2 can be implemented in Matlab, by use of a built-in function in the software. Typically, very few DCT coefficients are needed to reconstruct the original sequence. For example, Figure 6.1 shows an arbitrary array f in blue, representing a triangular function. The array was constructed as a function of the variable a, which varies in the range $1 - 200$ with a unitary step. The curve in orange in Figure 6.1 represents the reconstruction with the DCT based approach of the array f. In this example only three coefficients were used to reconstruct the simulated array. Despite this triangular function is a very difficult problem for the reconstruction, as it is characterised by sharp edges, the DCT based approach allows to restore the triangular function. Similarly, most of the depth and intensity images shown in this Thesis present several sharp edges, and the DCT based approach may help in the reconstruction of the image.
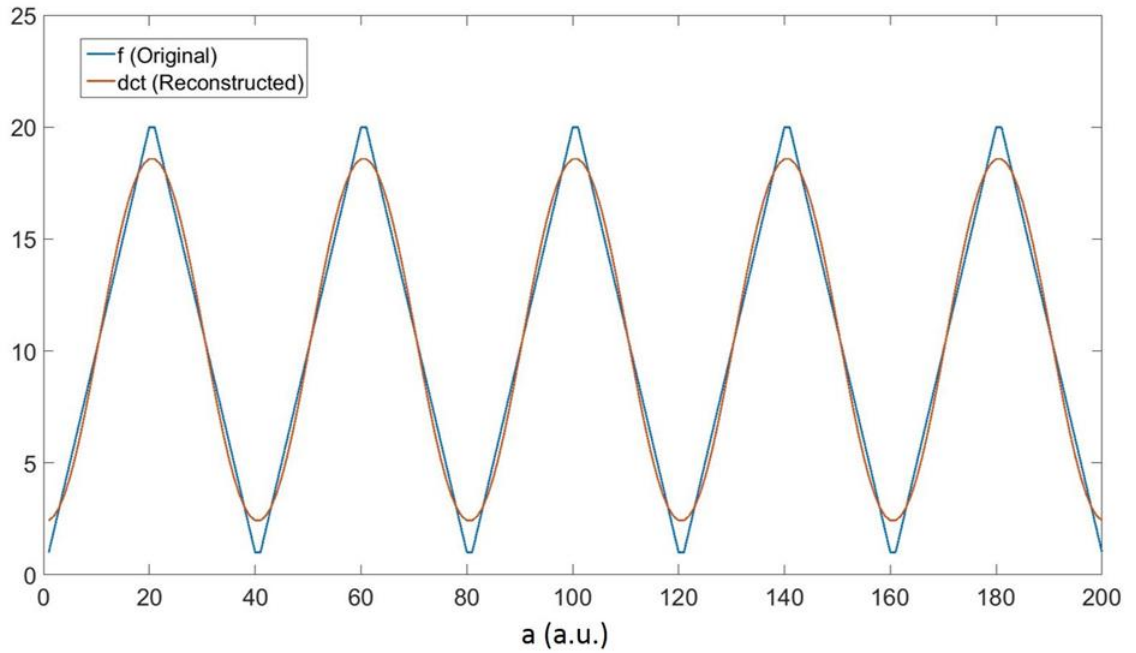
Figure 6.1. Example of array reconstruction with the DCT approach. The function in blue is a simulated array representing a triangular function of the variable a. The array in orange is the DCT function of the array.

When the DCT based method described by Equation 6.1 and 6.2 is applied to a matrix, each column of the matrix is treated as an independent array. Alternatively, the DCT based method can be applied in two dimensions, meaning that the same approach is followed for each column and then for each row of the matrix. For the two-dimensional case, a built-in function is also available in Matlab and was used in the script. In the results reported in this section, the DCT function is calculated in two dimensions on the depth and intensity maps.

The main structure of the algorithm is presented in Figure 6.2, while Figure 6.3 shows an example of processed images generated at the three main steps of the algorithm. In this example, the plastic pipe target was placed at a stand-off distance of 8 attenuation lengths. A 200×125 pixel scan was obtained using an average optical power of approximately $640\,\mu W$, and an acquisition time per pixel of $50\,ms$. In order to investigate shorter acquisition times and test the algorithm presented in this section, an acquisition time per pixel of $5\,ms$ was extracted from the original scan. Firstly, the depth was estimated with the pixel-wise cross-correlation approach (Figure 6.3a), as explained in section 5.5. Then, a median filter was applied on the depth map,

employing a 3×3 neighbourhood filter (Figure 6.3b). The median filter replaced the value of each pixel with the median value of 3×3 neighbouring pixels, thus including the original value in the calculation [2]. This allowed the exclusion of some of the noise in the image, and corrected spurious pixels without introducing a significant reduction in spatial resolution.
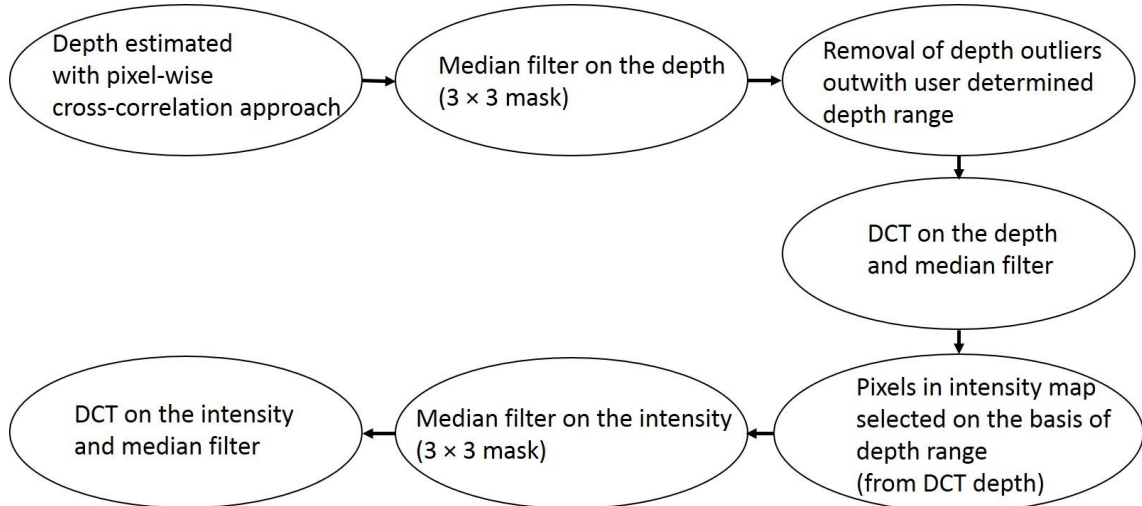

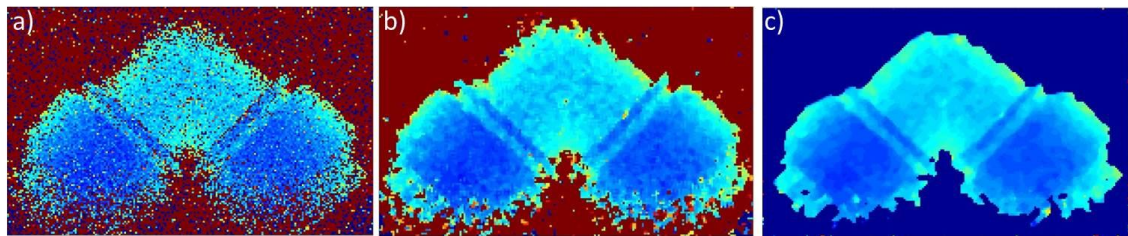Figure 6.2. Diagram of the operations performed by the algorithm to reconstruct the image.

Figure 6.3. A depth map of a 200 × 125 pixel scan of the plastic pipe target, performed in water with 0.012% of Maalox, equivalent to a stand-off distance of 8 attenuation lengths. An extracted 5 ms acquisition time per pixel was used, with an average optical power of 640 μW at the operational wavelength λ = 690 nm. The figure shows the depth map obtained with (a) the pixel-wise cross-correlation approach; then (b) median filtered over 8 neighbouring pixels and (c) after applying the DCT based model followed once again by the median filter.

The depth data obtained with the cross-correlation approach and corrected with the median filter are then restricted to a user-defined depth range. This is because as the acquisition time is reduced, an increasing number of histograms will contain such a

164

small number of events that only a few bins have a single event, while the bins corresponding to the target position are empty. An example is shown in Figure 6.4, which illustrates a histogram at a short acquisition time of 0.5 ms when the target is placed at a stand-off distance of 8 attenuation lengths. The figure shows in red the timing window where the return from the target is expected, which is empty. In this example, only a few bins have a single event, but they are outside the timing window of interest. In this case, the software performs the cross-correlation which, by default, will assign the depth value to the first non-empty bin. In the case for data shown in Figure 6.4, this will provide a depth value well outside of the expected range of interest and an over-estimation of the intensity.
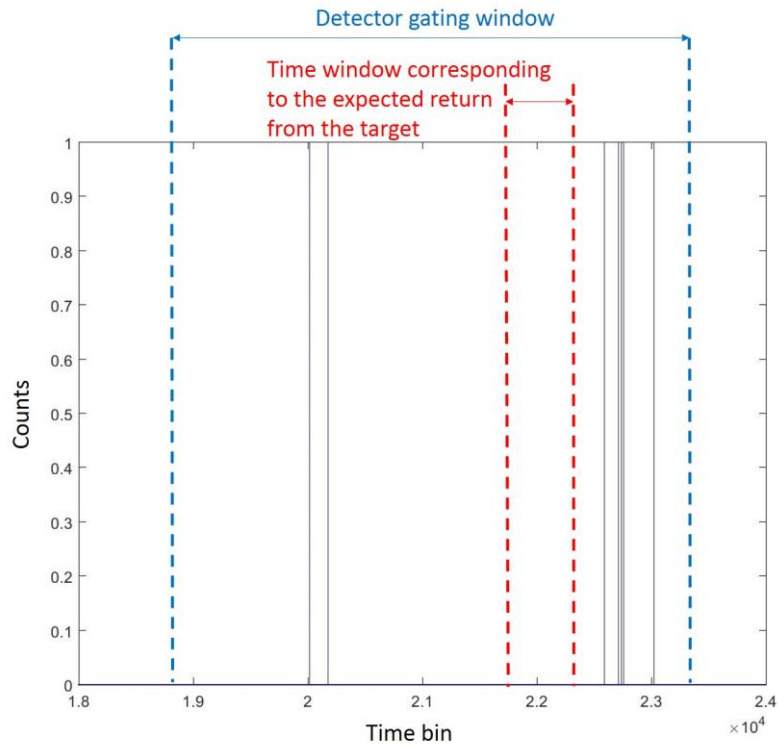

Figure 6.4. Example of histogram at the short acquisition time of 0.5 ms when the target is placed at a stand-off distance of 8 attenuation lengths. The dashed blue lines show the electrical gating window of the detector, and the dashed red lines show the time window where the return from the target is expected. The example shows that for short acquisition times some of the histograms may contain a low number of events, such that only a few bins have a single event and the bins corresponding to the target position are empty. This will lead to a cross-correlation peak positioned at the arrival time of the first photon event, causing both an erroneous depth and, possibly, an incorrect value for intensity.

It is worth noting that this range gating is different from the software gating explained in section 5.10, where the histogram was gated *before* calculating the cross-correlation.

The next step of the algorithm was calculating the DCT of the median filtered depth map keeping only two coefficients. Once the depth is reconstructed using the DCT based model, the aforementioned median filter is performed again in order to further smooth the image (Figure 6.3c).

Figure 6.5 shows the results of the algorithm on the intensity map. In particular, Figure 6.5a) shows the intensity map obtained by summing the events over a range of 30 bins centred on the highest value of the cross-correlation. By analysing the resulting reconstructed depth profile, pixels within a user-defined depth range are used to select the corresponding pixels in the intensity map on which to perform the same algorithm. Then the steps described previously are followed: the 3×3 neighbourhood median filter is performed on the intensity map (Figure 6.5b), the result is used to apply the DCT based model, and the median filter is applied once again (Figure 6.5c).
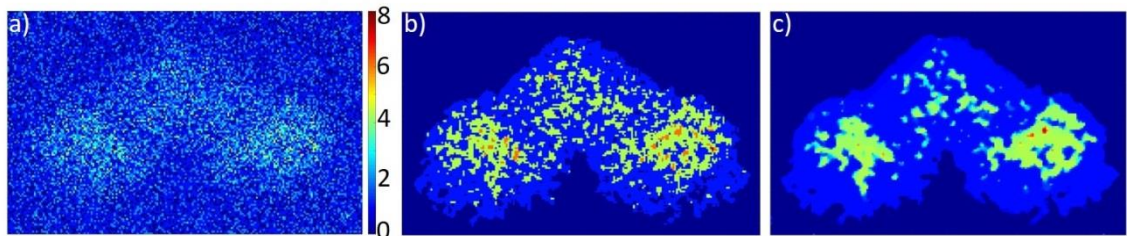

Figure 6.5. Intensity map of a 200×125 pixel scan of the plastic pipe target, performed in water with 0.012% of Maalox, equivalent to a stand-off distance of 8 attenuation lengths. An extracted 5 ms acquisition time per pixel was used, and an average optical power of 640 μW at the operational wavelength $\lambda = 690$ nm. The figure shows three different steps of the algorithm: (a) the intensity map obtained by summing the number of counts over 30 bins range centred on the highest value of the cross-correlation; (b) the intensity map obtained by selecting the pixels with the appropriate depth range and then median filtered over 8 neighbouring pixels; (c) the intensity map obtained by applying the DCT based model and a further application of the median filter.

From the results, it can be seen that the depth is reconstructed well, preserving millimetre sized features of the target. However, only the shape of the target can be obtained from the intensity map, mainly because of the low SNR in this case. It is important to note that this method permitted a reduction in the overall acquisition time from approximately 20 minutes to 2 minutes, showing how spatial correlations can be used to improve the results of scans with shorter acquisition times.

In order to further reduce the overall acquisition time, the same algorithm was applied to a 240×240 pixel scan of a section of the plastic pipe target placed at a stand-off distance of 8 attenuation lengths. The scan was performed using a higher value of average optical power of 2.6 mW, and an acquisition time per pixel of 30 ms. A per-pixel acquisition time of 0.5 ms was then extracted from the original scan data, meaning an overall acquisition time of less than 1 minute. The results on the depth and the intensity are reported in Figure 6.6 and Figure 6.7, respectively.
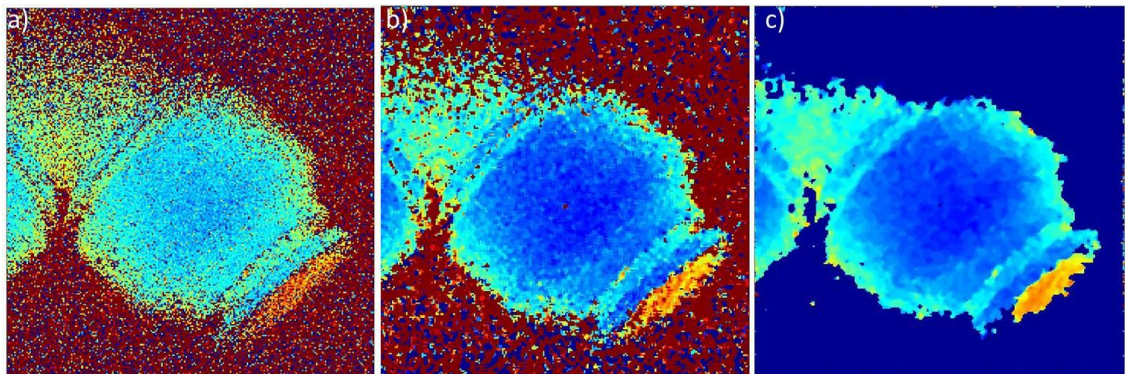

Figure 6.6. Depth map of a 240×240 pixel scan of the plastic pipe target, performed in water with 0.012% of Maalox, equivalent to a stand-off distance of 8 attenuation lengths. An extracted 0.5 ms acquisition time per pixel was used, with an average optical power of 2.6 mW. The figure shows (a) the depth map obtained using the pixel-wise cross-correlation approach, then (b) median filtered over 8 neighbouring pixels, and (c) after applying the DCT based model and again the median filter.
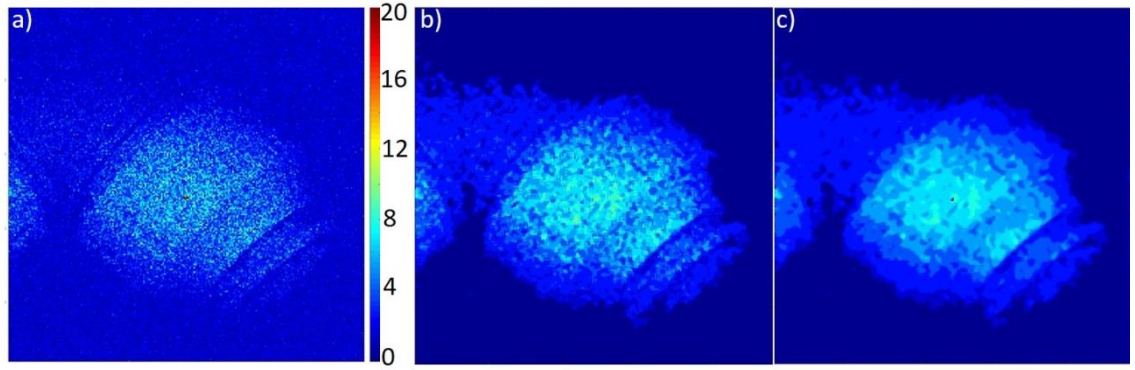
Figure 6.7. Intensity map of a 240 × 240 pixel scan of the plastic pipe target, performed in water with 0.012% of Maalox, equivalent to a stand-off distance of 8 attenuation lengths. An extracted 0.5 ms acquisition time per pixel was used, with an average optical power of 2.6 mW. The figure shows three different steps of the algorithm: (a) the intensity map obtained by summing the number of counts over a 30 bin range centred on the highest value of the pixel-wise cross-correlation; (b) the intensity map obtained by selecting the pixels with the appropriate depth range and then median filtered over 8 neighbouring pixels; (c) the intensity map obtained by applying the DCT based model and again the median filter.

The results show that using a higher average optical power allows the reconstruction of both depth and intensity, maintaining most of the details of the target whilst significantly reducing the overall acquisition time. To examine this further, a shorter acquisition time of 0.1 ms per pixel was extracted from the same scan data of Figure 6.6. The results obtained with the DCT based algorithm are shown in Figure 6.8 for the depth and in Figure 6.9 for the intensity. Due to the low level of returns, the pixel-wise cross-correlation approach is not able to estimate the depth for some of the pixels. This lack of information does not permit detailed reconstruction of the image with the DCT based method described in this section. However, the shape of the target can be recognised in both the depth and intensity maps reconstructed from the DCT based approach, whilst the pixel-wise cross-correlation approach is significantly less successful in reconstructing the intensity map, in particular.
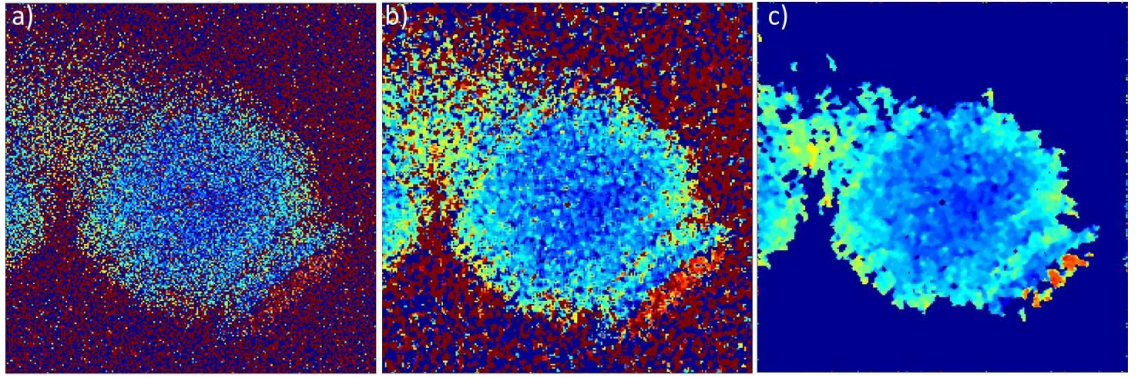
Figure 6.8. Depth map of a 240 × 240 pixel scan of the plastic pipe target, performed in water with 0.012% of Maalox, equivalent to a stand-off distance of 8 attenuation lengths. An extracted 0.1 ms acquisition time per pixel was used, with an average optical power of 2.6 mW. The figure shows (a) the depth map obtained using the pixel-wise cross-correlation approach, (b) then median filtered over 8 neighbouring pixels, and (c) after applying the DCT based model and again the median filter.
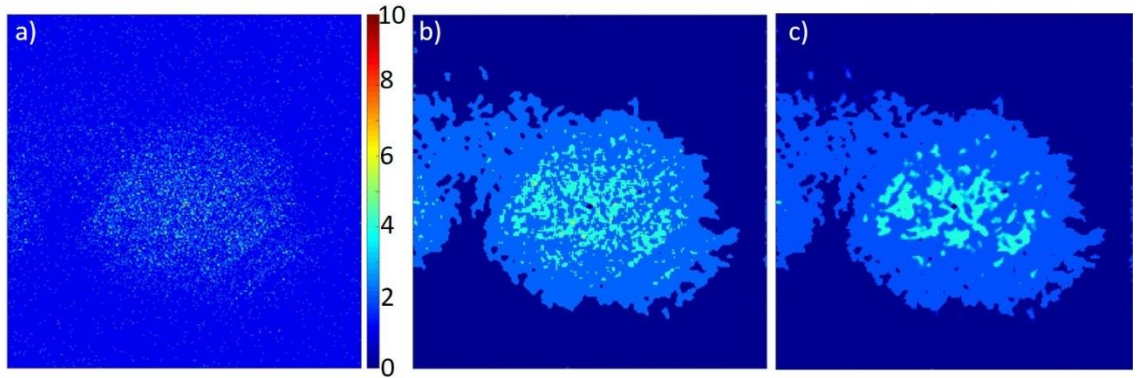

Figure 6.9. Intensity map of a 240 × 240 pixel scan of the plastic pipe target, performed in water with 0.012% of Maalox, equivalent to a stand-off distance of 8 attenuation lengths. An extracted 0.1 ms acquisition time per pixel was used, with an average optical power of 2.6 mW. The figure shows three different steps of the algorithm: (a) the intensity map obtained by summing the number of counts over a 30 bin range centred on the highest value of the cross-correlation; (b) the intensity map obtained by selecting the pixels with the appropriate depth range and then median filtered over 8 neighbouring pixels; (c) the intensity map obtained by applying the DCT based model and again the median filter.

169

A figure of merit describing a comparison between a reconstructed image and a reference image is the reconstruction-signal-to-noise-ratio (RSNR), defined as [3]

$$RSNR = 10\log_{10}\left(\frac{\|m\|^2}{\|m-\hat{m}\|^2}\right)$$

Equation 6.3

where m is the reference image, $\hat{m}$ is the reconstructed image, and $\|m\|^2$ is the norm given by $m^T m$, where m^T is the transpose of m. In the case of the proposed DCT based model, the RSNR was evaluated for several extracted acquisition times in order to perform a quantitative comparison between the reconstructed depth images at different acquisition times and a reference depth image. The scan considered for the comparison was the same used to obtain the results shown in Figure 6.6 and Figure 6.8. Due to the modifications applied to the depth map over several steps of the algorithm, it was only possible to compare the DCT depth images with a reference image in the same format. Therefore, the model was applied to the depth map with the longest acquisition time (t = 30 ms acquisition time per pixel) and the resulting DCT depth image was used as reference in Equation 6.3.

Figure 6.10 shows the RSNR evaluated for a range of acquisition times, varying from 0.01 to 1 ms acquisition time per pixel. As expected, the graph illustrates that the RSNR lowers as the acquisition time is reduced, in particular for acquisition times per pixel shorter than 0.05 ms.
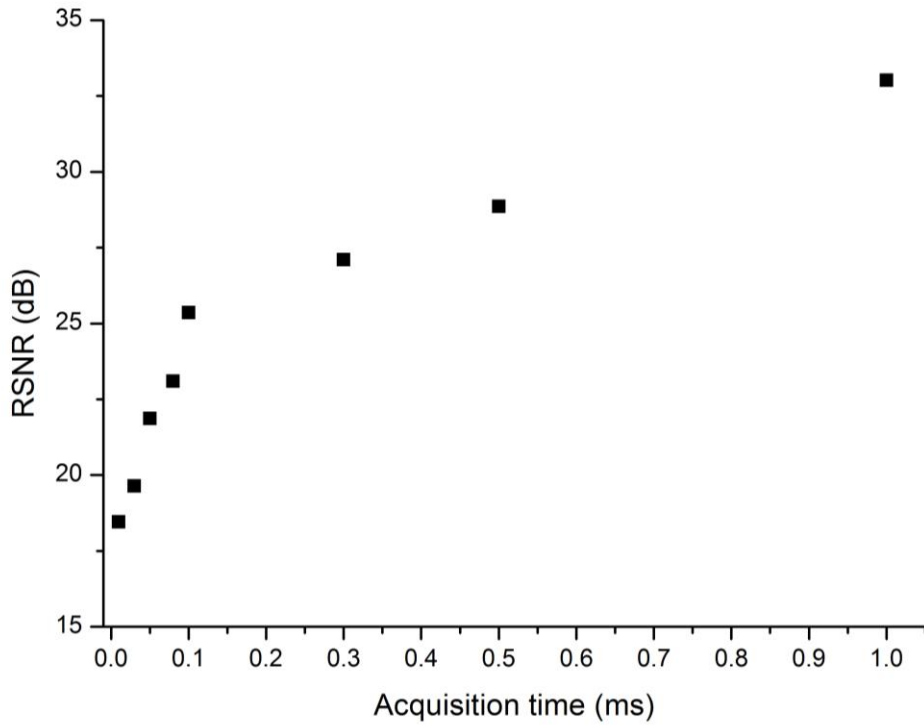
Figure 6.10. RSNR versus acquisition time comparing the DCT depth images at short acquisition time per pixel with the DCT depth obtained at 30 ms acquisition time per pixel.

Table 6.1 summarises the image quality as a function of acquisition time. Table 6.1 shows the DCT depth images as a function of acquisition time per pixel, the frame time, RSNR, and average detected photon events per pixel. From Table 6.1, it is important to note that the use of the DCT based model for image reconstruction allows the reduction of the overall acquisition time from approximately 30 minutes to few seconds, for example a 0.1 ms acquisition time per pixel means an overall acquisition time of approximately 6 seconds. In order to further reduce the time needed to perform the scan, a different pixel format can be selected. For example, a pixel format of 120×120 with an acquisition time per pixel of 0.1 ms leads to an overall acquisition time of 1.4 seconds, sufficiently short to allow implementation in a number of real underwater application scenarios.
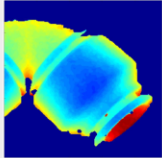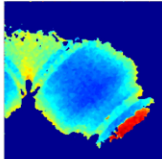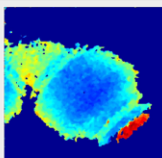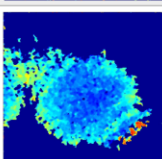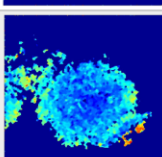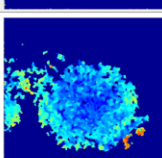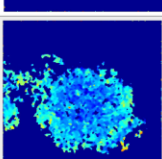
Acquisition time per pixel (ms)	Total acquisition time (seconds)	RSNR (dB)	Average number of photon events per pixel	DCT depth map
30	1728		127.09	
1	58	32.3	5.05	
0.5	29	28.3	2.79	
0.1	6	24.8	0.86	
0.05	3	24.5	0.63	
0.03	2	19.4	0.54	
0.01	0.6	18.2	0.45	

Table 6.1. The first column of the table shows the acquisition time per pixel. A 30 ms per pixel acquisition time was used to perform the scan of the plastic pipe target placed at a stand-off distance of 8 attenuation lengths, with an average optical power of 2.6 mW. The scans at shorter acquisition times were extracted by software from the scan with longest acquisition time (30 ms). The second column shows the overall acquisition time for each scan. The third column shows the reconstruction signal to noise ratio, obtained comparing the DCT depth map at each acquisition time with the DCT depth map obtained at 30 ms acquisition time per pixel (Figure 6.10). The fourth column shows the average number of photon events per pixel used to obtain the DCT depth map images shown in the last column.

Table 6.1 shows also the average number of photon events per pixel needed to obtain the DCT depth images in the last column. As stated above, the DCT was calculated from a starting point of depth data obtained with the cross-correlation approach and then restricted to a user-defined depth range to eliminate some of the depth results created by spurious scatters. In order to estimate the average number of events per pixel for each image, the same depth range was selected also in the DCT depth map. This allowed the removal of depth results due to scattering events that occur in pixels corresponding to optical field positions not occupied by the plastic pipe target. In the case of the results shown in Table 6.1, the depth range used was 4 cm. The use of this depth range allowed the selection of pixels with depth in the range of interest and in the area corresponding to the plastic pipe. As an example, the selection process is shown in Figure 6.11 for the case of 0.1 ms acquisition time, extracted from the scan discussed in Table 6.1 (performed using 2.6 mW average optical power, 240×240 pixel format, at a stand-off distance of 8 attenuation lengths). The same user-defined depth range is selected in the depth map obtained with the cross-correlation approach (Figure 6.11a) and the DCT depth map (Figure 6.11b). Figure 6.11c) shows in yellow the pixel selected to be included in the calculation of the average number of photon events per pixel.
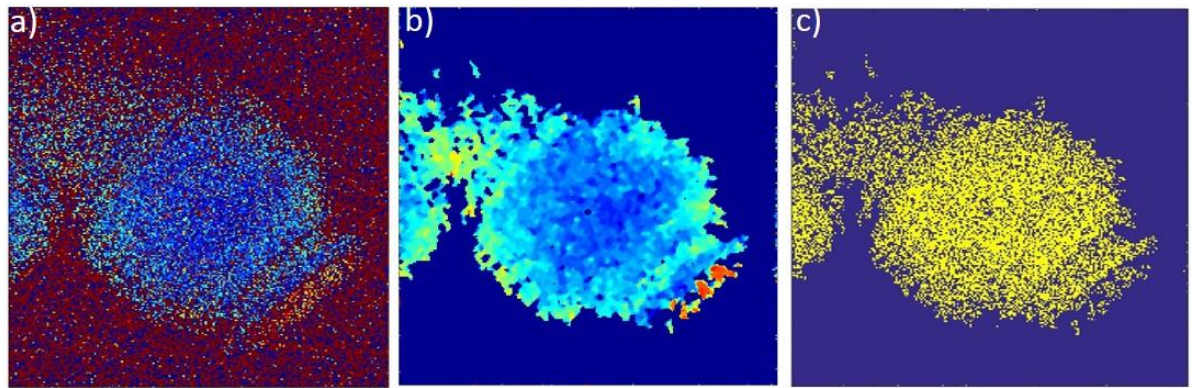
Figure 6.11. Example of pixel selection process. The acquisition time per pixel of the example is 0.1 ms, the same scan discussed in Figure 6.8. The same user-defined depth range is selected on (a) the depth map obtained with the cross-correlation approach to eliminate some of the depths created by spurious scatters, and (b) the DCT depth map to select the pixels corresponding to the target area. The pixel selected to be included in the calculation of the average number of photon events per pixel are shown in yellow in figure c).

The pixels that contain the required depth information are then selected in the intensity map, and are summed in terms of the number of pixel events in each cross-correlation (as before, summing the events over a 30 bins range centred in the highest value of the cross-correlation). The sum of all these events divided by the number of selected pixels gave an estimation of the average number of events per pixel. However, this sum still included photons reflected from the target as well as back-scattered and multiple scattered photons. The overall effect is that the recorded number of events did not scale linearly with acquisition time.

It is interesting to note that at 0.5 ms acquisition time per pixel only 2.79 average events per pixel are needed to obtain the corresponding DCT depth image, meaning that only 2 events per pixel are sufficient to maintain millimetre details of the target. At 0.1 ms acquisition time per pixel, the corresponding DCT image was obtained with only 0.86 average events per pixel, although fewer of the millimetre details of the target can be resolved.

The same algorithm was applied to depth and intensity maps with short extracted acquisition time per pixel of scans performed with the target placed at 9 attenuation lengths. In this case, the high level of scattering meant that noisy pixels contribute to the reconstruction of the image, making the algorithm less successful.

Two other methods were developed in order to improve the images. One of the models is based on a Markov chain Monte Carlo approach and the other on a Coordinate Descent Algorithm, and are discussed in the next section.

6.3. Reflectivity and depth profile restoration from sparse single-photon underwater data

Highly attenuating environments or shorter acquisition times cause a reduction in the number of photon events recorded per pixel, making target depth and reflectivity estimation an increasingly difficult task. In this case, advanced signal processing techniques can help improve the estimated images for single-photon sparse data.

Dr. Abderrahim Halimi developed two algorithms to recover the reflectivity and depth of the target, as the level of scattering is increased. The algorithms are based on a

hierarchical Bayesian model, which is a statistical model divided into multiple sub-levels. Each sub-level introduces an information via a *prior distribution*, where observed parameters can be related to one another to determine higher levels. All the sub-levels are then used to determine the *joint posterior distribution* through the Bayes' formula [2]. Both algorithms correlated neighbouring pixels of depth and reflectivity images obtained with the pixel wise cross correlation approach, assuming that the depth and the reflectance vary slightly between two consecutive pixels. This condition is implemented in both algorithms introducing two auxiliary variables, one for the depth and the other for the reflectivity. One algorithm used a Markov Chain Monte Carlo (MCMC) method [4] to generate a distribution which approximates the posterior distribution that includes appropriate priors, such as the knowledge of the attenuation coefficient, the target distance, and the correlation between adjacent pixels. This approach was fully automatic but required a long computational time, since the entire posterior distribution was generated for each pixel. Therefore, a second algorithm was developed to deal with this problem. In this case, the algorithm was based on a Coordinate Descent Algorithm (CDA) [5], meaning that for each pixel only one value of the posterior distribution is generated. Then, the same priors were used in order to optimise the depth and reflectivity information in each pixel and correlate neighbouring pixels. This approach greatly reduced the computational times, but it required manual intervention for the optimisation. The details of both algorithms are reported in a jointly authored paper [6].

The author helped design and solely performed the experiments to validate the algorithms, while the analysis was performed by Dr. Abderrahim Halimi. Therefore, the next two sections will describe the experiments and will show some of the results obtained with the new algorithms.

6.3.1. Reflectivity restoration

Several scans were performed in order to establish the performance of the algorithms in restoring the reflectivity of the target in highly scattering environments. The Spectralon targets with 10% and 99% reflectance were placed at a distance of approximately 5 cm apart in unfiltered tap water, with the 10% reflectance Spectralon target closer to the system, as shown in Figure 6.12. Due to the different travelling distances in water, the return from the 99% reflectance Spectralon target was attenuated more than the return from the 10% reflectance Spectralon target. This means that, increasing the attenuation

of the environment, the return from the 99% reflectance Spectralon target decreased faster than the return from the other target. Therefore, several scans of the two Spectralon targets were performed for different concentrations of Maalox in unfiltered tap water, until the same level of returns was obtained from both targets. In addition, a tank with dimensions of $40 \times 25 \times 25$ cm^3 was used in order to minimise the attenuation between the first Spectralon target and the system, as an attenuation coefficient of approximately $\alpha = 15$ was needed in order to obtain comparable returns from both targets. The tank and the targets are shown in the photograph in Figure 6.12. The tank was placed at a distance of 1.57 metres from the transceiver unit, as shown schematically in Figure 6.13. The transceiver unit and the detection and acquisition hardware used for this investigation were mainly the same as described in section 5.10. The only difference was in the objective lens, as in this case an objective lens of 50 mm focal length was chosen in order to obtain a uniformly illuminated field of regard (field seen in a full scan of the given image).

Figure 6.12. Photograph of the two Spectralon targets in a small tank filled with unfiltered tap water.
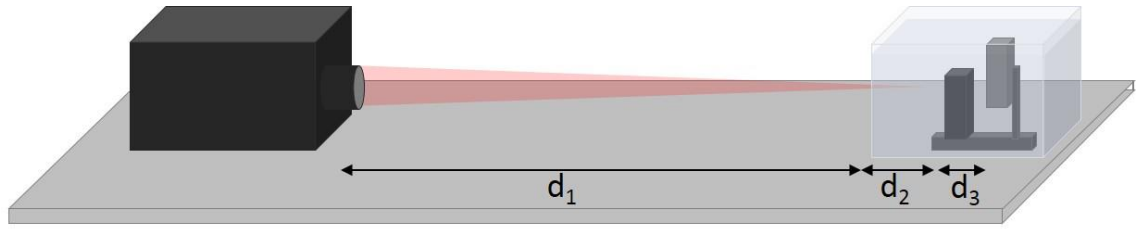
d_1 = Distance system to glass tank = 157 cm

d_2 = Distance glass tank to first target = 9.1 cm

d_3 = Distance between targets = 5.1 cm

Figure 6.13. Schematic of the transceiver unit and glass tank.

The scans were performed over an area of 50×50 mm^2, which included half area of each Spectralon target. The pixel format was 150×150, with an acquisition time of 10 ms per pixel, and 670 nW average optical power. The operational wavelength was λ = 690 nm in all cases, despite the level of scattering of the environment. This is because the same operational parameters were needed to validate the algorithms during this initial stage. A list of the main system parameters used for this experiment is reported in Table 6.2.

Parameter	Note
Targets	Spectralon 10% and Spectralon 99% placed 5 cm apart
Environment	Water with varying concentrations of Maalox
Target Stand-off Distance	~1.66 metres
Laser System	• NKT Photonics supercontinuum laser source (SuperK EXTREME EXW-12) • Source fibre-coupled to AOTF
Illumination Wavelengths	$\lambda = 690$ nm
Laser Repetition Rate	19.5 MHz (Clock for the TCSPC module and the PPG)
Average Optical Power Range	670 nW
Pixel format	150×150
Scan area	50 mm $\times$ 50 mm
Acquisition Time Per-Pixel	10 ms
Data Acquisition Hardware	HydraHarp 400 by PicoQuant • Synchronization rate of ~19.5 MHz • Internal sync divider: 8 • Acquisition mode: T3 mode
Binning Size	2 ps timing bin width
Detector	Silicon Single Photon Avalanche Diode (SPAD) • PDM series by Micro Photon Devices (fibre receptacle detector) • Used in gated mode
Temporal Response of System	≈ 60 ps at $\lambda = 690$ nm
Objective Lens	Canon EF 50mm f/1.8 II • Focal length: 50 mm • F-number: f/4
Background level	Dark conditions in laboratory (~60 cps – detector gated)

Table 6.2.   Summary of the main system parameters used for the experiment described in this section.

The attenuation of the propagation medium was varied by adding several concentrations of Maalox to unfiltered tap water, and the value of the attenuation coefficient α was measured before and after each scan. Five values of the attenuation coefficient were investigated:

- $\alpha_1 = 0.6$ (unfiltered tap water)

- $\alpha_2 = 5.2$ (unfiltered tap water with 0.02% of Maalox)

- $\alpha_3 = 11.3$ (unfiltered tap water with 0.05% of Maalox)

- $\alpha_4 = 14.8$ (unfiltered tap water with 0.07% of Maalox)

- $\alpha_5 = 17.3$ (unfiltered tap water with 0.09% of Maalox)

The data were analysed with the two developed algorithms and with the cross-correlation approach. For example, Figure 6.14 shows the results for three values of the attenuation coefficient α. On the top of the figure, the reflectivity was evaluated with the cross-correlation approach. It can be seen that as the level of scattering increases, the reflectivity of the 99% reflectance Spectralon target decreases faster than for the other 10% reflectance Spectralon panel, and for high level of scattering the two reflectivity levels are approximately the same. The middle and the bottom of the figure show the results obtained with the CDA and MCMC algorithms, respectively. Both models restore the correct value of reflectivity of the two Spectralon targets, by taking the attenuation properties of the propagation medium and the distance between the two targets into account. However, this also means that the algorithms are strongly dependent on the measured value of the attenuation coefficient, making the reflectivity difficult to restore when highly scattering environments are considered.
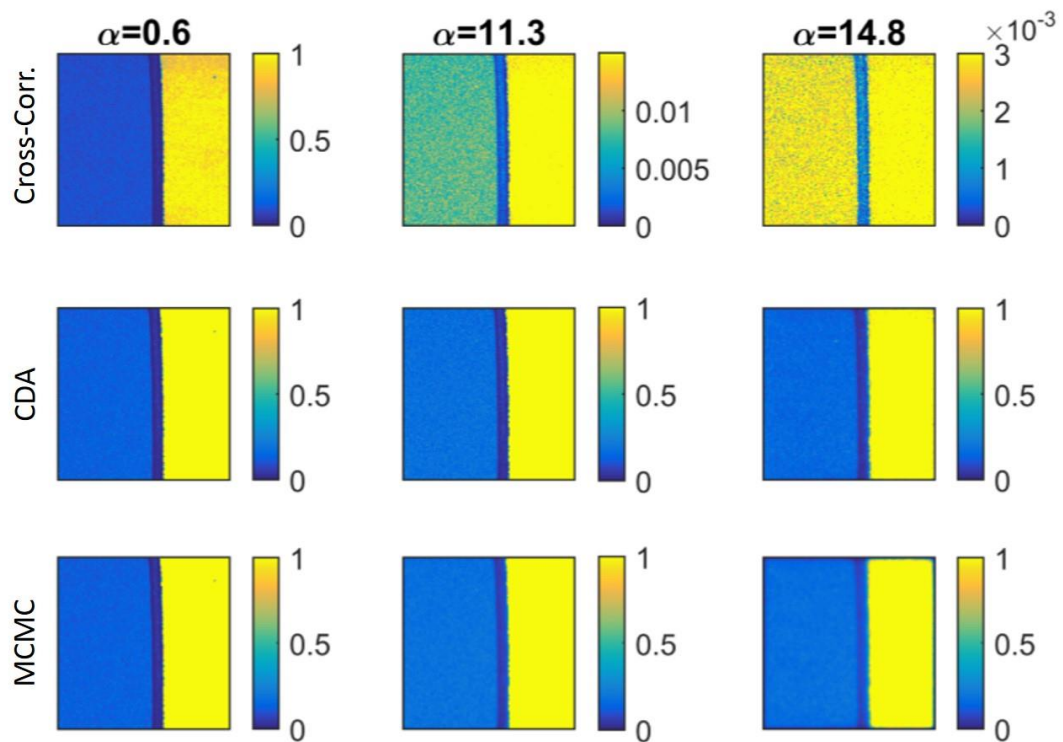

Figure 6.14. Reflectivity images of 150×150 pixel format, 10 ms acquisition time per pixel, and average optical power of approximately 670 nW. The results were analysed with (top line) the cross-correlation approach, (middle line) the CDA algorithm, and (bottom line) the MCMC algorithm. The results are shown for three values of attenuation coefficient. From [6].

The correction performed by the two algorithms is even more evident in Figure 6.15, where the average values for each column are shown for the two analytical approaches considered, as well with the cross-correlation approach. From the graph, it can be seen how the cross-correlation approach fails to recover the correct values of reflectivity of the two targets, while the CDA and MCMC methods allow the restoration of the reflectivity of both targets.
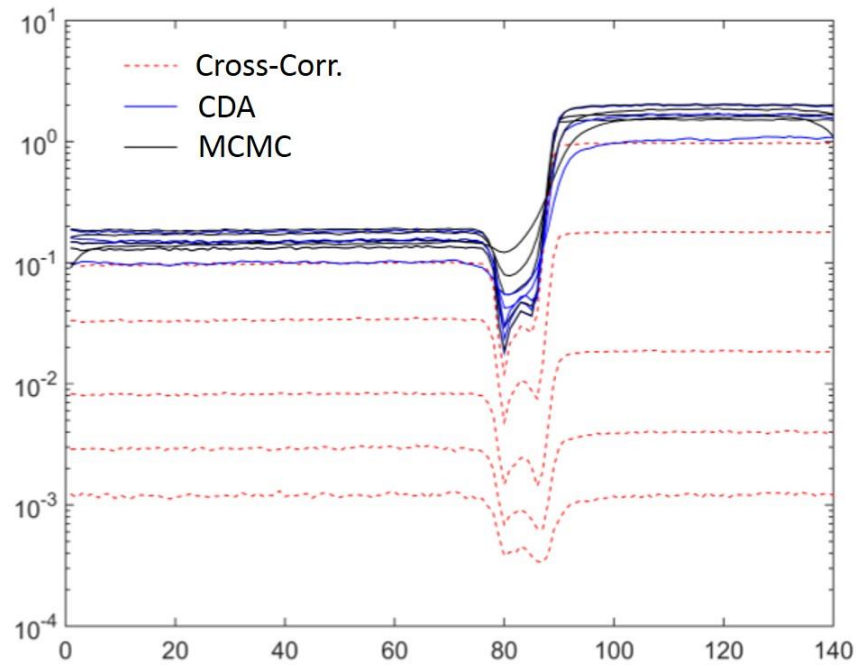

Figure 6.15. Reflectivity lines (150 pixels), representing the average calculated over each column, for all the investigated values of the attenuation coefficient. The graph shows the comparison between the results obtained with the cross-correlation approach, and the two proposed algorithms, CDA and MCMC. From [6].

These results allowed validating the algorithms with the use of two flat targets with known nominal reflectance. However, it is interesting to investigate the case of a generic target of unknown reflectivity. This scenario, with further considerations on the depth of the target, is considered in the next section.

6.3.2. Depth and reflectivity restoration

The performance of the algorithms was evaluated by performing scans of the plastic pipe in unfiltered tap water with several concentrations of Maalox. The plastic pipe target was placed in the 1.75 metres long tank, at a stand-off distance of 1.68 metres in

water. The attenuation of the propagation medium was measured before and after each measurement, hence the stand-off distance in attenuation lengths was estimated for each scan. The scans were performed with a pixel format of 100×100, 100 ms acquisition time per pixel, and the average optical power was adjusted depending on the level of scattering. This means that reference scans were needed in order to compare the scans of the plastic pipe target performed at different power levels. Therefore, the 99% reflectance Spectralon target was used to obtain these reference scans, selecting the same operational parameters used for the plastic pipe scan.

In addition, the objective lens of 200 mm focal length was used in order to detect the signal from the target up to several attenuation lengths. However, this came at the cost of a brighter area in the centre of the intensity map, due to the limited field of regard of the system. Since spatial correlations were performed to restore the reflectivity of the target, a uniformly illuminated area was requested in order to validate the algorithms. Therefore, the scanned area was reduced to $20 \times 20 \, \text{mm}^2$, and only a small detailed portion of the plastic pipe target was scanned, as shown in Figure 6.16.

Figure 6.16. Photograph of the plastic pipe target used for the experiments. The portion of the target scanned is highlighted by the red square.

The experimental setup used for these measurements is the same as described in section 5.10, and the list of the main parameters used is reported in Table 6.3.

Parameter	Note
Target	Plastic pipe
Environment	• Unfiltered tap water • Unfiltered tap water with Maalox
Target Stand-off Distance	~ 1.68 metres in water
Laser System	• NKT Photonics supercontinuum laser source (SuperK EXTREME EXW-12) • Source fibre-coupled to AOTF
Illumination Wavelengths	690 nm
Laser Repetition Rate	19.5 MHz (Clock for the TCSPC module and the PPG)
Average Optical Power Range	0.028 µW to 800 µW
Illumination Beam Diameter at Target	~ 200 µm
Pixel format	100×100
Acquisition Time Per-Pixel	100 ms
Scan area	20 mm $\times$ 20 mm
Data Acquisition Hardware	*HydraHarp 400 by PicoQuant* • Synchronization rate of ~19.5 MHz • Internal sync divider: 8 • Acquisition mode: T3 mode
Binning Size	2 ps timing bin width
Detector	Silicon Single Photon Avalanche Diode (SPAD) • PDM series by Micro Photon Devices (fibre receptacle detector) • Used in gated mode
Temporal Response of System	~ 60 ps at $\lambda = 690$ nm
Objective Lens	Canon EF 200mm f/2.8L II USM • Focal length: 200 mm • F-number: f/2.8
Background level	Lab under dark conditions (~ 60 cps – detector gated)

Table 6.3. Summary of the main system parameters used for the experiments described in this section.

The depth of the target was initially estimated with the pixel-wise cross-correlation approach, and the results are shown in the top line of Figure 6.17. The results show that the image quality degrades for highly scattering environments, where a number of

pixels have insufficient data to provide a depth result. At a stand-off distance equivalent to 9 attenuation lengths, the target is barely visible due to the high level of background.

Then, the analysis was performed using the two proposed algorithms, and the results are shown in Figure 6.17. The middle line of the figure reports the results obtained with the CDA algorithm, while the bottom line shows the results obtained with the MCMC algorithm. In both cases, the algorithms were able to remove the noise when the target is placed at 8 attenuation lengths, greatly improving the result of the scan. However, at the highest scattering level, the CDA algorithm over-smoothes the target, making it difficult to recognise the target, although some details are successfully recovered. The MCMC algorithm maintains the correct contour of the target, but it came at the cost of more noise in the image when compared to the CDA result.
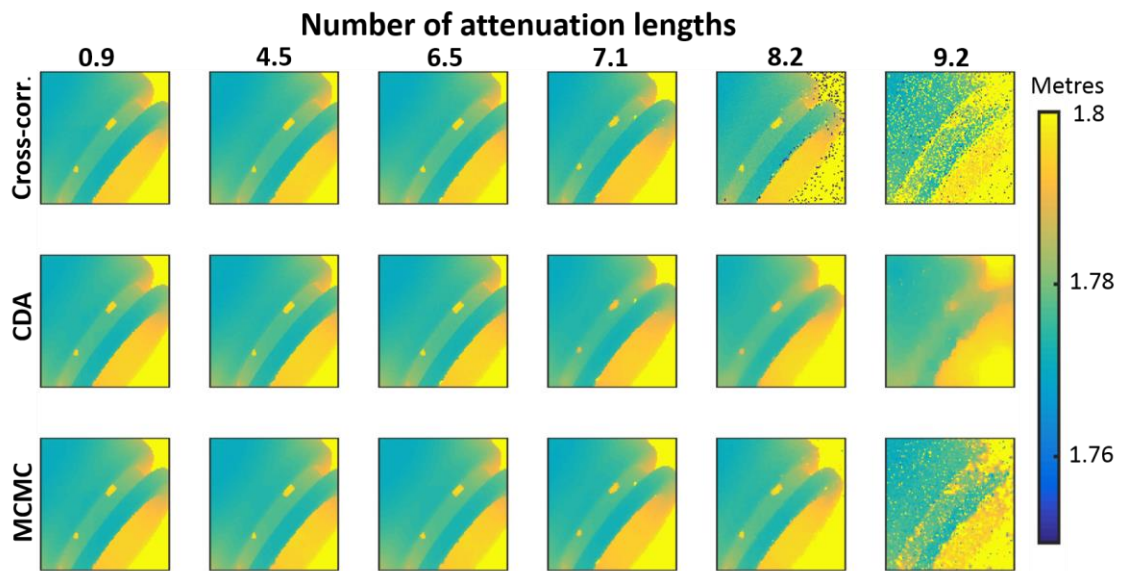

Figure 6.17.   Depth of the target estimated with the pixel-wise cross-correlation approach (top line), the CDA algorithm (middle line), and the MCMC algorithm (bottom line).

Figure 6.18 shows the RSNR comparing the depth maps in Figure 6.17 with the depth map obtained with the MCMC algorithm in clear water. As expected, the RSNR decreases as the scattering level increases. However, when the cross-correlation approach is used, the RSNR is significantly less at high attenuation than the RSNR for the CDA and MCMC approaches.
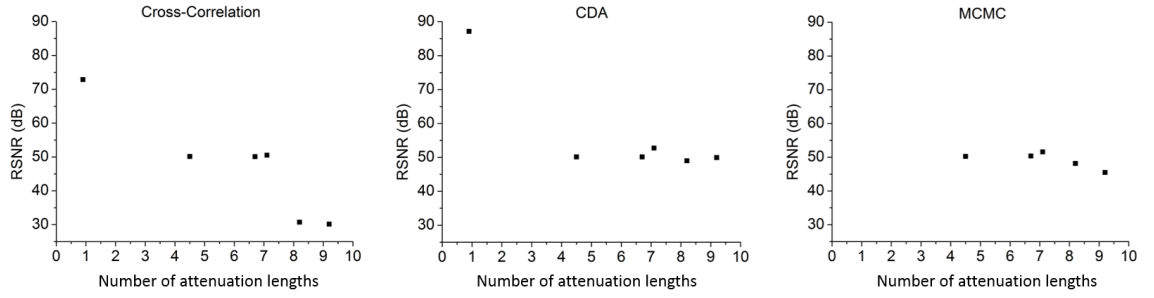
Figure 6.18. RSNR versus attenuation lengths comparing the depth images shown in Figure 6.17 with the depth map obtained in unfiltered tap water with the corresponding algorithm.

Figure 6.19 shows the reflectivity of the plastic pipe target estimated with the pixel-wise cross-correlation approach (top line), the CDA algorithm (middle line), and the MCMC algorithm (bottom line). The figure shows how the cross-correlation approach fails in providing the correct reflectivity of the target, making it not possible to discern the target within the scanned area when the scattering agent is added to unfiltered tap water. However, the proposed algorithms allow for the restoration of the reflectivity of the plastic pipe up to distances of approximately 7 attenuation lengths. When the target is at a stand-off distance equivalent to 8 attenuation lengths, the background level strongly reduces the SNR, thus limiting the performance of the algorithms. As the scattering level further increases, both algorithms are unable to restore the reflectivity of the target. It is important to also note that the image processing algorithms are strongly dependent on the measurement of the attenuation coefficient α, which is difficult to achieve in highly scattering environments. This, in conjunction with the low SNR, means that the algorithms overestimate the reflectivity at 8 attenuation lengths, and are unable to recover the reflectivity of the target at the stand-off distance equivalent to 9 attenuation lengths.
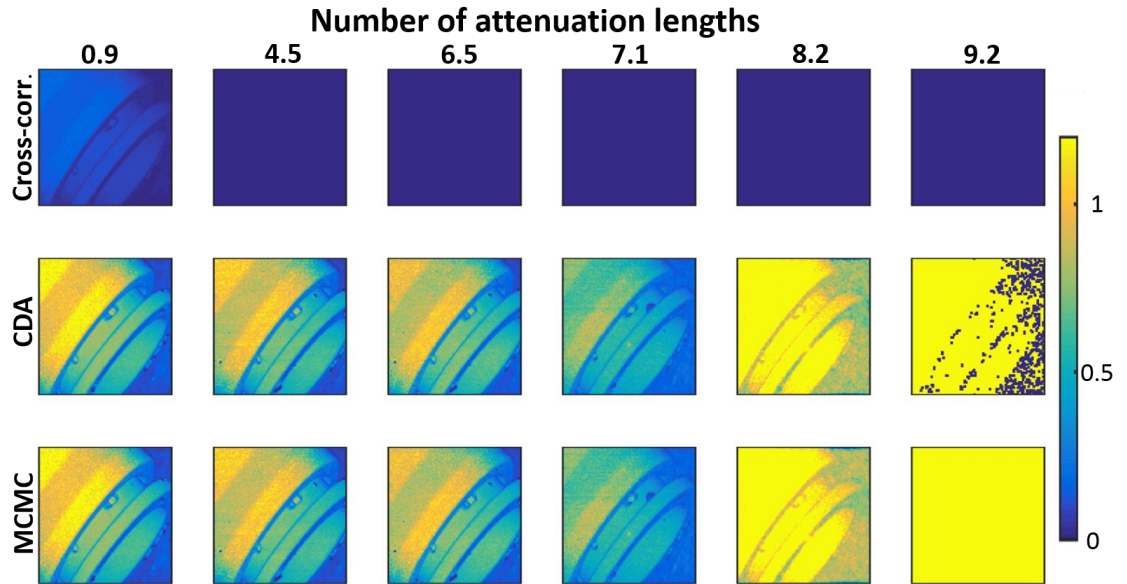
Figure 6.19. Reflectivity of the target estimated with the pixel wise cross correlation approach (top line), the CDA algorithm (middle line), and the MCMC algorithm (bottom line).

These results showed that the depth and reflectivity of the target can be successfully restored up to distances equivalent to more than 8 attenuation lengths. However, this was at the cost of a long acquisition time per pixel, and a study on the performance of the algorithms in photon-starved conditions is needed in order to establish the limitations of the models. Dr. Abderrahim Halimi performed this investigation under similar conditions [6], showing that the algorithms have an acceptable performance (meaning a reconstruction signal-to-noise-ratio above a limit selected by the user) when at least 30% of the pixels are not empty. Ideally, this means that the acquisition time can be reduced to few microseconds per pixel when the target is placed in clear water. As the attenuation of the propagation medium is increased, longer acquisition times per pixel should be considered accordingly.

6.4. Conclusions

Three algorithms were developed in order to improve the results obtained at stand-off distances equivalent to several attenuation lengths, and investigate a number of approaches which aim to reduce the overall acquisition time of a scan.

The first algorithm is based on the sparseness of the Discrete Cosine Transformation (DCT) coefficients. In general, the DCT based method is often able to reconstruct a

sequence with the use of only few coefficients. In this chapter, the DCT based method was applied on depth and intensity images obtained with short acquisition times per pixel and processed using the cross-correlation approach. The DCT based model was able to successfully reconstruct the images, allowing the use of short acquisition times per pixel when the target was placed at a stand-off distance equivalent to 8 attenuation lengths. With this technique, the overall acquisition time in highly scattering environments was reduced from almost 30 minutes to approximately few seconds, using an average optical power of 2.6 mW and a 240×240 pixel format. A smaller pixel format can be selected in order to further reduce the overall acquisition time, providing a significant contribution to the practicality of this approach. Alternatively, a different scan pattern can be chosen instead of a raster scan. For example, a set of pixels can be chosen for the system to scan, using a randomly generated pixel-mask created in software. Subsequently, the DCT based model can be used to reconstruct the depth and intensity maps. This technique, in conjunction with a low pixel format and a short acquisition time per pixel, can drastically reduce the overall acquisition time for scans in clear or in low scattering levels of water. The same scanning approach can also be used if the target is placed in a highly scattering environment. However, in this case it is possible that the cross-correlation approach is not able to evaluate the depth for several pixels. This means that the minimum number of pixels included in the mask will be strongly limited by the presence of empty pixels resulting from the low SNR. Therefore, it is necessary to investigate the percentage of non-empty pixels needed for the model to reconstruct the image. This investigation is also needed in order to evaluate the performance of the model depending on the number of pixels in the mask used, acquisition time per pixel, average optical power, and attenuation of the propagation medium.

When the target was placed at 9 attenuation lengths, the DCT based model was no longer able to reconstruct the images due to the high level of scattering in the water. This greatly reduced the SNR and caused the cross-correlation approach to be performed over the wrong peak in the histogram. In this case, the model included these noisy events in the reconstruction, causing the target to not be discernible in both the depth and intensity maps.

In order to investigate other analysis techniques, Dr. Abderrahim Halimi developed two algorithms based on a Bayesian approach. The first algorithm used a Markov Chain

Monte Carlo (MCMC) approach to generate samples distributed according to the posterior distribution. The method assumes prior knowledge about the attenuation of the environment and spatial correlation between neighbouring pixels. The algorithm was able to properly restore the depth of the plastic pipe target up to a stand-off distance equivalent to 8 attenuation lengths. When the target was placed at a stand-off distance equivalent to 9 attenuation lengths, the algorithm successfully preserved the contours of the target, although retaining some noise in the image.

As the algorithm simulated the entire posterior distribution, the computational times were of the order of approximately 500 seconds, using MATLAB R2015a on a computer with Intel(R) Core(TM) i7- 4790 CPU@3.60GHz and 32GB RAM. Therefore, another algorithm was developed in order to reduce the computational time. This second algorithm was based on a Coordinate Descent Algorithm (CDA), which generated only one value of the posterior distribution, including the same priors as the MCMC algorithm. In this case, the depth was well simulated for stand-off distances of up to 8 attenuation lengths, while at 9 attenuation lengths the algorithm over-smoothed the image. However, the computational times were reduced to approximately 20 seconds, successfully fulfilling the task.

Both algorithms were used to restore the reflectance of the scanned target. A preliminary test was performed processing the results obtained by scanning two Spectralon targets in highly scattering environments. The results showed that both algorithms restored the reflectance of the two targets, as long as the attenuation of the environment was known. The same analysis was performed with scans of the plastic pipe target, showing that both algorithms were able to restore the reflectivity of the target at stand-off distances equivalent up to 7 attenuation lengths. In highly attenuating environments, the estimation of the attenuation coefficient was a challenging task due to the high level of scattering. As the performance of the algorithms was strongly affected by the estimation of the attenuation coefficient, the target reflectivity was difficult to evaluate at longer attenuation lengths. This resulted in not achieving an image of the target at 9 attenuation lengths with the proposed methods.

It will be interesting to investigate the prospects of a new, alternative algorithm, which ignores spurious returns in the analysis. This should allow for discrimination between

the target and scattering events, thus reducing the effect of scattering and improving the image.

References

1.   R. C. Gonzalez, R. E. Woods, and S. L. Eddins, *Digital image processing using MATLAB* (McGraw Hill Education, 2010).

2.   R. C. Gonzalez, and R. E. Woods, *Digital image processing* (Pearson Education International, 2008).

3.   A. Halimi, Y. Altmann, A. McCarthy, X. Ren, R. Tobin, G. S. Buller, and S. McLaughlin, "Restoration of intensity and depth images constructed using sparse single-photon data," in *European Signal Processing Conference (EUSIPCO)*(IEEE, Budapest, Hungary, 2016).

4.   C. P. Robert, and G. Casella, *Monte Carlo Statistical Methods* (Springer-Verlag, New York, 1999).

5.   A. Halimi, C. Mailhes, J.-Y. Tourneret, and H. Snoussi, "Bayesian estimation of smooth altimetric parameters: application to conventional and delay/doppler altimetry," IEEE Trans. Geosci. Remote Sens. **54**, 4, 2207-2219 (2016).

6.   A. Halimi, A. Maccarone, A. McCarthy, S. McLaughlin, and G. S. Buller, "Object depth profile and reflectivity restoration from sparse single-photon data acquired in underwater environments," arXiv: 1608.06143 (2016).

Chapter 7

LiDAR equation based model

7.1.   Introduction

As seen in Chapter 5, the performance of the system described in this Thesis depends on several factors, including average optical power, attenuation of optical components, and attenuation of the environment, which all affect the number of events detected. It is often useful to be able to consider the expected performance of an experimental system and compare the achieved results with the projected outcomes. This chapter presents a theoretical model that considers fundamental characteristics of the system when addressing a single pixel in order to provide an evaluation of the performance of the experimental scanning system. The simulations performed to evaluate the experimental system will be presented, as well as a comparison with experimental data.

7.2.   Theoretical modelling

A model based on a photon-counting version of the LiDAR range equation [1] was developed to evaluate the system's time-of-flight ranging performance in water.

The most general form of the LiDAR range equation can be written as [1]

$$P(R) = KG(R)\beta(R)T(R)$$

Equation 7.1

where P is the power received from a distance R, which is dependent on the performance of the LiDAR system K, the range dependent geometrical factor $G(R)$, the backscatter coefficient $\beta(R)$, and the transmission term $T(R)$. Therefore, several parameters that contribute to the number of counts in the peak were included in the developed model. Intrinsic parameters consider the attenuation of each optical element, detector response, and operational parameters. Extrinsic parameters take in account the environmental attenuation, the stand-off distance of the target, and its optical properties. The following sections will consider how this general form can be adapted to apply to the system presented in this Thesis.

The model evaluates the number of photons in the bin with the highest count in the return peak from the target. The number of counts is strongly influenced by each of these parameters, hence any modification to the scanning system needs to be included in the model. The results presented in this chapter were obtained by modelling the system described in sections 5.10 and 5.11. However, it is important to note that the model gives an evaluation of the system performance for an optimised single pixel, and not for the entire scan – which may contain several sub-optimal pixels – therefore it is not possible to assume a full image will perform in a linearly scaled manner proportional to the number of pixels.

7.2.1. Average optical power and wavelength

The number of counts is linearly dependent on the average optical power used P_{Out}. Given the wavelength of the incident light, the average photon emission rate can be estimated from

$$r_{\gamma} = \frac{\lambda P_{Out}}{hc}$$

Equation 7.2

where h is Planck's constant and c is the speed of light in vacuo.

7.2.2. Acquisition time

The acquisition time per-pixel, t_{Dwell}, is the time spent by the system staring at each pixel to record the measurement. When a scan is performed, a good approximation for the overall acquisition time t_{Scan} is the acquisition time per-pixel multiplied by the number of pixels N. This is an approximation because it does not take in account the time the system needs to move the mirrors from one pixel to the next one, which is of the order of $t_M \sim 150$ μs using the current galvo-mirror configuration [2]. Therefore, in general the overall acquisition time for a scan can be expressed as

$$t_{Scan} = N\left(t_{Dwell} + t_M\right)$$

Equation 7.3

7.2.3. Target reflectance

The incoming light can be absorbed, specularly reflected, transmitted and scattered by the target. The target reflectance ρ quantifies the percentage of light that is scattered on reflection from the target [3].

7.2.4. Geometric factor

The system collects just a fraction of the light scattered by the target, so a geometric factor needs to be included in the equation. The intensity I_C collected by an objective lens of area A is the ratio

$$\frac{I_C}{I_S} = \frac{A_{Lens}}{4\pi R^2}$$

Equation 7.4

of the intensity I_S scattered in the solid angle 4π steradians by a target at a stand-off distance R [1]. The model is calibrated using experimental returns from the Spectralon diffuse reflecting target, described in section 5.8.1. Almost all the incoming light is scattered on reflection, with no light transmitted. Hence only half the overall solid angle possible has to be considered and, consequently, the factor of 4 in the denominator is reduced to 2. In the experimental setup used for the results presented in this thesis, the light travels a distance d in air, from the objective lens to the first end of the tank. Then it travels a distance r in water, from the first end of the tank to the target. Because of the change in the refractive index of the two different media, the distance to consider in the geometric factor is [4]

$$R = d + nr$$

Equation 7.5

where n is the refractive index of water. Hence the geometric factor to include in the photon-counting version of the LiDAR range equation is

$$\frac{I_C}{I_S} = \frac{A_{Lens}}{2\pi\left(d + nr\right)^2}$$

Equation 7.6

7.2.5. Environment attenuation

As discussed in Chapter 4, light is strongly attenuated in water by absorption and scattering. It is assumed that the medium is homogeneous, although in a field trial situation this may not be the case. In accordance with Equation 4.2, the attenuation of water C_W can be included in the model through the exponential term

$$C_W = e^{-2\alpha r}$$ Equation 7.7

where $2r$ is the round-trip distance that the light travels in water, and α is the attenuation coefficient.

7.2.6. Internal attenuation

The internal system attenuation coefficient C_{Int} considers the losses due to the optical elements, couplings and possible misalignments of the system. The attenuation coefficient was determined as the ratio between the average optical power after and before each optical component.
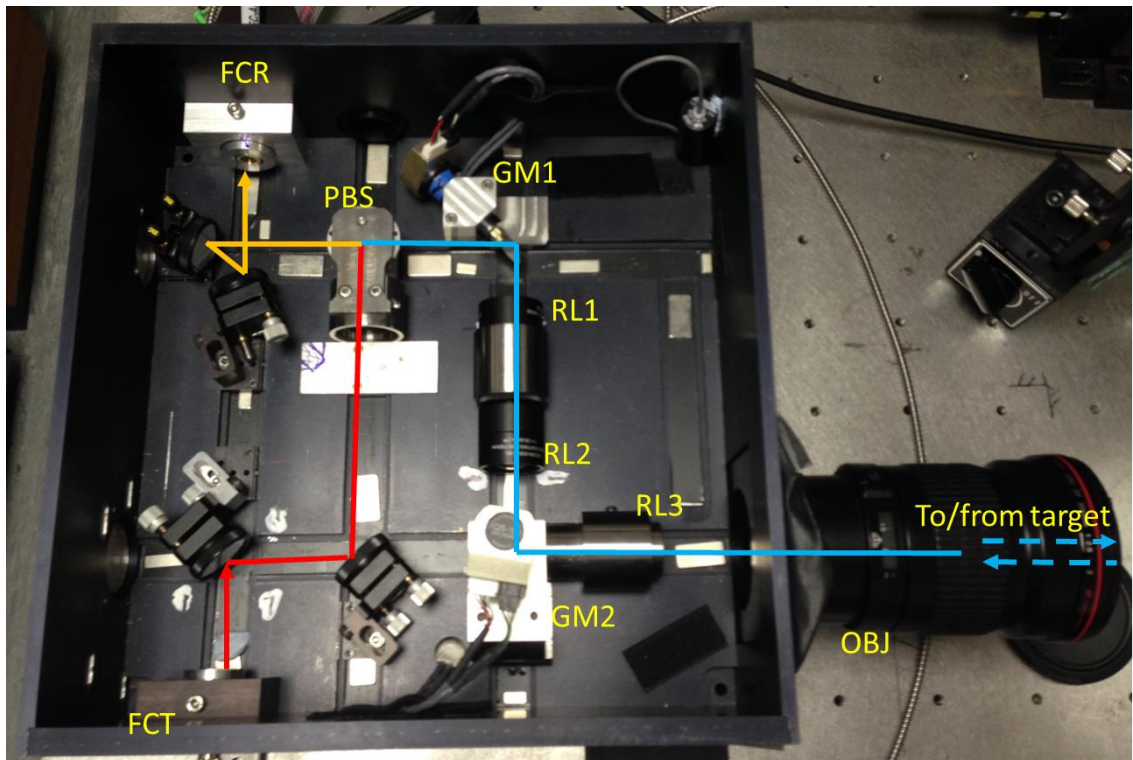
Figure 7.1. Plan view of the transceiver unit. The path in red indicates the transmit channel, and the path in orange the receive channel. The laser source and the detector were fibre-coupled to the transceiver unit via fibre collimation packages (FCT and FCR, respectively). The two channels are overlapped by the polarising beam splitter (PBS), and the common channel is shown by the blue path. The common channel comprises the two galvanometer mirrors (GM1 and GM2), three relay lenses (RL1-RL3), and the camera objective lens (OBJ).

To measure the attenuation coefficient of the transmit channel, the supercontinuum system was fibre-coupled to the collimation package FCT shown in Figure 7.1, and power readings were performed before and after each optical element along this channel (red and blue path). To determine the attenuation due to the objective lens, the light was focused on a target at a stand-off distance of approximately 2 metres, and the attenuation was calculated as the ratio between the optical power at the target and the power just before the objective lens. Then, the supercontinuum system was fibre-coupled to the collimation package of the receive channel, FCR (Figure 7.1). In this case, the attenuation was determined for the path in blue and the path in orange, as shown in Figure 7.1.

Table 7.1 reports typical attenuation values due to the optical elements in the transceiver unit for the wavelengths considered in this Thesis. An additional attenuation is considered for the polarising beam splitter in the receive channel, since the polarisation of the light returning via the receive channel is likely to be unpolarised. Hence, an average attenuation of 3 dB was added into the model.

Wavelength (nm)	Transmit Channel Attenuation (dB)	Receive Channel Attenuation (dB)
525	1.9	2.2 + 3
531	1.9	2.3 + 3
565	2.2	2.4 + 3
645	2.3	2.5 + 3
670	2.3	2.5 + 3
690	2.2	2.4 + 3

Table 7.1. Attenuation of transmit and receive channels, including the attenuation of the optical components in the common channel.

7.2.7. Temporal response coefficient

The temporal response coefficient C_{Det} takes in account the instrumental response of the system. This coefficient was determined from single pixel measurements performed on the Spectralon target. The return peak from the target was studied and the temporal response coefficient was determined as the ratio between the number of counts in the highest bin in the peak and the total number of photons in the peak.

7.2.8. Detector efficiency

The detector efficiency η has to be included in the model since it introduces additional attenuation to the light before being detected. Details about the detection efficiency of the detector were already provided in Chapter 3 and Chapter 5, therefore only the graph of the detection efficiency of the thin junction Si-SPAD by Micro Photon Devices versus the wavelength is shown here.
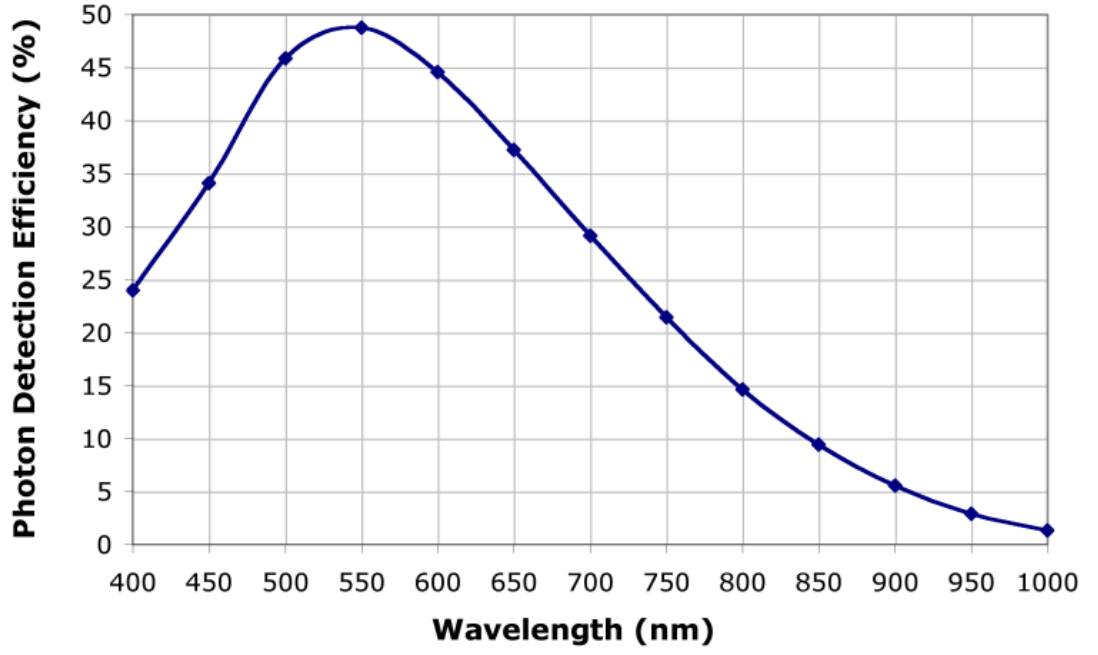
Figure 7.2. Photon detection efficiency of the Si-SPAD by Micro Photon Devices versus the wavelength. From [5].

7.2.9. Equation

The parameters described in the previous subsections provided the information needed to build the photon-counting equivalent of the LiDAR range equation, as in the form of Equation 7.1. The intrinsic parameters of the LiDAR system (K) include

- The average photon emission rate $r_\gamma = \dfrac{\lambda P_{Out}}{hc}$

- The acquisition time t_{Dwell}

- The internal attenuation C_{Int}

- The detector efficiency η and the temporal response of the detector C_{Det}

The geometrical factor $G(R)$ is described by Equation 7.6, as $G(R) = \dfrac{A_{Lens}\rho}{2\pi R^2}$. While the transmission term is $T(R) = e^{-2\alpha r}$.

Considering all these parameters, the photon-counting equivalent of the LiDAR range equation can be written as

$$n_p = \frac{P_{Out}\lambda}{hc} t_{Dwell} \frac{A_{Lens}\rho}{2\pi R^2} e^{-2\alpha r} C_{Int} C_{Det} \eta \qquad \text{Equation 7.8}$$

where n_p is the number of photons in the bin with the highest count in the return peak, as shown in red in Figure 7.3.
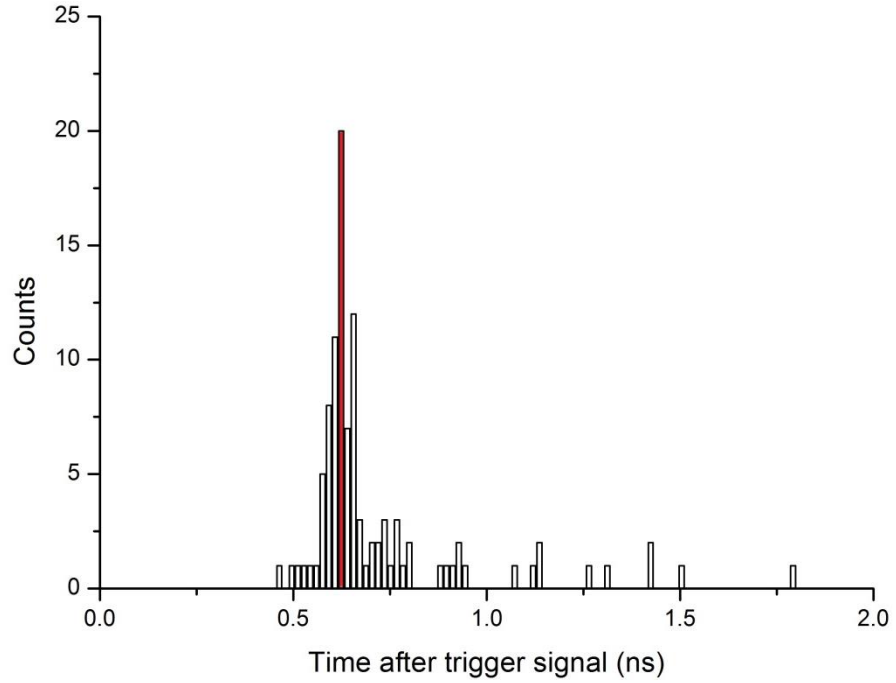

Figure 7.3. Example of histogram showing in red the number of photons in the highest bin in the peak, n_p. An arbitrary zero was chosen for the displayed time-scale.

7.2.10. Background noise

The background noise level was measured for every optical configuration and propagation medium selected. Therefore, several histograms with different integration times were recorded with the detector in free running mode and the laser switched off. Then, the model evaluated the average number of background counts per bin n_b as [6]

$$n_b = t_{Dwell} B f_{Re\,p} t_{Bin}$$

Equation 7.9

where B is the total number of background counts per second, f_{Rep} the laser repetition rate, t_{Bin} the bin size.

7.2.11. Signal to noise ratio

The number of photons in the highest bin in peak and the average number of background counts per bin were used to estimate the signal-to-noise ratio (*SNR*) as [7]

$$SNR = \frac{n_p}{\sqrt{n_p + n_b}}$$

Equation 7.10

7.2.12. Minimum SNR value

By specifying the parameters used in the experiment and the main characteristics of the system, the model calculates the SNR for several stand-off distances. Every SNR value is compared to a minimum required SNR (SNR$_{min}$), in order to evaluate the achievable performance of the system underwater. The SNR$_{min}$ was obtained studying histograms of pixels with a very low return from the target, and a threshold of SNR$_{min}$=1.4 was determined empirically using this simple pixel-wise processing approach. Other signal and image processing approaches could yield a lower effective SNR$_{min}$ value, but this value gives an estimate for the cross-correlation approach used to obtain the depth profiles reported in this Thesis.

7.3. Simulations

Several simulations were carried out with this model. In particular, different average optical power levels were considered in order to evaluate the maximum achievable distance for different environments. The wavelength was varied in accordance with the

environment considered, in order that the optimum wavelength for transmission was selected in each case, as reported in Table 7.2. It is important to note that the simulations for low and medium scattering environments were performed with the system described in section 5.10, while the system described in section 5.11 was used for the simulations performed in highly scattering environments. The difference between the two system configurations relied on the use of different relay lenses. When highly scattering environments were investigated (refer to section 5.11), the relay lenses were chosen with a higher transmittance (refer to section 5.10). In addition, the alignment of the transceiver unit was performed at the wavelength $\lambda = 690$ nm, thus the optimum wavelength experimentally determined for highly scattering environments.

A_{Lens}	$\pi 0.035^2$					
ρ	99%					
Environment	**Wavelength**	**α (m^{-1})**	**C_{Int} (dB)**	**η (%)**	**C_{Det} (MPD - Fibre-receptacle)**	**C_{Det} (MPD - Pigtailed)**
Unfiltered tap water	525 nm	0.14	5.19	48.30	-	0.10
Water with 0.003% Maalox	585 nm	1.44	5.40	45.97	-	0.11
Water with 0.01% Maalox	690 nm	3.55	5.42	29.34	0.02	0.12
Water with 0.0126% Maalox	690 nm	4.59	4.87	29.34	0.02	-
Water with 0.016% Maalox	690 nm	5.57	4.87	29.34	0.02	-

Table 7.2. Summary of fixed parameters used for the simulations. It is worth noting that two different optical configurations were considered here.

Figure 7.4 shows the achievable distance versus the power in unfiltered tap water for four different dwell times, 0.5 ms, 1 ms, 10 ms, and 100 ms. While Figure 7.5 shows the simulation results for water with 0.003% and water with 0.01% of Maalox. In this case, the achievable distance versus the power is simulated for two dwell times, 10 ms and 100 ms, for both environments.
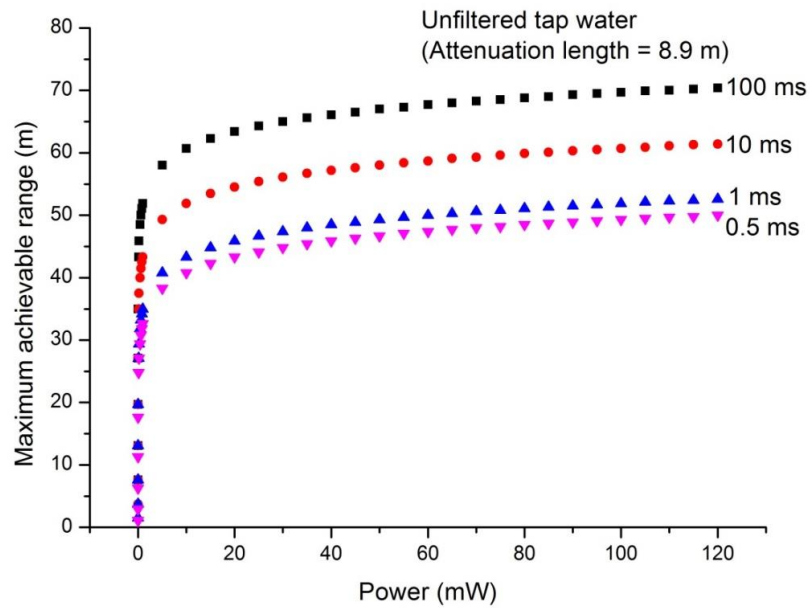
Figure 7.4.   The graph shows the results obtained from the LiDAR equation simulations.   The maximum achievable range is evaluated for different average optical powers in unfiltered tap water at 0.5 ms, 1 ms, 10 ms, and 100 ms acquisition times, and it is considered as the point when the SNR = 1.4.
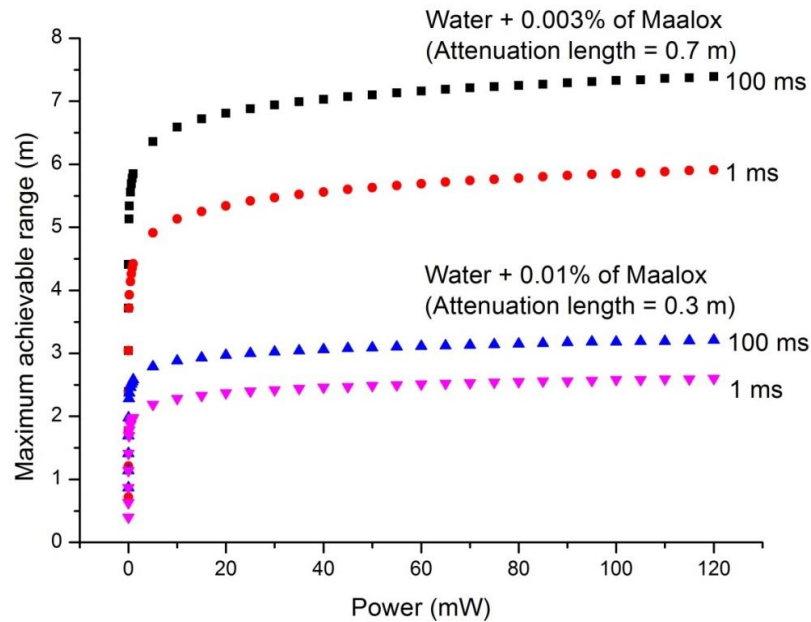

Figure 7.5.   Calculated maximum achievable range versus the average optical power for water with 0.003% and 0.01% Maalox at two different acquisition times, 10ms and 100ms.

Because of the exponential attenuation of light in water, increasing the average power above 80 mW corresponds to only a relatively small increase in the maximum achievable scanning range. This behaviour can be observed in Figures 7.7 and 7.8 for all the water samples considered, and it is evident that the increment in the achievable scanning range decreases as the attenuation length decreases. The simulation results also show that a significant improvement in the achievable range can be obtained by increasing the acquisition time per pixel, as expected. The same considerations can be made when the maximum achievable range versus the power is simulated for water with 0.0126% of Maalox (as shown in Figure 7.6) and water with 0.016% of Maalox (as shown in Figure 7.7).
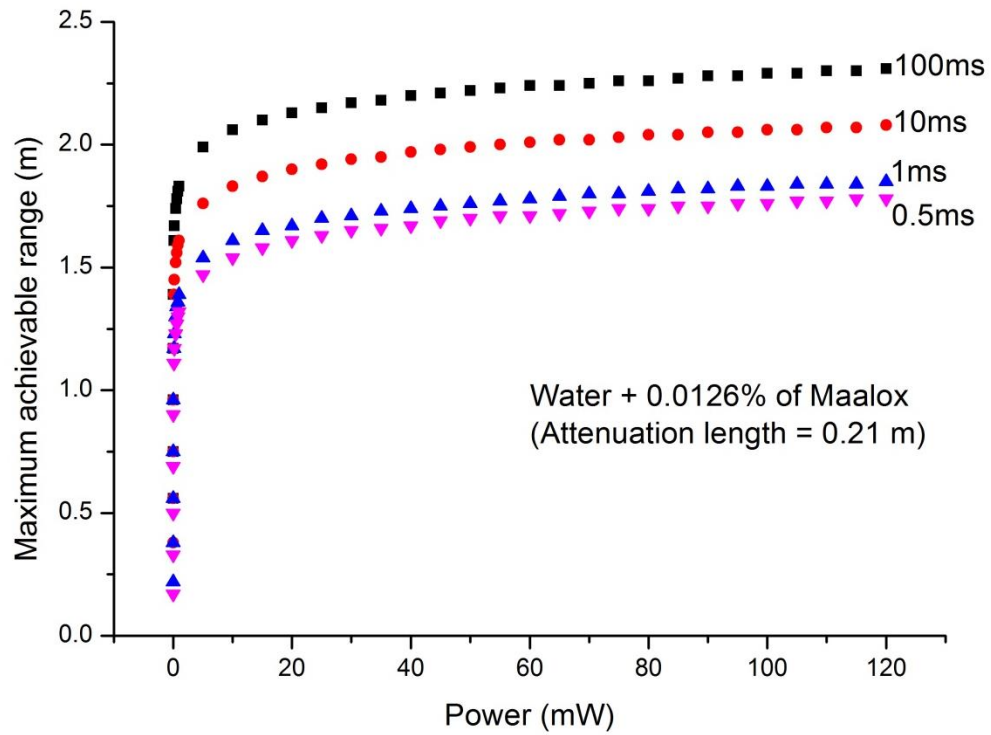
Figure 7.6. Calculated maximum achievable range is evaluated for different average optical powers in water with 0.0126% at 0.5 ms, 1 ms, 10 ms, and 100 ms acquisition times.
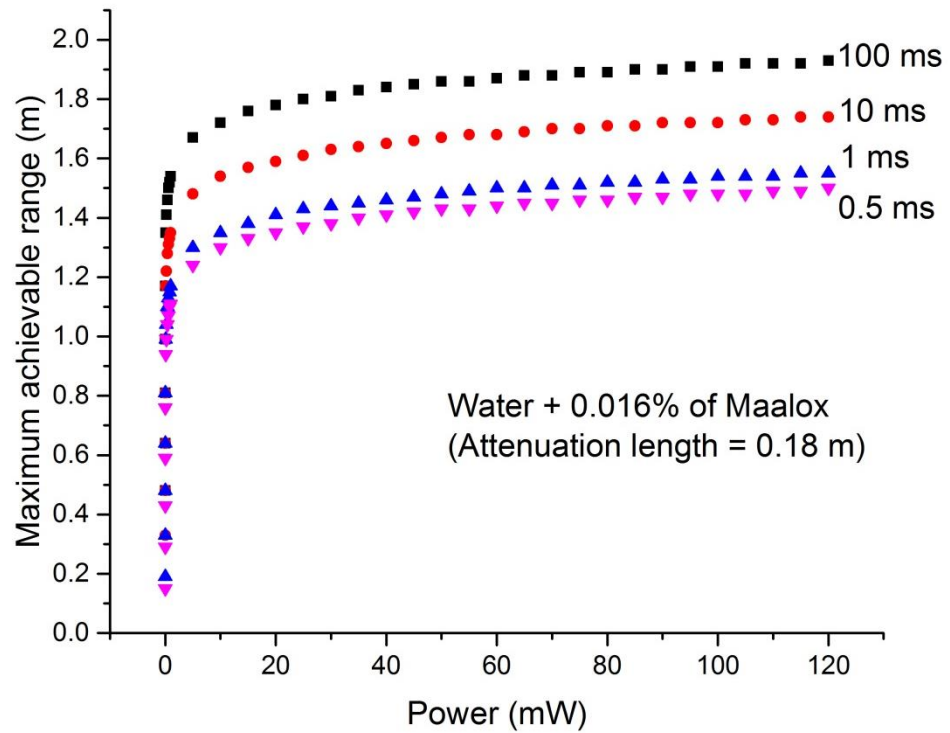
Figure 7.7. Calculated maximum achievable range is evaluated for different average optical powers in water with 0.016% at 0.5 ms, 1 ms, 10 ms, and 100 ms acquisition times.

Because the average optical power level used in the experiments reported in this Thesis was limited mostly to the sub-milliwatt regime, the simulations were carried out again in the optical power range from 0 to 1000 μW. The results are reported in Figures 7.8 and 7.9.
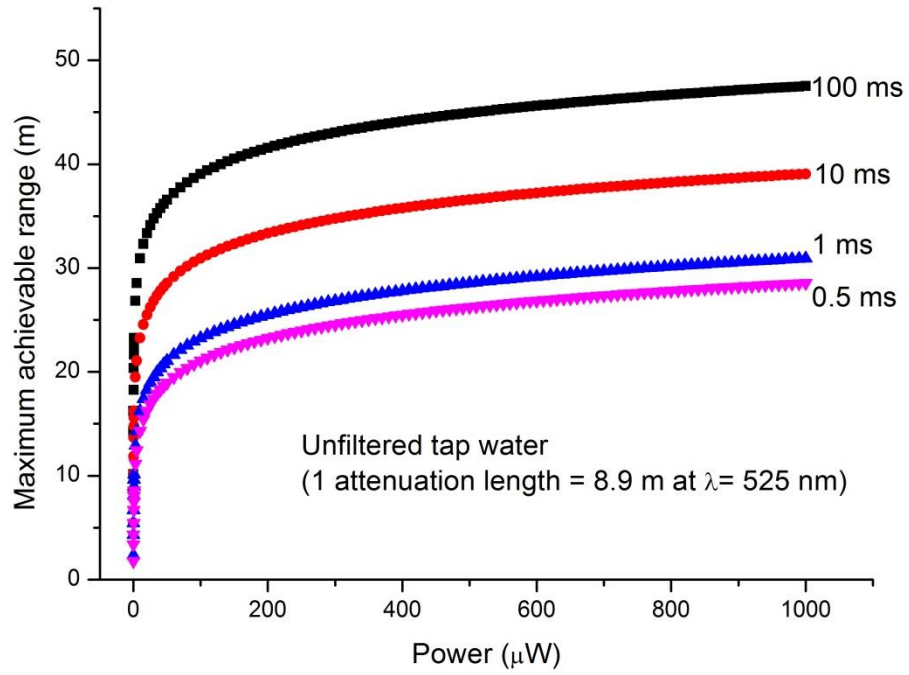
Figure 7.8. The calculated maximum achievable range is evaluated for different low levels average optical powers in clear water at 0.5 ms, 1 ms, 10 ms, and 100 ms acquisition times.
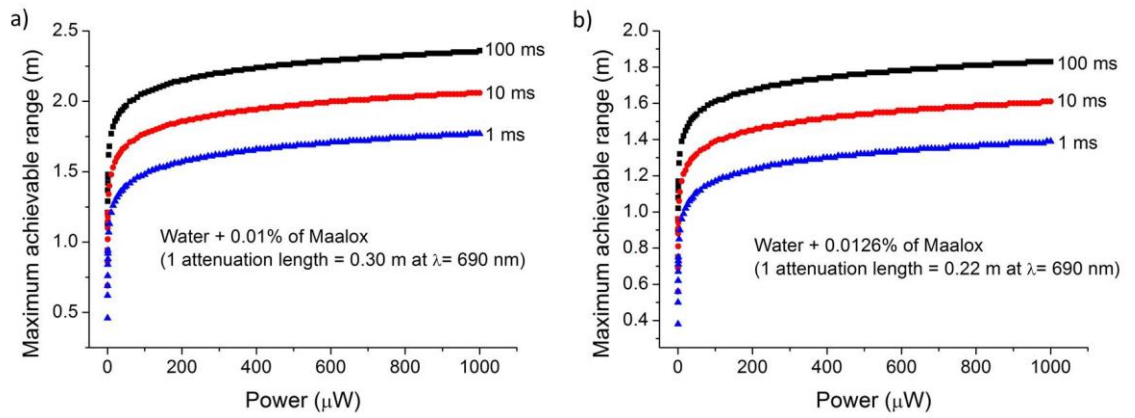

Figure 7.9. Calculated maximum achievable range evaluated for different low levels average optical powers in (a) clear water with 0.01% and (b) 0.0126% of Maalox at 1 ms, 10 ms, and 100 ms acquisition times.

7.4. Comparison with experimental results

The trend of the model was in close correlation with experimental results observed in the laboratory conditions described in this Thesis; i.e. using a range of different scattering environments, and short ranges limited by the dimensions of the tank. Figure 7.10 reports the comparison between the number of counts in the highest bin in

the peak predicted by the model and the number of counts obtained in the experiments for different acquisition times. Single pixel measurements were performed on the Spectralon target of 99% nominal reflectance placed at 1.7 m stand-off distance, in unfiltered tap water, using an average optical power of 0.25 μW at the wavelength λ = 690 nm, and in dark lab conditions (approximately 60 counts per second, in gated mode). A camera objective lens of 200 mm focal length was used to focus the transmitted light on the target, and the focus was adjusted before starting the experiment in order to maintain the same focus position for every measurement.
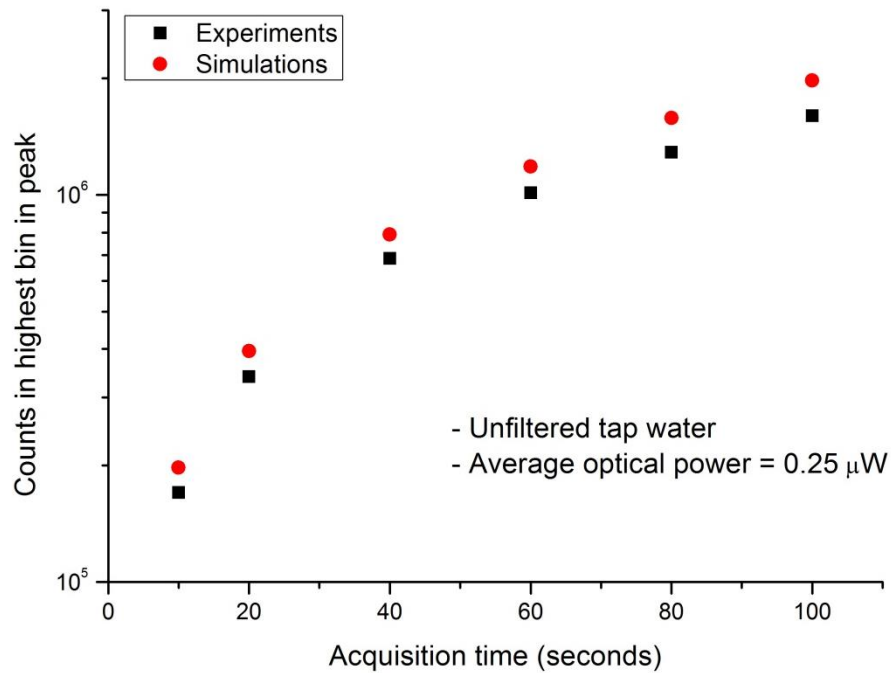

Figure 7.10. Comparison between model predictions (red dots) of the counts in the highest bin in the peak and experimental results (black squares) for different acquisition times. A camera objective lens of 200 mm focal lens was used for these measurements. The target was the test reference Spectralon target of 99% of reflectance, placed at a stand-off distance of approximately 1.7 m. For each measurement, an acquisition time of 100 s, the wavelength λ = 690 nm, and 0.25 μW of average optical power were used.

Another two sets of measurements were performed using a camera objective lens of 100 mm focal length mounted on the transceiver unit, in order to compare the model predictions with the experimental results for several concentrations of Maalox and

different stand-off distances. Figure 7.11 reports the first set of measurements and the model predictions for different concentrations of Maalox. Single pixel measurements were performed on the Spectralon target of 99% nominal reflectance placed at 1.7 m stand-off distance, using 100 s acquisition time, an average optical power of 60 μW at the wavelength $\lambda = 690$ nm, and in dark lab conditions. As before, the focus was the same for each measurement.
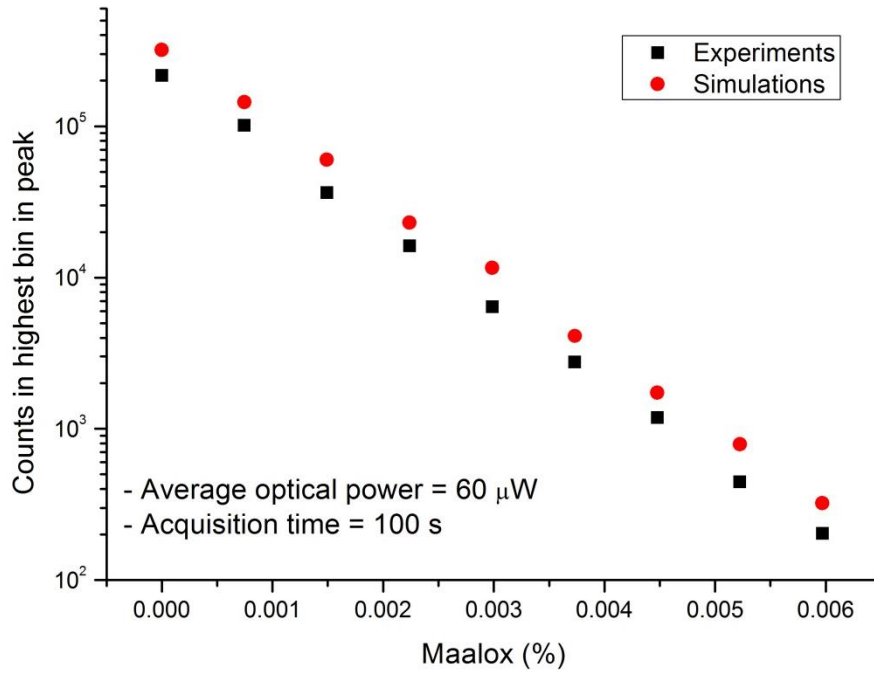

Figure 7.11. Comparison between model predictions (red dots) of the counts in the highest bin in the peak and experimental results (black squares) for different concentration of Maalox. A camera objective lens of 100 mm focal lens was used for these measurements. The target was the test reference Spectralon target of 99% reflectance, placed at a stand-off distance of approximately 1.7 m. For each measurement, an acquisition time of 100 s and 60 μW of average optical power at the wavelength $\lambda = 690$ nm were used.

Figure 7.12 reports the second set of measurements and the model predictions for different target stand-off distances. Single pixel measurements were performed on the Spectralon target of 99% nominal reflectance in water with 0.0126% of Maalox, using 100 s acquisition time, an average optical power of 60 μW at the optimum wavelength $\lambda = 690$ nm, and in dark lab conditions. In this case, the focus was adjusted before each

measurement in order to optimise the return from the target at the different stand-off distances.
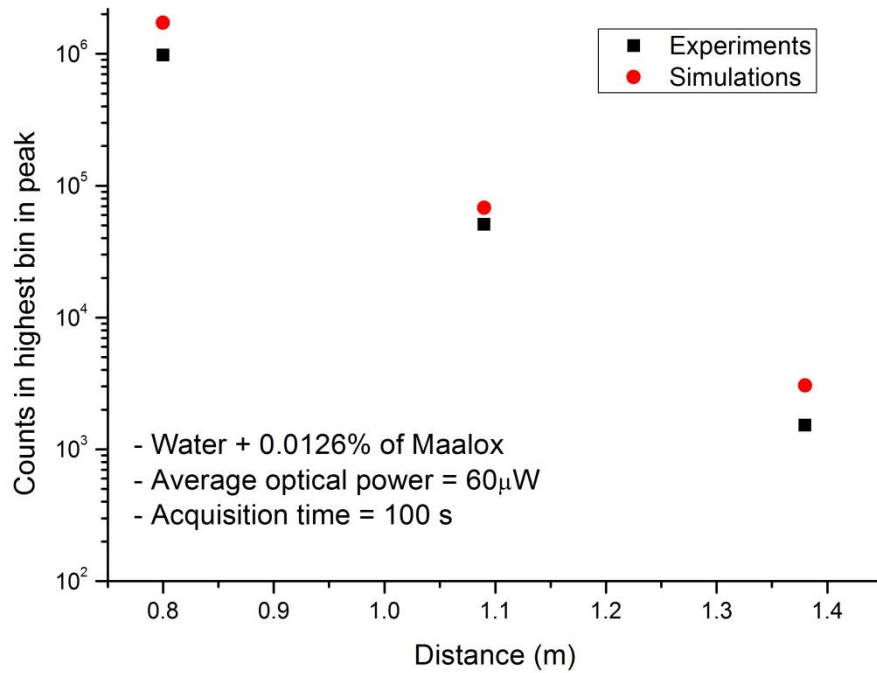

Figure 7.12. Comparison between the counts in the highest bin in the peak for the experimental measurements (black squares) and the model predictions (red dots) for different stand-off distances. A camera objective lens of 100 mm focal lens was used for these measurements. The target was the test reference Spectralon target of 99% reflectance, placed in water and 0.0126% of Maalox. For each measurement, the optimum wavelength $\lambda = 690$ nm, an acquisition time of 100 s, and 60 µW of average optical power were used.

The graphs in Figure 7.10 and Figure 7.11 show that the information about the collection aperture of the system is sufficiently included in the model. In addition, Figure 7.10 and Figure 7.11 show that the experimental and simulation results differ by approximately 1 dB. This difference suggests that one of the attenuation coefficients considered in Equation 7.8 was underestimated, leading the model to predict a higher number of counts in the highest bin in peak. It is not possible to know exactly which coefficient was underestimated and it may indeed be a compound error composed of several underestimations, and further investigations should be performed. The difference of 1 dB is constant over the graphs shown in Figure 7.10 and Figure 7.11, where the focus of the objective lens was adjusted only once before the set of

measurements. An additional error is introduced when the focus is varied for each measurement, as shown in Figure 7.12 where the focus was adjusted in accordance to the target stand-off distances. In this case, the difference between experimental results and model predictions is not constant over the graph.

In order to adapt the model to commonly used target materials, single pixel measurements were performed with different targets and normalized to the return from the Spectralon target of 99% reflectance. Figure 7.13 reports the maximum achievable range versus the power leaving the system. In particular, the graph shows the results of simulations done in unfiltered tap water, at the optimum wavelength $\lambda = 525$ nm, with an acquisition time of 10 ms and $SNR_{min} = 1.4$. The highest return with respect to the Spectralon target is obtained for a brushed transparent plastic board target, while the lowest return is obtained for a matt black aluminium board. Despite the low signature nature of this target, the maximum achievable range suggested by the model is around 40 metres in clear water using 100 mW of average optical power.
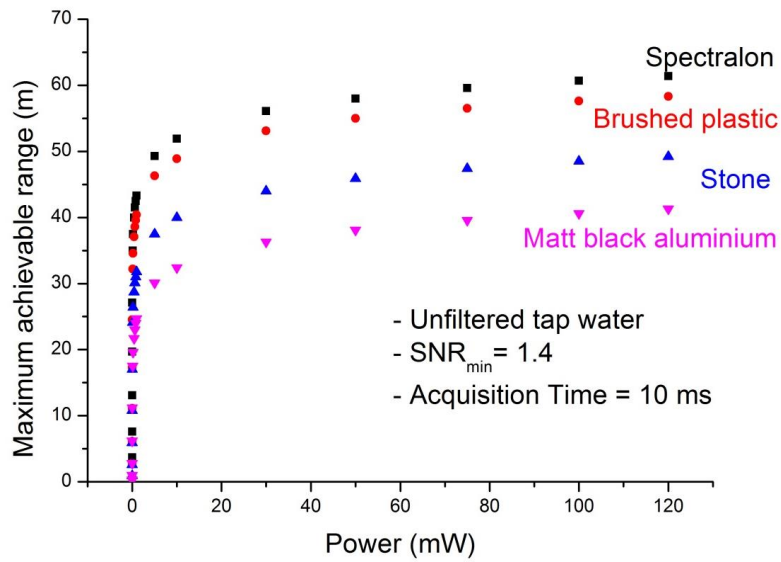
Figure 7.13. Simulations of the maximum achievable range versus the average power when different targets are considered. In particular, the graph shows the results for a brushed transparent plastic board, an example of a rock, and a matt black aluminium board. The case of the Spectralon target is shown for comparison. All simulations were performed using clear water conditions, $SNR_{min} = 1.4$, and 10 ms acquisition time.

In order to investigate how the results vary considering a higher value of SNR_{min}, a comparison was performed between the case where $SNR_{min} = 2$ and the case where $SNR_{min} = 1.4$ for the Spectralon target, as shown in Figure 7.14. In this case, the maximum achievable range obtained by the simulations with $SNR_{min} = 2$ is only a few metres less than the case with $SNR_{min} = 1.4$, in particular the difference is just 1 metre at low optical power and 3 metres at higher power.
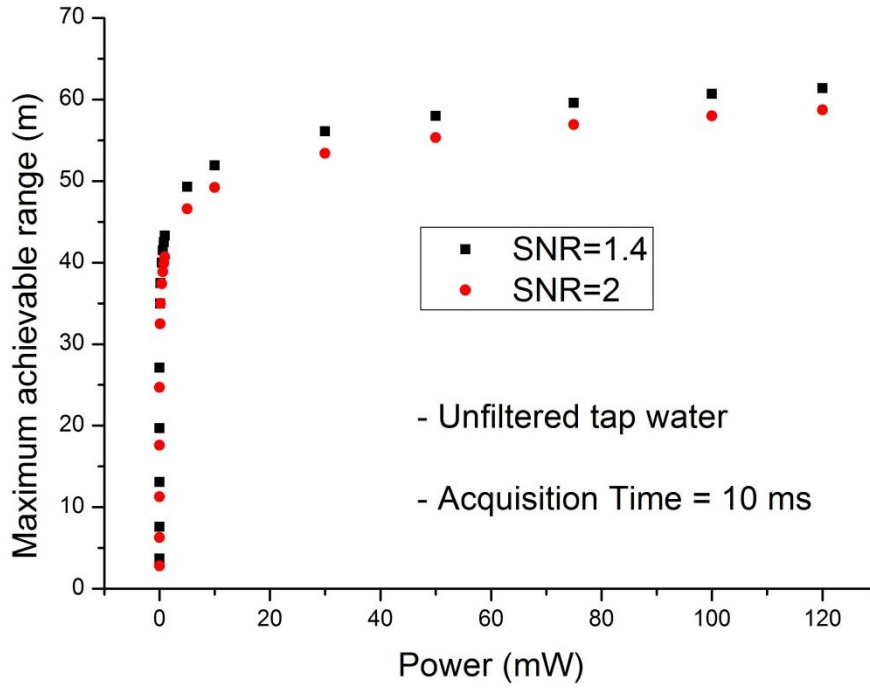
Figure 7.14. Comparison between the maximum achievable range versus average power for two different values of SNR$_{min}$, SNR$_{min}$ = 1.4 and SNR$_{min}$ = 2 for the Spectralon target in unfiltered tap water. For these simulations an acquisition time of 10 ms was chosen.

7.5. Conclusions

The model presented is based on the photon-counting version of the LiDAR equation. Several parameters were included in the model in order to evaluate the time-of-flight ranging performance of the system, including intrinsic and extrinsic parameters. Intrinsic parameters consider the attenuation of each optical element, detector response, and operational parameters. Extrinsic parameters take in account the environmental attenuation, the stand-off distance of the target, and its optical properties. Then, the photon-counting LiDAR equation evaluates the number of photons in the highest bin in the peak, which is used to calculate the signal-to-noise ratio (SNR) at several distances. Every SNR value is compared to a minimum required SNR, in order to evaluate the achievable performance of the system underwater. It is important to note that the evaluation is performed only for an optimised single pixel and not for the entire scan – which may contain several sub-optimal pixels. As seen in Chapter 6, additional signal processing can be performed in order to reconstruct the image, when the pixel-wise cross correlation approach is not able to recover the depth and intensity of the target. This means that a few sub-optimal pixels can be sufficient to discern the target also in photon-starved conditions.

The simulations carried out show how the maximum achievable scanning range depends on several factors, including average optical power, acquisition time, target reflectivity and minimum SNR value. The results suggest that when the average optical power is in the 10's mW high-speed depth images at distances of 30-60 metres in unfiltered tap water may be performed, even if the targets have a relatively low reflectance. In addition, an evaluation of the maximum range achievable with the system described in the Thesis suggests that stand-off distances equivalent to ten attenuation lengths can be achieved under optimum conditions. In Chapter 5, it was demonstrated that depth and intensity information of the white plastic pipe target can be obtained at stand-off distances of 9 attenuation lengths. However, it is important to say that the plastic pipe target has a lower reflectance with respect to the Spectralon target, which was used for these simulations. Therefore, more investigations including the reflectivity of different targets are required in order to validate the predictions of the LiDAR based model.

References

1.   C. Weitkamp, *Lidar - Range-Resolved Optical Remote Sensing of the Atmosphere* (Springer, 2005).

2.   "QuantumScan-7 & 10 Datasheet," (Nutfield Technology, 2004).

3.   R. D. Richmond, and S. C. Cain, *Direct-Detection LADAR Systems* (SPIE, Bellingham, Washington, 2010).

4.   E. Hecht, *Optics* (Addison-Wesley, United States, 1998).

5.   "MPD - PDM Series Datasheet," (Micro Photon Devices, 2013).

6.   N. J. Krichel, A. McCarthy, and G. S. Buller, "Resolving range ambiguity in a photon counting depth imager operating at kilometer distances," Opt. Express **18**, 9, 9192-9199 (2010).

7.   N. J. Krichel, A. McCarthy, I. Rech, M. Ghioni, A. Gulinatti, and G. S. Buller, "Cumulative data acquisition in comparative photon-counting three-dimensional imaging," J. Mod. Opt. **58**, 3, 244-256 (2011).

Chapter 8

Multispectral single-photon depth imaging

8.1. Introduction

This chapter will show how the system described in Chapter 5 can be used to obtain depth and spectral information at a number of different wavelengths. This allows for the estimation of depth, together with reflectivity-based images, providing dimensions and spectral information about each surface of the target. The work described in this chapter reports the experiments performed for a wider project, which is ongoing in collaboration with the Institute of Sensors, Signals and Systems (ISSS) at Heriot – Watt University. Particular attention will be given to the experimental results in order to assess the potential and the limitations of the system when multispectral measurements are performed, and a description of the experimental approach is given in section 8.2. At the same time, the experimental results obtained in free-space and image processing results will be presented in sections 8.3.1 and 8.3.2, in order to show how advanced image processing methods can be used to improve the recovery of depth and colour classification information extracted from experimental data. Section 8.4 will show preliminary experimental results obtained in unfiltered tap water, showing the potential of this approach for identification of foreign objects in underwater scenes.

8.2. Multispectral imaging based on TCSPC technique

The use of the TCSPC technique with multiple wavelengths has previously been investigated [1, 2], raising great interest on multispectral single-photon data in the signal and image processing community [2-4]. In the work presented in [1, 2], a wavelength routing system allowed use of up to six wavelengths simultaneously, with one single-photon detector for each wavelength. Therefore, the systems had the advantage of recording multiple wavelengths simultaneously. However, the number of wavelengths that could be measured simultaneously was limited by the design of the optical system and optomechanics of the wavelength routing systems. In the experiments described in this Chapter, the aim was providing single-photon time-of-flight data with at least 16 different wavelengths for the validation of advanced signal processing algorithms for multispectral single-photon data analysis, and a different approach was required to perform the measurements. Consequently, a scan for each

wavelength was performed with the system in sequence, meaning that the overall scan time for all wavelengths was necessarily long. However, these measurements were used to determine the number of wavelengths required for the analysis to be successful.

In collaboration with Heriot-Watt image processing specialists, Dr. Yoann Altmann, Prof. Andy Wallace, and Puneet S. Chhabra, several experiments were outlined for implementation in free-space and in unfiltered tap water, using different targets in both cases. The same system was used for all the measurements reported in this chapter, therefore the scanning transceiver was reconfigured to be used in either environment.

The widest wavelength range investigated was $500\,\text{nm} - 820\,\text{nm}$, hence the optical components were chosen with appropriate coatings that covered this wavelength range, and at the same time minimised back-reflections in the scanning system. The alignment of the transceiver unit was performed at the weighted wavelength $\lambda = 620\,\text{nm}$. In addition, several preliminary studies were performed in order to address specific requirements of the algorithms. Firstly, the spectral lines of the pulsed laser system had to be chosen in order to limit the overlap between two consecutive spectral lines. This required particular attention in the alignment of the AOTF, in order to minimise the FWHM for each wavelength. A spectral analysis performed with the spectrometer USB Series HR2B805 (by Ocean Optics, USA) revealed a maximum FWHM of approximately 8 nm (refer to section 5.3), which gave an estimation of the minimum step that could be used effectively. In addition, the wavelength range used was limited by the operational wavelength range of the detector and by the optical components of the system. Based on these considerations, the wavelength range $500\,\text{nm} - 820\,\text{nm}$ was chosen for the experiments performed in free space, and the wavelength was varied with a step-size of 10 nm, meaning a total of 33 wavelengths for each target.

Secondly, because of the narrow field of view of the system and the limited space available in the tank, special care had to be taken to ensure that the field of regard (the field seen in a full scan of the given image) was evenly illuminated. This effect was clearly visible in the results reported in Chapter 5, where the limited field of view of the system was an advantage, as it reduced the backscattered and forward scattered light detected. However, for the measurements reported in this Chapter it was important that the area scanned was as uniformly illuminated as possible, since the analysis relied

heavily on the intensity information. Therefore, an objective lens with a shorter focal length of 100 mm (Canon EF100mm f/2.8L IS USM) was selected in order to increase the field of regard of the system. A small number of scans were performed on a checker-board target, a black and white printed test reference target made of a geometrical progression of squares with initial side of 16 mm. The photograph of the checker-board target is shown in Figure 8.1, and the red line shows the area scanned when (a) a 200 mm focal length objective lens and (b) a 100 mm focal length objective lens was used to perform the scan. Below each photograph is the intensity map of 200 × 200 pixel format, with an acquisition time per pixel of 10 ms, and average optical power of approximately 16 nW. The results show the improvement of the field of view with the 100 mm focal length objective lens, and a uniformly illuminated area of approximately 32×32 mm^2 (Figure 8.1b). However, since the area to be scanned in the experiments was approximately 50×50 mm^2, reference scans at each wavelength were performed using the Spectralon target with 10% reflectance, allowing a correction of the non-uniformly illuminated field by software when needed. Hence, each experiment required the scans of the target and the Spectralon panel at each wavelength, with the same operational parameters.

It is worth noting that the intensity maps shown in Figure 8.1 highlight the presence of non-vertical lines in the image from the checker-board target. This is caused both by the non-ideal rotation point of the galvo-mirrors, and the optical axis of the beam incident on the y-mirror being out of the plane of rotation, leading to issues in the vertical direction, in particular. Previous results described in this Thesis were taken over a smaller field of regard than the measurements shown in Figure 8.1.
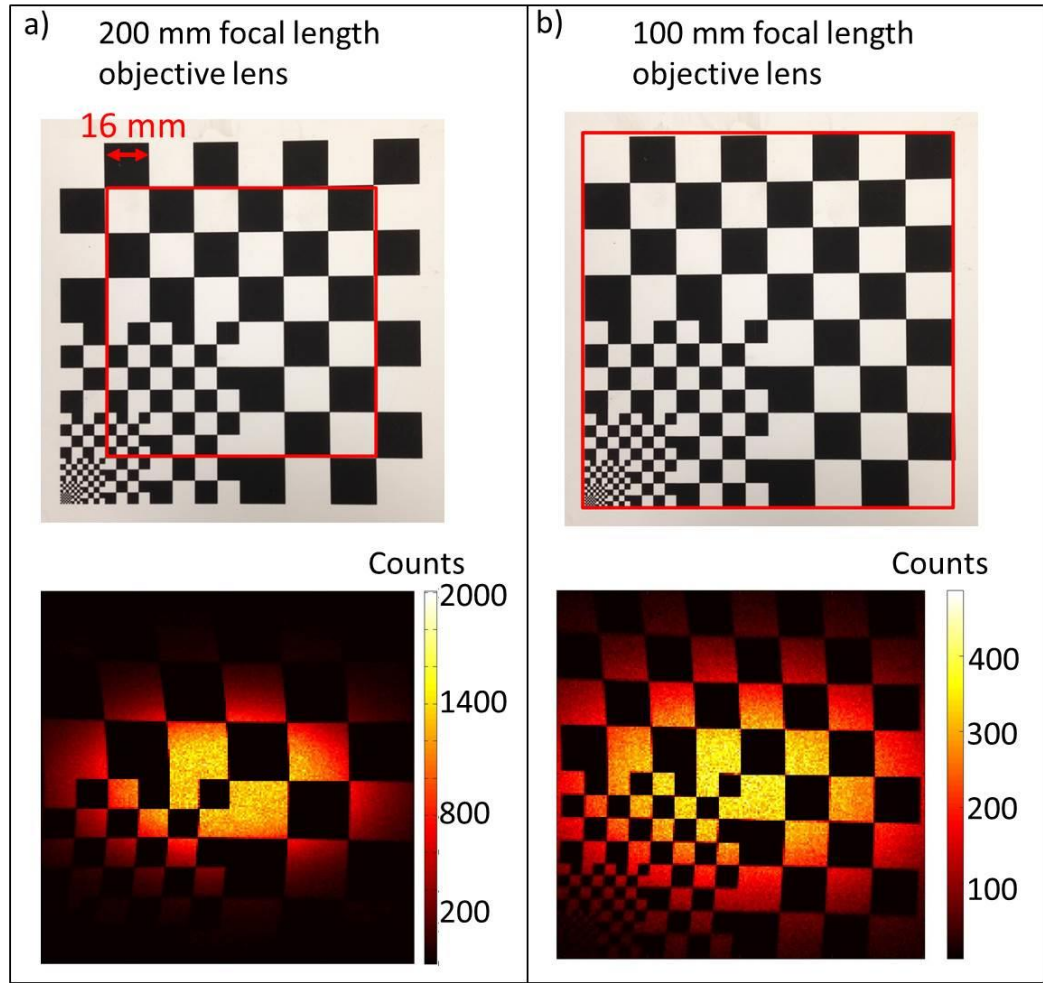
Figure 8.1. Photograph of the test reference target used to investigate the field of view of system. The area highlighted in red on the upper row represents the area scanned when the measurement was performed with (a) a 200 mm focal length objective lens and (b) with a 100 mm focal length objective lens. Below each of the photographs is the corresponding intensity map.

In addition, the position of the targets needed to be fixed for each set of scans in order to ensure that the observed intensity variation was dependent only on the wavelength, and not on a different target position or orientation. Therefore, for each experiment, the scans of the target were performed at each selected wavelength in the spectral range of interest, and then scans of the Spectralon target were obtained as reference. This required that the focus position was maintained for all the scans, hence the focus was adjusted before each experiment using the wavelength $\lambda = 620$ nm, which was the wavelength use for the alignment of the system. However, preliminary measurements also revealed a chromatic focal shift introduced by the system, leading to a variation in the intensity map for the other wavelengths. This effect is shown in Figure 8.2, where

intensity maps of the 10% reflectance Spectralon target are reported for six wavelengths. The area scanned was 50×50 mm^2, the same as the area of the targets used in the experiments. The effect of the focal shift could be corrected by software at all the wavelengths, however the aperture of the objective lens was reduced in order to improve the depth of field of the system and limiting this effect at least for the longer wavelengths (Figure 8.3).
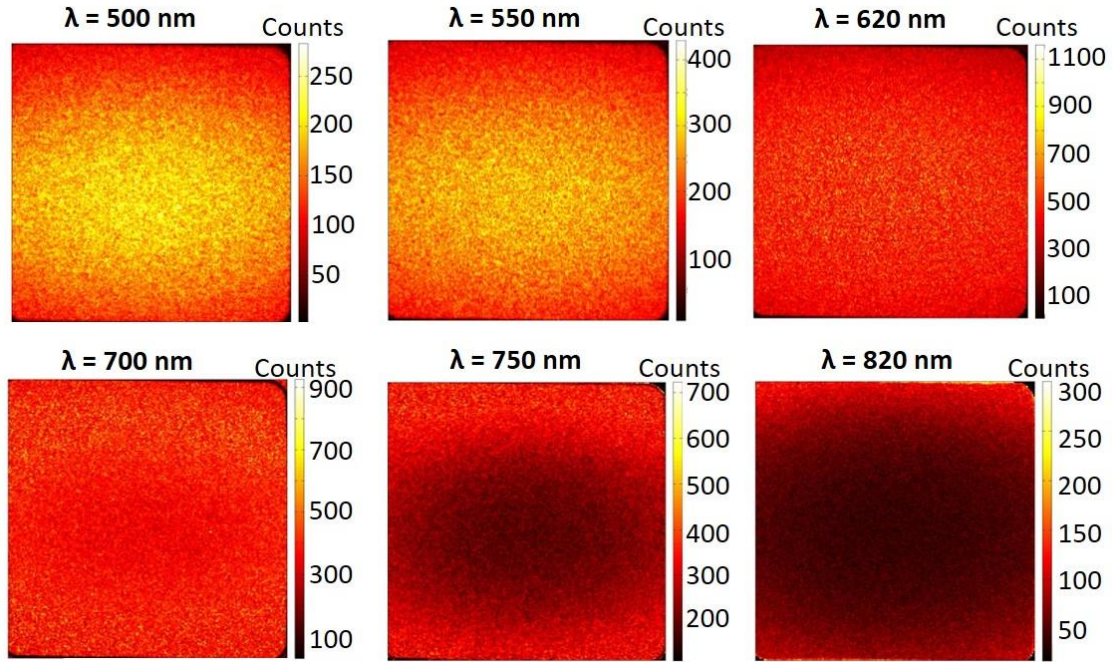

Figure 8.2. Intensity maps of the 10% reflectance Spectralon target for six different wavelengths, with a pixel format of 200×200, 10 ms acquisition time per pixel, and average optical power of approximately 200 nW. In this case the aperture of the objective lens was f/2.8.
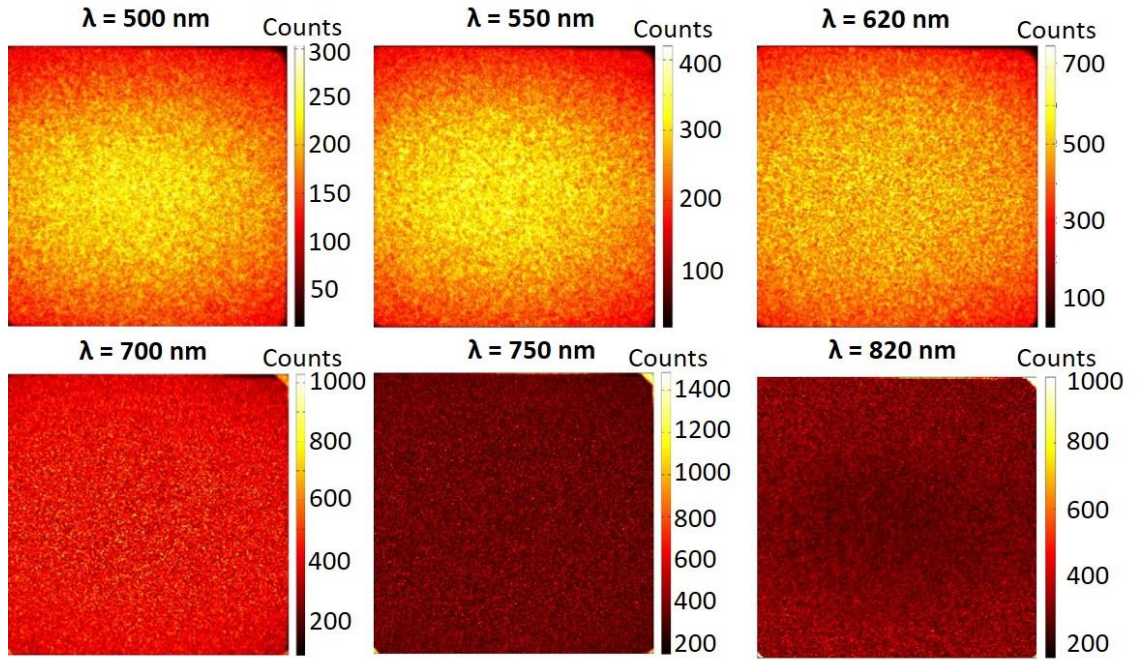
Figure 8.3. Intensity maps of the Spectralon 10% reflectance target for six different wavelengths, with a pixel format of 200 × 200, 10 ms acquisition time per pixel, and average optical power of approximately 500 nW. In this case the aperture of the objective lens was f/8.

It is worth mentioning that the case of an objective lens with 50 mm focal length was also considered. However, preliminary tests showed that the chromatic focal shift was significantly greater than the case of the 100 mm focal length objective lens, resulting in a poor spatial resolution.

8.3. Multispectral experiments in free-space

A set of experiments were performed in air, in order to validate classification and spectral unmixing algorithms. The main system parameters used for the experiments are summarised in Table 8.1, and they were maintained for all the scans performed in sections 8.3.1 and 8.3.2. For each experiment, the average optical power was adjusted in order to be approximately the same for every wavelength. For each target, a scan was performed at the wavelength $\lambda = 620$ nm with a greater pixel format and an acquisition time per pixel of 30 ms. This allowed for the accurate determination of the depth of the target with respect to the Spectralon panel, and placed more attention to the spectral signatures of the target.

Parameter	Note
Targets	- Polymer clays of different colours - Spectralon 10% (50 mm × 50 mm)
Environment	Free space
Target Stand-off Distance	~1.85 metres
Laser System	- NKT Photonics supercontinuum laser source (SuperK EXTREME EXW-12) - Source fibre-coupled to AOTF
Illumination Wavelengths	33 wavelengths with a step of 10 nm in the range 500 nm - 820 nm
Laser Repetition Rate	19.5 MHz (Clock for the TCSPC module and the PPG)
Average Optical Power Range	220 nW – 480 nW (at the target)
Illumination Beam Diameter at Target	~ 300 μm
Pixel format	200 × 200 for multiwavelength scans 400 × 400 for the ground truth
Scan area	50 mm × 50 mm
Acquisition Time Per-Pixel	10 ms for multiwavelength scans 30 ms for the ground truth
Data Acquisition Hardware	HydraHarp 400 by PicoQuant - Synchronization rate of ~19.5 MHz - Internal sync divider: 8 - Acquisition mode: T3 mode
Binning Size	2 ps timing bin width
Detector	Silicon Single Photon Avalanche Diode (SPAD) - PDM series by Micro Photon Devices (fibre receptacle detector) - Used in gated mode
Temporal Response of System	≈ 100 ps at $\lambda = 500$ nm ≈ 70 ps at $\lambda = 620$ nm ≈ 60 ps at $\lambda = 750$ nm ≈ 50 ps at $\lambda = 820$ nm
Objective Lens	Canon EF 100mm f/2.8L II USM - Focal length: 100 mm - F-number: f/8
Background level	Lab in dark conditions (~60 cps – detector gated)

Table 8.1. Summary of the main system parameters used for the experiments in free space.

8.3.1. Joint spectral clustering and range estimation for 3D scene reconstruction using multispectral LiDAR waveforms

Dr. Yoann Altmann, from ISSS (Heriot-Watt University), developed an algorithm for 3D scene analysis of multispectral data. The algorithm is based on a hierarchical Bayesian model [5], whose posterior distribution clusters the scanned area into classes sharing similar mean spectral signatures. The details of the model are reported in [6]. The prior distributions of the model included positivity constraints for the spectrum recovered in each pixel, and a high probability that neighbouring pixels belong to the same class, which basically correlated neighbouring pixels.

The number of classes associated with the number of different mean spectral responses can be chosen by the user, and the results presented in this section were obtained using 30 classes. In order to validate the model, multispectral scans were obtained using the target shown in Figure 8.4a). The target was made of polymer clays of different shades of green and brown, glued onto two leaves fixed on a hardboard painted with green acrylic colour. In this case, the scans were performed using an average optical power of approximately 220 nW. Figure 8.4b) reports the 3D depth profile obtained with the cross-correlation approach, at the wavelength $\lambda = 620$ nm.
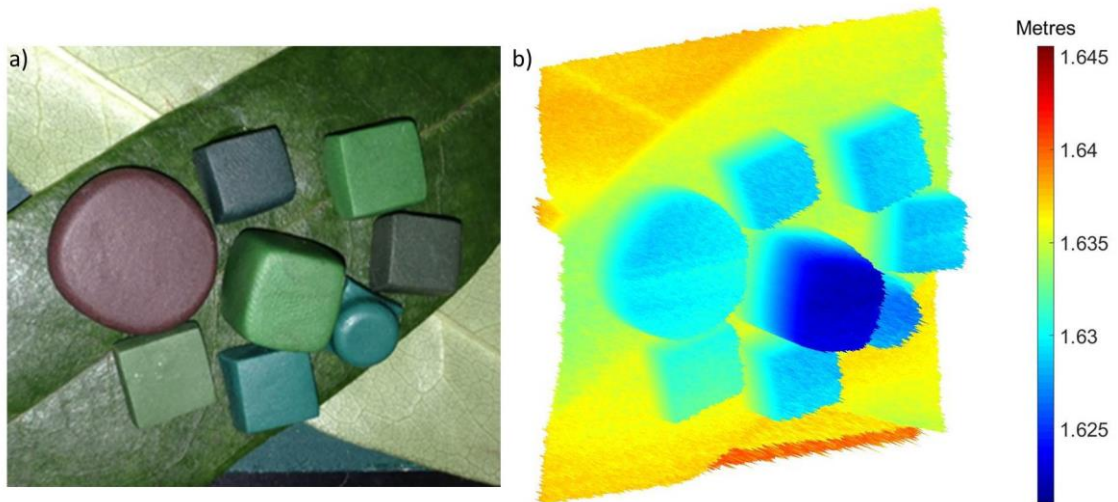

Figure 8.4. (a) Photograph of the target made of clays of different shades of green, plus brown, mounted on two tree leaves fixed on a hardboard painted with green acrylic colour. (b) 3D depth profile of the target, performed using 400×400 pixels, 30 ms acquisition time per pixel, and an average optical power of 220 nW.

Figure 8.5 shows the intensity maps obtained with the cross-correlation approach, for six wavelengths $\lambda_1 = 500$ nm, $\lambda_2 = 550$ nm, $\lambda_3 = 620$ nm, $\lambda_4 = 700$ nm, $\lambda_5 = 750$ nm, and $\lambda_6 = 820$ nm. From the experimental results, it can be observed how the intensity map of the scanned area changes with the wavelength, allowing the spectral signature of each element of the target to be extracted.
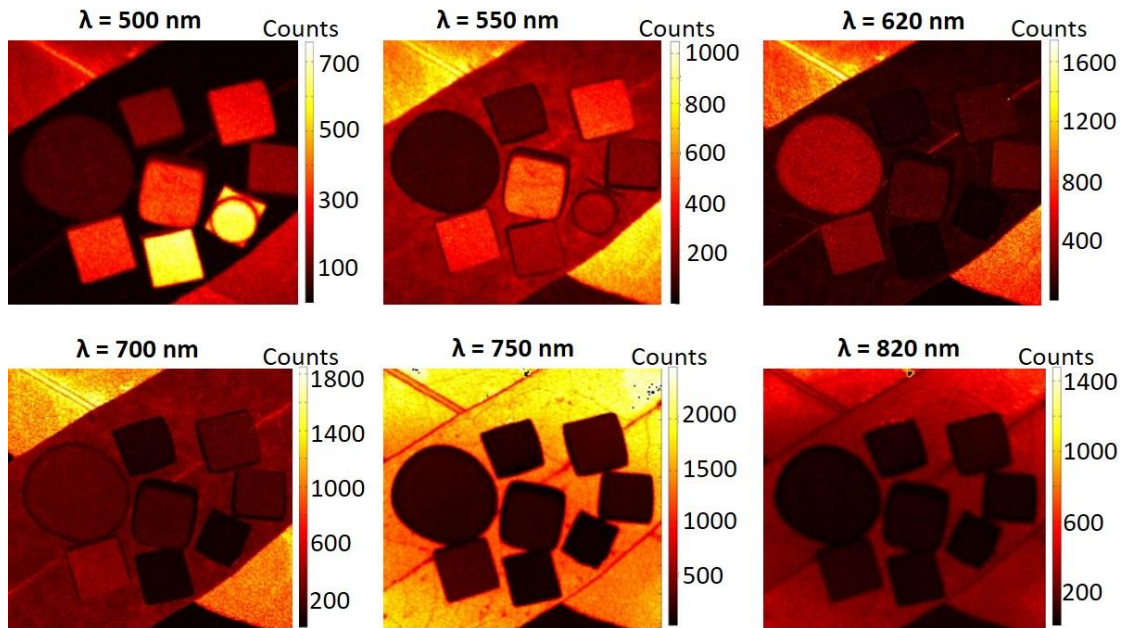

Figure 8.5. Intensity maps of 200 × 200 pixel format, at six different wavelengths, with 10 ms acquisition time per pixel, and average optical power of approximately 220 nW.

This intensity variation allowed the model to discriminate surfaces which are spectrally different, and to identify the material in a given region of the scanned area. For example, Figure 8.6a) shows the estimated spectral classification obtained when 30 classes are used during the analysis. The joint depth/spectral classification is shown in the 3D profile in Figure 8.6b), where only the main 14 classes are shown for clarity. In addition, the estimated spectral signatures of the classes associated with green clays and green leaves can be seen in Figure 8.7, showing how the reflectivity of the main target components changes with the wavelength. All classes are identified with the same colours in both Figure 8.6 and Figure 8.7.

The results show that clays and leaves are clearly spectrally resolved, with sharp separations between clays and leaves. It is evident that one class for each colour of the

clay objects is sufficient for the classification of the clays. However, more classes are needed for the leaves, because of the inhomogeneity of the front and back of the leaves.
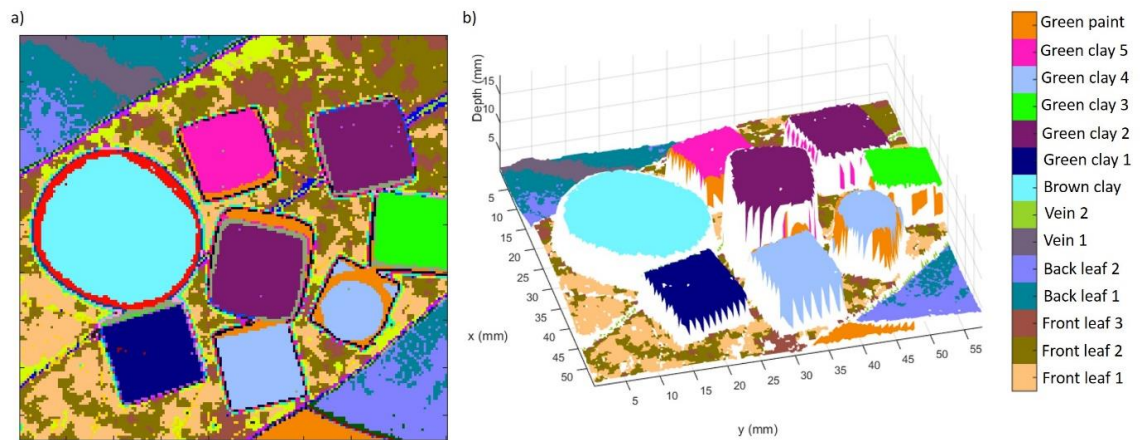

Figure 8.6. (a) Estimated spectral classification and (b) 3D distribution of the main spectral classes identified by the algorithm when 30 classes are used in the analysis. Both from [6].
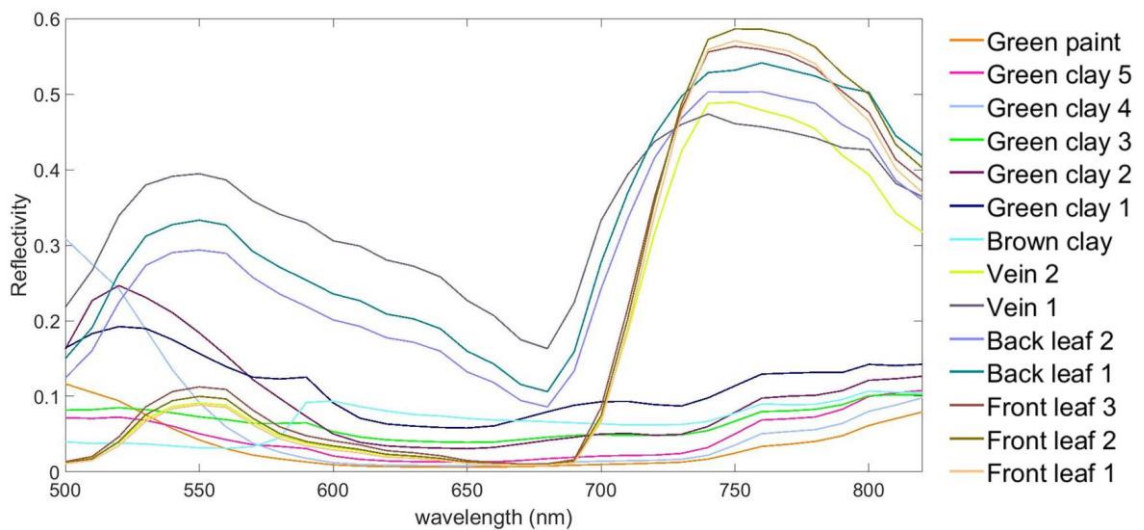

Figure 8.7. Estimated spectral signatures of the spectral classes associated with different green clays and the green leaves. From [6].

Decreasing the number of classes means that some classes merge, while increasing the number of classes can lead to the association of a single spectral class to isolated pixels that present anomalies. Furthermore, it is interesting to note that this model allows us to identify not only spectral variations due to materials and colours, but also due to the orientation of the surface. This can be observed on the edge of the clays, where more spectral classes are associated to the same object. In order to further investigate this

aspect, a new target was built with clays of several colours and different shapes, using more rounded edges and spherical shapes. However, several sharp-edged clay shapes were included for comparison. The clay shapes were glued to a hardboard backplane, and painted with a green acrylic paint different to that previously used in Figure 8.4a). The photograph of this target is shown in Figure 8.8a), while Figure 8.8b) shows the 3D depth profile obtained using the cross-correlation approach, at a wavelength $\lambda = 620$ nm. Figure 8.9 shows the intensity maps obtained with the cross-correlation approach for six wavelengths: $\lambda_1 = 500$ nm, $\lambda_2 = 550$ nm, $\lambda_3 = 620$ nm, $\lambda_4 = 700$ nm, $\lambda_5 = 750$ nm, and $\lambda_6 = 820$ nm. The average optical power used in this experiment was approximately 220 nW. The experimental results show again how the intensity map of the scanned area changes with the wavelength, providing information about the colour and the material of the target. On the intensity map shown in Figure 8.9, the brush strokes from painting are evident on the hardboard at the longer wavelength measurements.
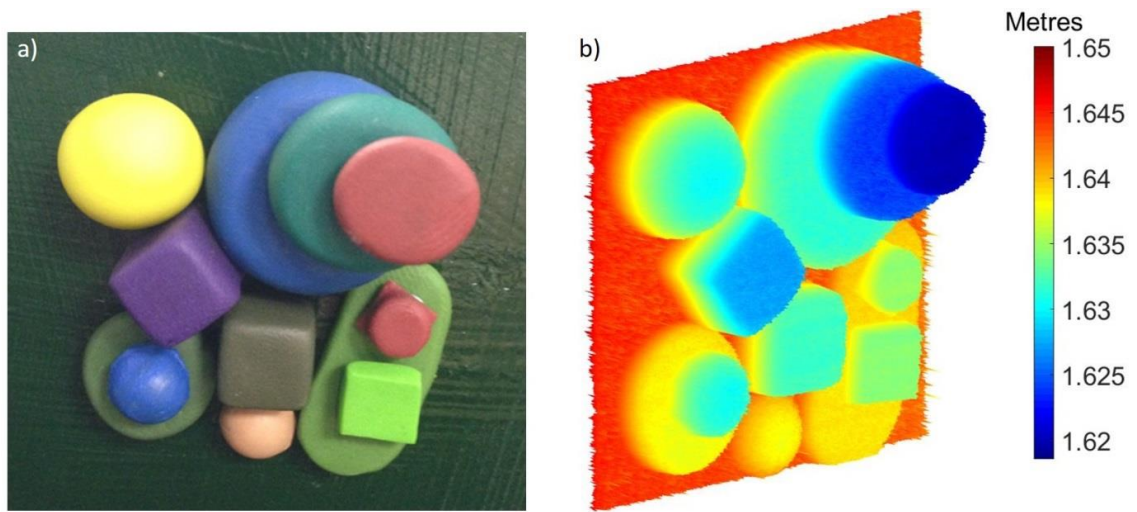

Figure 8.8. (a) Photograph of the target made of clays of different colours, glued on a backboard painted with green acrylic colour. (b) 3D depth profile of the target, performed using 400 × 400 pixels, 30 ms acquisition time per pixel, and an average optical power of 220 nW.
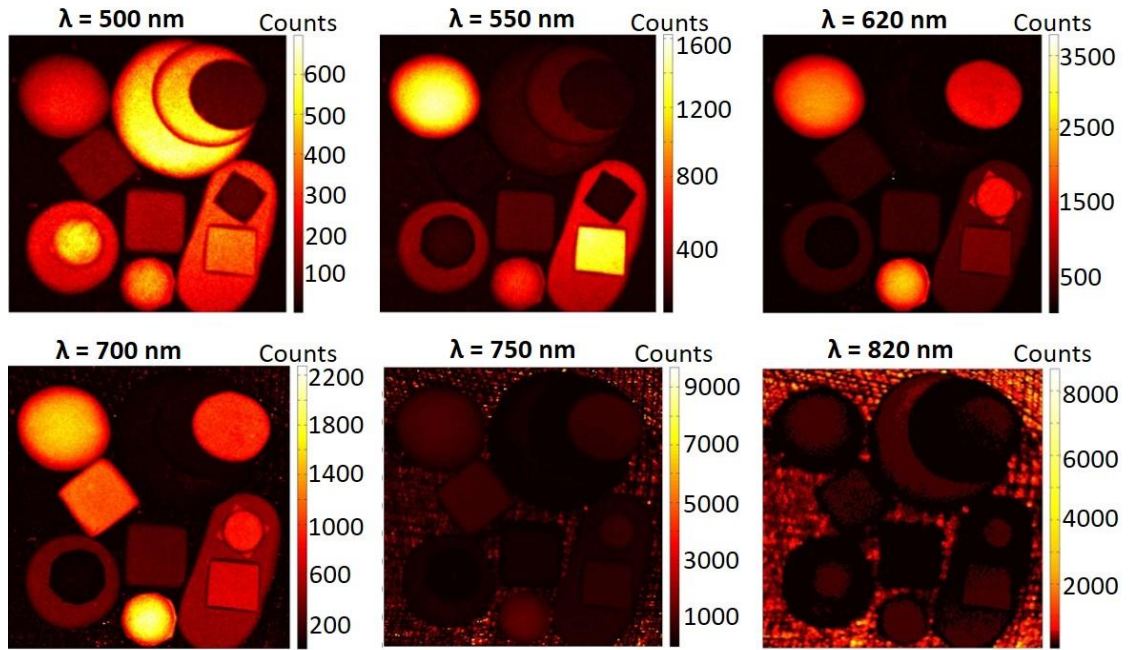
Figure 8.9. Intensity maps of 200 × 200 pixel format, at six different wavelengths, with 10 ms acquisition time per pixel, and average optical power of approximately 220 nW.

It is worth saying that the target was designed to include only clay objects, meaning that the target comprised only spectrally homogeneous objects. This allowed to modify the algorithm such as pixels in the same class are assumed to have the same spectral response [7], and not the same mean spectral response as considered in Figure 8.6.

The modified model was applied associating 30 classes with different colours, and the estimated spectral classification is shown in Figure 8.10a). In this case, more classes were associated with the curved clays because of the round edges, providing a tool to obtain more information about the shape of the target. In Figure 8.10b), the distribution of the main spectral classes is shown jointly with the depth estimation, where the effect of the round edges is clearly visible.
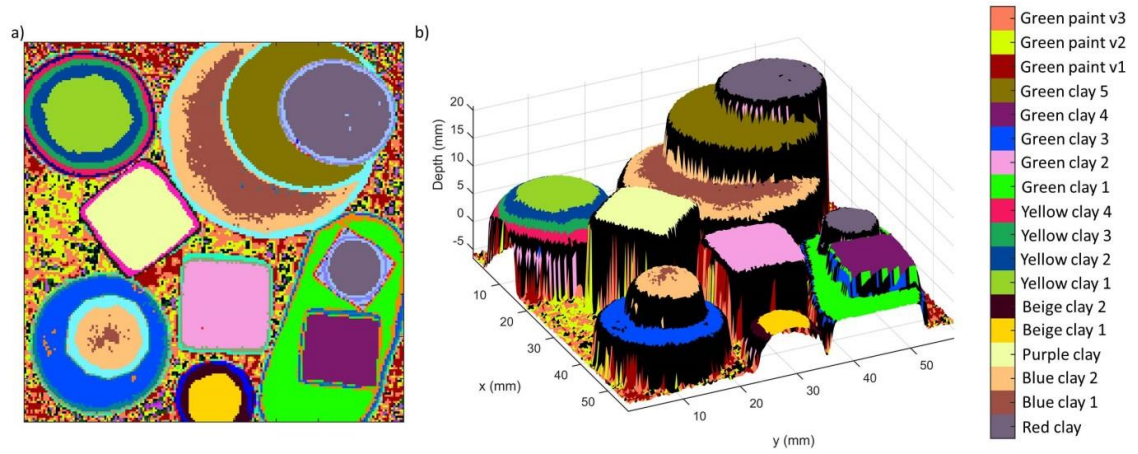
Figure 8.10. (a) Estimated spectral classification and (b) 3D distribution of the main spectral classes identified by the algorithm when 30 classes are used in the analysis. From [7].

It is interesting to note also the presence of several classes associated to the acrylic paint of the hardboard. Although a single colour was used to paint the hardboard, at least three classes can be found associated to it, as shown in Figure 8.11. From the graph it is evident that the classes merge in a single one for wavelengths shorter than $\lambda = 700$ nm, while for longer wavelengths the pattern left due to the brush strokes during painting leads to the splitting into more classes.
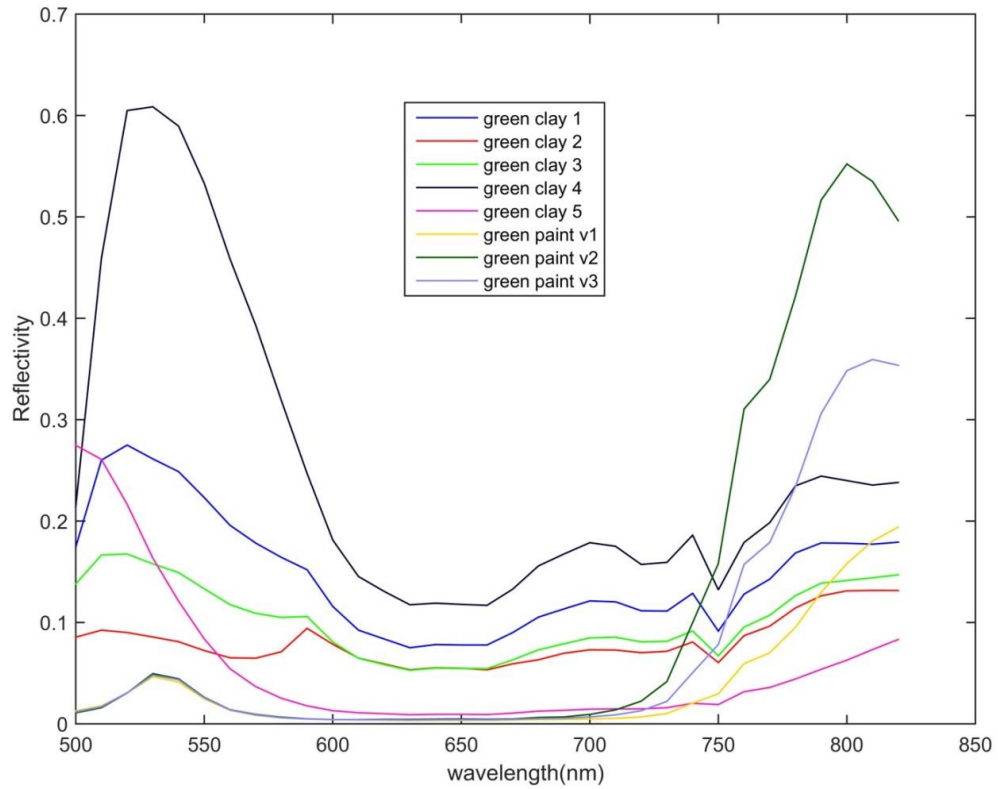
Figure 8.11. Estimated spectral signatures of the spectral classes associated with different green clays and the green paint. From [7].

8.3.2. Range estimation and material quantification from multispectral LiDAR waveforms

The previous section showed that spectral classification is a useful tool to investigate the properties of the target. However, more information can be obtained if the material abundances are identified. With this aim, Dr. Yoann Altmann developed a model in order to build a spectral unmixing algorithm for 3D scene analysis. In each pixel, the model decomposes the spectra of the target elements in a linear combination of known base materials, which are selected manually by the user. In a similar fashion to the spectral classification algorithm, spatial correlations are included considering a smooth variation in the spectral response between neighbouring pixels. Details about the model and algorithm can be found in [8].

The model was validated with multispectral scans performed using a target made of clays of different colours, glued on a black cardboard. Four base colours were used to build the clay objects, and the corresponding proportions for each clay are listed in Table 8.2, while Figure 8.12a) shows the photograph of the target. Figure 8.12b)

reports the 3D depth profile obtained with the cross-correlation approach, at the wavelength $\lambda = 620$ nm and average optical power of 480 nW.

Proportions / Colour	1 - 0	3/4 - 1/4	1/2 - 1/2	1/4 - 3/4	0 - 1	Proportions / Colour
Green	I	II	III	IV		Orange
Blue		V	VI	VII	VIII	Orange
Green		IX	X			Red
Blue	XI	XII		XIII	XIV	Red

Table 8.2. Main colours and proportions used to build the clays for the target. In each case only two colours were mixed, with the proportions shown in the top row. The first and last columns show the two colours that are mixed. In all a set of 14 colour mixtures were used in this measurement, and they are identified with Roman numerals in the photograph shown in Figure 8.12a).
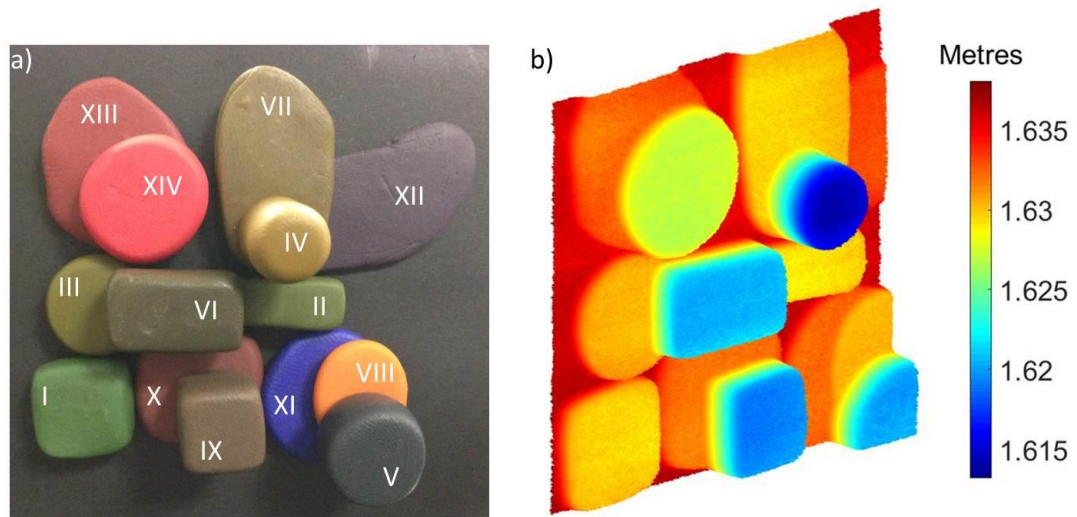
Figure 8.12. (a) Photograph of the target made of clays of fourteen different colours of known abundances, glued on a black cardboard. (b) 3D depth profile of the target, performed using 400×400 pixels, 30 ms acquisition time per pixel, and an average optical power of 480 nW. Each clay shape is identified with Roman numerals, and shown in Table 8.2 with the abundances used.

The intensity maps at six wavelengths obtained with the cross-correlation approach for this target are shown in Figure 8.13, where the different returns at each wavelength can be observed.

Figure 8.13. Intensity maps of 200 × 200 pixel format, at six different wavelengths, with 10 ms acquisition time per pixel, and average optical power of approximately 480 nW.

The estimated spectral signatures of the cardboard and the four base colours used to build the clays are shown in Figure 8.14a). From the graph, it can be seen that the signatures of the cardboard, the green and blue base colours are similar, making the spectral unmixing problem particularly difficult. However, the abundances estimated by the algorithm for each clay are in good agreement with the reference estimations, as shown in Figure 8.14b) and Figure 8.14c). Figure 8.14b) shows the reference images obtained assigning manually the colour proportions for each pixel, while Figure 8.14c) shows the reflectance map obtained with the proposed algorithm.

Significant differences can be observed between the blue clay and the cardboard estimations, despite their similar spectral signatures. This suggests that this method can be used to discriminate between similar colours, and between different materials of the same colour. This is the aim of the next experiment, for which the analysis was performed with a similar algorithm.
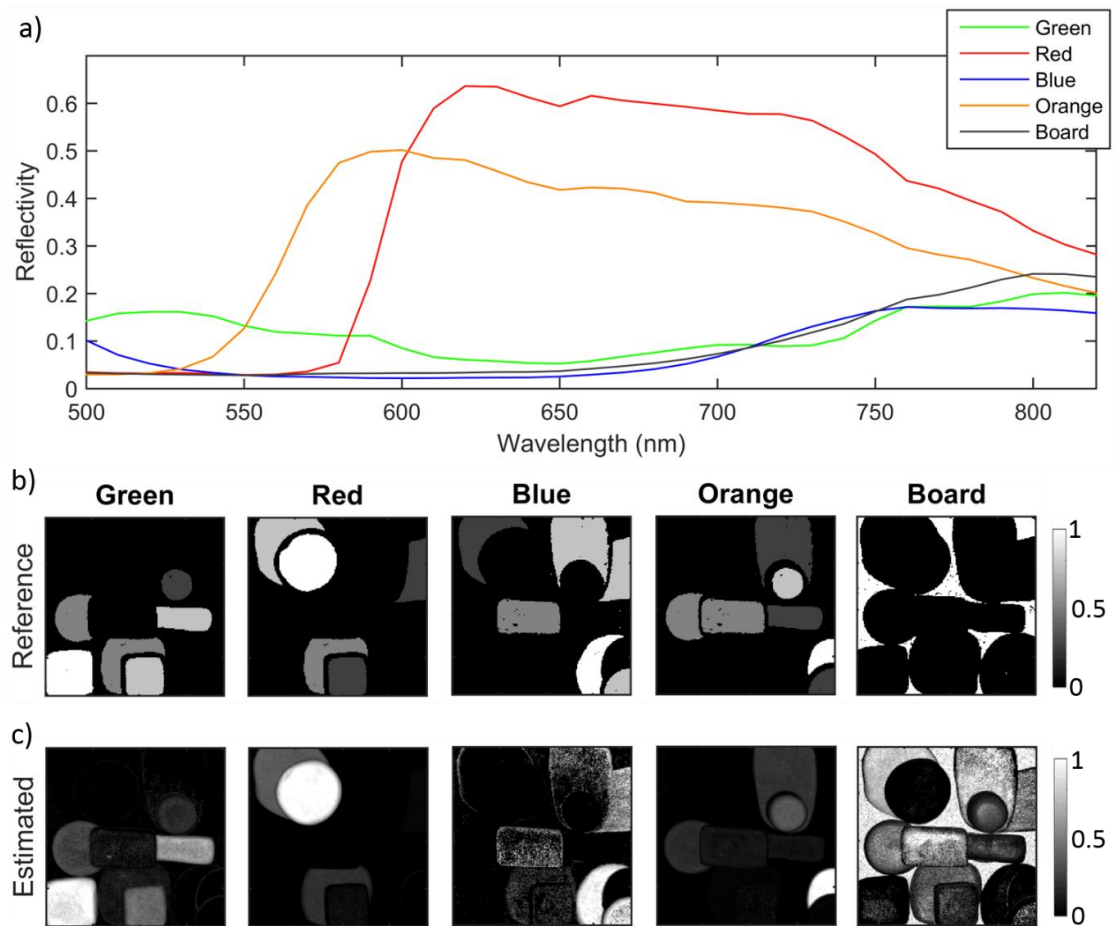
Figure 8.14. a) Spectral signature of the cardboard and the four base colours used to build the target components, as determined from experimental results. b) Reference abundances obtained associating the known base proportions for each pixel. c) Abundances estimated by the model using the spectra shown in a). Each column shows the reference and estimated images when only one base spectral response is used in the decomposition. From [8].

For the next experiment, the target comprised clays with different shades of green, as shown in Figure 8.15a). It is worth noting that in this case, each shade of green was not created by mixing of base colours, meaning that the abundances of base colours were not known. In addition, two leaves were added to include organic material. One of the leaves was reversed, as shown on the top left of the target, while the other leaf, showing the front, is visible on the lower right of the target. Figure 8.15b) shows the depth profile of the target obtained with the cross-correlation approach, at the wavelength $\lambda = 620$ nm, and average optical power of 480 nW. While Figure 8.16 reports the various intensity maps obtained with the cross-correlation approach, at six wavelengths.
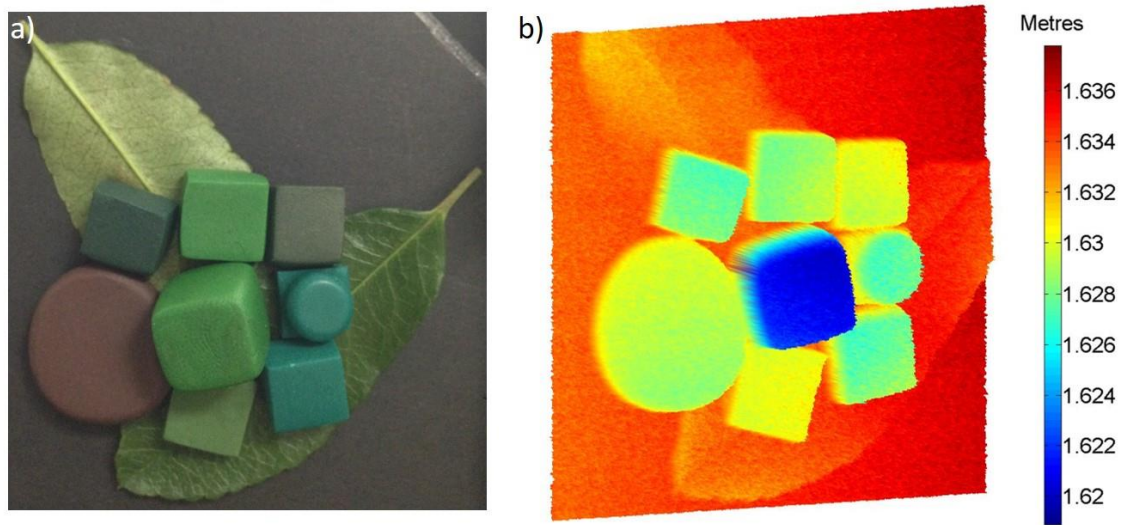
Figure 8.15. (a) Photograph of the target made of clays of different shades of green, plus brown, mounted on two tree leaves fixed on a black cardboard. (b) 3D depth profile of the target performed using 400 × 400 pixels, 30 ms acquisition time per pixel, and an average optical power of 480 nW.
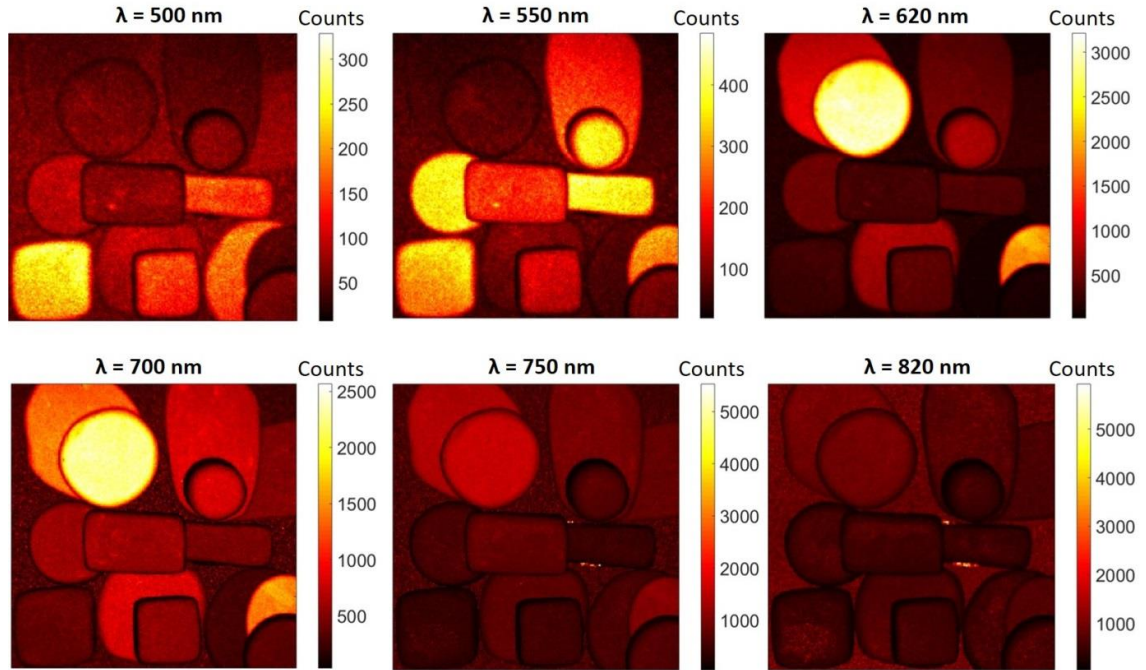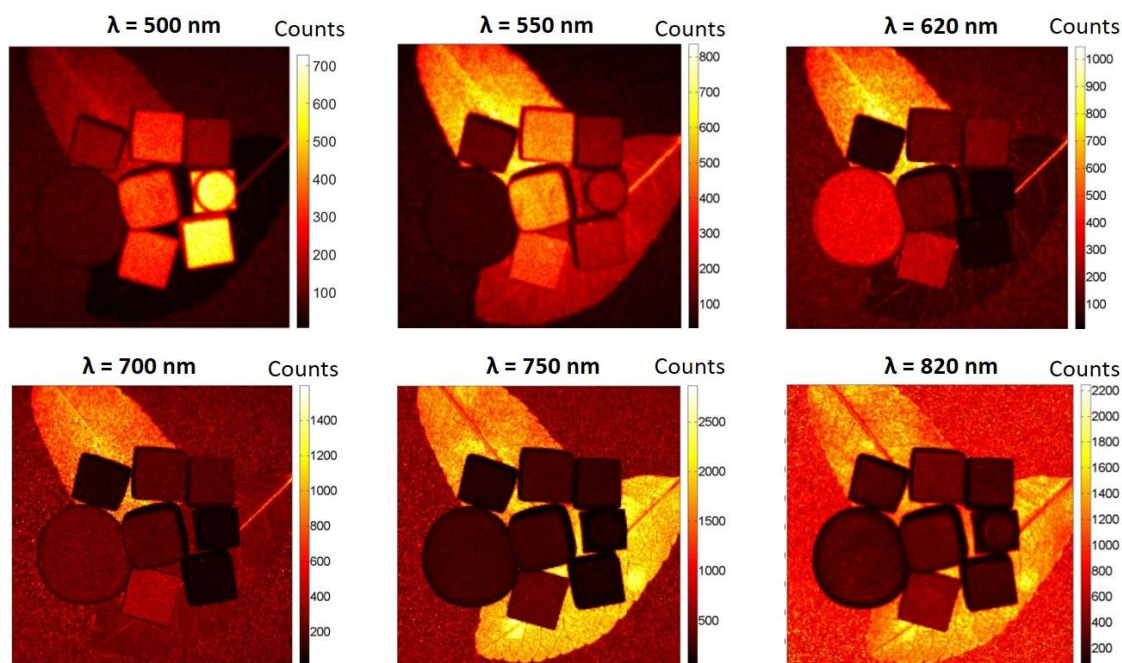
Figure 8.16. Intensity maps of 200 × 200 pixel format, at six different wavelengths, with 10 ms acquisition time per pixel, and average optical power of approximately 480 nW.

Similarly to the previous target, the model estimates the abundances of each clay and the two sides of the leaves. The model was slightly modified in order to optimise the computational time, and the details of the algorithm can be found in [9]. Figure 8.17 shows the estimated abundance maps for each element of the target. Although the green shades are quite similar, the spectral signatures of the leaves are significantly different from the spectral signatures of the clays, as shown in Figure 8.18.
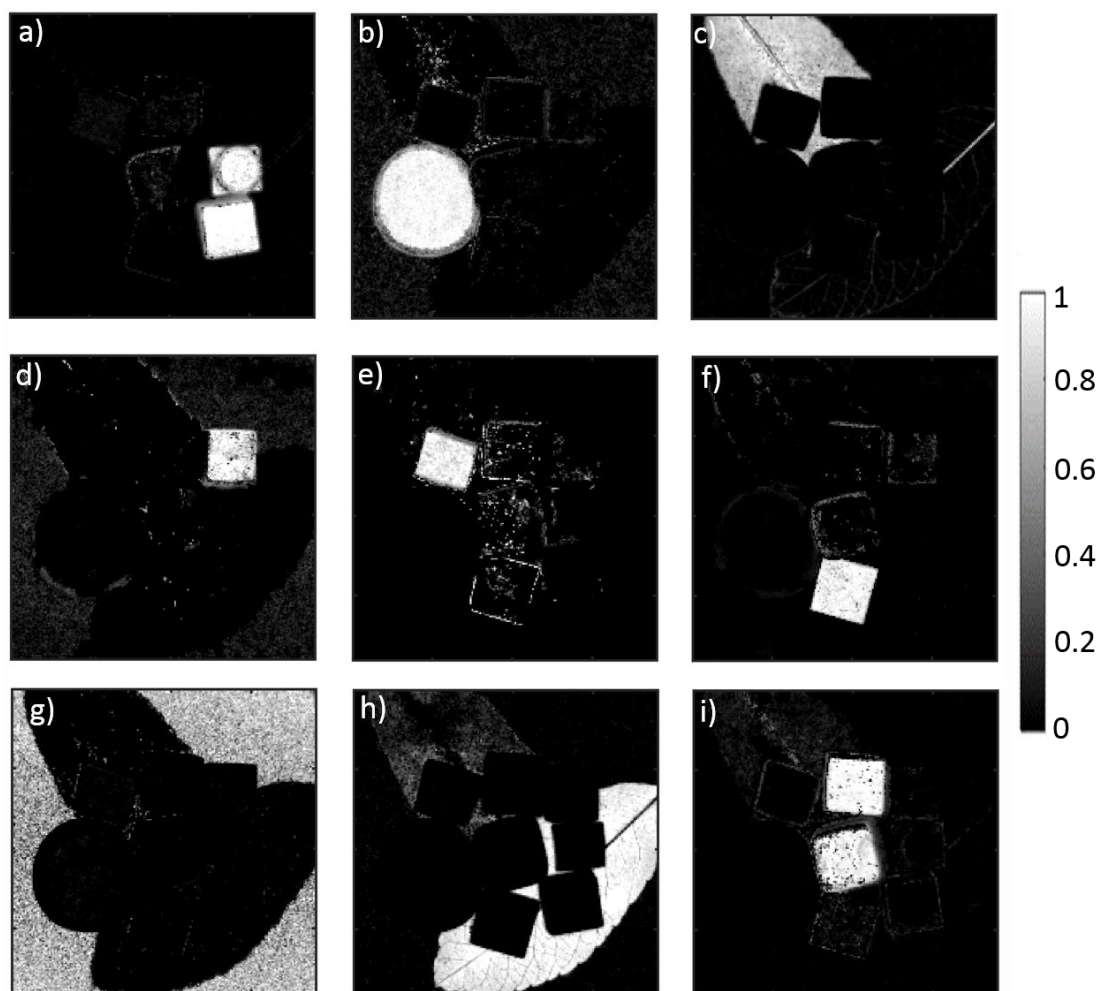
Figure 8.17. Abundance maps estimated by the algorithm for each element of the target. Each map corresponds to the graphs shown in Figure 8.18. From [9].
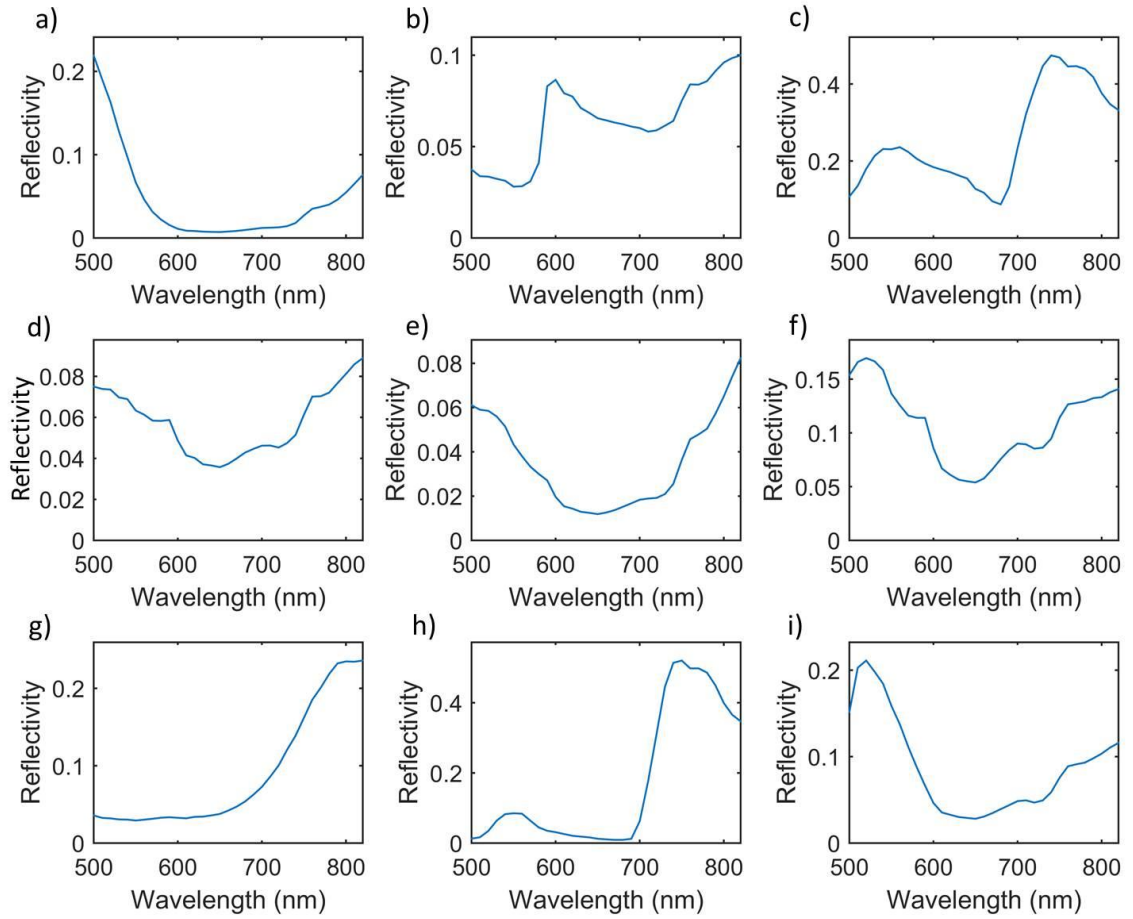
Figure 8.18. Spectral signature of each element of the target. Each graph corresponds to the maps shown in Figure 8.17. From [9].

The results presented in this section showed the potential of multispectral single-photon measurements in conjunction with advanced signal processing. In particular, the developed models allowed the classification of each element of the targets on the basis of their colour and material composition.

The same type of analysis can be performed underwater, opening the way to target recognition in either free-space or underwater. However, in an underwater environment several things should be considered, as will be explained in the following section.

8.4. Underwater target discrimination using multi-spectral LiDAR waveforms

Multi-spectral measurements were also performed underwater, and preliminary results showed promise for target recognition and underwater human-made target discrimination. This section will report some experimental results, which show how single-photon sensitivity can be used, in conjunction with advanced signal processing,

to identify objects partially buried in sand or concrete, or reveal target camouflaged by stones or algae.

Even if the measurement procedure is the same as described in the previous sections, some considerations must be included due to the attenuation of the environment. As discussed in Chapter 4, the attenuation of light in water has a minimum in the green region of the visible spectrum, and strongly increases for wavelengths longer than $\lambda = 700$ nm, making the detection of light difficult at longer wavelengths. In addition, the detection efficiency of the thin junction SPAD used for these experiments has a peak at 48% at the wavelength $\lambda = 550$ nm, and decreases below 30% at $\lambda = 700$ nm, and further decreases for longer wavelengths. Therefore, the combination of attenuation of water and the detector efficiency meant that it was not possible to detect the return from the target at wavelengths longer than $\lambda = 740$ nm. This led to a selection of a smaller operational wavelength range, and 16 wavelengths were selected with a step of 15 nm from $\lambda = 500$ nm to $\lambda = 725$ nm.

An average optical power of 330 nW was used in all the experiments presented in this section, while the pixel format was varied depending on the target composition and dimensions. The acquisition time was 10 ms per-pixel for the multispectral scans, and it was increased to 30 ms to determine the depth at the wavelength $\lambda = 620$ nm.

The main system parameters used for the experiments are summarised in Table 8.3.

Parameter	Note
Targets	- Plastic blocks and metallic spheres partially buried in sand, concrete or stones - Floating targets hidden by seaweed
Environment	Unfiltered tap water
Target Stand-off Distance	~1.33 metres in water
Laser System	- NKT Photonics supercontinuum laser source (SuperK EXTREME EXW-12) - Source fibre-coupled to AOTF
Illumination Wavelengths	16 wavelengths with a step of 15 nm in the range 500 nm -725 nm
Laser Repetition Rate	19.5 MHz (Clock for the TCSPC module and the PPG)
Average Optical Power Range	~ 330 nW (before the objective lens)
Illumination Beam Diameter at Target	~ 300 μm
Pixel format	Scan area = 50 mm × 50 mm 200 × 200 for multi-wavelength scans 400 × 400 for ground truth Scan area = 75 mm × 75 mm 300 × 300 for multi-wavelength scans 500 × 500 for ground truth
Acquisition Time Per-Pixel	10 ms for multiwavelength scans 30 ms for the ground truth
Data Acquisition Hardware	HydraHarp 400 by PicoQuant - Synchronization rate of ~19.5 MHz - Internal sync divider: 8 - Acquisition mode: T3 mode
Binning Size	2 ps timing bin width
Detector	Silicon Single Photon Avalanche Diode (SPAD) - PDM series by Micro Photon Devices (fibre receptacle detector) - Used in gated mode
Temporal Response of System	≈ 100 ps at $\lambda = 500$ nm ≈ 70 ps at $\lambda = 620$ nm ≈ 60 ps at $\lambda = 725$ nm
Objective Lens	Canon EF 100mm f/2.8L II USM - Focal length: 100 mm - F-number: f/8
Background level	Lab in dark conditions (~60 cps – detector gated)

Table 8.3.   Summary of the main system parameters used for the experiments in unfiltered tap water.

Several targets were scanned in unfiltered tap water, at a stand-off distance in water of 1.33 metres. For example, Figure 8.19 shows the photograph of four targets and the 3D profiles obtained with the pixel-wise cross-correlation approach. In Figure 8.19a) and Figure 8.19b), the targets were made of metallic spheres painted with textured charcoal spray painting, and partially buried in sand and concrete, respectively. In Figure 8.19a), a piece of plastic of approximately 1 cm was added to the target, in order to include also a non-metallic element. In Figure 8.19c) and Figure 8.19d), the targets were made of sand and concrete, respectively, in order to study the case of scans with the same background as Figure 8.19a) and Figure 8.19b) but without metallic objects. For each target, Figure 8.19 shows also the 3D depth profile of 400×400 pixel format, and 30 ms acquisition time per pixel, obtained with the cross-correlation approach.
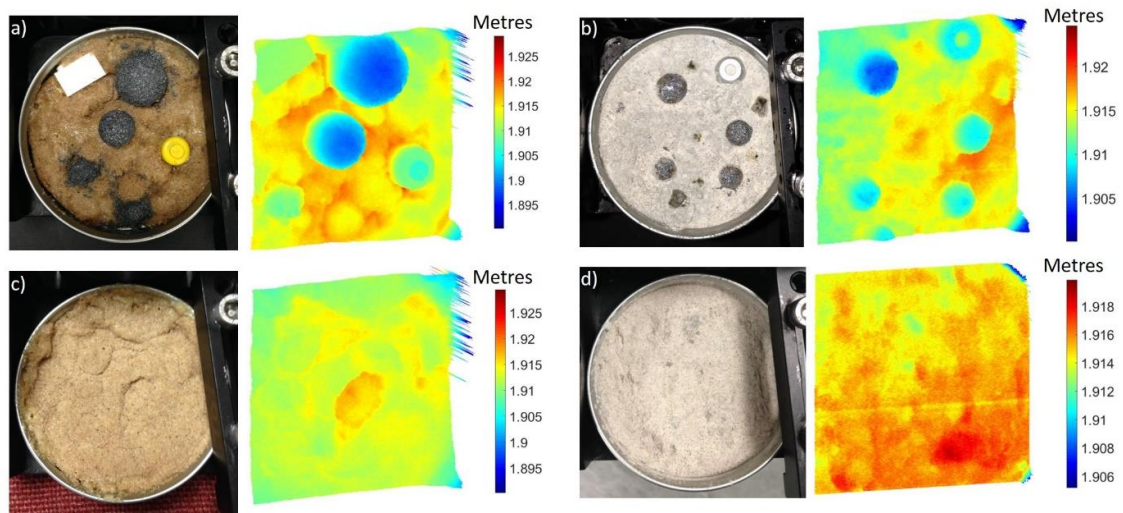
Figure 8.19. Each figure shows the photograph of the target on the left and the 3D depth profile on the right. The 3D depth profiles of the targets were obtained with 400×400 pixel format, 30 ms acquisition time per pixel, and an average optical power of 330 nW, at the wavelength $\lambda = 620$ nm. The analysis was performed with the pixel-wise cross-correlation approach.

From the 3D depth profiles, it can be seen that the objects included in the target are clearly resolved. However, solely from the 3D depth profile it is difficult to classify them as metallic objects. More information can be obtained from the spectral response. For example, Figure 8.20 shows the intensity maps for the target a) obtained with the cross-correlation approach, and only the results at five wavelengths are displayed, $\lambda_1 = 500$ nm, $\lambda_2 = 560$ nm, and $\lambda_3 = 620$ nm, $\lambda_4 = 680$ nm, $\lambda_5 = 725$ nm, with a pixel

format of 200×200, and 10 ms acquisition time per pixel. From the intensity maps, the plastic objects can be discriminated, while the rusted spheres have a return similar to the return from the sand at each wavelength, making it difficult to distinguish them. However, the shape is well defined, and combining depth and intensity information it is possible to recognise them as spherical objects.

An algorithm was developed by Puneet Chhabra and Prof Andy Wallace at Heriot-Watt University, which is based on a semi-supervised learning approach [10]. The algorithm builds the point cloud of the area scanned, resulting in a 3D plot combining depth and spectral information, and an example is shown in Figure 8.21. The main contribution of the algorithm is that it is able to discriminate the experimental target signatures, in order to automatically identify both material and geometrical characteristic of the different objects in the scanned area [11].

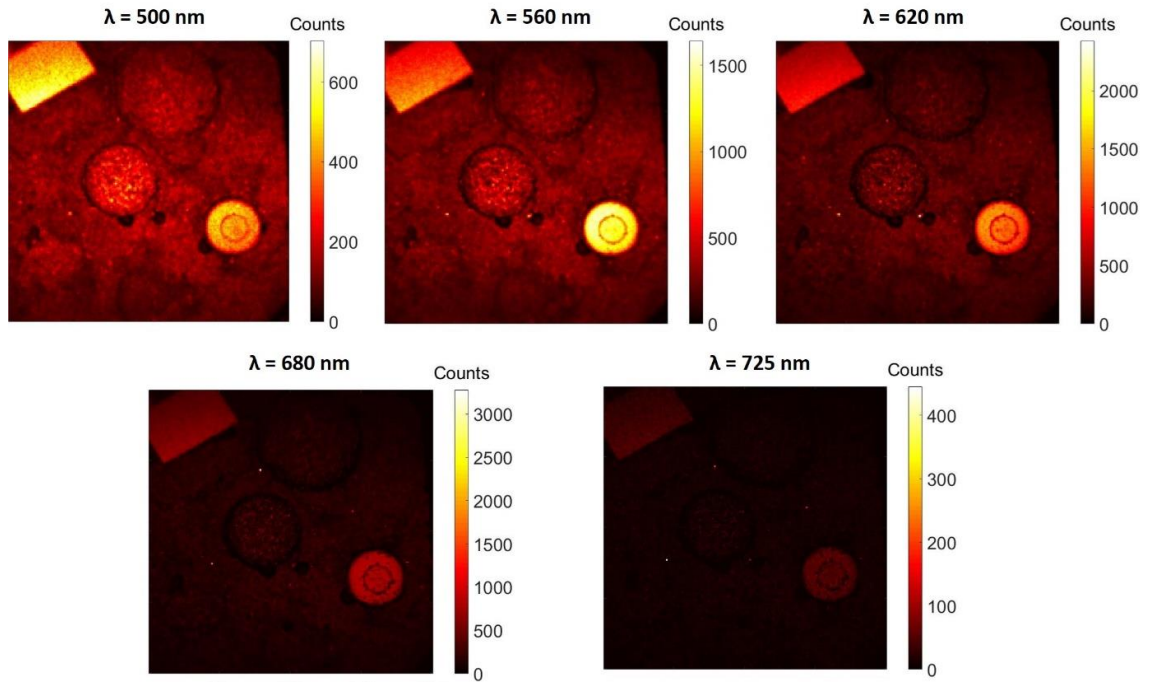*Figure 8.20. Intensity maps obtained with the cross-correlation approach for five wavelengths, $\lambda_1 = 500$ nm, $\lambda_2 = 560$ nm, and $\lambda_3 = 620$ nm, $\lambda_4 = 680$ nm, $\lambda_5 = 725$ nm. The pixel format was 200×200, with 10 ms acquisition time per pixel, and an average optical power of 330 nW.*
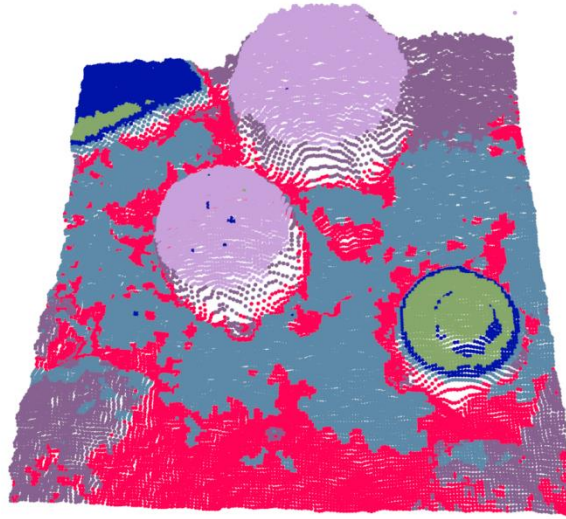
Figure 8.21.   Point cloud plot of the target, combining depth and spectral information. From [11].

Work is ongoing on the analysis with the same algorithm of the scans performed with the other targets shown in Figure 8.19. However, these preliminary results show promise for the multispectral single-photon measurements for underwater mine discrimination. The main limitation here seems due to the overall acquisition time for each set of measurements. In all the measurements reported in this chapter, a high pixel format and a long acquisition time per-pixel were chosen in order to validate the several algorithms developed. Therefore, a lower pixel format and shorter acquisition time per scan will greatly improve the overall acquisition time for each set. In addition, the depth can be estimated from one of the scans performed for the multi-wavelength measurements, avoiding the scan with a greater pixel format and longer acquisition time per pixel.

Two other cases were considered to validate the model described in [11] and to develop new analysis algorithms.   Figure 8.22 shows the results of multispectral scans performed using a target made of spherical metallic objects camouflaged in a rocky environment. In this case, the scanned area was approximately 7.5×7.5 cm^2, and the pixel format was increased accordingly. Figure 8.22a) shows the photograph of the target, while Figure 8.22b) shows the 3D depth profile obtained performing a scan of 500×500 pixel format and 30 ms acquisition time per-pixel. Figure 8.22 c) shows the intensity maps obtained performing scans of 300×300 pixel format and 10 ms

acquisition time per-pixel, and the cross-correlation approach was used to estimate the depth and the number of counts per pixel.
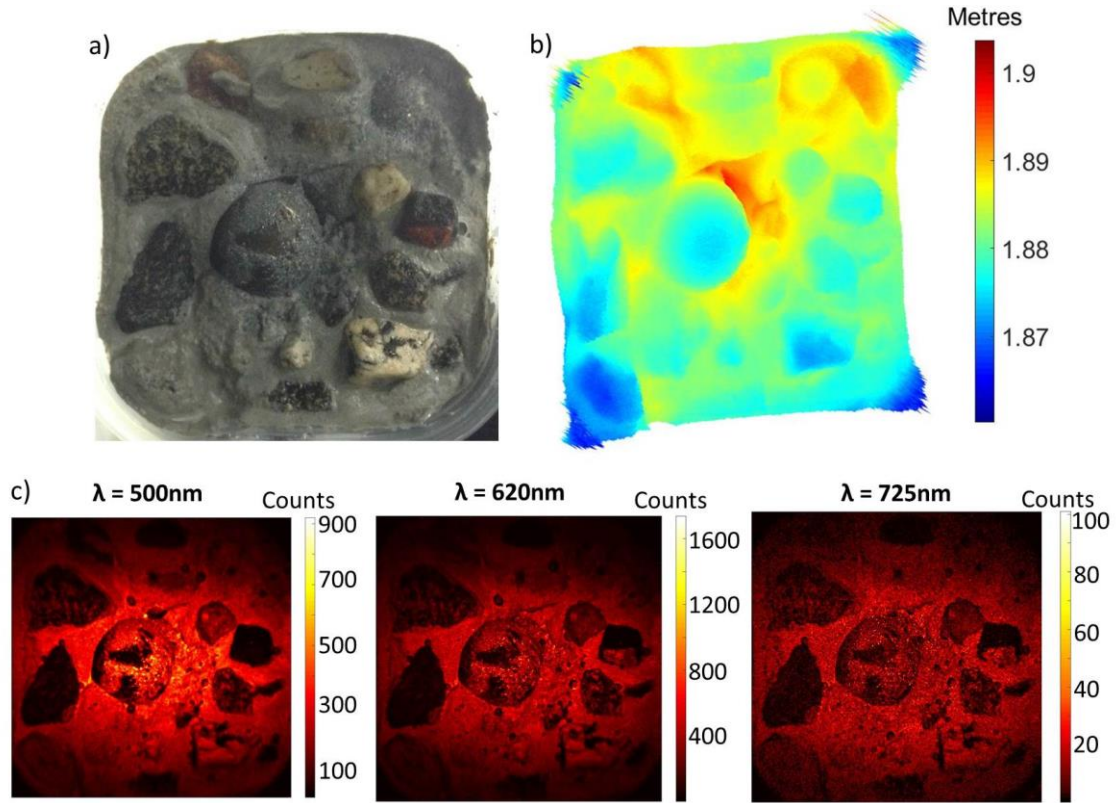
Figure 8.22. a) Photograph of the target made of clays of different colours of known abundances, glued on a black cardboard. b) 3D depth profile of the target, performed using 500×500 pixels, $30\,ms$ acquisition time per pixel, and an average optical power of $330\,nW$. c) Intensity maps obtained with the cross-correlation approach, using a 300×300 pixel format, and an acquisition time per-pixel of $10\,ms$. Three wavelengths are displayed, $\lambda_1 = 500\,nm$, $\lambda_2 = 620\,nm$, and $\lambda_3 = 725\,nm$.

The results suggest that the case of rusted metallic objects surrounded by stones could be easier for mine discrimination, as the stones seem having a spectral signature that differs greatly from the spectral signature of the metallic objects. In addition, it is worth noting that showing only three wavelengths allows the highlighting of differences in each component of the target. This suggests another method to further reduce the acquisition time for a set of scans, as reducing the number of wavelengths implies a reduced overall acquisition time for a set of measurements. However, this comes at the cost of a reduced amount of spectral information, and a study on the minimum number

of wavelengths needed to discriminate different objects is the main priority in order to reduce the overall acquisition time for a set of scans.

Another experiment was performed using a target built with the aim of simulating floating mines hidden by marine vegetation. The floating mines were simulated with metallic spheres painted with textured spray colour, and a piece of white plastic was added to include a non-metallic material. Five different aquatic plants were used to hide the floating targets, and a photograph of the entire target is shown in Figure 8.23. The scan was performed over an area of 7.5×7.5 cm^2, and it is highlighted in red in Figure 8.23. In addition, the figure shows where the floating targets were located.

Figure 8.24 reports the intensity maps at five different wavelengths obtained with the pixel-wise cross-correlation approach. In this case, the targets can be easily discriminated from the environment, mainly because the algae absorb visible wavelengths for the photosynthesis process. While for wavelengths longer than $\lambda = 700$ nm, the light is no longer involved in the photosynthesis process, hence it is not absorbed by the algae [12]. This allows us to discriminate the vegetation and the other objects included in the scene.
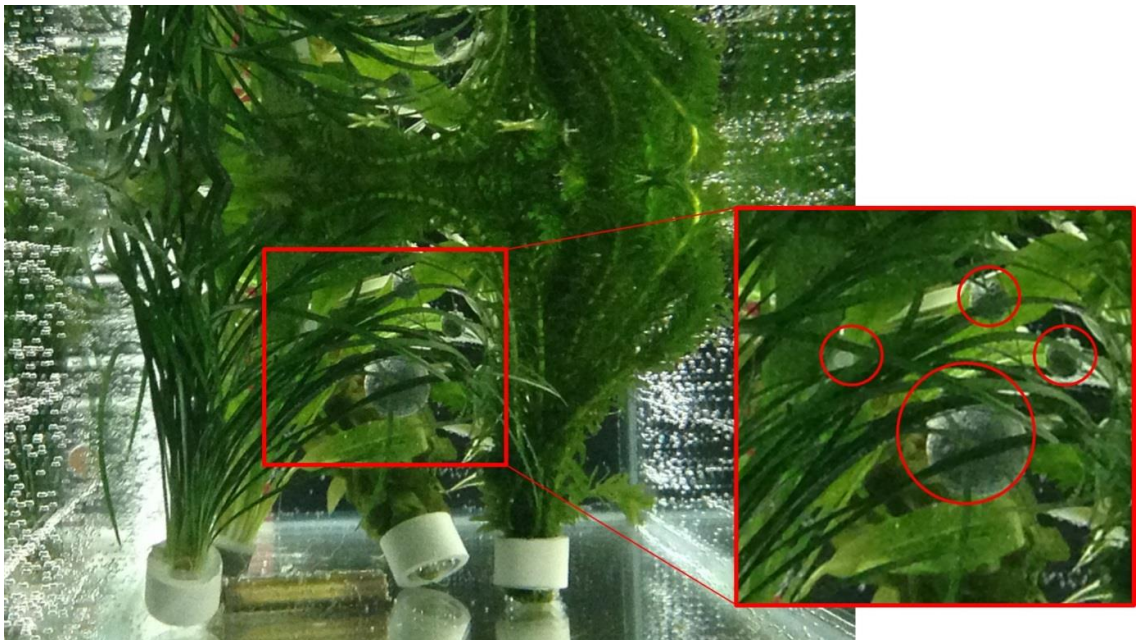
Figure 8.23. Photograph of underwater target simulating floating mines hidden by marine vegetation. The area in red shows the scanned area (7.5 cm × 7.5 cm), and highlights the hidden targets, three metallic rusted spheres and a small piece of white plastic.
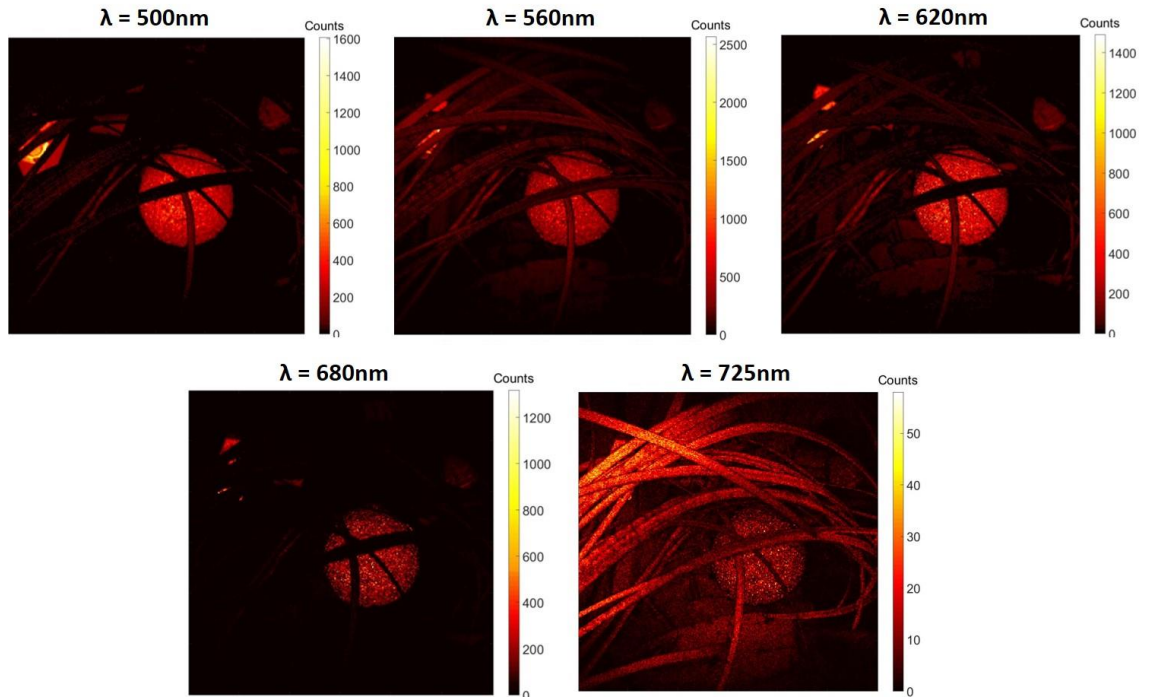
Figure 8.24. Intensity maps of 300 × 300 pixel format, 10 ms acquisition time per pixel, and average optical power of approximately 330 nW. The analysis was performed with the pixel-wise cross-correlation approach, and the results at five different wavelengths are reported.

Also in this case, there is no need to use all the 16 wavelengths selected to discriminate the floating targets. Figure 8.24 shows how few of the wavelengths selected provide enough information to discriminate the floating targets from vegetation, greatly reducing the overall acquisition time for a set of scans and making a clear contribution to the future practical implementation of this approach.

In addition, work is ongoing on another algorithm to investigate the possibility to identify targets in the scanned scenario and remove the surrounding environment from the image. This would allow, in conjunction with a reconstruction algorithm, to build an entire image of the partially hidden targets. However, such a model will require further investigation on the minimum number of wavelengths to use, different acquisition times, and different camouflages and target materials.

8.5. Conclusions

The preliminary results presented in this chapter show the potential of multispectral single-photon depth imaging in target discrimination and recognition, in free-space and underwater environments.

Several laboratory-based measurements were performed in free-space, using 33 wavelengths incremented by 10 nm, and average optical power in the range 220 nW to 480 nW, using a 200×200 pixel format, and 10 ms acquisition time per pixel. Joint depth estimation and spectral information were obtained for 3D scene reconstruction, validating several algorithms developed by Dr. Yoann Altmann, Puneet S. Chhabra, and Prof. Andy Wallace at Heriot-Watt University. Different targets were constructed to perform the experiments.

A set of experiments were designed to investigate classification due to colour and shape of each component of the targets in free-space, based on the spectral signature estimated in the investigated wavelength range. Once identified the spectral signature of each component of the targets, the scanned area was clustered into classes, resulting in a 3D representation in conjunction with the defined classes. This model allows for the identification of not only spectral variations due to materials and colours, but also due to the orientation of the surface, providing a useful tool to discriminate the shape of the targets.

Other experiments were performed in order to validate a model developed to investigate quantification of colour abundances in targets. With this aim, a target was constructed with clays of different colours, obtained as known combinations of four base colours. The spectral unmixing algorithm decomposes the spectra of the target elements in a linear combination of the base materials in each pixel. This allowed us to quantify abundances of materials whether or not the amount of base materials was known.

These results obtained in free-space showed promise in target discrimination, and more experiments were performed in unfiltered tap water. The same experimental setup was used to perform multispectral measurements underwater, and a few limitations were highlighted. Because of the strong attenuation of light in water and the low detection efficiency at longer wavelengths, return from the target disappeared for wavelengths

longer than $\lambda = 740$ nm. Hence, a smaller operational wavelength range was chosen for the experiments performed in unfiltered tap water, and 16 wavelengths were selected with a step of 15 nm from $\lambda = 500$ nm to $\lambda = 725$ nm.

Several targets were built in order to simulate man-made targets, partially buried in sand or concrete. Targets made only of sand or concrete were built in order to compare the cases with and without mines. Work is ongoing on the development of appropriate algorithms that discriminate mines underwater when multispectral single-photon data are available. The first model was developed to discriminate metallic objects partially buried in sand. Preliminary results showed that the algorithm is able to identify both material and geometrical characteristic of the different objects in the scanned area, providing a strong contribution to the underwater mine recognition research.

More targets with metallic objects were constructed in order to simulate mines camouflaged by stones, and floating mines covered by algae. Multispectral measurements were performed using these two targets in unfiltered tap water. The results were analysed only with the cross-correlation approach, showing how the mines can be discriminated from the natural components in the target without performing any spatial correlation. This strongly suggests that multispectral single-photon measurements have the potential of being a useful technique in underwater mine discrimination.

However, the main limitation of the approach described in this chapter was the long overall acquisition time which can be reduced for future applications as the algorithms are further developed. Firstly, it is worth noting that the scan performed with a longer acquisition time to estimate the depth is not necessary, it was an additional step performed in order to simplify the analysis and obtain a precise depth estimation. In general, the depth can be estimated from one of the scans performed with a shorter acquisition time per pixel. Alternatively, depth profiles can be obtained performing an average between the depth at each wavelength, providing an improved depth estimation. In addition, the preliminary results showed that a fewer number of wavelengths can be selected, drastically driving down the overall acquisition time. An investigation of the minimum number of wavelengths required by the algorithms will be part of future work, and the experimental setup and measurement procedure can be modified

consequently. For example, a wavelength routing system allows the use of multiple wavelengths at the same time [1, 2]. However, this is at the cost of using as many detectors as the number of wavelengths selected. Future work will examine the use of multiple wavelengths simultaneously in such single-photon depth imaging systems. If only four wavelengths are selected for the multispectral measurements, the same experimental setup used to obtain the results of this chapter can be used in conjunction with a wavelength routing system as described in [2]. In this case, the overall acquisition time would decrease from several hours to a few minutes. Additionally, a smaller pixel format and a lower acquisition time per pixel can further reduce the overall acquisition time.

If more wavelengths are required, a different approach should be considered. For example, the system used for the experiments described in this chapter can be used in conjunction with an interface unit programmed to control the software of the AOTF [13]. With appropriate modification to the software, the system would be able to automatically switch from one wavelength to the next, removing the time spent by the user for launching a new scan. This would contribute to a reduction of a few hours of the overall acquisition time, and, to further decrease it, the pixel format and the acquisition time per pixel must be reduced as much as possible. However, such experiment would require an appropriate filtering technique in the design of the system, in order to filter out ambient background light which may prevent the detection of the signal from the target.

Therefore, for a future practicality of this approach, a minimum number of operational wavelengths must be determined, and the pixel format and acquisition time per pixel must be reduced in order to minimise the overall acquisition time of a set of wavelengths.

References

1.   G. S. Buller, R. D. Harkins, A. McCarthy, P. A. Hiskett, G. R. MacKinnon, G. R. Smith, R. Sung, and A. M. Wallace, "Multiple wavelength time-of-flight sensor based on time-correlated single-photon counting," Rev. Sci. Instrum. **76**, 083112 (2005).

2.	A. M. Wallace, A. McCarthy, C. J. Nichol, X. Ren, S. Morak, D. Martinez-Ramirez, I. H. Woodhouse, and G. S. Buller, "Design and evaluation of multispectral LiDAR for the recovery of arboreal parameters," IEEE Trans. Geosci. Remote Sens. **52**, 8, 4942-4954 (2014).

3.	A. M. Wallace, C. J. Nichol, and I. H. Woodhouse, "Recovery of forest canopy parameters by inversion of multispectral LiDAR data," Remote Sens. **4**, 509-531 (2012).

4.	Y. Altmann, A. M. Wallace, and S. McLaughlin, "Spectral unmixing of multispectral LiDAR signals," IEEE Trans. Signal Process. **63**, 20, 5525-5534 (2015).

5.	R. C. Gonzalez, and R. E. Woods, *Digital image processing* (Pearson Education International, 2008).

6.	Y. Altmann, A. Maccarone, A. McCarthy, G. S. Buller, and S. McLaughlin, "Joint spectral clustering and range estimation for 3D scene reconstruction using multispectral LiDAR waveforms," in *European Signal Processing Conference (EUSIPCO)*(IEEE, Budapest, Hungary, August 2016).

7.	Y. Altmann, A. Maccarone, A. McCarthy, G. S. Buller, and S. McLaughlin, "Joint range estimation and spectral classification for 3D scene reconstruction using multispectral LiDAR waveforms," in *IEEE Statistical Signal Processing 2016* (Palma De Mallorca, June 2016).

8.	Y. Altmann, A. Maccarone, A. McCarthy, G. Newstadt, G. S. Buller, S. McLaughlin, and A. Hero, "Robust spectral unmixing of multispectral LiDAR waveforms," in *8th Workshop on Hyperspectral Image and Signal Processing: Evolution in Remote Sensing (WHISPERS)*(Los Angeles, USA, August 2016).

9.	Y. Altmann, A. Maccarone, A. Halimi, A. McCarthy, G. S. Buller, and S. McLaughlin, "Fast range estimation and material quantification from multispectral LiDAR waveforms," in *Sensor Signal Processing for Defence* (Edinburgh, UK, September 2016).

10.	O. Chapelle, B. Schölkopf, and A. Zien, *Semi-Supervised Learning* (The MIT Press, Cambridge, USA, 2006).

11.	P. S. Chhabra, A. Maccarone, A. McCarthy, A. M. Wallace, and G. S. Buller, "Discriminating underwater LiDAR target signatures using sparse multi-spectral depth codes," in *Sensor Signal Processing for Defence* (Edinburgh, UK, September 2016).

12.   R. S. Kingsley, *Photosynthetic pigments af algae* (Cambridge University Press, Cambridge, 1989).

13.   N. K. T. Photonics, "Fast wavelength switching using a SuperK SELECT and COMMAND (Application note)," (2012).

Chapter 9

Conclusions

9.1. Summary of conclusions

This Thesis presented work on the characterisation of a single-photon depth profiling system for imaging in highly scattering underwater environments. The system used the time of flight approach and the time-correlated single-photon counting technique (TCSPC). The system comprised a monostatic scanning transceiver fibre-coupled with a pulsed laser source and a silicon single-photon avalanche diode (Si-SPAD) used for detection of the returned optical signal. Laboratory-based measurements were performed over distances of less than two metres, achieving depth profiles at 9 attenuation lengths between the transceiver and target.

A brief review of the various systems developed to image man-made objects underwater was presented in Chapter 2. The main techniques used to obtain 2D and 3D images of objects underwater were described in order to explain how to limit the effects of back and forward scattered light when imaging in underwater environments. These techniques are based on temporal discrimination, spatial discrimination, or modulation discrimination. Most of the techniques shown demonstrated imaging at less than 4-5 attenuation lengths. However, a combination of these techniques allows imaging at a greater number of attenuation lengths. For example, pulsed-gated laser line scan as described in [1] allowed for 2D imaging at stand-off distances of up to approximately 7 - 7.5 attenuation lengths, but this came at the cost of using very high average laser power levels, of approximately 1.3 W. However, at 7.5 attenuation lengths the images showed poor contrast and spatial resolution, although it is worth noting that there was no attempt of post-processing the images, which may improve the results. At high scattering conditions, contrast and spatial resolution are significantly degraded due to the strong effects of scattering, and the target cannot be discerned. It is important to note that all the systems described use average optical powers in the range from few milli-watts to several Watts, mostly well in excess of eye-safety thresholds. The work presented in this thesis uses laser light levels at eye-safe conditions.

The work performed during this PhD project aimed to use the high sensitivity and precise temporal resolution of the TCSPC technique to provide high spatial and depth resolution imaging at stand-off distances equivalent to several optical attenuation lengths. To the best of the author's knowledge, the work described in this Thesis represents the first application of the TCSPC technique for underwater depth imaging and allowed for imaging in highly scattering underwater environments, achieving stand-off distances of up to 9 attenuation lengths using average optical powers in the sub-milliwatt range.

In order to provide a description of the technique used and the system, a review of the TCSPC technique is given in Chapter 3 explaining how picosecond optical transients can be measured in photon-starved regimes. Additionally, an overview of the main single-photon detectors was reported with particular attention to their key figures of merit, advantages, and limiting factors. Specific attention was given to silicon single-photon detectors, which were the detectors used in all the experiments reported in this Thesis. Si-SPADs are the best candidates for underwater imaging. At room temperature they offer high detection efficiencies in the visible wavelength range, which corresponds to a low attenuation for clear water and scattering environments. In addition, they offer low dark count rate, near room temperature operation and reliable long-term performance. Two different technologies of silicon detectors were used during this PhD project, a thick junction Si-SPAD manufactured by Perkin Elmer, and two thin junction Si-SPADs manufactured by Micro Photon Devices. The Perkin Elmer SPCM-AQR series thick junction offered a photon detection efficiency of approximately 65% at the wavelength $\lambda = 700$ nm, with a maximum dark count rate of 500 cps, as specified by the manufacturer. However, despite the high detection efficiency, the overall instrumental temporal response observed during the experiments was of the order of 530 ps. In order to improve the temporal response of the system, two thin junctions by MPD were tested during this project. Use of MPD thin junction SPADs in this system exhibited a jitter in the range $60 - 120$ ps, but this came at the cost of a lower detection efficiency than the thick junction SPADs. The two thin junction SPADs had a photon detection efficiency of up to 49% at $\lambda = 550$ nm, as stated by the manufacturer. In addition, the thin junctions MPD detectors include in the modules the appropriate circuitry to be electrically gated. Gated detectors offer the opportunity to control the deactivation of the detector at pre-determined time intervals

in order to exclude unwanted optical signals such as back-reflections in the system or backscattering events which may occur in highly scattering environments.

In order to examine the physical properties of the propagation media selected, Chapter 4 described the experiments performed to obtain transmittance and attenuation spectra of the water samples subsequently used for the depth profiles measurements. These preliminary measurements allowed for the selection of an operational wavelength in the range $525 - 690$ nm, depending on the level of scattering. At the same time, investigations of the settling times of the scattering agent used showed that this limited the maximum overall acquisition time for scans performed in different scattering conditions.

A full description of the system used to obtain the results reported in this Thesis was given in Chapter 5, as well with the alignment procedure followed before each experiment. Several configurations were studied in order to optimise the performance of the system and investigate its limitations. Preliminary measurements were performed using a thick junction SPAD detector in a free-running mode, meaning that back-reflections from the transceiver unit were detected, limiting the average optical power to the sub-microwatt region in order to not saturate the detector. As these preliminary measurements showed promise for measuring depth profiles of targets at stand-off distances equivalent to up to approximately 6 attenuation lengths, several modifications were performed to improve the performance of the system. A gated detection scheme was used in order to avoid detection of the back-reflections from the transceiver unit and allow for an increased average optical power. This configuration was implemented by replacing the thick junction SPAD with a thin junction SPAD detector, which offered a better temporal response even if this came at the cost of a slightly lower detection efficiency. This configuration allowed significantly higher average optical powers to be used (up to approximately 120 μW), providing a better signal-to-noise ratio (SNR) and faster data acquisition. In order to further improve the performance of the system, more modifications were performed including higher performance of the optical elements in the transceiver unit, and optimisation of the average optical power up to approximately 800 μW. Additionally, an improved data acquisition mode was implemented, resulting in less complicated electronics and less data storage memory usage, subsequently allowing for a greater number of pixels to be recorded. These

improvements allowed for scans of a plastic pipe target at stand-off distances up to 9 attenuation lengths to be obtained.

In addition, higher power levels were investigated and scans were performed using an average optical power of approximately 2.6 mW. This was accomplished with the use of the supercontinuum source in conjunction with optical filters instead of the AOTF. The use of the optical filters allowed for the selection of a 25 nm wide wavelength range centred at $\lambda = 690$ nm. In this case, high resolution scans of the plastic pipe at 8 attenuation lengths were achieved, showing all the features of the target in great detail. At 9 attenuation lengths, depth scans were possible but the depth and spatial resolutions were not preserved due to the high level of scattering which reduced the SNR.

Depth and spatial resolution were investigated, and the results showed that the smallest depth that could be resolved was approximately 300 µm when the target was placed at stand-off distances in the range 1 to 6 attenuation lengths. The achievable depth resolution decreased to a few millimetres as the level of scattering of the medium was increased so that the target was at a stand-off distance of 8 or 9 attenuation lengths. It is important to say that this study was performed with the configuration characterised by the lower average optical power investigated in this Thesis. Hence, these results established a lower limit for the achievable depth resolution which is strictly related to the instrumental response of the system, the attenuation of the environment, and the parameters chosen for the scan. Therefore, a higher average optical power may improve the achievable depth resolution. Studies on the spatial resolution showed that an angular resolution of approximately 60 µrad can be achieved in highly scattering underwater environments. Due to the limited field of view afforded by the transceiver unit, only a little degradation was observed in spatial resolution as the level of scattering was increased and the target was at a stand-off distance equivalent to 8 attenuation lengths.

Scans of the plastic pipe target were also performed at a stand-off distances equivalent to 10 attenuation lengths. However, a background component was introduced by the detector which was dependent on the count rate and could be related to afterpulsing [2]. This effect in conjunction with the high level of scattering, detected secondary back-reflections which contributed to the overall count rate, and the highly attenuated

return from the target, made imaging the target at 10 attenuation lengths not possible with the current system configuration.

All the depth profiles reported in Chapter 5 were formed using the pixel-wise cross correlation approach with no attempt to correlate neighbouring pixels. The problem of image reconstruction through use of spatial correlations was discussed in Chapter 6, which showed three different methods for the reconstruction of depth, intensity and reflectivity images. The first method was based on the sparseness of the Discrete Cosine Transform (DCT) domain [3], which allowed for the reconstruction of the depth and intensity images obtained with the cross-correlation approach. This method was used to investigate the implications of short overall acquisition times for scans in highly scattering environments. Different short acquisition times per pixel were extracted from an experimental scan of the target placed at 8 attenuation lengths, using 30 ms acquisition time per pixel, a 2.6 mW average optical power and a 240×240 pixel format. In this case, it was demonstrated that the DCT based approach allowed for a reduction in the overall acquisition time from approximately 30 minutes to only a few seconds, sufficiently short to allow implementation in a number of real underwater application scenarios. The same investigation was performed with the target placed at 9 attenuation lengths, but the high level of scattering meant that pixels containing only noise contribute to the reconstruction of the image, making the algorithm less successful. In order to investigate this higher attenuation level, Dr. Abderrahim Halimi developed two algorithms, the first based on Markov Chain Monte Carlo (MCMC) approach [4], and the second based on a Coordinate Descent Algorithm (CDA) [4]. The MCMC model generated an entire distribution that approximate the posterior distribution including appropriate priors, which comprised information about the attenuation of the environment and spatial correlation between neighbouring pixels. The algorithm was able to properly restore the depth of the plastic pipe target up to a stand-off distance equivalent to 8 attenuation lengths. When the target was placed at a stand-off distance equivalent to 9 attenuation lengths, the algorithm successfully preserved the contours of the target, although retaining some noise in the image. Although this approach was fully automatic, it required long processing times, of the order of approximately 500 seconds, when implemented using MATLAB R2015a on a computer with Intel(R) Core(TM) i7- 4790 CPU@3.60GHz and 32GB RAM. The CDA algorithm dealt with this problem, as it optimised the images generating only one point of the posterior distribution at each pixel. This approach allowed for a reduction

in the processing times to approximately 20 seconds, although the algorithm over-smoothed the depth image of the target at 9 attenuation lengths. In addition, both algorithms were able to restore the reflectivity of the target at stand-off distances equivalent to up to 7 attenuation lengths. At longer distances, the target reflectivity was difficult to evaluate because the performance of both algorithms was strongly affected by the estimation of the attenuation coefficient. This caused an overestimation of the target reflectance at 8 attenuation lengths, and a reflectance image at 9 attenuation lengths was not achieved.

A model based on the LiDAR equation [5] was developed in order to evaluate the system's time-of-flight ranging performance in water. The model evaluated the number of photon events in the highest bin in the histogram peak when addressing a single pixel, including in the evaluation several parameters such as average optical power, attenuation of the optical elements, detector photon efficiency and temporal response, wavelength, target reflectance, and attenuation of the environment. Several simulations were carried out in order to establish the maximum achievable scanning range. The results suggested that stand-off distances equivalent to 10 attenuation lengths can be achieved under optimum conditions, including average optical power in the 10s of mW and a high reflectivity target.

The potential of the system was investigated also for multispectral depth imaging. Several laboratory-based measurements were performed in free-space and in unfiltered tap water in order to validate bespoke algorithms for target classification and recognition. Several laboratory-based measurements were performed in free-space, using 33 wavelengths in the range 500 – 820 nm. Dr. Yoann Altmann developed two algorithms based on the MCMC approach [6-9]. One algorithm investigated target classification due to colour and shape of each component of the targets in free-space, based on the spectral signature estimated in the investigated wavelength range. The results demonstrated joint depth and spectral profiles, allowing for identification of spectral variations due to materials, colours, and orientation of the target surface. The second algorithm investigated quantification of colour abundances in targets, decomposing the spectra of the target elements in a linear combination of base materials in each pixel. The results demonstrated that the algorithm allowed for the quantification of material abundances, showing promise in target discrimination. Additional experiments were performed in unfiltered tap water, although due to the strong

attenuation of light in water a smaller operational wavelength range was chosen. In particular, 16 wavelengths were selected in the range from $\lambda = 500$ nm to $\lambda = 725$ nm. Puneet Chhabra and Prof. Andy Wallace developed an algorithm which builds a point cloud of the area scanned, resulting in a 3D plot combining depth and spectral information [10]. The main contribution of the algorithm is that it is able to discriminate the experimental target signatures in order to automatically identify both material and geometrical characteristics of the different objects in the scanned area.

9.2. Future work

Longer range depth images will be investigated with a new submerged transceiver in a controlled environment, and then in a real underwater environment. Dr. Aongus McCarthy is currently developing this new system design, which consists of three main parts: the transceiver, the watertight tube housing, and the support frame. The new optical design aims to overcome some of the limitations encountered during this PhD work, including minimising the detection of secondary back-reflections, a more uniformly illuminated field, and a wider optical field of regard. This will be accomplished by incorporating in the new design a pair of off-axis parabolic mirrors, which will replace the pair of relay lenses used between the galvanometer mirrors in the existing unit. The use of more reflecting optics will allow for less losses in the system, fewer back-reflections, easier alignment, and more straightforward change of operational wavelength.

However, several investigations can be performed with the existing system as described in this Thesis. In the results presented in the previous chapters, the target distance in attenuation lengths was increased acting only on the scattering properties of the medium, adding Maalox to unfiltered tap water. This means increasing the scattering albedo of the medium [11], resulting in a high background level. Therefore, future work will include investigating the case of targets placed at several attenuation lengths in a more absorbing medium. This can be accomplished adding an appropriate dye to unfiltered tap water similar to the previous work of Cochenour et al. [11]. In this case, attenuation measurements should be performed in order to identify the operational wavelength for which the propagation of light is optimised.

Additionally, with appropriate reconfiguration, the transceiver unit can operate with a detector array instead of the individual SPAD detector. Future work will include investigating the use of detector arrays for underwater imaging applications. This approach may improve the overall acquisition time, as the image of the target can be obtained with a pixel format equal to the array dimensions or by using structured illumination. However, this entails illuminating a wider area of the target, meaning that the use of a higher average optical power is necessary. In addition, the field of view in this case would be much wider than the case considered in this Thesis, hence it is likely that the forward and backscattered light will degrade contrast and spatial resolution. Therefore, such a configuration may have the advantage of fast acquisition times but at the cost of shorter achievable ranges. The use of Si CMOS SPAD detector arrays will be investigated to ascertain their ideal operating regime in underwater depth imaging scenarios.

In order to reduce the acquisition times at 9 attenuation lengths, further studies will be performed with the DCT, MCMC, and CDA approaches. Shorter acquisition times will be extracted from existing scans in order to investigate the effects of shorter measurement acquisition times on image quality in such a highly scattering environment. In addition, work is ongoing on the investigation of future applications of multispectral depth imaging. In particular, studies on the minimum number of wavelengths and short acquisition times will be performed in order to establish the limitations of the models.

References

1.   F. R. Dalgleish, F. M. Caimi, W. B. Britton, and C. F. Andren, "Improved LLS imaging performance in scattering-dominant waters," in *Ocean sensing and monitoring*, SPIE (2009).

2.   P. A. Hiskett, G. S. Buller, A. Y. Loudon, J. M. Smith, I. Gontijo, A. C. Walker, P. D. Townsend, and M. J. Robertson, "Performance and design of InGaAs/InP photodiodes for single-photon counting at 1.55 mm," Appl. Opt. **39**, 36, 6818-6829 (2000).

3.   R. C. Gonzalez, R. E. Woods, and S. L. Eddins, *Digital image processing using MATLAB* (McGraw Hill Education, 2010).

4.   A. Halimi, A. Maccarone, A. McCarthy, S. McLaughlin, and G. S. Buller, "Object depth profile and reflectivity restoration from sparse single-photon data acquired in underwater environments," arXiv: 1608.06143 (2016).

5.   C. Weitkamp, *Lidar - Range-Resolved Optical Remote Sensing of the Atmosphere* (Springer, 2005).

6.   Y. Altmann, A. Maccarone, A. McCarthy, G. S. Buller, and S. McLaughlin, "Joint spectral clustering and range estimation for 3D scene reconstruction using multispectral LiDAR waveforms," in *European Signal Processing Conference (EUSIPCO)*(IEEE, Budapest, Hungary, August 2016).

7.   Y. Altmann, A. Maccarone, A. McCarthy, G. S. Buller, and S. McLaughlin, "Joint range estimation and spectral classification for 3D scene reconstruction using multispectral LiDAR waveforms," in *IEEE Statistical Signal Processing 2016*(Palma De Mallorca, June 2016).

8.   Y. Altmann, A. Maccarone, A. McCarthy, G. Newstadt, G. S. Buller, S. McLaughlin, and A. Hero, "Robust spectral unmixing of multispectral LiDAR waveforms," in *8th Workshop on Hyperspectral Image and Signal Processing: Evolution in Remote Sensing (WHISPERS)*(Los Angeles, USA, August 2016).

9.   Y. Altmann, A. Maccarone, A. Halimi, A. McCarthy, G. S. Buller, and S. McLaughlin, "Fast range estimation and material quantification from multispectral LiDAR waveforms," in *Sensor Signal Processing for Defence*(Edinburgh, UK, September 2016).

10.   P. S. Chhabra, A. Maccarone, A. McCarthy, A. M. Wallace, and G. S. Buller, "Discriminating underwater LiDAR target signatures using sparse multi-spectral depth codes," in *Sensor Signal Processing for Defence* (Edinburgh, UK, September 2016).

11.   B. Cochenour, L. Mullen, and J. Muth, "Effect of scattering albedo on attenuation and polarization of light underwater," Opt. Lett. **35**, 12, 2088-2090 (2010).